

INAUGURAL - DISSERTATION

zur Erlangung der Doktorwürde der
Naturwissenschaftlich-Mathematischen Gesamtfakultät
der Ruprecht-Karls-Universität Heidelberg

A Quantum Chemical Look at Energy and Charge Transfer in N-Heteropolycycles

vorgelegt von

Jie Han

Master of Science

aus Changchun, China

Gutachter

Prof. Dr. Andreas Dreuw

Prof. Dr. Oriol Vendrell

Datum der mündlichen Prüfung

11. Mai 2020

Preface

For My Family

And

All The People Who Still Love Me

At My Most Unlovable

Abstract

The transport of charge and energy are two essential processes in optoelectronic devices. In this thesis, using quantum chemical methods, molecular properties, as well as charge and energy transfer performance are studied in novel N-heteropolycycles. N-heteropolycycles are formally N-doped heterocyclic nanographene segments. The position and number of the nitrogen substitution, as well as further modification, can fine-tune their molecular properties such as energy levels, diradical characters, and charge and energy transfer rates. For the investigation of energy transfer, particular interest lies in singlet fission (SF), which has the potential to dramatically increase solar cell efficiency by converting one singlet exciton to two free triplet excitons or a correlated triplet pair. In **chapter 3**, quantum chemical methods based on DFT and constrained DFT are applied to rationalize how SF is affected by systematic chemical modifications introduced into phenazinothiadiazoles (PTD). The results indicate that unlike unsubstituted tetracene, PTDs fulfill the energetic requirement of SF ($E(S_1) \geq 2 \times E(T_1)$), and the effective coupling can be up to 75.8 meV. Hence, PTDs are promising candidates for SF. In **chapter 4**, a single-reference DFT-based protocol is proposed to simulate the absorption spectra of excited states involved in SF. The resulting spectra show good agreement with the experiment. This could be helpful for the identification of various species in SF and the understanding of SF dynamics. On the other hand, N-heteroacenes are known as electron-poor counterparts of the acenes, and they are electron transport (n-type) materials. Since the charge transport moiety in bulk films of azaacenes is thought to be the radical anion, in **chapter 5**, the energetics, electronic structures, and spectroscopic properties of negatively charged N-heteroacenes are investigated. It is found that the anions of the azapentacenes and their derivatives are stable with respect to electron loss and disproportionation into the dianion and the neutral compound. This motivates a further look into their electron transport properties. The results of electron transfer integrals and charge mobilities are demonstrated in **chapter 6**. Excellent performance of electron transport has been proved for halogenated 6,13-Diethynyl-5,7,12,14-tetraazapentacenes, especially for the bromine and iodine derivatives.

Zusammenfassung

Ladungs- und Energietransfer sind zwei fundamentale Prozesse, die in optoelektronischen Halbleiterbauelementen ablaufen. In dieser Dissertation stelle ich meine quantenchemischen Untersuchungen zur Effizienz von Ladungs- und Energietransferprozessen in neuartigen N-Heteropolyzyklen als auch meine Studien zu deren molekularen Eigenschaften dar. N-Heteropolyzyklen sind formal betrachtet N-dotierte Nanographene. Durch die Position und Anzahl der Stickstoffsubstitutionen sowie auch durch andere Modifikationen am Nanographen, können dessen molekulare Eigenschaften wie z.B. Energieniveaus, Diradikal-Charakter und Ladungs- und Energietransferraten verändert bzw. eingestellt werden. Bei der Untersuchung von Energietransferprozessen wird ein besonderes Augenmerk auf die sogenannte Singulett-Spaltung – im Englischen Singlet Fission (SF) – gelegt werden. Der Grund hierfür liegt unter anderem darin, dass durch den Prozess des Singlet Fission die Effizienz von Solarzellen signifikant erhöht werden kann, nämlich aufgrund der Umwandlung eines Singulett-Exzitons in zwei Triplett-Exzitone oder ein korreliertes Triplett-Paar. **Kapitel 3** beschäftigt sich mit der Fragestellung, in wie fern der SF Prozess durch systematische chemische Modifikationen an Phenazinothiadiazolen (PTDs) beeinflusst wird. Für die Untersuchungen werden verschiedene quantenchemische Methoden basierend auf der Dichtefunktionaltheorie (DFT), u.a. die sogenannte constrained-DFT-Methode verwendet. Die Ergebnisse meiner Rechnungen weisen darauf hin, dass im Gegensatz zum unsubstituierten Tetrazen, PTDs die energetischen Voraussetzungen für SF nämlich, dass gilt: ($E(S_1) \geq 2 \times E(T_1)$), erfüllen und die effektive Kopplung bis zu 75.8 meV beträgt. Hieraus lässt sich schließen, dass PTDs vielversprechende Kandidaten für SF sind. In **Kapitel 4** wird eine Vorgehensweise zur Simulation von Absorptionsspektren von Systemen in denen SF abläuft vorgestellt. Die berechneten Spektren stimmen gut mit experimentellen Spektren überein. Dies ist ein vielversprechendes Ergebnis, da die Vorgehensweise nicht nur hilfreich bei der Identifikation verschiedener Arten angeregter Zustände die an SF Prozessen beteiligt sind sein kann, sondern über dies hinaus auch zu einem besseren Verständnis von SF Dynamiken beitragen kann. Auf der anderen Seite sind N-Heteroazene als elektronarme Pendants zu Azenen bekannt und sie sind

Elektrontransport-(n-Typ)-Materialien. Da angenommen wird, dass der molekulare Part in Azaazen Bulk-Schichten, in dem der Ladungstransport abläuft, das Radikal-Anion ist, diskutiere ich in **Kapitel 5** hauptsächlich die Energien, die elektronische Strukturen und spektroskopische Eigenschaften von negativ geladenen N-Heteroazenen. Es wird festgestellt, dass Anionen von Azapentacenen und Azapentacen Derivaten stabil gegenüber Elektronenverlust und Zerfall in Dianion und neutrale Verbindung ist. Dieses Resultat regt mich dazu an, die Elektrontransport-Eigenschaften dieser molekularen Systeme weiter und näher zu erforschen. In **Kapitel 6** werden die Ergebnisse der Berechnungen von Elektrontransfer Integralen und Ladungsträgermobilitäten vorgestellt und diskutiert. Für halogenierte 6,13-Diethynyl-5,7,12,14-tetraazapentacene, insbesondere für die bromierten und iodierten Derivate, wurde eine ausgezeichnete Performanz des Elektrontransports nachgewiesen.

Contents

Preface.....	i
Abstract.....	ii
Zusammenfassung.....	iii
Contents	v
1. Introduction.....	1
2. Theoretical Methods	5
2.1 Basic concepts of quantum chemistry.....	5
2.1.1 Stationary state Schrödinger equation for molecules	5
2.1.2 Born-Oppenheimer Approximation.....	6
2.2 Electronic ground-state methods.....	8
2.2.1 Hartree-Fock Theory	8
2.2.2 Configuration interaction.....	14
2.2.3 Perturbation theory	18
2.2.4 Density functional theory	21
2.3 Electronic excited-state methods	24
2.3.1 Single excitation configuration interaction (CIS).....	24
2.3.2 Time-dependent density functional theory	28
2.4 Basic theory of charge transfer and excitation energy transfer.....	33
2.4.1 Rate equations.....	33
2.4.2 Non-adiabatic coupling in adiabatic representation	34
2.4.3 Diabatic representation	36

2.4.4	Constrained density-functional theory—configuration interaction...	37
3.	Tailoring Ultrafast Singlet Fission by the Chemical Modification of Phenazinothiadiazoles.....	39
3.1	Abstract.....	39
3.2	Introduction.....	40
3.2.1	Molecular Geometries.....	44
3.3	Computational Methods.....	46
3.3.1	Excited-State Energies and Calculation of Transient Absorption Spectra.....	46
3.3.2	Diradical Character of the Ground State.....	46
3.3.3	Electronic Coupling Calculations.....	47
3.4	Results.....	50
3.5	Discussion.....	55
3.6	Conclusions.....	62
4.	Evaluation of Single-reference DFT-based Approaches on Spectroscopic Signatures of Excited States Involved in Singlet Fission.....	64
4.1	Abstract.....	64
4.2	Introduction.....	65
4.3	Computational Details.....	69
4.4	Results and Discussion.....	72
4.4.1	TIPS-Pentacene Monomer Calculated with TDDFT/TDA/UTDDFT	72
4.4.2	TIPS-Pentacene Monomer Calculated with QR-TDDFT/SLR-TDDFT/SF-TDDFT.....	85
4.4.3	BP0 Dimer Calculated with TDDFT/UTDDFT/BS-TDDFT.....	91

4.5 Conclusion	109
5. Theoretical Description and Prediction of Molecular Properties of <i>N</i> -Heteropolycycles.....	111
Abstract.....	112
5.1 Introduction.....	113
5.2 Computational Details	116
5.3 Results and Discussion	116
5.3.1 Azapentacenes	116
5.3.2 Br ₄ -TAP	126
5.3.3 bis-TAP.....	129
5.3.4 Quino-CF ₃	133
5.4 Conclusions.....	137
6. Theoretical Simulation of Electron Transport Process in Halogenated <i>N</i> -Heteroacenes.....	140
6.1 Abstract.....	140
6.2 Introduction.....	141
6.2.1 Acenes	141
6.2.2 <i>N</i> -Heteroacenes	143
6.2.3 Halogenated TIPS-TAP-Derivatives	144
6.2.4 Aim of this Work.....	145
6.3 Theory.....	146
6.3.1 Organic Semiconductors.....	146
6.3.2 Charge-Transport Mechanism	149
6.3.3 Reorganization Energy	151

6.3.4 Electronic Coupling.....	153
6.4 Methods.....	155
6.4.1 Analysis of Crystal Structures	155
6.4.2 Computational Details	156
6.5 Results and Discussion	157
6.5.1 Transfer Integrals.....	157
6.5.2 Reorganization Energies.....	163
6.5.3 Marcus Electron Transfer Rates	165
6.5.4 Electron Mobilities	166
6.6 Conclusion and Outlook	168
7. Global Summary and Outlook	170
Acknowledgments.....	171
References.....	173
Publications During Ph.D. Study	194

1. Introduction

The transport of charge and energy are two fundamental processes in semiconductor materials and optoelectronic devices.^[1] The creation, spatial redistribution, diffusion, and annihilation of charges and excitons, as well as reorganization of molecular geometries, are involved in the interconversion of electric and light energies. The understanding of transfer phenomena in molecular systems requires quantum chemical treatment that should not only be able to describe the properties of the ground state, but also characterize the electronic couplings and transfer rates between excited states. On the other hand, it is of great importance to discover novel materials that exhibit superior charge and energy transfer properties. Quantum chemical calculations provide an efficient and economical way to screen for the materials and predict the performance.

Organic semiconducting (optoelectronic) materials are organic materials with semiconductor properties, which is an interdisciplinary research frontier encompassing chemistry, physics, materials science. Organic photovoltaic materials have the advantages of low cost, easy processing, excellent flexibility, and large-scale production. They are widely used in organic electronic devices, such as field-effect transistors (OFETs),^[2-4] light-emitting diodes (OLEDs)^[5, 6], and solar cells (OSCs)^[7-10]. The research field of organic electronics started from the discovery of the electrical conductivity of p-type doped trans-polyacetylene by Shirakawa *et al.* in 1977.^[11] Since then, the research in the field of organic semiconductors and its application into technology resulted in the development of organic photovoltaics nowadays. Especially the ease of solution processing in comparison to inorganic semiconductors and the possibility of printing onto flexible substrates has triggered high interest in academia as well as industry.

Depending on the character of the major charge carrier, organic semiconductors can be classified into hole and electron transport materials. When the ionization energy closely matches the Fermi level of the electrode, the material can be assigned to the first category. In case the electron affinity lies in energetic proximity to the Fermi level of

the electrode, the molecule belongs to the class of electron-transport materials.^[3] The critical quantity that characterizes the charge transport properties of either class is the carrier mobility μ which describes the ability of a charge carrier to move within a bulk semiconductor under a given electric field.^[12]

While hole transport materials with high charge carrier mobilities are well-known, the development of effective electron transport materials still proves to be a challenge to the scientific community. However, in 2007 Winkler and Houk identified nitrogen-rich oligoacenes as potential candidates for n-channel semiconductors.^[13] Two years later, Bunz *et al.* experimentally verified this hypothesis by the synthesis of 6,13-Diethynyl-5,7,12,14-tetraazapentacene (TIPS-TAP).^[14] TIPS-TAP exhibits, in comparison to its carbon-analog, distinctly decreased frontier orbital energies, which results in the improved electron transport properties. The molecular class of azapentacenes, therefore, represents a promising approach in the development of novel electron transport materials with high charge carrier mobilities.

In conventional solar cells, the absorption of a photon generates a singlet exciton (S_1). The exciton can hop to the chromophore–acceptor interface, and then separate into a hole and an electron. However, due to radiative and radiationless decays from the singlet exciton to the ground state, the photoelectric conversion efficiency cannot surpass 33%, which is called Shockley–Queisser limit.^[15]

Singlet fission (SF) is a multiple exciton generation process in which a singlet exciton shares its energy with neighboring ground-state chromophores and splits into two triplet excitons.^[9, 10] Due to the doubled number and long lifetime of triplet excitons, it has been proposed that SF could provide a path to exceed the Shockley-Queisser limit.^[16] Therefore, SF can dramatically increase solar cell efficiency. Materials undergoing SF are promising candidates for next-generation solar cells.

SF has been a hot topic in recent years, but the debate regarding its underlying mechanism continues to today.^[9, 17-19] Figure 1.1 shows primary routes and processes for a dimer to undergo SF. The phenomenon initiates with the absorption of a photon to generate a bright singlet state S_1S_0 . S_1S_0 undergoes internal conversion to a dark state, which has been characterized by quantum chemical calculations based on multi-reference methods as two triplets coupled into an overall singlet, $^1(TT)$. The $^1(TT)$ state is often referred as the multiexciton or doubly excited state. Moreover, a recent

experiment found direct evidence for the existence of $^1(\text{TT})$ state using time-resolved two-photon photoemission (TR-2PPE) spectra.

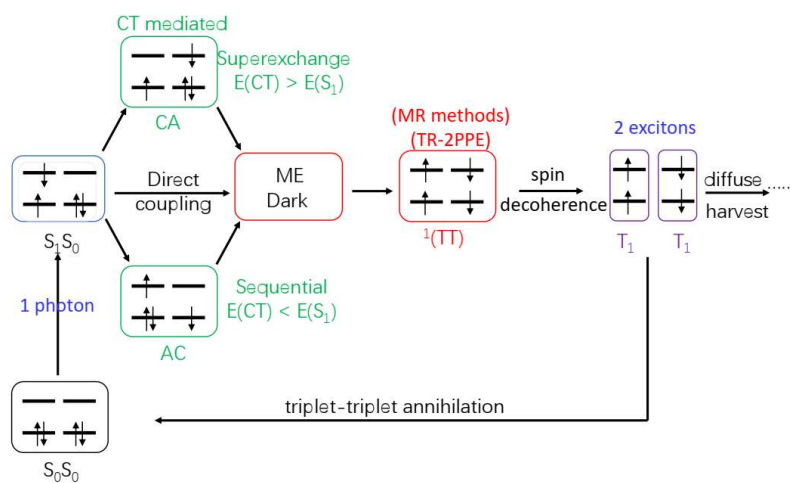


Figure 1.1. Schematic representation of routes and processes for singlet fission in a dimer.

It is generally agreed that the formation of $^1(\text{TT})$ can occur by the following mechanisms: (1) direct coupling between S_1 and $^1(\text{TT})$ states by a simultaneous two-electron process, or (2) S_1 converts to $^1(\text{TT})$ via the involvement of charge-transfer (CT) states as intermediates. If the CT state lies below S_1 , a sequential CT-mediated process might take place, whereas if the CT state is higher in energy than S_1 , a superexchange mechanism would be responsible.

Spin and electronic decoherence of the $^1(\text{TT})$ state can make it possible to populate a quintet state, $^5(\text{TT})$, or to generate two non-interacting free triplet states ($T_1 + T_1$). The free triplet states are then available for “harvesting” at the chromophore–acceptor interface. In the absence of either decoherence or triplet diffusion, the system can decay to the ground state through other channels such as triplet-triplet annihilation.

In this thesis, various quantum chemical methods have been applied to study molecular properties, as well as charge and energy transfer performance in novel N-heteropolycycles. A short introduction and description of the employed methods is given in **chapter 2**. In **chapter 3**, the effect of systematic chemical modifications introduced into phenazinothiadiazoles on SF is investigated. The results indicate that the electronic coupling is more sensitive to the geometrical changes than to the changes

in the electronic properties. In **chapter 4**, I evaluate the performance of various single-reference DFT-based approaches on the spectroscopic signatures of excited states involved in SF. The results show good feasibility and applicability of single-reference DFT-based methods, in combination with a rational choice of the exchange-correlation functional. In **chapter 5**, the molecular properties of a series of N-heteropolycycles and their charged species are investigated. Subsequently, the electron transport properties of TIPS-TAP and its halogenated derivatives are discussed in **chapter 6**.

2. Theoretical Methods

2.1 Basic concepts of quantum chemistry

2.1.1 Stationary state Schrödinger equation for molecules

Molecules are many-particle systems composed of nuclei and electrons. There are complicated interactions between the particles, which determine the motions of the nuclei and electrons, as well as properties of molecules.

If we apply quantum mechanics to study a molecule at a stationary state, we need to solve the time-independent Schrödinger equation (SE),

$$\hat{H}\Psi = E\Psi, \quad (2.1)$$

\hat{H} is the Hamiltonian of the molecular system. Solving equation (2.1) will result in eigenvalues of energies E_n and the corresponding eigenfunctions Ψ_n ($n = 0, 1, 2, \dots$). We can obtain information about the molecular system from the eigenvalues and eigenfunctions, such as energy levels, charge population, etc.

The Hamiltonian of a molecular system includes kinetic energies and potential energies of all electrons and nuclei. Therefore, the total Hamiltonian for a molecule in atomic units ($\hbar = m_e = e = 1$) is

$$\hat{H}^T = \sum_{\alpha} \frac{-1}{2M_{\alpha}} \nabla_{\alpha}^2 + \sum_i \frac{-1}{2} \nabla_i^2 + \sum_i \sum_{j>i} \frac{1}{r_{ij}} - \sum_{\alpha} \sum_i \frac{Z_{\alpha}}{r_{\alpha i}} + \sum_{\alpha} \sum_{\beta>\alpha} \frac{Z_{\alpha} Z_{\beta}}{R_{\alpha\beta}}, \quad (2.2)$$

where the first and second terms are kinetic energy operators of nuclei \hat{T}^N and electrons \hat{T}^e , respectively. The last three terms refer to potential energy operators between electrons and nuclei, \hat{V}^{ee} , \hat{V}^{eN} , and \hat{V}^{NN} . Therefore, the total Hamiltonian can be rewritten as

$$\hat{H}^T = \hat{T}^N + \hat{T}^e + \hat{V}^{ee} + \hat{V}^{eN} + \hat{V}^{NN}. \quad (2.3)$$

2.1.2 Born-Oppenheimer Approximation

The total Hamiltonian and the wave function of the molecule depend on the positions of nuclei \mathbf{R} and electrons \mathbf{r} , explicitly including the positions in equation (2.3), we get

$$\hat{H}^T(\mathbf{r}, \mathbf{R}) = \hat{T}^N(\mathbf{R}) + \hat{T}^e(r) + \hat{V}^{ee}(r) + \hat{V}^{eN}(\mathbf{r}, \mathbf{R}) + \hat{V}^{NN}(\mathbf{R}). \quad (2.4)$$

Since electrons move much faster than nuclei, due to relatively large nuclear mass, the Born-Oppenheimer (BO) Approximation (also called adiabatic approximation) states that one can separate the electronic and nuclear motions, and the total wave function can be expressed as a product of nuclear and electronic wave functions

$$\Psi^T = \Psi^N \Psi^e. \quad (2.5)$$

At any given instant, the position of the nuclei \mathbf{R} can be considered as fixed parameters that define an effective Hamiltonian for the electrons.

At any fixed configuration of the molecule, the electrons “feel” the effective Hamiltonian that depends on the positions of the nuclei,

$$\hat{H}^e(\mathbf{r}, \mathbf{R}) = \hat{T}^e(r) + [\hat{V}^{ee}(r) + \hat{V}^{eN}(\mathbf{r}, \mathbf{R}) + \hat{V}^{NN}(\mathbf{R})], \quad (2.6)$$

where \mathbf{R} denotes the dependence of \hat{H}^e on all the nuclear positions $\{\mathbf{R}\}$ at once. Hence \hat{H}^e is an operator in the electronic space that depends parametrically on \mathbf{R} . Its eigenvalues $E_i^e(\mathbf{r}, \mathbf{R})$ and eigenfunctions $\Psi_i^e(\mathbf{r}, \mathbf{R})$ satisfy the electronic SE

$$\hat{H}^e \Psi_i^e(\mathbf{r}, \mathbf{R}) = E_i^e \Psi_i^e(\mathbf{r}, \mathbf{R}). \quad (2.7)$$

This is the key concept of the BO Approximation, which allows us to compute the electronic structure of a molecule very accurately without saying anything about the quantum mechanics of the nuclei.

The $E_i^e(\mathbf{R})$ will give us the potential energy surfaces experienced by the nuclei. After solving the electronic SE, we can obtain the effective Hamiltonian and wavefunction for the nuclei,

$$\hat{H}^N |\Psi^N\rangle = [\hat{T}^N(\mathbf{R}) + E_i^e(\mathbf{R})] |\Psi^N\rangle = E^N |\Psi^N\rangle. \quad (2.8)$$

2.2 Electronic ground-state methods

The calculation of the ground state is the most fundamental procedure in quantum chemistry. In this section, different strategies for the description of the ground state are introduced. This section is mostly based on the books “*Modern Quantum Chemistry*” by A. Szabo and N. S. Ostlund,^[20] “*Ideas of Quantum Chemistry*” by L. Piela,^[21] as well as the literature by J. B. Foreman.^[22]

2.2.1 Hartree-Fock Theory

Slater determinant

For an N-electron system, considering the electrons are independent, the electronic wave function Ψ can be written as a Hartree-product,

$$\Psi_n^{HP} = \chi_1(X_1)\chi_2(X_2) \dots \chi_n(X_n). \quad (2.9)$$

where $\chi_n(X_n)$ is called a spin-orbital, which is the product of a spatial orbital and either the α or β spin function,

$$\begin{aligned} \chi_n(X_n) &= \phi_n(r)\alpha(s), \\ \chi_n(X_n) &= \phi_n(r)\beta(s). \end{aligned} \quad (2.10)$$

However, *Pauli exclusion or antisymmetry principle* states that if two electrons are in the same orbital, they must have opposite spin. In order to fulfill the antisymmetry principle, Slater determinants were introduced. Therefore, an N-electron wave function can be approximated by a single Slater determinant,

$$\psi^{SD} = \frac{1}{\sqrt{N!}} \begin{vmatrix} \chi_1(X_1) & \chi_1(X_2) & \dots & \chi_1(X_N) \\ \chi_2(X_1) & \chi_2(X_2) & \dots & \chi_2(X_N) \\ \vdots & \vdots & \ddots & \vdots \\ \chi_N(X_1) & \chi_N(X_2) & \dots & \chi_N(X_N) \end{vmatrix} \equiv |\chi_1\chi_2 \dots \chi_N\rangle, \quad (2.11)$$

where $\frac{1}{\sqrt{N!}}$ is a normalization factor. The single Slater determinant is constructed from one-electron spin-orbitals, which are also called molecular orbitals (MOs). The Slater determinant enforces an antisymmetric wavefunction. If we interchange the coordinates of two electrons, the corresponding rows of the Slater determinant have to be interchanged as well, which results in a change of the sign of the wave function.

Hartree-Fock energy

The Slater determinant based on the Hartree-product assumes that each electron moves independently, but it feels an effective Coulomb potential coming from the average positions of all electrons. This is also the underlying assumption of the Hartree-Fock (HF) theory; hence HF theory is also referred to as an independent particle model or a mean-field theory.

Now that we know the form of the electronic wave function (single Slater determinant), we can obtain the energy of the electronic system, by computing the expectation value of the electronic Hamiltonian,

$$E^e = \langle \Psi^{SD} | \hat{H}^e | \Psi^{SD} \rangle. \quad (2.12)$$

Using the physicist's notation, in which the complex conjugates are collected on the left-hand side of the operator, and integrating out the spin, we first define one-electron and two-electron operators and integrals.

A one-electron operator \hat{h} is expressed as follows

$$\hat{h}(\mathbf{r}_i) = -\frac{1}{2} \nabla_i^2 - \sum_A \frac{Z_A}{r_{iA}}. \quad (2.13)$$

For electron i , this operator yields its kinetic energy and its attraction to all nuclei.

The one-electron integrals are written as

$$\langle i | \hat{h} | j \rangle = \int \phi_i^*(\mathbf{r}_1) \hat{h}(\mathbf{r}_1) \phi_j(\mathbf{r}_1) d\mathbf{r}_1. \quad (2.14)$$

A two-electron operator $\hat{v}(i, j)$ can be defined as

$$\hat{v}(i, j) = \frac{1}{r_{ij}}, \quad (2.15)$$

which represents the Coulomb repulsion between electrons i and j .

The antisymmetrized two-electron integrals are then defined as

$$\langle ij||kl \rangle = \langle ij|kl \rangle - \langle ij|lk \rangle, \quad (2.16)$$

where

$$\langle ij|kl \rangle = \int \phi_i^*(\mathbf{r}_1) \phi_j^*(\mathbf{r}_2) \frac{1}{r_{12}} \phi_k(\mathbf{r}_1) \phi_l(\mathbf{r}_2) d\mathbf{r}_1 d\mathbf{r}_2. \quad (2.17)$$

The electronic Hamiltonian can be written in a much more straightforward way, as

$$\begin{aligned} \hat{H}^e &= \sum_i \hat{h}(i) + \sum_{i<j} \hat{v}(i, j) + \hat{V}^{NN} \\ &= \sum_i \hat{h}(i) + \frac{1}{2} \sum_{i,j} \hat{v}(i, j) + \hat{V}^{NN}. \end{aligned} \quad (2.18)$$

According to the BO approximation, V^{NN} is a constant for a given set of nuclear coordinates $\{\mathbf{R}\}$, and we will ignore it for now.

Therefore, using Slater-Condon rules (see next section), the HF energy E_{HF} in terms of integrals of the one- and two-electron operators can be expressed as:

$$\begin{aligned} E_{\text{HF}} &= \langle \Psi | \hat{H}^e | \Psi \rangle \\ &= \sum_i \langle i | \hat{h}(i) | i \rangle + \frac{1}{2} \sum_{i,j} \langle ij||ij \rangle \\ &= \sum_i \langle i | \hat{h}(i) | i \rangle + \frac{1}{2} \sum_{i,j} \langle ij|ij \rangle - \langle ij|ji \rangle \\ &= \sum_i h_{ii} + \frac{1}{2} \sum_{i,j} J_{ij} - \mathcal{K}_{ij}, \end{aligned} \quad (2.19)$$

where J_{ij} is called ‘‘Coulomb integral’’, which refers to the Coulomb repulsion between electron 1 in orbital i and electron 2 in orbital j ; \mathcal{K}_{ij} is the ‘‘Exchange integral’’.

Slater-Condon rules

To evaluate the expectation value of equation (2.12), we can apply the Slater-Condon rules. Briefly, Slater-Condon rules (also called Slater’s rules) allow us to express the matrix elements of the electronic Hamiltonian $H_{ij} = \langle \Psi_i | \hat{H} | \Psi_j \rangle$ in terms of one- and two electron integrals. Since they are needed later in many derivations, the rules are listed below. The derivation of these rules can be found in Szabo’s book, section 2.3.4. After the determinants are arranged in maximum coincidence, we can see how many spin orbitals they differ by, and the following rules can be applied:

1. Identical Determinants:

$$\begin{aligned} \langle \Psi_1 | \hat{H} | \Psi_1 \rangle &= \sum_m^N \langle m | \hat{h} | m \rangle + \sum_{m>n}^N \langle mn || mn \rangle \\ &= \sum_m^N h_{mm} + \frac{1}{2} \sum_{m,n}^N \langle mn || mn \rangle. \end{aligned} \quad (2.20)$$

2. Determinants that Differ by One Spin Orbital:

$$\begin{aligned} |\Psi_1\rangle &= |\dots mn \dots\rangle, \\ |\Psi_2\rangle &= |\dots pn \dots\rangle, \\ \langle \Psi_1 | \hat{H} | \Psi_2 \rangle &= \sum_m^N \langle m | \hat{h} | p \rangle + \sum_n^N \langle mn || pn \rangle \\ &= \sum_n^N \langle mn || pn \rangle. \end{aligned} \quad (2.21)$$

3. Determinants that Differ by Two Spin Orbitals:

$$|\Psi_1\rangle = |\dots mn \dots\rangle, \quad (2.22)$$

$$|\Psi_2\rangle = |\dots pq \dots\rangle,$$

$$\langle\Psi_1|\hat{H}|\Psi_2\rangle = \langle mn||pq\rangle.$$

4. Determinants that Differ by More than Two Spin Orbitals:

$$|\Psi_1\rangle = |\dots mno \dots\rangle,$$

$$|\Psi_2\rangle = |\dots pqr \dots\rangle, \quad (2.23)$$

$$\langle\Psi_1|\hat{H}|\Psi_2\rangle = 0.$$

Hartree-Fock equation

Minimizing the HF energy with respect to the orbitals results in the HF equations for the orbitals,

$$\left[\hat{h}_i(r_1) + \sum_i^N \hat{J}(r_1) - \hat{K}(r_1) \right] \psi_i(r_1) = \epsilon_i \psi_i(r_1). \quad (2.24)$$

Here we further define the Fock operator

$$\hat{f}(r_1) = \hat{h}_i(r_1) + \sum_i^N \hat{J}(r_1) - \hat{K}(r_1). \quad (2.25)$$

The Fock operator \hat{f} working on any molecular orbital ψ_i yields the orbitals energy ϵ_i times the orbital

$$\hat{f}(r_1)\psi_i(r_1) = \epsilon_i\psi_i(r_1). \quad (2.26)$$

It is noted that the sum of the orbital energies ϵ_i is not equivalent to the total energy of the ground state. Using Slater-Condon rule and adding up the orbital energies ϵ_i , we get,

$$\sum_i^N \epsilon_i = \sum_i^N \langle i | \hat{f} | i \rangle = \sum_i^N \langle i | \hat{h}_i | i \rangle + \sum_{i,j}^N \langle ij || ij \rangle, \quad (2.27)$$

whereas the total energy writes as equation (2.19),

$$E_{\text{HF}} = \sum_i \langle i | \hat{h}_i | i \rangle + \frac{1}{2} \sum_{i,j} \langle ij | ij \rangle - \langle ij | ji \rangle. \quad (2.28)$$

We can see that the difference lies in the factor $\frac{1}{2}$ in the second term.

Roothan-Hall equation

Now we introduce a basis set and express orbitals as a linear combination of atomic orbitals (LCAO),

$$\psi_i = \sum_{\mu} C_{\mu i} \varphi_{\mu}. \quad (2.29)$$

We can then convert the HF equation into a much simpler linear algebra problem,

$$\begin{aligned} \hat{f}(r_1) \psi_i(r_1) &= \epsilon_i \psi_i(r_1), \\ \hat{f} \sum_{\mu} C_{\mu i} \varphi_{\mu} &= \epsilon_i \sum_{\mu} C_{\mu i} \varphi_{\mu}. \end{aligned} \quad (2.30)$$

When multiplying $\varphi_{\lambda i}^*$ from the right and integrating, equation (2.30) is transformed into a matrix equation,

$$\sum_{\lambda} F_{\mu\lambda} C_{\mu i} = \epsilon_i \sum_{\lambda} S_{\mu\lambda} C_{\mu i}, \quad (2.31)$$

which is called the Roothaan equation. $F_{\mu\lambda} = \langle \mu | f | \lambda \rangle$ represents the Fock matrix and $S_{\mu\lambda} = \langle \mu | \lambda \rangle$ is the overlap between the atomic orbitals φ_{μ} and φ_{λ} .

If the basis functions are orthonormal to each other, then $S_{\mu\lambda} = 1$ and the Roothaan equation can be written in a shorter form as

$$\mathbf{FC} = \epsilon_i \mathbf{C}. \quad (2.32)$$

As can be seen from the Roothaan equations, \mathbf{C} collects the expansion coefficients for each orbital expressed as a LCAO. However, \mathbf{C} depends on \mathbf{F} , and \mathbf{F} depends on its own eigenvectors \mathbf{C} , to solve the Roothaan equation, the self-consistent field (SCF) method is usually employed.

Remember that HF *replaces* the instantaneous electron-electron repulsion with the repulsion of each electron with an average electron charge cloud. However, according to Coulomb's law, electrons repel each other, with the repulsion energy r_{ij}^{-1} . This introduces an *error* in the wavefunction and the energy. The energy error is called the *correlation energy*. The correlation energy is defined as the difference between the exact energy and HF energy.

$$E_{corr} = \epsilon_0 - E_{HF}. \quad (2.33)$$

2.2.2 Configuration interaction

Full configuration interaction

To compute the exact energy and include electronic correlation, one can allow for the explicitly correlated motion of multiple electrons. This can be realized by the full configuration interaction (FCI) method. In FCI, the exact ground state wave function Φ^0 is represented as a linear combination of all possible substitutions (or excitations) of n electrons from the HF "reference" wave function Ψ_0^{HF} ,

$$\Phi_0 = c_0 |\Psi_0^{HF}\rangle + \sum_{i,a} c_i^a |\Psi_i^a\rangle + \sum_{i<j,a<b} c_{ij}^{ab} |\Psi_{ij}^{ab}\rangle + \sum_{\substack{i<j<k, \\ a<b<c}} c_{ijk}^{abc} |\Psi_{ijk}^{abc}\rangle + \dots, \quad (2.34)$$

where $|\Psi_i^a\rangle$ means the Slater determinant formed by replacing spin-orbital i in $|\Psi_0^{HF}\rangle$ with spin-orbital a , etc., with the indices i, j, k, l referring to the occupied orbitals and a, b, c, d to the virtual orbitals.

Impose intermediate normalization $\langle\Psi_0^{HF}|\Phi^0\rangle = 0$, then $c_0=1$. And include a factor $(1/n!)^2$ in front of the summation to remove the restriction (e.g., $i < j, a < b$, etc.) and ensure a given excited determinant is included in the sum only once.

$$\Phi_0 = |\Psi_0^{HF}\rangle + \left(\frac{1}{1!}\right)^2 \sum_{ia} c_i^a |\Psi_i^a\rangle + \left(\frac{1}{2!}\right)^2 \sum_{ijab} c_{ij}^{ab} |\Psi_{ij}^{ab}\rangle + \left(\frac{1}{3!}\right)^2 \sum_{\substack{abc \\ ijk}} c_{ijk}^{abc} |\Psi_{ijk}^{abc}\rangle + \dots \quad (2.35)$$

Φ^0 can also be written in the following shorthand notation,

$$\Phi_0 = |0\rangle + c_s|S\rangle + c_d|D\rangle + c_t|T\rangle + c_q|Q\rangle + \dots, \quad (2.36)$$

where $|S\rangle, |D\rangle, |T\rangle$ and $|Q\rangle$ represent blocks of singly, doubly, triply, and quadruply excited determinants, respectively.

Then the general structure of the CI matrix is

$$\begin{pmatrix} \langle 0|\mathcal{H}|0\rangle & \langle 0|\mathcal{H}|S\rangle & \langle 0|\mathcal{H}|D\rangle & \langle 0|\mathcal{H}|T\rangle & \langle 0|\mathcal{H}|Q\rangle & \dots \\ \langle S|\mathcal{H}|0\rangle & \langle S|\mathcal{H}|S\rangle & \langle S|\mathcal{H}|D\rangle & \langle S|\mathcal{H}|T\rangle & \langle S|\mathcal{H}|Q\rangle & \dots \\ \langle D|\mathcal{H}|0\rangle & \langle D|\mathcal{H}|S\rangle & \langle D|\mathcal{H}|D\rangle & \langle D|\mathcal{H}|T\rangle & \langle D|\mathcal{H}|Q\rangle & \dots \\ \langle T|\mathcal{H}|0\rangle & \langle T|\mathcal{H}|S\rangle & \langle T|\mathcal{H}|D\rangle & \langle T|\mathcal{H}|T\rangle & \langle T|\mathcal{H}|Q\rangle & \dots \\ \langle Q|\mathcal{H}|0\rangle & \langle Q|\mathcal{H}|S\rangle & \langle Q|\mathcal{H}|D\rangle & \langle Q|\mathcal{H}|T\rangle & \langle Q|\mathcal{H}|Q\rangle & \dots \\ \vdots & \vdots & \vdots & \vdots & \vdots & \ddots \end{pmatrix} \quad (2.37)$$

Reducing the size of the Full configuration interaction space

In order to perform the CI calculations in a reasonable time, the FCI matrix needs to be truncated. We can first simplify the matrix by the fact that many of the off-diagonal blocks are zero.

First, the Hamiltonian matrix \mathbf{H} is Hermitian; if only real orbitals are used, as is usually the case, then the Hamiltonian is also symmetric.

$$\langle 0|H|S\rangle = \langle S|H|0\rangle, \langle D|H|S\rangle = \langle S|H|D\rangle. \quad (2.38)$$

Second, Brillouin's theorem states that singly excited determinants do not couple with the HF ground state,

$$\langle \Psi_0^{HF} | \hat{H} | \Psi_i^a \rangle = h_{ia} + \sum_{k \in \Psi_0} \langle ik || ak \rangle = F_{ia} = 0, \quad (2.39)$$

where the Fock matrix element F_{pq} is defined as

$$F_{pq} = h_{pq} + \sum_{k \in \Psi_0} \langle pk || qk \rangle. \quad (2.40)$$

Therefore,

$$\langle 0|H|S\rangle = \langle S|H|0\rangle = 0. \quad (2.41)$$

Furthermore, according to the Slater Condon rules, matrix elements of the Hamiltonian operator are zero, when determinants differ by more than two spin-orbitals

$$\langle 0|H|T\rangle = \langle T|H|0\rangle = 0, \langle S|H|Q\rangle = \langle Q|H|S\rangle = 0. \quad (2.42)$$

Therefore, the FCI matrix becomes a diagonally dominated matrix

$$\mathbf{H} = \begin{matrix} \langle \Phi_0 | \\ \langle S | \\ \langle D | \\ \langle T | \\ \langle Q | \\ \vdots \end{matrix} \begin{bmatrix} \langle \Phi_0 | H | \Phi_0 \rangle & & & & & \dots \\ 0 & \langle S | H | S \rangle & & & & \dots \\ \langle D | H | \Phi_0 \rangle & \langle D | H | S \rangle & \langle D | H | D \rangle & & & \dots \\ 0 & \langle T | H | S \rangle & \langle T | H | D \rangle & \langle T | H | T \rangle & & \dots \\ 0 & 0 & \langle Q | H | D \rangle & \langle Q | H | T \rangle & \langle Q | H | Q \rangle & \dots \\ \vdots & \vdots & \vdots & \vdots & \vdots & \vdots \end{bmatrix} \quad (2.43)$$

Moreover, there are still some blocks $\langle X|H|Y\rangle$ which are not necessarily zero; for example, the matrix element $\langle \Psi_{ij}^{ab} | H | \Psi_{klmn}^{cdef} \rangle$ of the block $\langle D|H|Q\rangle$, will be nonzero only if i and j are contained in the set $\{k, l, m, n\}$, and if a and b are contained in the set $\{c, d, e, f\}$.

Configuration interaction singles and doubles

Since only the doubles directly couple with the Hartree-Fock reference, double excitations are expected to make the most substantial contributions to the CI wavefunction. Singles are much less critical to the energy than doubles, however, because they have relatively small number and greater importance in describing one-electron properties such as dipole moment, singles are generally included in CI treatments

Therefore, in practice, one always only includes “singly and doubly excited” Slater determinants into the total wave function, then we have total CI Singles and Doubles (CISD) wave function

$$\begin{aligned} |\Phi_{CISD}\rangle &= |\Psi_0^{HF}\rangle + \sum_{i,a} c_i^a |\Psi_i^a\rangle + \sum_{i<j,a<b} c_{ij}^{ab} |\Psi_{ij}^{ab}\rangle \\ &= |\Psi_0^{HF}\rangle + |\Psi_{CIS}\rangle + |\Psi_{CID}\rangle. \end{aligned} \quad (2.44)$$

Excitation operators

Now we define excitation operators as operations act on a reference determinant to generate excited determinants times coefficients,

$$T_1|\Psi_0\rangle = \sum_{ia} t_i^a |\Psi_i^a\rangle, \quad (2.45)$$

$$T_2|\Psi_0\rangle = \frac{1}{4} \sum_{ijab} t_{ij}^{ab} |\Psi_{ij}^{ab}\rangle. \quad (2.46)$$

The doubly-excited determinants have two distinct contributions:

1. from pure double excitations: *connected* doubles, t_{ij}^{ab} is referred to as a *connected cluster amplitude*.

$$T_2|\Psi_0\rangle = \frac{1}{4} \sum_{ijab} t_{ij}^{ab} |\Psi_{ij}^{ab}\rangle. \quad (2.47)$$

2. from products of single excitations: *disconnected* doubles, products such as $t_i^a t_j^b$ are referred to as *disconnected cluster amplitudes*. Disconnected terms vanish whenever one or several indices are identical.

$$T_1^2|\Psi_0\rangle = \sum_{ia} \sum_{jb} t_i^a t_j^b |\Psi_{ij}^{ab}\rangle. \quad (2.48)$$

The total amplitude for a specific excitation class is hence the sum of all *connected and disconnected amplitudes*.

In the configuration-interaction (CI) theory, we retain only the connected excitations.

With this notation, CISD is just

$$|\Phi_{CISD}\rangle = (1 + T_1 + T_2)|\Psi_0^{HF}\rangle. \quad (2.49)$$

2.2.3 Perturbation theory

Except for CI, perturbation theory is another powerful tool to approximate the correlation energy of molecules. The general concept of Rayleigh-Schrödinger Perturbation Theory (RSPT) is a partitioning of the exact Hamiltonian H into two parts. The first part H_0 , with known exact eigenfunctions, and the second part V , which is called perturbation.

$$H_{ele}|\Psi_0\rangle = (H_0 + V)|\Psi_0\rangle = E_0|\Psi_0\rangle. \quad (2.50)$$

Expand the exact eigenfunctions and eigenvalues as a Taylor series in λ , and set $\lambda = 1$,

$$E_0 = E_0^{(0)} + E_0^{(1)} + E_0^{(2)} + \dots, \quad (2.51)$$

$$|\Psi_0\rangle = |\Psi_0^0\rangle + |\Psi_0^1\rangle + |\Psi_0^2\rangle + \dots, \quad (2.52)$$

where the subscript 0 indicates the ground state, and the superscript (0) is the reference function.

In the case of Møller-Plesset (MP) perturbation theory (PT), the zeroth-order Hamiltonian is the Fock operator

$$H_0 = F = \sum_i^N f_i, \quad (2.53)$$

while the perturbation V is the difference between the HF mean-field interaction and the exact $\frac{1}{r_{ij}}$ operator

$$V = H_{ele} - F = \sum_{i<j} \frac{1}{r_{ij}} - \sum_i v^{HF}(i). \quad (2.54)$$

Since the canonical MOs are eigenvectors of f ,

$$f_i \phi_i = \varepsilon_i \phi_i, \quad (2.55)$$

then the zeroth-order problem is

$$H_0 |\Psi_0^0\rangle = E_0^{(0)} |\Psi_0^0\rangle = \sum_i^N \varepsilon_i |\Psi_0^0\rangle. \quad (2.56)$$

The first-order energy correction is

$$E_0^{(1)} = \langle \Psi_0^0 | V | \Psi_0^0 \rangle = \langle \Psi_0^0 | H_{ele} | \Psi_0^0 \rangle - \langle \Psi_0^0 | H_0 | \Psi_0^0 \rangle = E_0^{HF} - \sum_i^N \varepsilon_i, \quad (2.57)$$

which is just the difference between the HF energy E^{HF} and the sum of MOs' energies.

The second-order energy correction can be expressed as

$$\begin{aligned}
E_0^{(2)} &= \Delta E^{\text{MP2}} \\
&= \langle \Psi_0^{(0)} | V | \Psi_0^{(1)} \rangle \\
&= \sum_{n \neq 0} \frac{|\langle \Psi_0^{(0)} | V | \Psi_n^{(0)} \rangle|^2}{E_0^{(0)} - E_n^{(0)}},
\end{aligned} \tag{2.58}$$

Because singly excited Slater determinants do not contribute due to the Brillouin theorem, and we only have $\langle \Psi_0 | V | \Psi_{ij}^{ab} \rangle \neq 0$, the second-order formula is written in a basis of doubly excited Slater determinants.

$$\Delta E^{\text{MP2}} = \sum_{\substack{i < j \\ a < b}} \frac{|\langle \Psi_0^{(0)} | V | \Psi_{ij}^{ab} \rangle|^2}{\epsilon_i + \epsilon_j - \epsilon_a - \epsilon_b}. \tag{2.59}$$

Using Slater Condon rules, and expanding the numerator in terms of occupied and virtual orbitals, we obtain

$$\begin{aligned}
\Delta E^{\text{MP2}} &= \sum_{\substack{i < j \\ a < b}} \frac{|\langle ij || ab \rangle|^2}{\epsilon_i + \epsilon_j - \epsilon_a - \epsilon_b} \\
&= \sum_{\substack{i < j \\ a < b}} \frac{|\langle ij || ab \rangle|^2}{\Delta_{ab}^{ij}} \\
&= \frac{1}{4} \sum_{ijab} \frac{|\langle ij || ab \rangle|^2}{\Delta_{ab}^{ij}}.
\end{aligned} \tag{2.60}$$

Since the eigenfunctions of H_0 form an orthonormal complete set of functions and they can be applied to express any other function, the wave function $|\Psi_0^{(1)}\rangle$ is given by

$$|\Psi_0^{(1)}\rangle = \sum_{n \neq 0} c_n^{(1)} |\Psi_n^{(0)}\rangle. \tag{2.61}$$

as shown above, $|\Psi_0^{(1)}\rangle$ in MP2 is essentially a linear combination of $|\Psi_{ij}^{ab}\rangle$,

$$\begin{aligned}
|\Psi_0^{(1)}\rangle &= T_2 |\Psi_0^{(0)}\rangle \\
&= \frac{1}{4} \sum_{ijab} t_{ij}^{ab} |\Psi_{ij}^{ab}\rangle \\
&= \frac{1}{4} \sum_{ijab} \frac{\langle ij || ab \rangle}{\Delta_{ab}^{ij}} |\Psi_{ij}^{ab}\rangle,
\end{aligned} \tag{2.62}$$

where t_{ij}^{ab} is defined as MP2 *t-amplitude*

$$t_{ij}^{ab} = \frac{\langle ij || ab \rangle}{\Delta_{ab}^{ij}}. \tag{2.63}$$

2.2.4 Density functional theory

Density Functional Theory (DFT) is a theory that uses the electron density distribution as the primary variable to study the ground-state properties of multi-particle systems. It started from the Thomas-Fermi model in the 1920s, and combined with Hohenberg-Kohn theorems into modern DFT. Since the establishment of DFT under the local density approximation in the 1960s (1964), and the derivation of the famous Kohn-Sham (KS) equation, DFT has been the most popular tool for computing electronic structures and properties in the field of condensed matter physics. Since DFT uses the electron density as the basic variable, rather than the electronic wave function, it dramatically simplifies theoretical calculations and opens up a new way for the development of quantum chemistry.

Hohenberg-Kohn theorems

The principle of DFT is: physical properties of the ground states of atoms and molecules can be described as a function of electron density $\rho(\mathbf{r})$. In 1964, using the Thomas-Fermi model, Hohenberg and Kohn proposed the famous Hohenberg-Kohn (HK) first and second theorems. These two theorems are the theoretical basis of DFT and can be summarized as:

The first HK theorem: “the ground state of any interacting many-particle system with a given fixed inter-particle interaction is a unique functional of the electron density $\rho(\mathbf{r})$ ” (Hohenberg and Kohn, 1964). That is, $\rho(\mathbf{r})$ determines the physical properties of the ground state of the system.

The second HK second theorem: there is an energy functional $E[\rho]$ for non-degenerate ground states, the energy functional takes the minimum value when the density is the true ground state density. The variation of the energy functional with respect to the density gives the energy $E_G[\rho]$ of the ground state of the system.

The Hamiltonian of a multi-electron system is

$$\hat{H} = \hat{T} + \hat{U} + \hat{V}, \quad (2.64)$$

where \hat{T} represents the kinetic energy term of electrons, \hat{U} represents the Coulomb repulsion term, and \hat{V} represents the local potential $v(\mathbf{r})$, which is the effect of the external field. For a given local potential $v(\mathbf{r})$, the energy $E[\rho]$ is defined as a function of the electron density $\rho(\mathbf{r})$:

$$E(\rho) \equiv \int d\mathbf{r} v(\mathbf{r})\rho(\mathbf{r}) + \langle \phi | T + U | \phi \rangle. \quad (2.65)$$

Further define an unknown functional which is unrelated to the external field $F[\rho]$,

$$F[\rho] \equiv \langle \phi | T + U | \phi \rangle, \quad (2.66)$$

$$F[\rho] = T[\rho] + \frac{1}{2} \iint d\mathbf{r} d\mathbf{r}' \frac{\rho(\mathbf{r})\rho(\mathbf{r}')}{|\mathbf{r} - \mathbf{r}'|} + E_{XC}[\rho]. \quad (2.67)$$

The first two terms of equation (2.67) are the kinetic energy of the electrons and the Coulomb repulsion between them, the last term $E_{XC}[\rho]$ is called exchange-correlation energy, it represents all the interaction terms which are not included in the non-interacting electron model.

Kohn-Sham equations

Kohn and Sham replaced the corresponding terms in the interacting electronic Hamiltonian with the non-interacting electron model, and were able to include the differences to interacting electrons into the exchange-correlation functional $E_{XC}[\rho]$, thereby converting them into a single-electron equation:

$$\rho(\mathbf{r}) = \sum_{i=1}^N |\phi_i(\mathbf{r})|^2. \quad (2.68)$$

The $T[\rho]$ term is replaced by kinetic energy functional of the non-interacting electrons $T_s[\rho]$,

$$T_s[\rho] = \sum_{i=1}^N \int d\mathbf{r} \phi_i^*(\mathbf{r}) (-\nabla^2) \phi_i(\mathbf{r}). \quad (2.69)$$

Substitute the variation of the energy with the variation of $\phi_i(\mathbf{r})$, we get

$$\frac{\delta\{E[\rho(\mathbf{r})] - \sum_{i=1}^N E_i[\int d\mathbf{r} \phi_i^*(\mathbf{r}) \phi_i(\mathbf{r}) - 1]\}}{\delta\phi_i}(\mathbf{r}) = 0, \quad (2.70)$$

$$\left\{ -\nabla^2 + v(\mathbf{r}) + \int d\mathbf{r}' \frac{\rho(\mathbf{r}')}{|\mathbf{r} - \mathbf{r}'|} + \frac{\delta E_{XC}[\rho]}{\delta\rho(\mathbf{r})} \right\} \phi_i(\mathbf{r}) = E_i \phi_i(\mathbf{r}). \quad (2.71)$$

Define an effective potential as,

$$V_{eff}(\mathbf{r}) = v(\mathbf{r}) + \int d\mathbf{r}' \frac{\rho(\mathbf{r}')}{|\mathbf{r} - \mathbf{r}'|} + \frac{\delta E_{XC}[\rho]}{\delta\rho(\mathbf{r})}. \quad (2.72)$$

Equations (2.68), (2.71), and (2.72) are called Kohn-Sham equations. Solving equation (2.71) and equation (2.68) will give us the electron density of the ground state.

2.3 Electronic excited-state methods

Theoretical calculations of excited states are essential for obtaining spectroscopic properties and investigating photochemical reactions. Since there is great diversity in electronic excited-state methods, here I will only briefly introduce approaches based on a single-reference ansatz. This section is based mainly on the literature of *A. Dreuw et. al.*^[23, 24] and the book “Fundamentals of time-dependent density functional theory” by *Marques et. al.*^[25]

2.3.1 Single excitation configuration interaction (CIS)

CIS Matrix

Except for the application to the electronic ground state, CI can also be used to describe excited states. The excited states can be obtained by the higher eigenvalues and respective eigenvectors of the CI matrix.

Expanding the block represented by $\langle S|H|S\rangle$ yields the CIS matrix. The matrix is hermitian if real basis functions are employed as usual.

$$\begin{pmatrix} \langle \Psi^0 | \mathcal{H} | \Psi^0 \rangle & 0 & 0 & \dots \\ 0 & \langle \Psi_i^a | \mathcal{H} | \Psi_i^a \rangle & \langle \Psi_j^b | \mathcal{H} | \Psi_i^a \rangle & \dots \\ 0 & \langle \Psi_i^a | \mathcal{H} | \Psi_j^b \rangle & \langle \Psi_j^b | \mathcal{H} | \Psi_j^b \rangle & \dots \\ \vdots & \vdots & \vdots & \ddots \end{pmatrix} \quad (2.73)$$

CIS energy equations

The CIS excited state wave function is a linear combination of all possible singly excited Slater determinants.

$$|\Psi_{CIS}\rangle = \sum_{i,a} c_i^a |\Psi_i^a\rangle. \quad (2.74)$$

Plugging Equation (2.74) to the time-independent electronic Schrödinger equation gives us

$$\sum_{i,a} H |\Psi_i^a\rangle c_i^a = E_{CIS} \sum_{ia} |\Psi_i^a\rangle c_i^a, \quad (2.75)$$

the CIS total energy E_{CIS} can be obtained as a projection onto space of singly excited determinants, that is, multiplying Equation (2.75) from the left with $\langle \Psi_j^b |$, yields

$$|\Psi_{CIS}\rangle = \sum_{i,a} c_i^a |\Psi_i^a\rangle, \quad (2.76)$$

$$\sum_{ia} \langle \Psi_j^b | H |\Psi_i^a\rangle c_i^a = E_{CIS} \sum_{ia} \langle \Psi_j^b | \Psi_i^a\rangle c_i^a = E_{CIS} \sum_{ia} c_i^a \delta_{ij} \delta_{ab}, \quad (2.77)$$

and for a closed-shell HF reference, the general matrix element expression of the CIS matrix is

$$\langle \Psi_j^b | H |\Psi_i^a\rangle = (E_{HF} + \epsilon_a - \epsilon_j) \delta_{ij} \delta_{ab} + \langle aj || ib \rangle, \quad (2.78)$$

where ϵ_a and ϵ_j are the orbital energies of the single-electron orbitals φ_a and φ_i , respectively, $\langle aj || ib \rangle$ is an antisymmetrized two-electron integral. A detailed derivation of CIS matrix elements is in the next section.

Insertion of the matrix element expression Equation (2.78) in the CIS energy equation Equation (2.77), and subtraction of E_{HF} on both side, yield an expression for the excitation energies

$$\omega_{CIS} = \Delta_{CIS} = E_{CIS} - E_{HF}, \quad (2.79)$$

$$\sum_{ia} \{(\epsilon_a - \epsilon_i) \delta_{ij} \delta_{ab} + \langle aj || ib \rangle\} c_i^a = E_{CIS} \sum_{ia} c_i^a \delta_{ij} \delta_{ab} - E_{HF} \sum_{ia} c_i^a \delta_{ij} \delta_{ab} \quad (2.80)$$

$$\begin{aligned}
&= (E_{CIS} - E_{HF}) \sum_{ia} c_i^a \delta_{ij} \delta_{ab} \\
&= \omega_{CIS} \sum_{ia} c_i^a \delta_{ij} \delta_{ab}.
\end{aligned}$$

In matrix form, the CIS energy equation can be rewritten as an eigenvalue problem for solving excitation energy

$$\mathbf{A}\mathbf{X} = \omega\mathbf{X}, \quad (2.81)$$

$\mathbf{A} = \mathbf{H} - E_{HF}$ is the shifted CIS matrix. \mathbf{X} is the matrix of the CIS expansion coefficients, ω is the diagonal matrix of the excitation energies. The eigenvalues and eigenvectors of the shifted CIS matrix correspond to excitation energies and excited-state wave functions.

The matrix elements of \mathbf{A} are given as

$$A_{ia,jb} = (\epsilon_a - \epsilon_i) \delta_{ij} \delta_{ab} + \langle aj || ib \rangle. \quad (2.82)$$

Derivation of the matrix element of CIS matrix

When $i \neq j$ and $a \neq b$, the singly excited determinants may differ from each other by two spin orbitals. If so, the determinants are already in maximum coincidence, and the matrix element is of the form

$$\langle \Psi_i^a | \hat{H} | \Psi_j^b \rangle = \langle \dots a \dots j \dots | \hat{H} | \dots i \dots b \dots \rangle = \langle aj || ib \rangle = -\langle ja || ib \rangle, \quad (2.83)$$

or

$$\langle \Psi_i^a | \hat{H} | \Psi_j^b \rangle = \langle \dots j \dots a \dots | \hat{H} | \dots b \dots i \dots \rangle = \langle ja || bi \rangle = -\langle aj || bi \rangle. \quad (2.84)$$

For the case $i = j$, $a \neq b$, the matrix elements are

$$\begin{aligned}
\langle \Psi_i^a | \hat{H} | \Psi_i^b \rangle &= \langle \dots a \dots | \hat{H} | \dots b \dots \rangle \\
&= h_{ab} + \sum_{k \in \Psi_0, k \neq i} \langle ak || bk \rangle \\
&= F_{ab} - \langle ai || bi \rangle.
\end{aligned} \tag{2.85}$$

Likewise, for the case $i \neq j$, $a = b$, the matrix elements are

$$\begin{aligned}
\langle \Psi_i^a | \hat{H} | \Psi_j^a \rangle &= \langle \dots i \dots a \dots | \hat{H} | \dots a \dots j \dots \rangle \\
&= -h_{ij} - \sum_{k \in \{\Psi_0 + a\}} \langle ak || bk \rangle \\
&= -F_{ij} - \langle ia || ja \rangle.
\end{aligned} \tag{2.86}$$

When $i = j$ and $a = b$,

$$\begin{aligned}
\langle \Psi_i^a | \hat{H} | \Psi_i^a \rangle &= \sum_{k \in \Psi_0} h_{kk} + \frac{1}{2} \sum_{k, l \in \Psi_0} \langle kl || kl \rangle - h_{ii} + h_{aa} - \sum_{k \in \Psi_0} \langle ki || ki \rangle \\
&\quad + \sum_{k \in \Psi_0} \langle ka || ka \rangle - \langle ia || ia \rangle \\
&= E_{HF} - F_{ii} + F_{aa} - \langle ia || ia \rangle \\
&= E_{HF} - \varepsilon_i + \varepsilon_a - \langle ia || ia \rangle.
\end{aligned} \tag{2.87}$$

Finally, using Kronecker deltas and supposing the orbitals to be real-valued, one obtains the following general expression

$$\langle \Psi_i^a | \hat{H} | \Psi_j^b \rangle = E_{HF} \delta_{ij} \delta_{ab} + F_{ab} \delta_{ij} - F_{ij} \delta_{ab} + \langle aj || ib \rangle. \tag{2.88}$$

And for a closed-shell HF reference

$$\langle \Psi_i^a | \hat{H} | \Psi_j^b \rangle = (E_{HF} + \varepsilon_a - \varepsilon_j) \delta_{ij} \delta_{ab} + \langle aj || ib \rangle. \tag{2.89}$$

2.3.2 Time-dependent density functional theory

Time-dependent density functional theory (TDDFT) is a theory to study the properties and dynamics of many-body systems in the presence of time-dependent potential (electric or magnetic field). With the influence of the electric or magnetic field, TDDFT can be used to analyze the excitation energies, frequency-dependent response properties, and absorption spectra of molecules and solids. TDDFT is an extension of DFT. They share basic concepts and fundamental theory. However, DFT is limited to systems independent of time and is only applicable to the study of ground-state properties of the system. In order to study the properties of excited states, Runge and Gross proposed the Runge-Gross theory based on HK theorems, that is, there is a one-to-one correspondence between the time-dependent electron density and the time-dependent external potential. The establishment of TDDFT can be divided into two stages: the first is its derivation and proof of the time-dependent KS equation; the second is, expressions of the excitation energies and the transition moments based on linear-response theory.

Runge-Gross Theorems

The approximation proposed by Runge and Gross considers a single Slater determinant system in the presence of time-dependent external potential. the Hamiltonian of this system is described as,

$$\hat{H}(t) = \hat{T} + \hat{U} + \hat{V}_{ext}(t), \quad (2.90)$$

where $\hat{V}_{ext}(t)$ is the time-dependent external potential. In fact, the external potential involves the interaction between electrons and nuclei. The many-body wave function is developed based on the time-dependent Schrödinger equation,

$$\hat{H}(t)|\Psi(t)\rangle = i\hbar \frac{\partial}{\partial t} |\Psi(t)\rangle. \quad (2.91)$$

Taking the time-dependent Schrödinger equation (TDSE) as the starting point, the Runge-Gross Theorem shows that there is a one-to-one correspondence between the electron density and the external potential,

$$\Psi(t) = \Psi[\rho(t)](t)e^{-\alpha(t)}. \quad (2.92)$$

This theory can be proven in two steps: the first is assuming that the external potential can be expanded as Taylor series around a given time such that at least some of the expansion coefficients differ by more than a constant; the second step is to show that different current densities correspond to different electron densities.

Time-dependent Kohn-Sham equation

For a given potential, the Runge-Gross Theorem shows that there is a one-to-one correspondence between the electron density and the external potential. According to the KS approximation, we know that assuming a non-interacting system, particles move under the potential energy of a fixed time, and the density formed at this time is equivalent to the density in the interacting system. The advantage of this process is that it is easier to deal with non-interacting systems (non-interacting wave functions can be represented by a single Slater determinant of single-particle orbitals), while single-particle orbitals are determined by a partial differential equation with a single variable. The kinetic energy of a non-interacting system can be accurately expressed according to their orbitals. The solution, therefore, depends on the potential energy $V_S(r, t)$ or $V_{KS}(r, t)$.

The Hamiltonian of a non-interacting system can be written as

$$\hat{H}_S(t) = \hat{T} + \hat{V}(t). \quad (2.93)$$

Solving the TDSE gives the Slater determinant,

$$\hat{H}_s(t)|\Psi(t)\rangle = i \frac{\partial}{\partial t} |\Psi(t)\rangle. \quad (2.94)$$

The single-electron orbitals can be obtained by single-electron SE,

$$\left(-\frac{1}{2}\nabla^2 + v_s(r, t)\right)\psi_i(r, t) = i \frac{\partial}{\partial t} \psi_i(r, t). \quad (2.95)$$

Time-dependent density can be expressed as

$$\rho_s(r, t) = \sum_{i=1}^N |\psi_i(r, t)|^2. \quad (2.96)$$

Here $\rho_s(r, t)$ is equivalent to the electron density of the interacting system $\rho(r, t)$.

Then the one-particle potential can be derived,

$$v_s(r, t) = v(r, t) + \int d^3 r' \frac{\rho(r', t)}{|r - r'|} + \frac{\partial A_{xc}[\rho]}{\partial \rho(r, t)}, \quad (2.97)$$

where A_{xc} is the exchange-correlation part of the so-called action integral. Inserting equation (2.97) into (2.95) gives us the time-dependent Kohn-Sham equation

$$i \frac{\partial}{\partial t} \psi_i(r, t) = \left(-\frac{1}{2}\nabla_i^2 + v(r, t) + \int d^3 r' \frac{\rho(r', t)}{|r - r'|} + \frac{\partial A_{xc}[\rho]}{\partial \rho(r, t)}\right)\psi_i(r, t). \quad (2.98)$$

Since no approximation was introduced in the derivation of the time-dependent KS equation, this equation is exact. However, to solve the exact solution of the time-dependent KS equation, the approximation to the exchange-correlation part has to be introduced. Currently, the most widely used is the adiabatic local density approximation (ALDA). It assumes that the density of the system changes slowly with time, then time-independent local exchange-correlation functionals substitute the time-dependent exchange-correlation kernel.

Linear-response time-dependent density functional theory

After establishing the KS equation, there are two different methods to obtain the energy and oscillator strength of the excited state: one is the real-time TDDFT method, which propagates the time-dependent KS wave function in time; the other is the linear-response TDDFT, which examines the linear response of the KS equation. The latter is the most commonly used.

Assuming that the external perturbation of the system is small, that is, the ground state structure of the system is not entirely destroyed, linear-response TDDFT can be applied. In this case, the linear response of the system can be analyzed. The advantage of this method is that, for the first-order response, the variables of the system depend only on the wave function of the ground state, so all the properties of DFT can be simply used. The linear response equation is further obtained by analyzing the linear response of the KS equation. Then for a standard time-independent KS equation, the density matrix can be expressed as

$$\sum_q (F_{pq}^{(0)} P_{qr}^{(0)} - P_{pq}^{(0)} F_{qr}^{(0)}) = 0. \quad (2.99)$$

Hence, the time-dependent KS equation can be written as,

$$\sum_q (F_{pq} P_{qr} - P_{pq} F_{qr}) = i \frac{\partial}{\partial t} P_{pr}, \quad (2.100)$$

F and P refer to the KS density matrix.

When a time-dependent external field is applied to the system, the corresponding density matrix and Hamiltonian will produce a specific response. Here, only the first-order linear response is considered, and it is treated as a perturbation of the system. Then according to perturbation theory, the density matrix and the Hamiltonian of the system are respectively equal to the sum of the first-order time-dependent change and the non-perturbative ground state amount, i.e.,

$$F_{pq} = F_{pq}^{(0)} + F_{pq}^{(1)}, \quad (2.101)$$

$$P_{pq} = P_{pq}^{(0)} + P_{pq}^{(1)}. \quad (2.102)$$

Plugging F_{pq} and P_{pq} into the time-dependent KS equation (2.100), we get

$$\sum_q (F_{pq}^{(0)} P_{qr}^{(1)} - P_{pq}^{(1)} F_{qr}^{(0)} + F_{pq}^{(1)} P_{qr}^{(0)} - P_{pq}^{(0)} F_{qr}^{(1)}) = i \frac{\partial}{\partial t} P_{pr}^{(1)}. \quad (2.103)$$

After a series of transformation, the matrix representation of the non-Hermitian eigenvalue equation for the LR-TDDFT method can be obtained

$$\begin{bmatrix} A & B \\ B^* & A^* \end{bmatrix} \begin{bmatrix} X \\ Y \end{bmatrix} = \omega \begin{bmatrix} 1 & 0 \\ 0 & 1 \end{bmatrix} \begin{bmatrix} X \\ Y \end{bmatrix}, \quad (2.104)$$

with \mathbf{X} and \mathbf{Y} as the TD-DFT excitation and “de-excitation” amplitudes and ω as the excitation energy.

The matrix elements of \mathbf{A} and \mathbf{B} are given as

$$\begin{aligned} A_{ia,jb} &= \delta_{ij} \delta_{ab} (\varepsilon_a - \varepsilon_i) + \langle ij|ab \rangle + \langle ij|f_{xc}|ab \rangle, \\ B_{ia,jb} &= \langle ib|aj \rangle + \langle ib|f_{xc}|aj \rangle. \end{aligned} \quad (2.105)$$

2.4 Basic theory of charge transfer and excitation energy

transfer

Although charge transfer and excitation energy transfer are different processes, they share similar strategies in computing the couplings. This section is mainly based on books: “*Charge and Energy Transfer Dynamics in Molecular Systems*” by V. May and O. Kühn^[26], and “*Multimode Molecular Dynamics Beyond the Born-Oppenheimer Approximation*” by H. Köppel, W. Domcke and L. S. Cederbaum^[27], as well as the literature by Hsu et al.^[1, 28] and Van Voorhis et al.^[29, 30]

2.4.1 Rate equations

Fermi’s golden rule

The rate of ET and ET processes can be described by Fermi’s golden rule

$$k_{i \rightarrow f} = \frac{2\pi}{\hbar} |V_{if}|^2 \delta(E_i - E_f), \quad (2.106)$$

in which V_{if} is the electronic coupling describing the transition between the initial and final electronic states (i and f). $\delta(E_i - E_f)$ is the density of states at the energy E_f of the final states. Therefore, the rate constant k is proportional to the square of the electronic coupling V between i and f states.

Marcus equation

Based on Fermi’s golden rule, the Marcus rate equation can be derived,

$$k_{i \rightarrow f} = \frac{2\pi}{\hbar} |V_{if}|^2 \frac{1}{\sqrt{4\pi\lambda k_B T}} e^{-\frac{(\Delta G + \lambda)^2}{4\lambda k_B T}}. \quad (2.107)$$

Again, V_{if} is the electronic coupling, λ is the reorganization energy, which is the energy cost due to geometry modifications to go from the initial to the final state. ΔG is the Gibbs free energy change, which will be equal to 0 for self-exchange processes such as charge transfer in homogenous materials. T is the temperature, and k_B is the Boltzmann constant, \hbar is the reduced Planck constant.

As indicated by the formula, at any given temperature T , large electronic coupling and small reorganization energy will result in a high transfer rate k .

2.4.2 Non-adiabatic coupling in adiabatic representation

As can be seen from equations (2.106) and (2.107), the electronic coupling is essential to determine the transition rate. However, it cannot be obtained within the BO approximation. Because the BO approximation does not allow two electronic states to cross. The BO approximation fails to predict the transition between the two states. In this case, we need to consider the exact SE.

Within the adiabatic (BO) representation, we can obtain a set of electronic eigenfunctions $\{\Psi_i^e(\mathbf{r}, \mathbf{R})\}$, which forms a complete basis in the electronic space at any value of \mathbf{R} . Therefore, we can write the exact total wavefunction Ψ^T as a linear combination of the electronic eigenfunctions (basis) of \hat{H}^e ,

$$\Psi^T(\mathbf{r}, \mathbf{R}) = \sum_i \chi_i(\mathbf{R}) \Psi_i^e(\mathbf{r}, \mathbf{R}). \quad (2.108)$$

Equation (2.108) is called Born-Huang expansion. The expansion coefficient χ_i is just the nuclear wave function. Inserting the expanded wave function into the SE leads to

$$\hat{H}^T \Psi^T = E \Psi^T, \quad (2.109)$$

$$(\hat{T}^N + \hat{H}^e) \Psi^T = E^T \Psi^T, \quad (2.110)$$

$$(\hat{T}^N + \hat{H}^e - E^T) \Psi^T = 0, \quad (2.111)$$

$$(\hat{T}^N + \hat{H}^e - E^T) \sum_i |\Psi_i^e\rangle \chi_i = 0, \quad (2.112)$$

$$\hat{T}^N \sum_i |\Psi_i^e\rangle \chi_i + (E^e - E^T) \sum_i |\Psi_i^e\rangle \chi_i = 0. \quad (2.113)$$

Multiply equation (2.113) by $\langle \Psi_i^e |$ and integrate over the electronic space,

$$\sum_i [\langle \Psi_j^e | \hat{T}^N \chi_i | \Psi_i^e \rangle] + (E^e - E^T) \sum_i [\langle \Psi_j^e | \Psi_i^e \rangle] \chi_i = 0, \quad (2.114)$$

$$\sum_i [\langle \Psi_j^e | T^N \chi_i | \Psi_i^e \rangle] + (E^e - E^T) \chi_i = 0. \quad (2.115)$$

Rewrite $\langle \Psi_j^e | = \langle j |$, $|\Psi_i^e\rangle = |i\rangle$, and $\hat{T}^N = -\frac{1}{2M} \nabla^2$, using $\nabla^2 AB = (\nabla^2 A)B + 2\nabla A \cdot \nabla B + A\nabla^2 B$,

$$-\frac{1}{2M} \sum_i [\langle j | \nabla^2 \chi_i | i \rangle] + (E^e - E^T) \chi_i = 0, \quad (2.116)$$

$$-\frac{1}{2M} \sum_i [\langle j | \nabla^2 \chi_i | i \rangle + 2\langle j | \nabla \chi_i \nabla | i \rangle + \langle j | \chi_i \nabla^2 | i \rangle] + (E^e - E^T) \chi_i = 0, \quad (2.117)$$

$$T^N \chi_i - \frac{1}{2M} \sum_i \{ [2\langle j | \nabla | i \rangle \nabla + \langle j | \nabla^2 | i \rangle] \chi_i \} + (E^e - E^T) \chi_i = 0. \quad (2.118)$$

Setting

$$F_{ji}(\mathbf{R}) = \langle j | \nabla | i \rangle, \quad (2.119)$$

$$G_{ji}(\mathbf{R}) = \langle j | \nabla^2 | i \rangle. \quad (2.120)$$

We finally get

$$(\hat{T}^N + E^e - E^T)\chi_i - \frac{1}{2M} \sum_t [2F_{ji}\nabla + G_{ji}]\chi_i = 0. \quad (2.121)$$

The second term is referred to as non-adiabatic coupling Λ_{ji} , which gives transitions between the BO states.

$$\begin{aligned} \Lambda_{ji} &= \frac{1}{2M} (2F_{ji}\nabla + G_{ji}) \\ &= \frac{1}{2M} (2 \langle j|\nabla|i \rangle \nabla + \langle j|\nabla^2|i \rangle). \end{aligned} \quad (2.122)$$

Inserting Λ_{ji} into the total SE we get the nuclear wave function

$$(\hat{T}^N + E^e - E^T)\chi_i - \Lambda_{ji}\chi_i = 0. \quad (2.123)$$

We note that the G_{ji} term refers to scalar coupling (also called the diagonal BO correction), which is usually quite small and can be neglected. On the other hand, the F_{ji} term, called derivative coupling, can be quite large. The derivative coupling is usually referred to as the non-adiabatic coupling term (NACT).

2.4.3 Diabatic representation

Equation (2.122) indicates that the transition between electronic states can be given by the NACT. However, in order to compute NACT in adiabatic representation, we need to do derivatives of electronic wave functions with respect to nuclear coordinates (\mathbf{R}). This calculation is very complicated and expensive.

Fortunately, we can get rid of the dependence of nuclear coordinates (\mathbf{R}) by expressing the electronic Hamiltonian in the so-called diabatic representation. In this way, the electronic coupling is just the off-diagonal element of the diabatic electronic Hamiltonian, which is much easier to compute. By definition, the strict diabatic electronic states do not depend on \mathbf{R} , and so derivative coupling between any two states vanishes at every possible nuclear configuration, \mathbf{R}

$$F_{ji}(\mathbf{R}) \equiv \langle \Psi_j^d | \frac{\partial}{\partial \mathbf{R}} \Psi_i^d \rangle \equiv 0. \quad (2.124)$$

The diabatic states can be obtained by a unitary transformation of the adiabatic electronic wavefunctions

$$|\Psi^d\rangle = \mathbf{U}|\Psi^{\text{ad}}\rangle. \quad (2.125)$$

The matrix \mathbf{U} is called the adiabatic-to-diabatic transformation (ADT) matrix. \mathbf{U} is essentially a rotation operation, for a two-state system, it can be written as

$$\mathbf{U} = \begin{pmatrix} \cos\theta & -\sin\theta \\ \sin\theta & \cos\theta \end{pmatrix}. \quad (2.126)$$

Then the electronic Hamiltonian in diabatic representation:

$$\mathbf{U}\hat{H}^d = \mathbf{U}^+\hat{H}^{\text{ad}}\mathbf{U}, \quad (2.127)$$

with the matrix elements of the diabatic electronic Hamiltonian given by

$$H_{ij}^d = \langle \Psi_j^d | \hat{H}^d | \Psi_i^d \rangle. \quad (2.128)$$

2.4.4 Constrained density-functional theory—configuration interaction

There are many strategies to construct diabatic states and compute the couplings between them. Since in my doctoral studies, I mainly applied constrained density-functional theory-configuration interaction method (CDFT-CI), here I will only introduce the idea of CDFT-CI.

The basis of the CDFT approach is that diabatic states can be obtained by optimizing the wave function subject to a constraint on the density,

$$\int w_C(\mathbf{r})\rho(\mathbf{r})d\mathbf{r} - N_C = 0, \quad (2.129)$$

where w_C refers to a weighting function, ρ is the total electron density, and N_C is the constraint value.

Adding an extra external potential $V_C w_C$ to the usual KS equation,

$$\left[-\frac{1}{2}\nabla^2 + v_n(\mathbf{r}) + \int \frac{\rho(\mathbf{r}')}{|\mathbf{r} - \mathbf{r}'|} d\mathbf{r}' + v_{xc}(\mathbf{r}) + V_C w_C(\mathbf{r}) \right] \phi_i = \varepsilon_i \phi_i, \quad (2.130)$$

and minimizing the KS energy under the constraint of equation (2.129) will give us the solution of an effective KS equation, where V_C is a Lagrange multiplier which will satisfy equation (2.129) at convergence.

Subsequently, the diabatic-like states obtained from CDFT can be used to build a CI matrix. However, the pure constrained states are not orthogonal, because they are eigenstates of different Hamiltonians. For a two-state system, electronic coupling matrix element in the nonorthogonal basis can be written as

$$H_{AB} = \langle \Psi_A | H_B^{KS} | \Psi_B \rangle. \quad (2.131)$$

By symmetric orthogonalization, we can finally obtain the off-diagonal element between the orthogonal states,

$$H'_{AB} = \frac{1}{1 - S_{AB}^2} (H_{AB} - S_{AB} H_{BB}), \quad (2.132)$$

where $S_{AB} = \langle \Psi_A | \Psi_B \rangle$ is the overlap between the wave functions.

3. Tailoring Ultrafast Singlet Fission by the Chemical Modification of Phenazinothiadiazoles

This chapter is largely based on the results of theoretical calculations presented in published work:

N. Alagna, **J. Han (co-first author)**, N. Wollscheid, J.L. Perez Lustres, J. Herz, S. Hahn, S. Koser, F. Paulus, U.H.F. Bunz, **A. Dreuw**, T. Buckup, and M. Motzkus, Tailoring Ultrafast Singlet Fission by the Chemical Modification of Phenazinothiadiazoles. *Journal of the American Chemical Society*, 2019. 141(22): p. 8834.

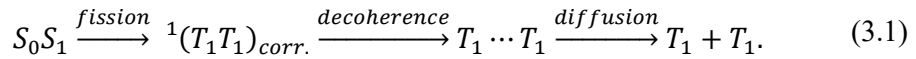
3.1 Abstract

Quantum chemical methods based on DFT and CDFT are applied to rationalize how singlet fission (SF) is affected by systematic chemical modifications introduced into phenazinothiadiazoles (PTD). Substitution of the terminal aromatic ring of TIPS-tetracene by a thiadiazole group leads to a considerable change in the relative energies of its S_1 and T_1 states. Thus, in contrast to TIPS-tetracene, SF becomes exothermic for various PTD derivatives, which show S_1-2T_1 energy differences as high as 0.15 eV. This enables SF in PTD as corroborated by femtosecond transient absorption spectroscopy and TD-DFT calculations. The latter report T-T spectra consistent with thin film UV-vis femtosecond transient absorption of PTDs at long delays. TD-DFT calculations also show that the S_1-T_1 energy gap can be rationally tuned by introducing N atoms into the aromatic scaffold and by the halogenation of one side ring of the PTD. In addition, the specific S_1 -to- $^1(T_1T_1)$ electronic coupling depends on the crystal morphology and the electronic properties simultaneously. Thus, both of them govern the strength and the interplay between direct and superexchange couplings, which in

the most favorable cases shows 75.8 meV effective coupling value. Remarkably, direct coupling was found to contribute considerably to the total effective coupling and even to dominate it for some PTDs investigated here.

3.2 Introduction

The prospect of economic and population growth, on the one hand, and environmental factors, on the other hand, have fostered research on renewable energies based on solar energy conversion.^[31, 32] The design of new materials for photovoltaics, in particular, organic dyes, has emerged as an important research field promising to supersede inorganic semiconductors.^[33-35] Tailored organic dyes have pushed the efficiency of photovoltaic devices by extending the usable spectral window for light harvesting and by the multiplication of charge carriers via a process called singlet fission (SF).^[16] First observed in anthracene^[36, 37] and tetracene^[38] crystals, SF converts an excited singlet exciton into two triplet states of nearly half energy. Thereby, the absorption of a single photon is able to produce two charge carriers through an ultrafast spin-allowed process. The underlying mechanism is summarized in equation (3.1).^[9] S_1S_0 represents an on-contact molecular pair, where one of the partners is in the photoexcited singlet state S_1 and the other remains in ground electronic state S_0 . ${}^1(T_1T_1)_{\text{correlated}}$ is the correlated triplet pair, also known as the multiexcitonic state. S_1S_0 may form a coherent superposition with the ${}^1(T_1T_1)_{\text{correlated}}$ state.^[39, 40] The latter is subject to decoherence processes and finally diffuses apart to form two isolated triplets T_1 . SF is the process occurring from left to right, while triplet fusion takes place essentially in the opposite direction.



Several materials displaying SF have been exploited for charge multiplication, for which thermodynamic and geometric requirements have to be fulfilled. Energy conservation, for example, demands that the first-excited singlet state S_1 has twice the energy of the ensuing triplets T_1 : $E(S_1) \geq 2E(T_1)$. This unusual condition is nearly fulfilled by tetracene, for which an activation energy for SF of about 1500 cm^{-1} was

obtained in crystals.^[41] This barrier seems to be surmounted at room temperature,^[41] so that SF efficiently competes with other deactivation channels and constitutes the main decay route in crystals and films. Recent studies indicate, however, that ultrafast SF is temperature-independent in tetracene crystals, which was explained by entropic effects or tunneling.^[39, 42-45] In contrast, covalently linked bis-tetracenes exhibit prompt and delayed fluorescence signals with relative contributions depending on the geometry of the linker.^[46] SF has been used to explain the rapid decay of the prompt fluorescence, while delayed fluorescence results from the fusion of the triplet pair. In parallel, triplet-triplet annihilation may also quench the triplet pair. The respective rates and activation energies depend on the linker architecture, demonstrating that geometric factors play an important role in the coupling of the singlet exciton to the triplet pair and in the survival probability of the triplets.^[47-49]

Another molecular system intensively investigated in the context of SF is pentacene.^[9, 50-56] Pentacene shows a favorable energetic balance for SF because $E(S_1) - 2E(T_1)$ is calculated to be 900 cm^{-1} .^[9] Accordingly, SF was observed in microcrystalline pentacene thin films^[51-53] and cross-conjugated dimers.^[55, 56] Organic photovoltaic cells based on pentacene and using a fullerene as an electron acceptor were reported to reach an internal quantum efficiency of 160% for irradiation at 670 nm.^[57, 58] The performance of pentacene has also been optimized by functionalization via the covalent linking of triisopropylsilylethynyl (TIPS) groups at positions 6 and 13, favoring both solubility and the capability of self-assembly by stacking.^[59] More recently, diaza and tetraaza substitution of aromatic carbon atoms of TIPS-pentacene has been shown to increase the chemical stability of the parent molecule and to accelerate SF substantially in spin-coated films, as demonstrated by femtosecond broadband transient absorption.^[60, 61] In addition, the halogenation of singlet fission chromophores has also been suggested as a design strategy for promoting SF.^[62]

In parallel, computational studies pointed to rational approaches to protect acenes from oxidation. This can be first achieved by introducing sp^2 nitrogen atoms into the aromatic scaffold and by halogenation,^[63] which lead to the stabilization of the frontier orbitals. This, however, distorts SF because electronegative atoms such as nitrogen tend to localize the molecular orbitals, reducing the diradical character of the parent compound, making SF less exothermic for pentacene or even endothermic for tetracene.^[64, 65]

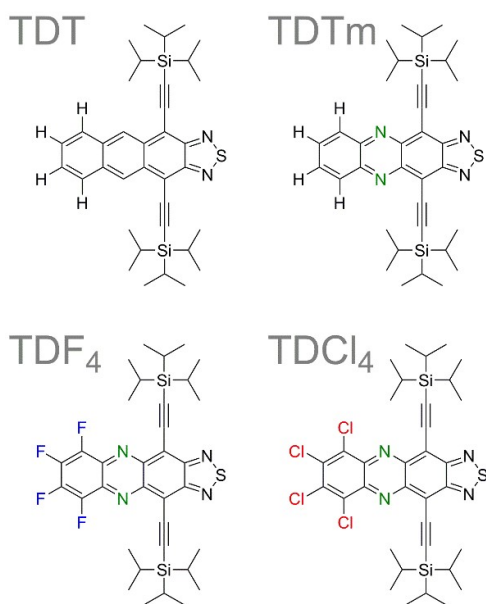
Alternatively, the replacement of the benzene ring with a thiophene ring has been shown to have a large influence on the diradical character^[66] and hence on the energy-matching condition for SF. The frontier orbital energies, $E(S_1)$ and $E(T_1)$, induced by the thiophene ring can be rationally tuned by the position and number of thiophene rings as well as the connection patterns between benzene units and thiophene rings.^[67]

In spite of the significant contributions made by femtosecond spectroscopy^[39, 40, 42, 50-56, 68-75] and quantum chemistry^[63, 76-84] to the current understanding of early stages in SF and the structural parameters controlling the coupling strength between the S_1S_0 and T_1T_1 states,^[46, 47, 81] there are still conflicting interpretations. One of the most controversial points is the nature of the reaction intermediates. For instance, the coherent superposition of the S_1S_0 and T_1T_1 states was observed on the femtosecond time scale by the two-photon photoemission spectroscopy of pentacenes.^[40, 76, 85] Ultrafast formation of the correlated triplet pair was also invoked in femtosecond transient absorption experiments addressing SF in tetracene derivatives^[41, 79] and N-substituted pentacenes.^[61] In turn, Marciniak et al. concluded from their analysis of the femtosecond transient absorption of microcrystalline pentacene films at various excitation incidence angles that a long-living excitonic singlet state mediates SF.^[52, 77] This intermediate state of singlet character would result from Davydov splitting of the monomeric S_1 states.^[52] SF was proposed to be thermally activated and would occur in the picosecond time window. In contrast, other authors found no indication of intermediate states in transient absorption experiments on pentacene films^[50, 51, 55] and oligoacene heterodimers.^[85] A similar variance is deduced from a number of quantum chemical studies on SF. Excimer-like states^[52] and a dark doubly excited singlet state^[86] were suggested to mediate SF in pentacene dimers. The latter explanation, which favored an indirect mechanism mediated by coupling to a low-lying charge-transfer state, was refuted by Zeng et al.^[87] This view was in turn challenged by quantum chemical calculations and femtosecond transient absorption measurements in bipentacenes, which demonstrate that SF rates do not depend on solvent polarity and hence question the role of charge-transfer states.^[88] More recently, studies in substituted bipentacenes evidenced polarity effects and showed that charge-transfer states may either enhance SF by indirect coupling or participate as intermediates in the reaction.^[89] While some of those apparent contradictions may be explained by experimental and/or computational conditions, they also hint at the possibility that SF may follow diverse

pathways depending on molecular structure and environmental factors. Therefore, an accurate characterization of SF entails structural information, a knowledge of electronic states in the neighborhood of the first-excited singlet state, and time-resolved spectroscopy over a vast range of time scales so that a microscopic quantum dynamical model can be put forward.^[86, 90-92]

To address the interplay of geometrical factors and chemical substitution, a new family of molecules for SF is investigated here with femtosecond spectroscopy and quantum chemistry: phenazinothiadiazoles (PTD, **Chart 1**).^[88] The substitution of a terminal benzene ring of TIPS-tetracene by a thiadiazole and the introduction of two or more N atoms into the aromatic scaffold strongly affect the SF in PTD polycrystalline films. The process is studied by broadband transient absorption from the femtosecond to the microsecond time scales. Experimental crystal structures are used as input geometries to find by quantum chemical calculations the coupling mechanisms relevant to SF. Our results indicate that halogen substitution in the opposite terminal ring fine tunes the SF rate. Moreover, the influence of the substitution pattern and packing geometry on the coupling strength is discussed.

Chart 1. Molecular structures of the phenazinothiadiazoles analyzed in this work. Acronyms are indicated for every structure.



3.2.1 Molecular Geometries.

The dimer geometries of TDT, TDCl₄, and TDF₄ were obtained from crystal structures archived in the Cambridge Crystallographic Data Centre.^[88, 93] The crystal structures show two dimer geometries susceptible to involvement in SF. Both dimer pairs (named A and B) were considered in quantum chemical calculations (Figure 3.1).

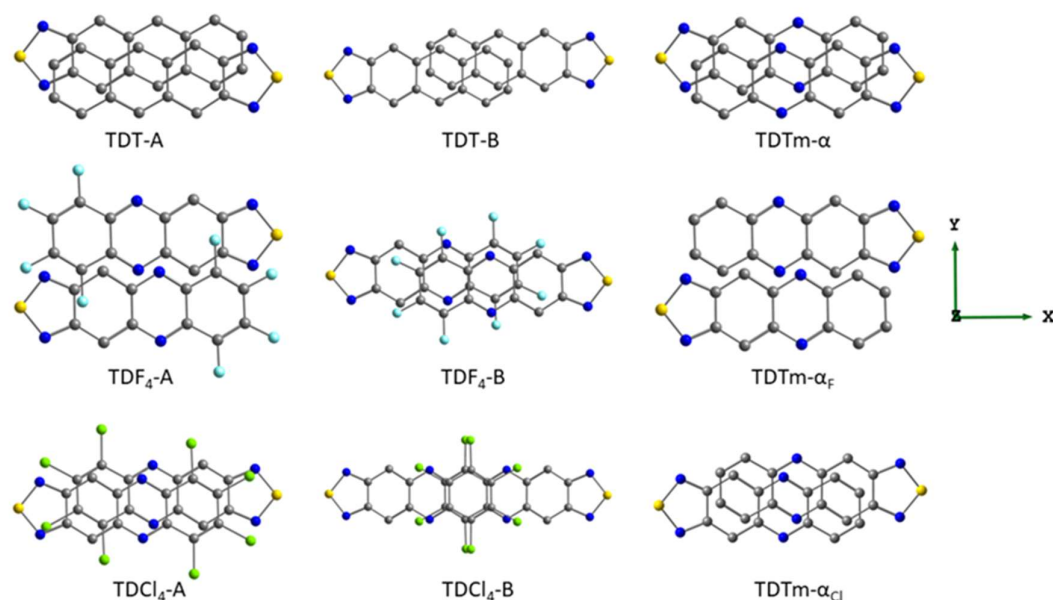


Figure 3.1. Dimer pair geometries considered in the computational part of this work. TIPS side groups and hydrogen atoms are not shown. A and B geometries were obtained from the experimental crystal structures of TDT, TDF₄, and TDCl₄. m-α geometries were constructed by replacing two -CH with nitrogen atoms, four fluorine atoms with hydrogen atoms, and four chlorine atoms with hydrogen in TDT-A, TDF₄-A, and TDCl₄-A, respectively.

Moreover, because the geometry of the TDTm dimer pair is experimentally unavailable from crystal structures, three different dimer pairs were artificially modified by replacing two -CH with N, four F with H, and four Cl with H in the TDT-A, TDF₄-A, and TDCl₄-A structures, respectively. Therefore, these three compounds are chemically the same (i.e., TDTm), but the dimers were artificially constructed using the A

geometry of the respective original dimer. The artificial geometries of TDTm thus contain suffixes with labels making reference to the geometry and structure of the parent compound: TDTm- α (for TDT-A), TDTm- α_F (for TDF₄-A), and TDTm- α_{Cl} (for TDCl₄-A). These geometries are of course experimentally unavailable but are very helpful in understanding how SF coupling depends on electronic structure and dimer geometry. As shown in Figure 3.1, the incorporation of the thiadiazole moiety into the aromatic structure leads to a slip-stacked crystallization motif, which was also observed for TIPS-pentacene.^[9, 60, 84] This contrasts with the herringbone packing typical of tetracene^[92, 94] and the distorted herringbone-like packing of TIPS-tetracene. Both TDCl₄ and TDF₄ exhibit the same brick-wall-type packing in their crystal structures. The π - π distances are very similar for all three compounds, which, however, show a larger variance in their shifts along the long and short molecular axes (Table 3.1 and Figure 3.1).

Table 3.1. Relative Shift along x , y , and z axes (Å) in Figure 3.1 for Dimer Pairs of TDT, TDTm, TDF₄, and TDCl₄, as Obtained from the Crystal Structure

dimer pair	long axis (Δx)	short axis (Δy)	π - π (Δz)
TDT A	1.81	1.21	3.35
TDT B	5.87	1.05	3.40
TDTm α	same as TDT-A		
TDF ₄ A	2.15	3.07	3.43
TDF ₄ B	4.65	0.82	3.29
TDTm α_F	same as TDF ₄ -A		
TDCl ₄ A	3.18	1.32	3.44
TDCl ₄ B	6.72	0.17	3.34
TDTm α_{Cl}	same as TDCl ₄ -A		

3.3 Computational Methods

All calculations were performed with Q-Chem version 4.4.^[95] In the following section, detailed protocols for the various topics addressed in this work are described.

3.3.1 Excited-State Energies and Calculation of Transient Absorption Spectra

The ground-state geometries of the monomers were optimized at the RB3LYP/6-31G* level of theory. Single-point calculations with the M06-2X functional and the 6-31G* basis set were performed to obtain the energies of the frontier molecular orbitals and the vertical excitations to all singly excited states involved in SF. Specifically, the energies of the S₁ and T₂ states were evaluated with closed-shell TD-DFT,^[96] while for the T₁ states the Tamm–Dancoff approximation (TDA)^[97] was applied. This combined M06-2X/TD-DFT/TDA protocol was found to agree with high-level wave function-based methods in SF chromophores.^[98, 99] For further validation, TIPS-tetracene UV–vis absorption and phosphorescence^[72] show that the S₁ and T₁ states are located 2.30 and 1.20–1.30 eV above the ground state. Respective values of 2.43 and 1.40 eV are computed for the gas phase, suggesting an accuracy of 0.2 eV. Triplet excited state absorption (ESA) spectra were obtained by computing transition dipole moments between excited states with RB3LYP. Very good agreement with experimental transient absorption spectra of the long-lived species was found.

3.3.2 Diradical Character of the Ground State

The diradical characters (γ_0) of the optimized molecules were computed on the broken-symmetry solution for the ground states with spin-projected unrestricted Hartree–Fock (PUHF)^[100] and the 6-31+G* basis set, following the procedure of Nakano et al.^[65, 101] The value of γ_0 ranges from 0 (closed-shell) to 1 (pure open-shell). It was suggested that increasing the diradical character tends to decrease $E(T_1)$. Thus, molecular systems with intermediate diradical character are expected to fulfill energy requirements for SF.^[65, 84, 101] In the framework of PUHF, γ_0 is defined as

$$y_0 = 1 - \frac{2T_0}{1 + T_0^2}, \quad (3.2)$$

where T_0 can be expressed in terms of non-spin-projected occupation numbers of the HONO (highest occupied natural orbital) and LUNO (lowest unoccupied natural orbital), n_{HONO} and n_{LUNO} , respectively, obtained from UHF calculations

$$T_0 = \frac{n_{\text{HONO}} - n_{\text{LUNO}}}{2}. \quad (3.3)$$

3.3.3 Electronic Coupling Calculations

To evaluate the effective coupling between the S_0S_1 and ${}^1(\text{TT})$ states, direct and charge-transfer (CT)-mediated mechanisms were considered in the framework of second-order perturbation theory.^[90]

$$\langle S_0S_1^{(1)} | \hat{H}_{el} | T_1T_1^{(1)} \rangle \approx V_{S_0S_1,TT} - \frac{2(V_{S_0S_1,CA}V_{CA,TT} + V_{S_0S_1,CA}V_{AC,TT})}{[E_{CT} - E_{TT}] + [E_{CT} - E_{S_0S_1}]}, \quad (3.4)$$

The first term on the rhs of **Eq. (3.4)** corresponds to the direct coupling $\langle S_0S_1^{(0)} | \hat{H}_{el} | T_1T_1^{(0)} \rangle$, while the second term accounts for the charge-transfer-mediated superexchange coupling mechanism. Note that the charge-transfer states contribute to the S_0S_1 - T_1T_1 coupling indirectly by simultaneous interaction with the S_0S_1 and the T_1T_1 states but the charge-transfer states do not become populated in the superexchange mechanism. It is, however, conceivable that polar interactions downshift the charge transfer states and thereby affect the second-order contribution to the S_0S_1 - T_1T_1 coupling. The energies of diabatic states ($E(\text{CT})$, $E(\text{TT})$ and $E(S_0S_1)$) were computed with Constrained-DFT (CDFT)^[102] and the maximum overlap method (MOM).^[103] CA and AC refer to the *cationic-anionic* configurations in the dimer and vice versa. The electronic couplings were calculated with CDFT based configuration interaction (CDFT-CI).^[30] It is important to note that the effective coupling results from the *sum* of the direct and super-exchange contributions with their signs. Once the effective coupling is obtained, only the *absolute value* is relevant since the rate is assumed to be

proportional to the magnitude of the effective coupling strength squared, according to Fermi's Golden Rule. Further details are given in next paragraph. All CDFT-CI calculations were performed at B3LYP/6-31G* level.

Diabatic $|S_0S_1\rangle$, $|CT\rangle$ ($|AC\rangle$ and $|CA\rangle$) as well as $|^1(T_1T_1)\rangle$ states were considered to be involved in SF in this work. The spin-adapted multireference states were constructed by proper linear combinations of twelve spin-impure single-reference states (eq. (3.5)-eq. (3.8)).

$$|S_0S_1\rangle = \frac{1}{\sqrt{2}} \left(\left| \uparrow\downarrow \downarrow \right\rangle - \left| \uparrow\downarrow \uparrow \right\rangle \right), \quad (3.5)$$

$$|AC\rangle = \frac{1}{\sqrt{2}} \left(\left| \uparrow\downarrow \downarrow \right\rangle - \left| \uparrow\downarrow \uparrow \right\rangle \right), \quad (3.6)$$

$$|CA\rangle = \frac{1}{\sqrt{2}} \left(\left| \uparrow \downarrow \right\rangle - \left| \downarrow \uparrow \right\rangle \right), \quad (3.7)$$

$$|^1(T_1T_1)\rangle = \frac{1}{\sqrt{3}} \left(\left| \uparrow \downarrow \right\rangle + \left| \downarrow \uparrow \right\rangle \right) - \frac{1}{2\sqrt{3}} \left(\left| \downarrow \downarrow \right\rangle + \left| \uparrow \uparrow \right\rangle + \left| \downarrow \uparrow \right\rangle + \left| \uparrow \downarrow \right\rangle \right). \quad (3.8)$$

Here the broken-symmetry S_0S_1 -like states were obtained by maximum overlap method (MOM) employing Δ SCF procedure, while CT-like (CA and AC) and $^1(TT)$ -like states were calculated with Constrained-DFT (CDFT) by constraining charge and spin on each monomer in the dimer system. The promolecule method was applied to the CT-like and $^1(TT)$ -like states to get better monomer densities.

The energy of spin-adapted $|S_0S_1\rangle$ state was estimated by spin purification formula (equation (3.9)),^[103]

$$E(|S_0S_1\rangle) = 2E \left(\left| \uparrow\downarrow \downarrow \right\rangle \right) - E \left(\left| \uparrow\downarrow \uparrow \right\rangle \right), \quad (3.9)$$

while the energies of CT and $^1(TT)$ states were estimated by the energies of spin-impure states in which the small couplings of CT and $^1(TT)$ states were ignored.

The electronic couplings between spin-pure states were calculated using constrained-DFT based configuration interaction (CDFT-CI). Moreover, generalized Slater-Condon

rule^[104, 105] was applied for nonorthonormal molecular orbitals to simplify the electronic coupling to the sum of couplings between selected spin configurations (equations (3.10)-(3.14)).

$$\langle S_0 S_1 | \hat{H} | TT \rangle = \sqrt{\frac{3}{2}} \left(\langle \uparrow\downarrow \downarrow | \hat{H} | \downarrow \uparrow \rangle + \langle \uparrow\downarrow \downarrow | \hat{H} | \uparrow \downarrow \rangle \right), \quad (3.10)$$

$$\langle S_0 S_1 | \hat{H} | CA \rangle = \left(\langle \uparrow\downarrow \downarrow | \hat{H} | \uparrow \downarrow \rangle - \langle \uparrow\downarrow \downarrow | \hat{H} | \uparrow \uparrow \rangle \right), \quad (3.11)$$

$$\langle S_0 S_1 | \hat{H} | AC \rangle = \left(\langle \uparrow\downarrow \downarrow | \hat{H} | \uparrow \downarrow \rangle - \langle \uparrow\downarrow \downarrow | \hat{H} | \uparrow \uparrow \rangle \right), \quad (3.12)$$

$$\langle CA | \hat{H} | TT \rangle = \sqrt{\frac{3}{2}} \left(\langle \uparrow \uparrow\downarrow | \hat{H} | \downarrow \uparrow \rangle + \langle \uparrow \uparrow\downarrow | \hat{H} | \downarrow \downarrow \rangle \right), \quad (3.13)$$

$$\langle AC | \hat{H} | TT \rangle = \sqrt{\frac{3}{2}} \left(\langle \uparrow \uparrow\downarrow | \hat{H} | \downarrow \uparrow \rangle + \langle \uparrow \uparrow\downarrow | \hat{H} | \downarrow \downarrow \rangle \right). \quad (3.14)$$

Because CDFT states are eigenstates of different Hamiltonians, they are not orthogonal, electronic couplings in the orthogonal basis (V_{ij} in equation (3.4)) were obtained by proper orthogonalization,^[105, 106] for example,

$$V_{S_0 S_1, TT} = \sqrt{\frac{3}{2}} \left(\frac{2E_{TS} - S_{TS}(E_{TT} + E_S)}{2(1 - S_{TS}^2)} \right), \quad (3.15)$$

where

$$E_{TS} = \langle \uparrow\downarrow \downarrow | \hat{H} | \downarrow \uparrow \rangle + \langle \uparrow\downarrow \downarrow | \hat{H} | \uparrow \downarrow \rangle,$$

$$S_{TS} = \langle \uparrow\downarrow \downarrow\downarrow | \uparrow \rangle + \langle \uparrow\downarrow \downarrow\uparrow | \downarrow \rangle$$

$$E_{TT} = \langle \uparrow \uparrow\downarrow | \hat{H} | \uparrow \downarrow \rangle$$

$$E_S = \left\langle \begin{array}{c} \uparrow\downarrow \\ \uparrow \\ \downarrow \end{array} \middle| \hat{H} \middle| \begin{array}{c} \downarrow \\ \uparrow\downarrow \\ \uparrow \end{array} \right\rangle.$$

Finally, we obtained CDFT-CI Hamiltonian matrix in orthogonalized basis, for example, for TDT(A) dimer,

$$\hat{H}_{el} = \begin{array}{c} S_0S_1 \\ T_1T_1 \\ CA \\ AC \end{array} \begin{pmatrix} S_0S_1 & T_1T_1 & CA & AC \\ 1377 & -59 & -147 & -84 \\ -59 & 1655 & -189 & 169 \\ -147 & -189 & 2346 & 0 \\ -84 & 169 & 0 & 2170 \end{pmatrix}$$

where the off-diagonal elements are electronic couplings V_{ij} , the diagonal elements are energies of diabatic states. Since $E(\text{CT})$ is greater than $E(S_0S_1)$ and $E(^1(\text{TT}))$, the sequential CT-mediated pathway is excluded, while the superexchange mechanism is considered as equation (3.4).

3.4 Results

Single-point M06-2X/6-31G* calculations were performed to calculate the energies of the HOMO and LUMO orbitals and to locate the S_1 , T_1 and T_2 states of the compounds investigated in this work (monomer forms, **Chart 1**). TIPS-tetracene (TIPS-Tn) was also computed for comparison.

The chemical modifications here analyzed impact the HOMO–LUMO energy gap, excited state energies and diradical character. The influence of the thiadiazole ring is summarized first. It considerably lowers the HOMO–LUMO energy gap and induces the stabilization of S_1 and T_1 . The S_1 energy is lowered from 2.432 eV in TIPS-Tn to 1.915 eV in TDT. In the case of T_1 , there is a stabilization from 1.398 to 0.883 eV. This is accompanied by a significant increase of the diradical character (y_0): it grows from 0.342 in TIPS-Tn to 0.503 in TDT. In contrast to the slightly endoergic SF in TIPS-Tn, which shows an energy difference $\Delta E(S_1-2T_1)$ (in short ΔSF) of -0.364 eV, SF becomes exothermic in TDT. ΔSF is predicted to be 0.150 eV for TDT, reflecting the stronger stabilization of the T_1 state compared to S_1 . A further introduction of two N atoms to the aromatic scaffold of TDT (TDTm) increases in turn the HOMO–LUMO energy gap.

This increases $E(S_1)$ more than $E(T_1)$ and reduces the diradical character ($y_0 = 0.488$). An orbital localization effect induced by the nitrogen atoms (Figure 3.2) explains the change in the diradical character. Finally, the introduction of halogenated atoms to form the TDF₄ and TDCl₄ compounds contributes to a decrease of the HOMO–LUMO energy gap and to a simultaneous increase of the diradical character. It is noted that while chlorine is less electronegative than fluorine, the former is more effective in lowering HOMO and LUMO energies. This is consistent with earlier studies and is attributed to conjugation effects of chlorine with the aromatic ring.^[107, 108] The S_1 (1.932 eV for TDF₄ and 1.916 eV TDCl₄) and the T_1 energies (0.902 eV in TDF₄ and 0.914 eV in TDCl₄) are reduced.

Table 3.2. Frontier orbital energies, HOMO-LUMO energy gap [$\Delta E(\text{LUMO-HOMO})$]^a and vertical excitation energies [$E(S_1)$, $E(T_1)$ and $E(T_2)$]^b [in eV] as well as diradical characters (y_0)^c for TIPS-Tn, TDT, TDTm, TDF₄ and TDCl₄ molecules

	TIPS-Tn	TDT	TDTm	TDF4	TDCl4
$E(\text{LUMO})$	-1.932	-2.667	-3.048	-3.374	-3.456
$E(\text{HOMO})$	-5.932	-6.095	-6.558	-6.803	-6.857
$\Delta E(\text{LUMO-HOMO})$	4.000	3.429	3.510	3.429	3.401
$E(S_1)$	2.432	1.915	2.016	1.932	1.916
$E(T_1)$	1.398	0.883	0.952	0.902	0.914
$E(T_2)$	2.634	2.341	2.420	2.274	2.227
$\Delta E(S_1-2T_1)$	-0.364	0.150	0.113	0.128	0.089
$\Delta E(T_2-2T_1)$	-0.162	0.576	0.517	0.469	0.400
y_0	0.342	0.503	0.488	0.496	0.493

^aComputed with M06-2X/6-31G*. ^bCalculated using TD-DFT for $E(S_1)$ and $E(T_2)$, TDA for $E(T_1)$ with M06-2X/6-31G*. ^cEvaluated from occupation numbers of unrestricted natural orbitals at PUHF/6-31+G*.

Summarizing, the intermediate diradical characters of $0.488 < y_0 < 0.503$, and the exothermic ΔSF values ranging from 0.089 to 0.150 eV in the PTD molecules indicate an energetically favorable SF process. In addition, comparing with TDT, further N substitution and halogenation reduce ΔSF , making $2E(T_1)$ closer to $E(S_1)$, and reducing the energy loss for SF. Calculated energy levels for the triplet states also show that triplet–triplet annihilation^[9] could play a significant role for TIPS-Tn ($T_2 < 2T_1$), while it may be less efficient for the PTD compounds investigated here, for which greater $\Delta E(T_2-2T_1)$ values are calculated (Table 3.2). This already hints to much higher SF rates and longer TT lifetimes for the PTD compounds compared to TIPS-Tn. From the viewpoint of energy loss, TDCl₄ shows smallest $\Delta SF = 0.089$ eV and is expected to perform SF most efficiently.

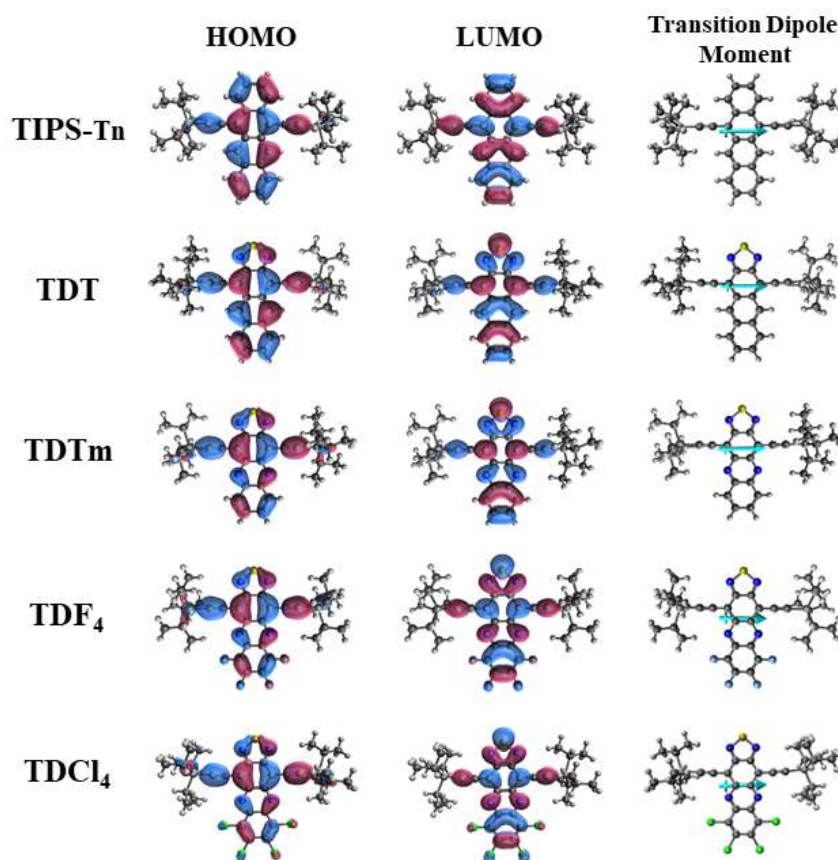


Figure 3.2. Kohn–Sham frontier molecular orbital diagrams (isodensity value: ± 0.05 a.u.) and direction of transition dipole moment between ground and S_1 states for TIPS-Tn, TDT, TDTm, TDF₄ and TDCl₄ at DFT(TD-DFT)/M06-2X/6-31G*.

Electronic coupling strengths calculated via CDFT-CI are shown in Table 3.3 (detailed values of each coupling term in equation (3.4) are listed in Table 3.4). The comparison of electronic couplings between A and B dimer pairs shows that the electronic coupling is very sensitive to packing structure. The focus is placed on the electronic couplings of the A-type pairs. The effective couplings of B pairs are calculated to be much smaller and hence, SF is expected to be much slower for the B geometry. Monomers in A pairs exhibit more symmetric displacements in transversal and longitudinal directions, the longitudinal (Δx) shifts are also shorter as in the B dimers (Table 3.1) throughout this series of compounds.

Table 3.3. Electronic coupling values (meV) calculated via CDFT-CI at B3LYP/6-31G* for dimer pairs in Figure 3.1.

Dimer pair	Direct coupling	Superexchange coupling	Effective coupling
TDT A	-59.4	-16.4	-75.8
TDT B	0.1	10.9	11.0
TDTm α	-40.2	39.0	-1.1
TDF ₄ A	0.5	-39.9	-39.4
TDF ₄ B	14.4	-15.6	-1.2
TDTm α_F	1.0	67.3	68.2
TDCl ₄ A	3.2	-23.4	-20.2
TDCl ₄ B	0.0	-0.1	-0.1
TDTm α_{Cl}	-5.8	14.6	8.8

The effective coupling strength decreases in the order TDT-A > TDF₄-A > TDCl₄-A. Introduction of a thiadiazole group in the TIPS-tetracene backbone leads to a dimer geometry TDT-A with the shortest longitudinal shift ($\Delta x = 1.81 \text{ \AA}$, Table 3.1), TDT-A also shows a strong effective coupling of -75.8 meV , the largest among the dimer structures of PTDs (Table 3.3). The lateral (short-axis) and longitudinal (long-axis) displacements in the A dimers of TDF₄ and TDCl₄ become larger and this structural change is accompanied by a decrease of the direct coupling contribution and a

simultaneous increase of the superexchange part. To summarize, these results indicate that the direct coupling tends to be maximized for relatively small displacements of the stacked π systems. As the overlap decreases, the contribution of the superexchange part increases for moderate symmetrical shifts and decreases again as the two π systems shift by more than 4–5 Å. In particular, due to the largest longitudinal shift and almost zero transversal shift, the TDCl₄–B dimer exhibits nearly vanishing coupling for both direct and superexchange contributions.

The general trend shown by the coupling strength as a function of the dimer geometry (A forms of TDT, TDCl₄ and TDF₄) was outlined above. It is, however, deduced from the comparison of dimers with different electronic structures so that the geometrical, steric and polarizing contributions of the substituents cannot be disentangled. Corroborating results are obtained for the artificial α geometries, which show highest direct coupling for best overlap (TDTm- α , -40.2 meV) and highest superexchange coupling for moderate xy displacements in TDTm- α_F : 67.3 meV. Qualitatively, the calculations point to a transition from direct to superexchange coupling mechanisms as the geometry of the dimer is distorted by transversal and longitudinal shifts. Note that the TDTm- α_F -like geometry is assumed for the crystal structure of TDTm. It will be shown that this geometry exhibits the best matching between the calculated SF coupling and the experimental SF rate constant.

Table 3.4. Electronic couplings (meV) of various terms in equation (3.4) for dimer pairs in Figure 3.1 at CDFT-CI/B3LYP/6-31G* level of theory. V_{ex} is the superexchange coupling and V_{eff} refers to the effective coupling.

		$V_{SOSI,TT}$	$V_{SOSI,CA}$	$V_{SOSI,AC}$	$V_{CA,TT}$	$V_{AC,TT}$	$V_{SOSI,CA}V_{CA,TT}$	$V_{SOSI,AC}V_{AC,TT}$	V_{ex}	V_{eff}
TDT	A	-59.4	-142.2	-83.6	-188.6	169	27731.1	-14136.1	-16.4	-75.8
TDT	B	0.1	-147	-97.2	43.3	41	-6152.4	-3980.7	10.9	11
TDTm	α	-40.2	-3.3	149.2	-155.7	-153.9	506.3	-22947.7	39	-1.1
TDF₄	A	0.5	113.7	98	122.8	117.6	13960.2	11525.2	-39.9	-39.4
TDF₄	B	14.4	2.5	-63.2	143.1	-143.2	359.9	9048.8	-15.6	-1.2
TDTm	α_F	1	154.5	-125.9	-176	165	-27195	-20771.2	67.3	68.2
TDCl₄	A	3.2	26.8	58.4	100.5	99.3	4334.9	5804.5	-23.4	-20.2
TDCl₄	B	0	43.1	46.5	1.1	1.1	29.5	49.1	-0.1	-0.1
TDTm	α_{Cl}	-5.8	29	71.1	-87.8	-87.4	-2542.4	-6215.7	14.6	8.8

3.5 Discussion

First of all, an unambiguous corroboration of the ultrafast formation of triplet states originates from the comparison between the calculated oscillator strength of the triplet state with the transient absorption signal at 5 ps in thin film (Figure 3.3). The spectral position of the calculated optical transitions (525 nm, 570 nm, 580 nm, 590 nm, 628 nm) are in very good agreement with the experimental ESA peaks (530 nm, 575 nm, 620 nm) (Figure 3.3). The small spectral shift between calculated and experimental values are partially explained by spectral distortion induced by the overlap of ESA and ground-state bleach and by an underlying vibrational progression. This also explains the different relative amplitudes of the transient absorption features compared to the calculated oscillator strengths.

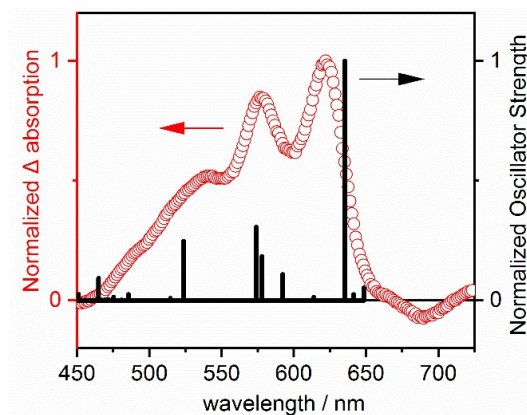


Figure 3.3. Transient absorption spectrum of TDCl_4 at 5 ps delay (red circles). Triplet–triplet optical transitions calculated with TD-DFT/RB3LYP/6-31G(d) (black vertical bars), amplitudes are proportional to the corresponding oscillator strengths.

The effect of chemical substitutions and geometry on ultrafast SF can be finally rationalized by the computational results, in particular, the electronic coupling between S_1S_0 and $^1(T_1T_1)$ states (Table 3.3). Geometry effects cannot be directly quantified in the transient absorption measurements of this work. Nevertheless, both A and B geometries are present in the respective crystal structures and a comparison between

experimental and theoretical trends is possible because one of the geometries, namely A, shows in all cases clearly stronger coupling values. TDT with its single nitrogen-pair substitution (via the thiadiazole group) shows the fastest SF with a time constant of 63 fs, followed very close by TDTm with a time constant of about 110 fs. TDCl₄ and TDF₄ show slower SF (413 and 370 fs, respectively) compared to TDT. Such a trend of SF *rates* (TDT > TDTm > TDF₄ > TDCl₄) matches very well the trend obtained for the *effective couplings* (Table 3.3): The two molecules with the fastest experimentally observed SF, TDT and TDTm, possess the largest effective couplings of |-75.8| and 68.2 meV, respectively, while in the other two cases, TDF₄ and TDCl₄, SF showed both the smallest effective coupling values of |-39.4| and |-20.2| meV, respectively, and the longest time constants of about 300–400 fs. It is, however, important to note that the effective coupling value for TDTm is affected by a larger error because its crystal structure is unknown. The dimer geometry of TDF₄-A is assumed for TDTm (TDTm- α_F), as suggested by the best matching between calculated coupling strength and experimental SF rate constant.

Further insight can be obtained by connecting the characteristic SF time constant and the S₀S₁-T₁T₁ coupling strength through a damped Rabi oscillation between the two nearly degenerate states. The period of this oscillation, which would characterize the SF time constant, ranges from 100 to 300 fs if effective coupling strengths of 100 to 50 meV are assumed. Alternatively, Fermi's Golden Rule reports characteristic times of 70 ρ_M eV fs and 260 ρ_M eV fs, for effective coupling strengths of 100 and 50 meV, respectively. Under this assumption, Franck–Condon weighted densities of states ρ_M of about 1 eV⁻¹ for the nearly degenerate coupling of the S₀S₁-T₁T₁ states are expected. This suggests that the interplay between the direct and superexchange coupling mechanisms predicts the right order of magnitude for the coupling and captures the main underlying physics.

Such a remarkable agreement between experiment and quantum chemical calculations underlines the effect of chemical substitution and, in particular, the interplay between nitrogen and halogen substitution as a means of fine-tuning the coupling strength relevant for SF. On the one hand, the introduction of the thiadiazole group tunes the HOMO, LUMO and excited state energies, increasing thereby the chemical stability, and renders SF exothermic. Notably, the effective coupling (V_{eff}) is dominated by the

direct contribution in TDT. This contrasts with the trend shown by unsubstituted acenes calculated with the Model Hamiltonian approach,^[9, 10, 86] where the direct coupling typically amounts to 5 meV and is usually ignored. In TDTm, the introduction of two aromatic nitrogens further enhances the chemical stability and ΔSF but reduces the effective coupling, which is detrimental for SF, as also evidenced by a slower SF rate. A similar dependence of the number of nitrogen substitution on SF rate has been observed for TIPS-pentacene and its aza-derivatives.^[60, 61] On the other hand, halogenation was shown to enhance the electron mobility.^[108, 109] It also makes the PTDs more stable and less exothermic for the SF process, leading potentially to faster SF. Unfortunately, halogenation causes at the same time a significant *decrease* of the effective coupling and SF rate, slowing down SF. Our results suggest that electron-withdrawing substituents do not necessarily enhance the effective coupling and rate. An improvement of charge transport and SF rate might require different chemical modification strategies.

In order to further separate the dependence of packing and chemical effects on the electronic coupling, we have performed coarse scans of the intermolecular distances for TIPS-Tn, TDT, TDTm and TDF₄ dimers. For this purpose, TIPS- groups were truncated by H₃Si- to ensure computational tractability without introducing significant error. Starting from the perfectly stacked geometry and fixing the Δz value at 3.5 Å, one monomer was displaced along the x- and y-axis by 2 Å steps up to $\Delta x = 6$ Å and by 1 Å up to $\Delta y = 3$ Å, respectively. The electronic couplings were calculated at each displacement. The values for TDT are shown in Figure 3.4. Values for all other dimers are summarized in Table 3.5 to Table 3.8.

Although the electronic coupling strength varies differently for each dimer system, several general trends can be established for the dependence on the packing geometry. First, the effective coupling almost vanishes for the perfectly stacked geometry ($\Delta x = 0$, $\Delta y = 0$), which is mainly attributed to negligible contributions from $V_{S0S1,TT}$, and $V_{CT,TT}$. Displacement along the x axis shows a strong decrease for both types of couplings, while transversal displacement (i.e., along the y axis) leads to strong sign and magnitude changes for both kinds of coupling. The magnitude of $V_{S0S1,TT}$ increases at $\Delta y = 1$ Å, decreases at $\Delta y = 2$ Å, and increases again at $\Delta y = 3$ Å. A similar trend is found for product terms $V_{S0S1,CA} \cdot V_{CA,TT}$ and $V_{S0S1,AC} \cdot V_{AC,TT}$, which involve charge-

transfer states. At $\Delta y = 1 \text{ \AA}$, the direct coupling $V_{S0S1,TT}$ reaches its maximum absolute value. At this geometry, the couplings involving the charge-transfer states show high values too, but they bear different signs. Consequently, the superexchange coupling interferes destructively, possibly canceling out completely, and the direct coupling ($V_{S0S1,TT}$) dominates V_{eff} . The cancellation effect disappears at $\Delta y = 2$ and 3 \AA . Eventually, the superexchange coupling reaches its maximum absolute value at $\Delta y = 3 \text{ \AA}$, where it achieves the major contribution to V_{eff} .

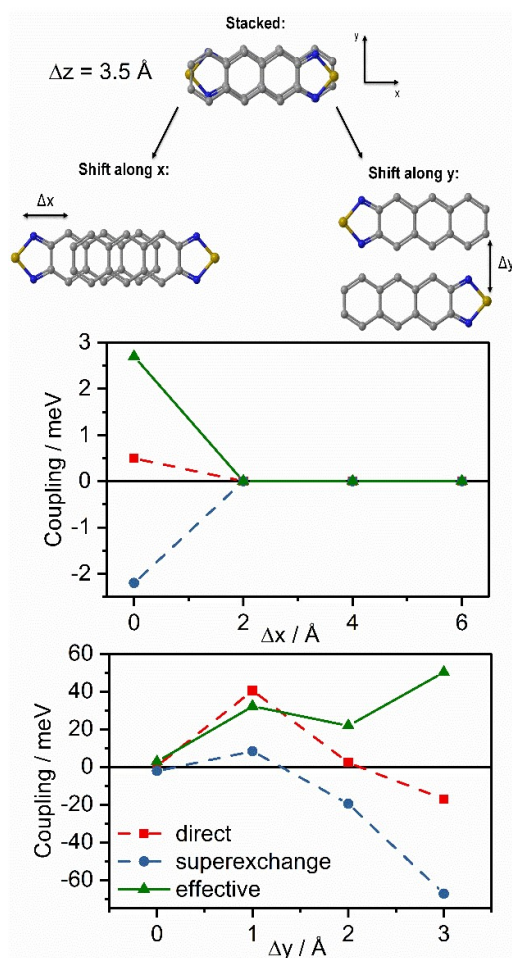


Figure 3.4. Electronic couplings for the truncated TDT dimer at various displacements along the long (Δx) and short (Δy) intermolecular axes.

Table 3.5. Electronic couplings (meV, CDFT/B3LYP/6-31G*) of various terms in equation (3.4) for **H₃Si-Tn** dimers with different displacement along x and y directions at $\Delta z = 3.5 \text{ \AA}$. V_{ex} is the super-exchange coupling and V_{eff} refers to the effective coupling. The displacement (in \AA) is given after the characters X or Y, which indicate the shift direction.

Shift	$V_{S0S1,TT}$	$V_{S0S1,CA}$	$V_{S0S1,AC}$	$V_{CA,TT}$	$V_{AC,TT}$	$V_{S0S1,CA} \cdot V_{CA,TT}$	$V_{S0S1,AC} \cdot V_{AC,TT}$	V_{ex}	V_{eff}
Shift along x axis									
X0Y0	1.1	131.9	-154.3	-2.7	2.3	-351.2	-356.6	3.8	4.9
X2Y0	0	-201.9	369.4	-0.5	0.3	90.9	125.9	-0.3	-0.4
X4Y0	0.2	133.6	-265.8	0.1	-0.5	19.5	129.8	-0.2	-0.1
X6Y0	0	-240.7	-240.4	0.1	0.2	-24.7	-50.8	0.1	0.1
Shift along y axis									
X0Y0	1.1	131.9	-154.3	-2.7	2.3	-351.2	-356.6	3.8	4.9
X0Y1	60.9	-162.2	298.4	83.2	86	-13499.2	25656.1	-20.8	40.2
X0Y2	-0.7	-129.3	-225.9	54.8	31.9	-7077.9	-7210.1	27.9	27.2
X0Y3	-23	-102.8	-244.2	187.1	147	-19229.5	-35903.4	96	72.9

Table 3.6. Electronic couplings (meV, CDFT/B3LYP/6-31G*) of various terms in equation (3.4) for **H₃Si-TDT** dimers with different displacement along x and y directions at $\Delta z = 3.5 \text{ \AA}$. V_{ex} is the super-exchange coupling and V_{eff} refers to the effective coupling. The displacement (in \AA) is given after the characters X or Y, which indicate the shift direction.

Shift	$V_{S0S1,TT}$	$V_{S0S1,CA}$	$V_{S0S1,AC}$	$V_{CA,TT}$	$V_{AC,TT}$	$V_{S0S1,CA} \cdot V_{CA,TT}$	$V_{S0S1,AC} \cdot V_{AC,TT}$	V_{ex}	V_{eff}
Shift along x axis									
X0Y0	0.5	140.5	151.1	-3	-3	-424.3	-459.5	2.2	2.7
X2Y0	0	148.3	-264.2	-0.1	0.1	-12.3	-19.5	0	0.1
X4Y0	0	-108.3	200.2	-0.1	-0.1	12	-23.3	0	0
X6Y0	0	-150	-58.2	0.1	-0.1	-9.3	3.2	0	0
Shift along y axis									
X0Y0	0.5	140.5	151.1	-3	-3	-424.3	-459.5	2.2	2.7
X0Y1	40.5	-173.3	-270.7	84.3	-82	-14617.8	22204.6	-8.3	32.2
X0Y2	2.3	138.9	-137.8	-48.6	38.6	-6748.1	-5314.4	19.5	21.8
X0Y3	-17.1	-87.9	253.8	168.4	-146.1	-14807.3	-37077	67.3	50.2

Table 3.7. Electronic couplings (meV, CDFT/B3LYP/6-31G*) of various terms in equation (3.4) for **H₃Si-TDTm** dimers with different displacement along x and y directions at $\Delta z = 3.5 \text{ \AA}$. V_{ex} is the super-exchange coupling and V_{eff} refers to the effective coupling. The displacement (in \AA) is given after the characters X or Y, which indicate the shift direction.

Shift	$V_{S0S1,TT}$	$V_{S0S1,CA}$	$V_{S0S1,AC}$	$V_{CA,TT}$	$V_{AC,TT}$	$V_{S0S1,CA} \cdot V_{CA,TT}$	$V_{S0S1,AC} \cdot V_{AC,TT}$	V_{ex}	V_{eff}
Shift along x axis									
X0Y0	0.0	-212.0	-212.0	-6.7	-6.7	1420.4	1420.4	-4.2	-4.2
X2Y0	0.0	142.1	-142.1	-0.5	0.5	-71.1	-71.1	0.2	0.2
X4Y0	0.0	93.2	-127.8	0.1	0.1	9.3	-12.8	0.0	0.0
X6Y0	0.0	-54.2	79.0	0.1	0.1	-5.4	7.9	0.0	0.0
Shift along y axis									
X0Y0	0.0	-212.0	-212.0	-6.7	-6.7	1420.4	1420.4	-4.2	-4.2
X0Y1	-40.6	114.6	-117.7	88.3	87.9	10119.2	-10345.8	0.4	-40.2
X0Y2	-4.1	-52.8	-87.2	2.7	26.3	-142.6	-2293.4	4.4	0.4
X0Y3	5.2	96.5	71.1	-110.8	-76.5	-10692.2	-5439.2	26.0	31.2

Table 3.8. Electronic couplings (meV, CDFT/B3LYP/6-31G*) of various terms in equation (3.4) for **H₃Si-TDF₄** dimers with different displacement along x and y directions at $\Delta z = 3.5 \text{ \AA}$. V_{ex} is the super-exchange coupling and V_{eff} refers to the effective coupling. The displacement (in \AA) is given after the characters X or Y, which indicate the shift direction.

	$V_{S0S1,TT}$	$V_{S0S1,CA}$	$V_{S0S1,AC}$	$V_{CA,TT}$	$V_{AC,TT}$	$V_{S0S1,CA} \cdot V_{CA,TT}$	$V_{S0S1,AC} \cdot V_{AC,TT}$	V_{ex}	V_{eff}
Shift along x axis									
X0Y0	0	195.2	-195.2	-5.7	5.7	-1106.5	-1114.9	3.4	3.4
X2Y0	0	-167	-167	1.4	1.4	-236	-236	0.6	0.6
X4Y0	0	75.7	-98.1	0	0	2.5	-1.7	0	0
X6Y0	0	-62.5	-77.2	0.1	-0.1	-7.7	10	0	0
Shift along y axis									
X0Y0	0	195.2	-195.2	-5.7	5.7	-1106.5	-1114.9	3.4	3.4
X0Y1	-36.8	-98	-84.6	-83.7	92.4	8194.5	-7811.6	-0.7	-37.5
X0Y2	0.1	54.1	-67.5	1.1	-0.9	57.4	61.5	-0.2	-0.2
X0Y3	-2.3	79.8	-74.3	112.4	-103.4	8970.5	7677.5	-27	-29.3

It is important to note that the direct coupling also dominates the truncated TIPS-Tn dimer at $\Delta y = 1 \text{ \AA}$. This indicates that the stronger direct coupling is a consequence of the packing geometry rather than the change in electronic properties induced by the chemical modification. Similar behavior was predicted by CDFT-CI calculations^[110] of the TIPS-pentacene dimer at y -axis displacements of around 1 \AA (0.89 \AA). Therefore, it is expected that the direct coupling values tend to be underestimated by computational methods which assume frozen monomer orbitals.^[9, 87] In turn, its important role in SF can be revealed by methods such as CDFT-CI, which take orbital relaxation effects into account.

In general, our results are consistent with previous studies for ethylene, unsubstituted acene, and oligorylene dimers,^[10, 82, 111, 112] where effective couplings are found to be generally small in the case of perfect stacking. The slip-stacked dimer configuration is in turn favorable for SF. Moreover, an intermediate slip along the direction of the HOMO to LUMO transition dipole moment in the individual chromophores (y axis direction in our case, see Table 3.8) would produce sizable coupling strength whereas a too large slip would reduce it. Conversely, a shift perpendicular to the transition dipole moment does not increase the coupling strength. Michl et al. also suggested that the almost vanishing coupling at perfect stack might be avoided by polarizing the molecular orbitals by substituent effects.^[9] This could not be corroborated for face-to-face stacking in the PTDs.

Once the strong influence of the packing geometry on SF coupling has been established, it remains a question of how variations in the electronic structure impact SF. The influence of electronic properties on SF can be clearly seen by comparing the coupling values of A and m- α dimer pairs because both kinds of dimers have the same packing geometry but different electronic structure. For instance, TDTm- α shows an almost vanishing V_{eff} value of -1.1 meV , indicating a tremendous reduction by the introduction of an additional nitrogen pair in the aromatic scaffold. The decrease in effective coupling by nitrogen substitution is not due to weaker direct and superexchange couplings (superexchange coupling is even enhanced) but rather is due to a *cancellation* between both coupling mechanisms: the superexchange coupling has a magnitude that is similar to the direct coupling, but they bear opposite signs (Table 3.3). The main reason for this effect rests on the significant changes in the signs and magnitudes of

coupling terms involving charge-transfer states (Table 3.4). Moreover, the effect of halogenation on the strength of direct coupling is small but substantial for superexchange contributions. A comparison of TDF₄-A and TDCl₄-A with TDTm- α_F and TDTm- α_{Cl} , respectively, shows that for the same geometry fluorination reduces the superexchange coupling while chlorination enhances it. Consequently, although all m- α dimer pairs are chemically the same, the cancellation of direct and superexchange contributions does not take place for TDTm- α_F and TDTm- α_{Cl} geometries, which can only be explained by their different packing motifs.

3.6 Conclusions

SF in PTD derivatives was characterized by quantum chemical calculations based on DFT and CDFT. The work focused on specific chemical changes and their effect on the SF process. The first modification was the introduction of a thiadiazole group into the TIPS-Tn skeleton. This leads to a slip-stacked arrangement and renders the SF process exothermic for the PTD derivatives investigated. Further chemical modifications with electronegative atoms on these derivatives lead to the same brick-wall-type packing with similar π - π separation and improved energy matching condition but different dimer geometries and triplet formation time constants in thin films. Triplet formation has been observed for all compounds on a time scale faster than a few hundred femtoseconds. The SF rate typical for TIPS-Tn is thus accelerated by chemical modification, leading to a quantum yield of 200% on the early picosecond time scale for all compounds studied here. The dependence of the characteristic triplet formation time on the number of carbon-to-nitrogen substitutions qualitatively matches previous observations for TIPS-pentacene and its aza-derivatives.^[60, 61] Here, the additional introduction of two nitrogen atoms in PTD leads to a deceleration of the SF process, similar to the deceleration observed for tetraaza TIPS-pentacene compared to diaza TIPS-pentacene. This trend was rationalized by the calculation of the effective coupling strength via CDFT-CI. The computational methods applied here reproduce the same structural dependence of S₀S₁-T₁T₁ coupling strengths as experimentally observed for the triplet formation rates. Moreover, they provide the relative contributions of the

direct and superexchange mechanisms to the effective coupling. Remarkably, calculations show that one of the possible dimer geometries, namely A, shows the highest effective coupling strength. In the cases studied, the most effective geometry also shows a relatively small displacement between the π systems of the partners. However, the dominant mechanism depends on the electronic structure and dimer configuration of the compound: for TDT, direct coupling is stronger, while for TDF₄ and TDCl₄, the superexchange mechanism makes the strongest contribution for the same kind of dimer geometry (A). Thus, depending on the PTD derivate, there is an optimal geometry leading to a large effective coupling strength. The latter can stem either from direct or superexchange contributions.

In summary, this work suggests that the PTDs are promising candidates for SF, and direct and superexchange couplings can make comparable contributions compatible with ultrafast SF. Chemical modification by the introduction of thiadiazole and electron-withdrawing groups can fine-tune the chemical stability, diradical character, excitation energies, SF rate, and electronic coupling. The effect of chemical modification is divided into pure geometrical changes in the dimers and changes in the electronic structure. Our results indicate that the electronic coupling is more sensitive to the geometrical changes than to the changes in the electronic properties. On the basis of improved electronic properties, future synthesis endeavors should aim to maximize the SF process by proper displacement of the respective chromophores.

4. Evaluation of Single-reference DFT-based Approaches on Spectroscopic Signatures of Excited States Involved in Singlet Fission

4.1 Abstract

Singlet fission (SF) has the potential to dramatically increase solar cell efficiency by converting one singlet exciton to two free triplet excitons or a correlated triplet pair. Identification and characterization of excited states involved in SF are of great importance for understanding the dynamics and the end product of SF, and the latter also determines the strategy for harvesting electrons from the triplets. However, it is non-trivial to distinguish species in transient absorption spectra due to their spectral overlaps and ultrafast feature. Theoretical modeling of SF and the electronically excited state absorptions (ESAs) is always challenging due to the multiexciton nature of the correlated triplet pair, which usually requires description from expensive high-level *ab initio* method. In this work, we attempt to use single-reference DFT-based methods to simulate ESAs of SF. In particular, the correlated triplet pair and its ESAs are characterized by broken symmetry DFT and TDDFT, and the role of orbital relaxation is highlighted. The singlet and triplet ESAs are evaluated by TDDFT, QR-TDDFT, SLR-TDDFT, SF-TDDFT, and UTDDFT With a rational choice of exchange-correlation functionals. The resulting spectra show good agreement with experiments, and they could be even more consistent than high-order CI methods.

4.2 Introduction

Singlet fission (SF) is a multiple exciton generation process in which a singlet exciton shares its energy with neighboring ground-state chromophores and splits to two triplet excitons.^[9, 10] Due to the doubled number and long lifetime of triplet excitons, it has been proposed that SF could provide a path to exceed the limit of power conversion efficiency in conventional solar cells (~33%, i.e., the Shockley-Queisser limit).^[16]

According to earlier and more recent experimental and theoretical literature,^[9, 18, 80, 113-115] the kinetic model of SF can be approximately written as $S_0 + hv \rightarrow S_1 \rightarrow {}^1(T_1T_1) \rightarrow {}^1(T_1\dots T_1) \rightarrow T_1 + T_1$. After an initial excitation to the first bright S_1 state, chromophores undergo singlet fission and rapidly convert to a dark multiexciton state, ${}^1(T_1T_1)$, which usually refers to be a correlated triplet-pair state in a simplistic dimer picture. The ${}^1(T_1T_1)$ state is an overall spin-singlet state with two constituent triplets coupled with spin and electronic coherence. Because the transition from S_1 to ${}^1(T_1T_1)$ states is a spin-allowed process, the formation of the ${}^1(T_1T_1)$ state is essentially an internal conversion which can occur on an ultrafast timescale. In the case of SF in aggregates or crystalline solids, i.e., intermolecular SF (xSF), the ${}^1(T_1T_1)$ state can lose the electronic coherence but maintain the spin correlation, and form ${}^1(T_1\dots T_1)$ state via spatial diffusion of the two triplets and coupling to the phonon bath. The spin dephasing and intersystem crossing in the ${}^1(T_1\dots T_1)$ state will eventually result in two separated triplets ($T_1 + T_1$), which can be harvested for solar cell applications.^[39, 114-116] Whereas, for SF in oligomers or polymers (intramolecular SF, iSF), the ${}^1(T_1T_1)$ state is likely trapped on the molecular system up to hundreds of nanoseconds, and hardly decays to the ${}^1(T_1\dots T_1)$ state or separates into free triplets.^[70, 117-120] However, triplet part states of quintet character, ${}^5(T_1T_1)$, might be produced by strong exchange coupling at much longer timescale.^[121] In the end, the electrons could be directly extracted from the bound ${}^1(T_1T_1)$ state by multi-electron acceptors.^[122, 123]

The identification and characterization of excited states involved in SF are crucial for understanding SF dynamics. In this context, electronic spectroscopic signatures obtained from ultrafast laser technologies in conjunction with quantum chemical simulation could play an essential role in uncovering the populations and

interconversion of different excitons. Experimentally, femtosecond transient absorption (TA) spectroscopy serves as the most commonly used technique for the study of ultrafast SF process.^[54] The TA signal is recorded by taking the difference of the absorbance between excited and unexcited molecules at any given time delay. In this way, one can observe negative contributions in the differential absorption such as ground state bleaching (GSB) and stimulated emission (SE), as well as positive signals resulting from excited state absorption (ESA) or photoproduct absorption (PA).^[124] Although earlier TA investigations successfully assigned the spectral features of S_1 and T_1 states,^[54, 60, 73] demonstrating the initial and final states of SF, the signatures of the mysterious and most challenging correlated triplet pair states were overlooked, since the spectra of $^1(T_1T_1)$, $^1(T_1\dots T_1)$ and triplet excitons always largely overlap. The correlated triplet pair states are not only critical intermediate states of the SF process but also of significant fundamental interests due to their multiexcitonic nature. With the advances of time-resolved TA technique, distinct spectral features of the correlated triplet pair states were observed in recent experiments.^[18, 122, 125, 126] The TA signal of the $^1(T_1T_1)$ state was first assigned from concentrated solutions of bis(triisopropylsilylethynyl)(TIPS)—tetracene by Friend and coworkers in 2015.^[72] The ESA of the $^1(T_1T_1)$ state resembled the absorption of free triplets in the UV-Vis spectral region and was systematically blue-shifted by 5-10 meV on a broad background. The similarities and subtle differences with free triplets indicate a dual singlet-triplet character and nonnegligible interaction within the bound pair of triplets. Similar findings have also been evidenced on crystalline TIPS-tetracene^[127] and TIPS-pentacene^[115], as well as their derivatives^[114, 127] and oligomers^[55, 118, 128]. On the other hand, because the $^1(T_1\dots T_1)$ state is spectroscopically indistinguishable from the free T_1 state, it was missing in the earlier kinetic model of SF^[9, 10]. Pensack et al. measured TA spectra on solids of pentacene derivatives and first proposed that the separation of the $^1(T_1T_1)$ state required an additional noninteracting triplet-pair state $^1(T_1\dots T_1)$. When including the $(T_1\dots T_1)$ state in the kinetic model of SF, a better global target analysis of the TA data was achieved.^[114] They also concluded that the S_1 , $^1(T_1T_1)$, and $^1(T_1\dots T_1)$ states could be clearly distinguished in the near-infrared (NIR) spectral region. Grieco et al. further extended the TA measurement to the mid-infrared region, where new electronic transitions of the S_1 and $^1(T_1T_1)$ states were identified.^[115] Besides, Trinh et al. probed SF in an end-connected pentacene dimer (BP0) where the bound $^1(T_1T_1)$ state

is confined and presents a much longer lifetime than that in the condensed phase.^[118] They assigned distinct ESA peaks at around 1 and 1.8 eV to $^1(T_1T_1)$ -to-singlet transitions, which also suggests the singlet character of the $^1(T_1T_1)$ state and the strong coupling between the two constituent triplets. Although it is impossible to convert the $^1(T_1T_1)$ state to the $^1(T_1\dots T_1)$ state in BP0, the spin evolution from the $^1(T_1T_1)$ to $^5(T_1T_1)$ state was manifested by experiment applying both time-resolved TA and electron spin resonance spectroscopic techniques.^[121]

While TA techniques have been successfully used to probe SF in recent years, it is always quite challenging to assign the species involved in SF due to their spectral overlaps and ultrafast transitions, and an incomplete kinetic model could even lead to a confusing interpretation of the TA data.^[18] Therefore, theoretical modelings of the electronic spectra, though are seldom reported, could be powerful tools to facilitate the assignment and characterization of excited states involved in SF. Zimmerman and coworkers pioneered the first quantum chemical description of the $^1(T_1T_1)$ state on a pentacene dimer, by using the complete-active space self-consistent field (CASSCF) method.^[80] Later on, they further simulated ESAs of SF on quinoidal bithiophene (QOT2)^[117, 123] and tetracene dimer^[129] by calculating transition dipole moments (TDM) in the framework of restricted active space spin-flip with double spin-flip (RAS-2SF). By comparing the ESAs obtained from RAS-2SF TDM with experiment TA data, they suggested that spectral signatures of $^1(T_1T_1)$ should be similar, though shifted, to the triplet in tetracene, which is consistent with previous experimental work;^[72] in contrast, the triplet separation or conversion to quintet is not feasible in QOT2 due to enormous binding energy in the $^1(T_1T_1)$ state. On the other hand, Khan and Mazumdar performed multiple reference singles and doubles configuration interaction (MRSDCI) calculations within the π -electron Pariser-Parr-Pople (PPP) Hamiltonian to rationalize the ESA measurements in crystalline pentacene^[130], BP0^[119], as well as heteroacene dimers of TIPS-pentacene and TIPS-tetracene^[120]. The detailed analysis distinguished the ESAs of $^1(T_1T_1)$ and free T_1 states, further provided additional insight on how the subtle difference between those transient signals was affected by molecular packing and intermolecular coupling.

The accurate description of excited states in SF is of great importance and interest, especially for the $^1(T_1T_1)$ state. However, computational characterizations are not easy

to make owing to the intrinsic multiexcitation nature of the $^1(T_1T_1)$ state, and strong electron correlation in π -conjugated systems^[119, 131]. Therefore, linear response single reference methods which are incapable of computing multiple excitations such as time-dependent density functional theory (TDDFT)^[23] cannot be used in processes involving multiexcitons, due to limitations of its standard adiabatic approximation. Although active-space or multireference CI methods such as CASSCF/CASPT2, RAS-2SF, and MRSDCI have been successfully applied to investigate SF in a variety of materials^[78, 117, 119, 120, 123, 129, 130, 132-135], the computational cost of these high-level *ab initio* methods grows dramatically with the size of the systems. Furthermore, they also suffer from the limitation of the choice of the active space. This could lead to unbalanced descriptions of excitation energies and ESAs^[119, 122].

Although conventional TDDFT is not capable of dealing with double excitations and hence the $^1(T_1T_1)$ state, it exhibits achievable accuracy for the calculations of S_1 and T_1 states. Recent benchmark studies proved that TDDFT with the Tamm/Dancoff approximation (TDA), and Δ SCF formalisms could yield a good agreement on the vertical and adiabatic excitation energies of S_1 and T_1 with more sophisticated post-Hartree–Fock methods.^[98, 99] It is also suggested that single-reference methods could describe excitations with dominant (>85%) single-excitation character^[136], and this is usually the case for the S_1 and T_1 states in most SF chromophores^[98]. In addition, TD-DFT based methods such as quadratic response (QR-TDDFT)^[137] and more recent second linear-response (SLR-TDDFT)^[138] have been successfully applied to estimate the S_1 ESAs of large conjugated polymers.^[139, 140]

With respect to the multireference and multiexcitation problems in DFT and TDDFT, there have been considerable efforts to provide alternative solutions. First of all, it is well known that broken symmetry DFT (BS-DFT) can describe ground states with diradical character.^[65, 141] Casida et al. further demonstrated that BS-TDDFT is reliable for calculating excited states of biradicaloids as long as the spin is conserved. In addition, Rinkevicius et al. discovered that spin-flip TDDFT (SF-TDDFT) showed remarkable improvement in the description of excited states with double and mixed excitation characters in polyene oligomers.^[142] DFT, in conjunction with a modified Δ SCF algorithm (Initial Maximum Overlap Method), was also found to be a promising approach for modeling excited states with strong double excitation character.^[143] More

importantly, constrained DFT (CDFT) and configuration interaction with CDFT (CDFT-CI) methods^[102] have been recently employed to construct the $^1(T_1T_1)$ state and rationalize trends of SF rates in a variety of acene derivatives.^[110, 127]

In view of the limitations of high-level *ab initio* methods in computing ESAs involved in SF and motivated by the above-mentioned improvements over the standard DFT and TDDFT, in this work, we present a simple and computationally less demanding approach to obtain the energies and ESAs of excited state involved in SF. Herein, the $^1(T_1T_1)$ state and its ESA is obtained by BS-DFT and BS-TDDFT, respectively. The ESAs of S_1 and T_1 are estimated by TDDFT, QR-TDDFT, SLR-TDDFT, SF-TDDFT, and unrestricted TDDFT (UTDDFT), along with 10 exchange-correlation (XC) functionals. By taking TIPS-Pn monomer and BP0 dimer as examples, and comparing our results with extensive experiments and high-level *ab initio* methods^[55, 73, 76, 115, 118, 119], we found that single reference DFT based methods with a rational choice of functionals can provide an adequate description of energies and electronic transitions of excited states involved in SF. In particular, the ESA of the $^1(T_1T_1)$ state computed by BS-TDDFT could be more consistent with the experiment than far more expensive multireference or active space methods. This entirely DFT based study provides an efficient way to facilitate the identification and assignment of transient species in SF, especially when it comes to large molecular systems.

4.3 Computational Details

Since the previous benchmark study suggested that PBE0 provided the closest structure with CASPT2 on small π systems,^[98] ground state geometries of TIPS-pentacene monomer and BP0 dimer (Figure 4.1) were optimized at PBEh-3c/def2-mSVP level of theory. The PBEh-3c^[144] is a reparameterized version of PBE0, which gives almost as good geometries as PBE0 or MP2 with larger basis sets and is more reliable than the most commonly used B3LYP/6-31G* protocol. To simulate the experimental solvent environment^[55] for the geometries, the chloroform solvation effects were incorporated by the polarizable continuum model (PCM) using the integral equation formalism

variant (IEFPCM)^[145, 146]. It is noted that the solvatochromic shifts of the ground state absorptions (GSAs) and ESAs are negligible (see Ref. ^[76]). Thus upon the optimized structures, additional gas-phase single-point calculations were performed to compute vertical excitation energies, spectra of GSAs, and ESAs. More specifically, the vertical excitation energies and GSAs were first estimated with TDDFT and TDA^[97] by taking spin-restricted closed-shell S_0 as reference states. Once the TDDFT/TDA calculations are done, the excitation energies and approximated wave functions can be obtained, and then the state-to-state oscillator strengths can be evaluated by

$$f_{ij} = \frac{2}{3} \varepsilon_{ij} |\langle \Psi_i | \hat{\mu} | \Psi_j \rangle|^2,$$

where the Ψ_i and Ψ_j are the wave functions of initial and final excited states, ε_{ij} refers to energy difference, and $\langle \Psi_i | \hat{\mu} | \Psi_j \rangle$ represents TDM. In this way, the S_1 and T_1 ESAs are simulated in the framework of spin-restricted TDDFT/TDA. Alternatively, the excitation energy and absorption spectra of the T_1 state were also computed with spin-unrestricted DFT (UDFT) and TDDFT (UTDDFT) approach. Taking open-shell T_1 state as the reference state allows orbital relaxation/optimization. Hence the results are, in principle, more reliable than spin-restricted TDDFT, as long as the spin contamination is small.

Orbital relaxation effects could affect excited state properties such as energies and electronic dipole moments^[147, 148], which are not included in standard TDDFT. Therefore, we applied QR-TDDFT and SLR-TDDFT to evaluate the orbital relaxation effects on the S_1 ESAs. In the context of QR-TDDFT, the transition properties between two excited states are determined by the double residue of the quadratic-response function.^[149, 150] In the framework of SLR-TDDFT, the state-to-state transition properties are evaluated by comparing the transition dipoles from two LR calculations.^[138, 140] The former is the standard LR-TDDFT, and the second LR calculation is performed on a ground state perturbed by the excited state of interest. The results of SLR-TDDFT depend on the choice of perturbation intensity λ and criterion for relabeling the roots C_{tol} in the second LR calculation. In addition, SF-TDDFT^[151] within the TDA formalism was also used to account for the double excitations on the S_1 ESA spectra. The non-collinear exchange-correlation kernel^[152] was used for all SF-TDDFT calculations.

Finally, the energy and ESA of the $^1(T_1T_1)$ state in the BP0 dimer were computed by BS-DFT and BS-TDDFT. More precisely, we partitioned the BP0 dimer into two quartet TIPS-pentacene monomers with opposite spin directions, the initial guess of $^1(T_1T_1)$ was subsequently constructed from the superposition of the converged MOs on each fragment. An additional self-consistent field (SCF) procedure on the dimer system allowed the fragment MOs to relax and generated the wave function of a BS $^1(T_1T_1)$. This approach was based on equations of the locally projected SCF for molecular interactions, which was initially proposed to speed up SCF for large systems.^[153] The BS $^1(T_1T_1)$ state is a single determination spin-incomplete state since it only contains one spin configuration $\left| \begin{array}{c} \uparrow \\ \uparrow \end{array} \begin{array}{c} \downarrow \\ \downarrow \end{array} \right\rangle$, the ideal $\langle S^2 \rangle$ value should be 2. Performing UTDDFT on the BS $^1(T_1T_1)$ reference state eventually gave us the $^1(T_1T_1)$ ESA.

It is well known that the results of TDDFT calculations depend on the choice and the exact exchange admixture of the employed exchange-correlation (XC) functionals. We evaluated the performance of 10 XC functionals with various amounts of exact exchange for the vertical excitation energies, GSA, and ESAs of S_1 and T_1 on the TIPS-pentacene monomer. This includes generalized gradient approximation (GGA) functional BLYP (0%),^[154, 155] global hybrid GGA (GH-GGA) functionals B3LYP (20%),^[156, 157] PBE0 (25%),^[158, 159] BHHLYP (50%),^[160] GH meta-GGA functionals TPSSh (10%),^[161] BMK (42%),^[162] M06-2X(54%);^[163] and range-separated hybrid GGA functionals CAM-B3LYP (19-65%, $\omega = 0.33$),^[164] ω B97X-D (22.2-100%, $\omega = 0.20$),^[165] LRC- ω PBE (0-100%, $\omega = 0.30$).^[166] Functionals with good performance were further employed in the calculations of BP0 dimer. The 6-31G* basis set^[167] was used for all the excited state calculations, increasing the size of the basis set or adding diffuse functions only showed negligible changes in the spectra.

All the geometry optimizations, restricted/unrestricted TDDFT, SF-TDDFT, as well as BS-DFT/TDDFT calculations were performed with Q-Chem version 5.2^[168]. Dalton 2018^[169] and NWChem 6.6^[170] were used to conduct QR-TDDFT and SLR-TDDFT, respectively. The geometry relaxation and vibronic broadening effects on the absorption spectra were neglected. All spectra were plotted by Multiwfn 3.6^[171] and were broadened using Gaussian functions with a full-width at half-maximum of 0.2 eV.

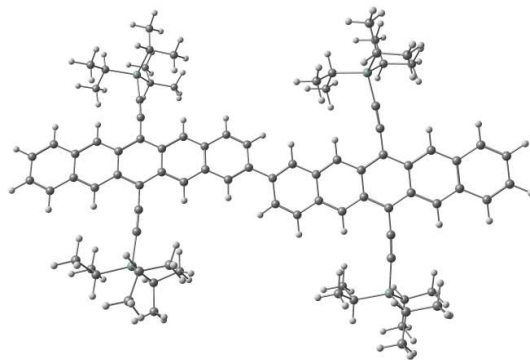


Figure 4.1. Geometric structure of BP0 dimer optimized at PBEh-3c/def2-mSVP/PCM(chloroform).

4.4 Results and Discussion

4.4.1 TIPS-Pentacene Monomer Calculated with TDDFT/TDA/UTDDFT

Vertical excitation energies

Table 4.1 compares TDDFT/TDA/UDFT calculated S_1 and T_1 vertical excitation energies with PPP-MRSDCI and experimental values. In general, our results of low-lying excitation energies are consistent with previous benchmark literatures, for detailed discussion, please refer to references [98, 99, 172, 173]. The GSA, S_1 , and T_1 ESA spectra are also plotted in Figure 4.2 and Figure 4.3, in comparison with the corresponding experimental spectra. Here we mainly focus on the discussion of those electronic absorption spectra.

Table 4.1. Excitation energies of TIPS-pentacene in eV of references and calculated by TDDFT/TDA/UDFT/6-31G* with 10 XC functionals (listed by increasing HF exchange percentage) at ground state geometry for TIPS-pentacene monomer. The experimental T_1 energy was derived from the maxima of phosphorescence emission spectrum.

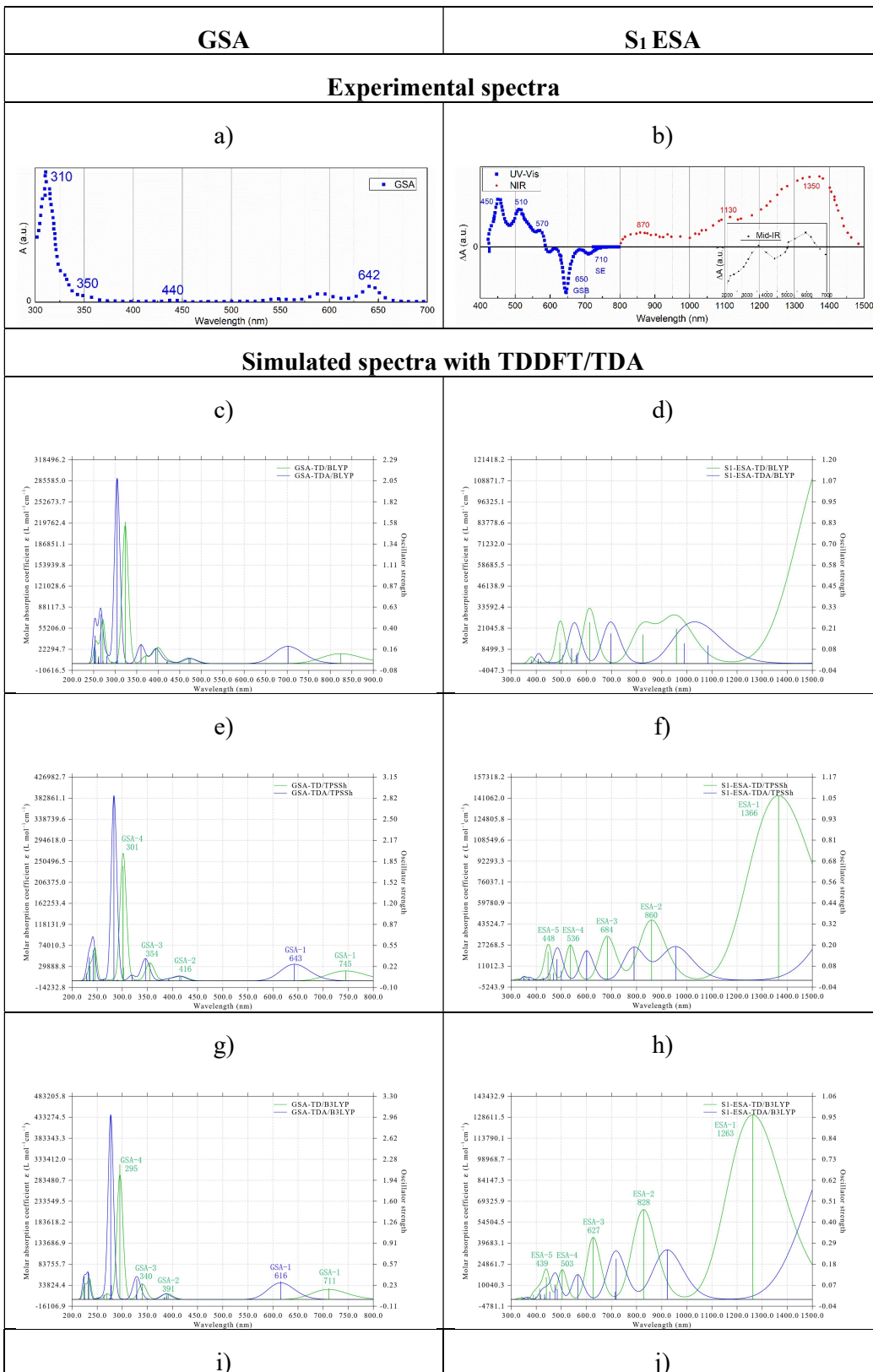
		S_1		T_1		
Reference						
Experiment		1.93 ^[118]		0.78 ^[56]		
PPP-MRSDCI ^[119]		1.88		0.89		
TDDFT/TDA/UDFT/6-31G*						
Functional	HF exchange [%]	TDA	TD	TDA	TD	UDFT
BLYP	0	1.77	1.51	0.82	0.73	0.82
TPSSh	10	1.93	1.67	0.81	0.46	0.79
B3LYP	20	2.02	1.74	0.84	0.47	0.84
PBE0	25	2.07	1.80	0.82	/	0.80
BMK	42	2.24	1.95	0.95	/	0.94
BHLYP	50	2.29	2.02	0.82	/	0.75
M06-2X	54	2.33	2.04	1.05	0.72	1.02
CAM-B3LYP	19-75, $\omega = 0.33$	2.34	2.04	0.88	/	0.84
ω B97X-D	22-100, $\omega = 0.2$	2.39	2.08	0.92	/	0.88
LRC- ω PBE	0-100, $\omega = 0.3$	2.49	2.17	0.89	/	0.83

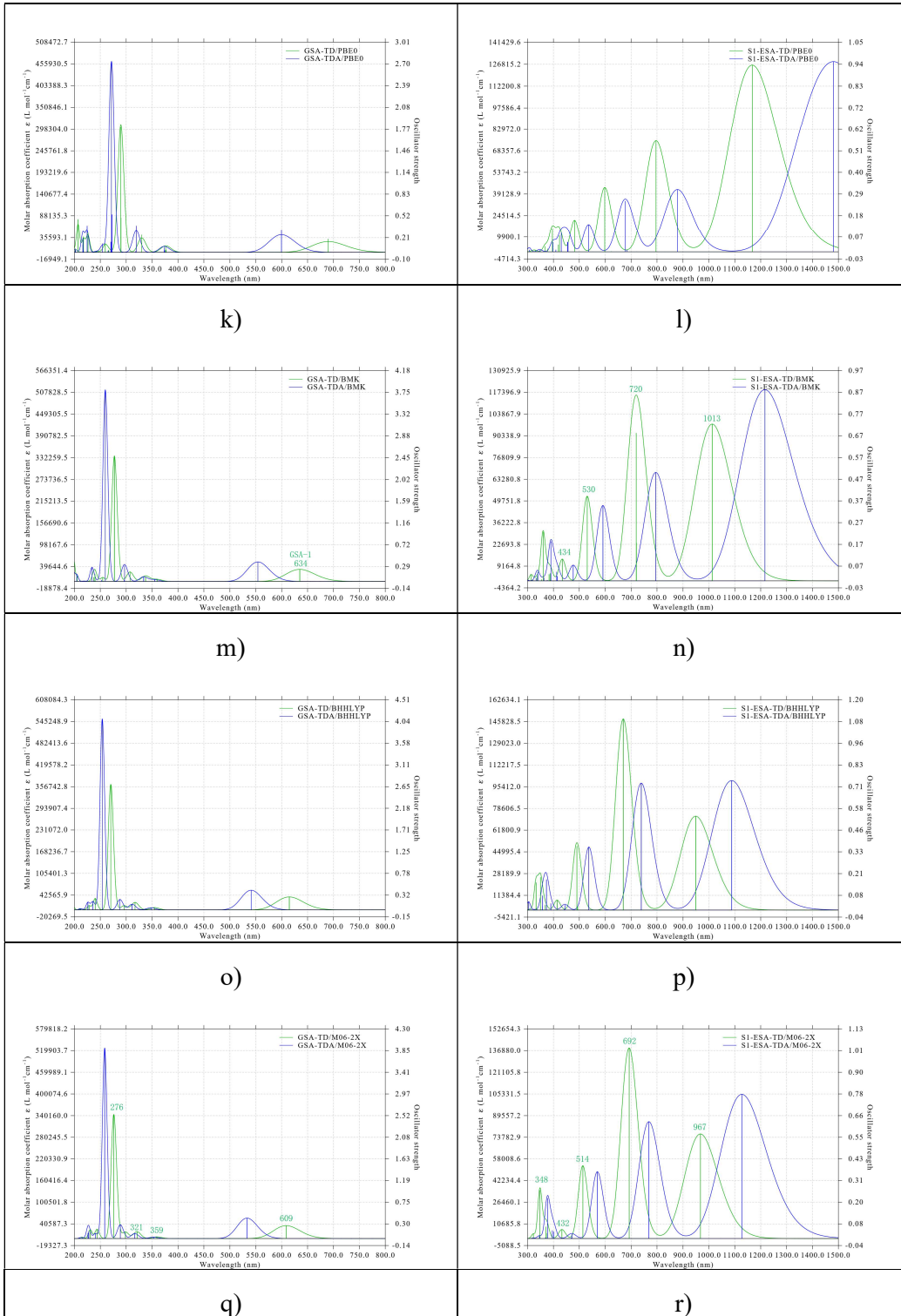
GSA and S_1 ESA spectra of TDDFT/TDA

We first discuss the singlet excited states, GSA and S_1 ESA spectra. As expected, TDA leads to a systematic blue shift for the GSA spectra compared to TDDFT. Whereas the blueshift of the GSA-1 band (first bright state, S_1 for TIPS-pentacene) is more pronounced than GSA-n bands ($n > 1$). The upshift for the S_1 excitation energy can be up to 0.32 eV for LRC- ω PBE. On the other hand, it can be clearly seen that the GSA spectra are progressively blue-shifted with an increasing amount of exact exchange. In the context of TDDFT, functionals with high HF exchange or long-range correction such as BMK and CAM-B3LYP gave adequate S_1 energy, while functionals with less HF admixture such as TPSSh and B3LYP produce too much red-shifted GSA-1 bands, they provide more consistent GSA-n bands ($n > 1$), compared with experiment. TDA can further improve the accuracy of the GSA-1 band for low exact exchange functionals. Consequently, the GSA spectra of TDA/TPSSh shows the lowest deviations with the experiment.

In contrast with the GSA spectra, the S_1 ESA spectra are systematically red-shifted by TDA, based on the fact that TDA has more impact on S_1 than S_n ($n > 1$). Similar to the GSA spectra, increasing the HF admixture gradually brings the S_1 ESAs to a higher

energy region. The experimental S_1 ESA spectrum of TIPS-pentacene in dilute solution shows maxima at 450, 510-570, 870, and 1350 nm and in the UV-Vis and NIR spectral region (Figure 4.2b). It is noted that the absorption band at 1130 nm corresponds to vibrational progression of the band at 1350 nm, and negative absorptions at 650 and 710 nm are assigned to GSA and SE.^[56] Additional absorption in the Mid-IR region was recently observed and further assigned as a transition from S_1 to a doubly excited state by CASSCF calculation.^[115] This lower-lying doubly excited state cannot be captured by TDDFT and hence is absent on our S_1 ESA spectra. However, for the absorption spectra in the UV-Vis and NIR region, TDDFT can provide good agreement with the experiment. For example, there are 5 ESA bands on the S_1 ESA spectrum of TDDFT/TPSSh, at 448, 536, 684, 860, and 1366 nm. The ESA-3 band at 684 nm is likely overlapped with the GSB and canceled out on the experimental S_1 ESA spectrum. For the other 4 S_1 ESA bands of TDDFT/TPSSh, the errors are within 0.01 eV. The S_1 ESA spectrum of B3LYP/TD is also acceptable, with minor blue-shift compared to TDDFT/TPSSh. Functionals with more substantial HF exchange such as BMK, M06-2X, and CAM-B3LYP produce only 4 S_1 ESA bands and generally shift the NIR band to around 950-1000 nm, but absorptions at around 450 and 550 nm are still manifested on their S_1 ESA spectra. This motivates us to examine the character of the allowed S_1 - S_n transitions. A comparison of electron-hole pair analysis between TDDFT/TPSSh (Table 4.2) and TDDFT/CAM-B3LYP (Table 4.3) indicates that the S_1 ESA-1,2,4,5 bands of TDDFT/TPSSh correspond to the S_1 ESA-1,2,3,4 bands of TDDFT/CAM-B3LYP, since the final states exhibit almost identical $\pi \rightarrow \pi^*$ transition character. This also suggests that the lower energy S_1 - S_n transitions undergo much stronger blueshift than the higher energy transitions by switching from low HF exchange functionals to the higher ones. In addition, there is no corresponding allowed transitions in TDDFT/CAM-B3LYP for the S_1 ESA-3 band at 684 nm in TDDFT/TPSSh. The hole density of the final state (S_8) mainly appears on the TIPS- side groups, which might be attributed to the difference in delocalization errors of different functionals.





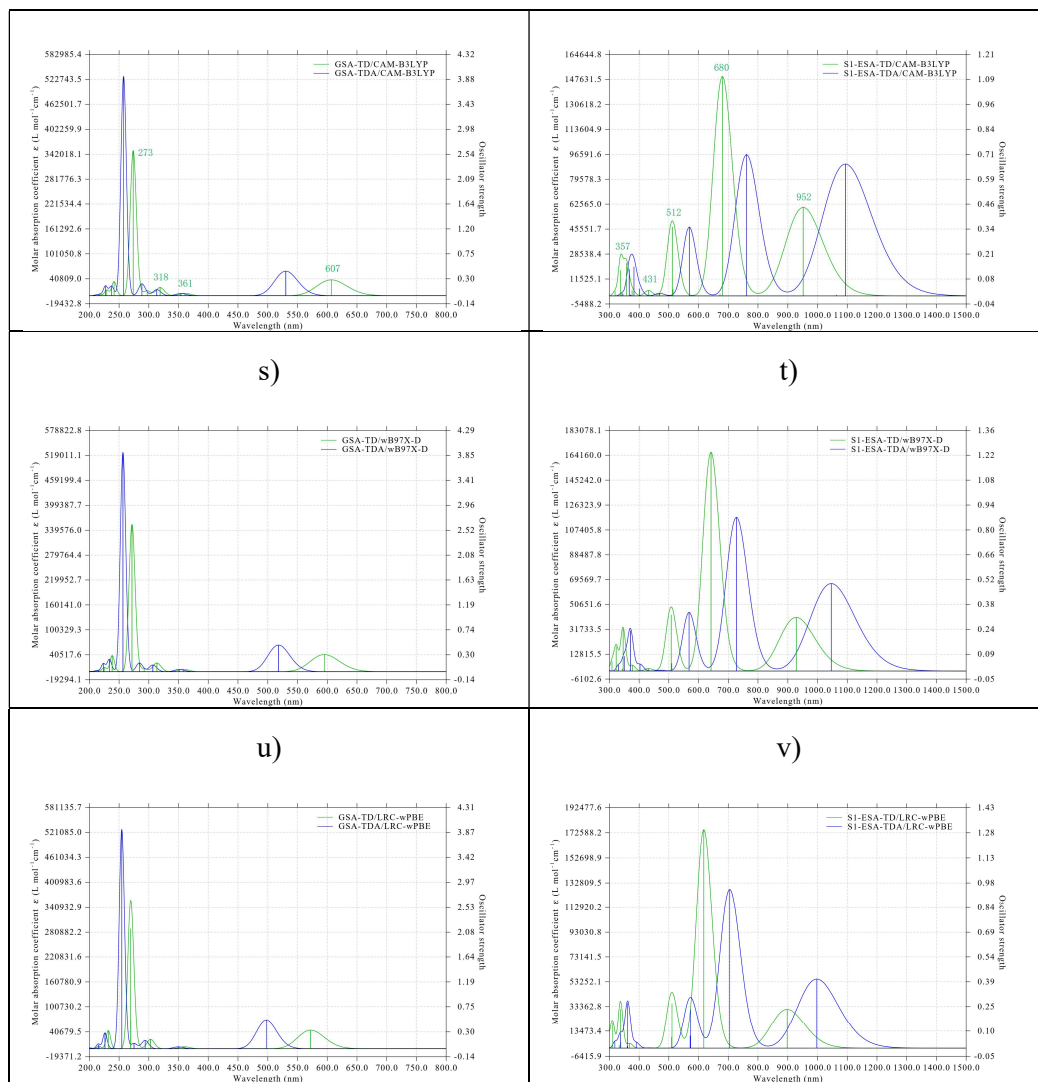


Figure 4.2. GSA and S_1 ESA of TIPS-pentacene extracted from experiments (a and b) and calculated at TDDFT/TDA/6-31G* with 10 XC functionals (c-v). The experimental GSA spectrum was taken from Ref. [115], and the S_1 ESA spectrum was extracted and combined from Ref. [72] and [114].

Table 4.2. Transition analysis of GSA and S_1 ESA of TIPS-pentacene calculated of TIPS-pentacene at TDDFT/TPSSH/6-31G* level. Isosurface values for electron and hole densities: 0.0005 a.u..

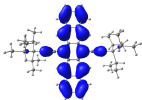
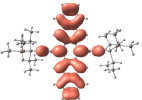
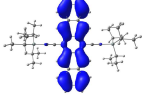
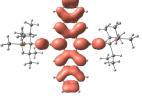
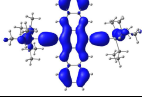
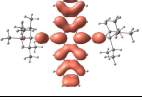
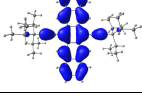
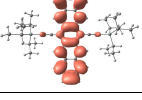
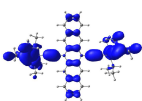
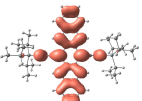
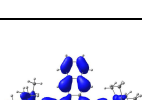
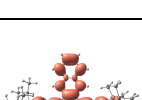
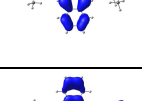
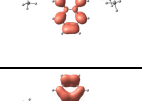
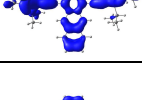
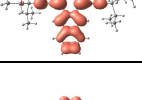
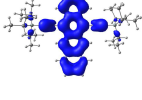
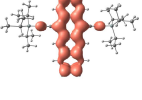
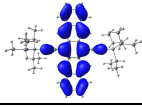
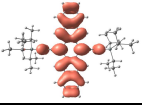
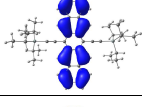
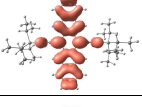
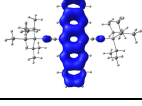
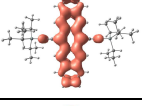
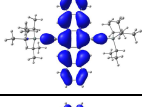
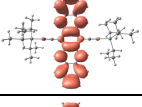
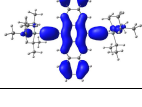
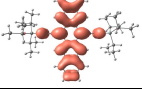
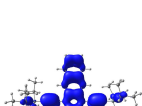
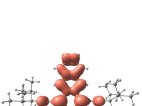
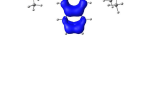
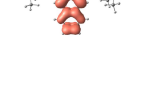
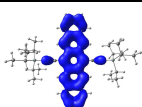
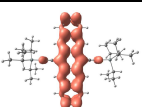
S0 → Sn							S1 → Sn			
State	eV	nm	f	MO Transition	Hole	Electron	Label	eV	nm	f
S1	1.67	745	0.15	H → L 100.8%						
S2	2.57	482	0.00	H-1 → L 90.3% H → L+1 9.2%			ESA1	0.91	1365	1.06
S3	2.97	418	0.07	H-2 → L 84.5% H → L+2 15.0%						
S4	3.11	399	0.00	H → L+1 88.7% H-1 → L 8.6%			ESA2	1.44	860	0.35
S8	3.48	356	0.01	H-5 → L 68.5% H-6 → L 15.4% H-4 → L 11.6%			ESA3	1.82	684	0.25
S9	3.50	355	0.27	H → L+2 76.3% H-2 → L 12.8% H-7 → L 5.9%						
S11	3.98	312	0.00	H-8 → L 86.6% H → L+4 11.1%			ESA4	2.31	536	0.20
S14	4.11	302	1.77	H → L+3 54.9% H-3 → L 33.4% H-10 → L 10.6%						
S20	4.44	279	0.00	H → L+4 71.0% H-8 → L 8.7% H-3 → L+1 6.5% H-13 → L 5.2%			ESA5	2.77	447	0.16

Table 4.3. Transition analysis of GSA and S_1 ESA of TIPS-pentacene calculated at TDDFT/CAM-B3LYP/6-31G* level. Isosurface values for electron and hole densities: 0.0005 a.u..

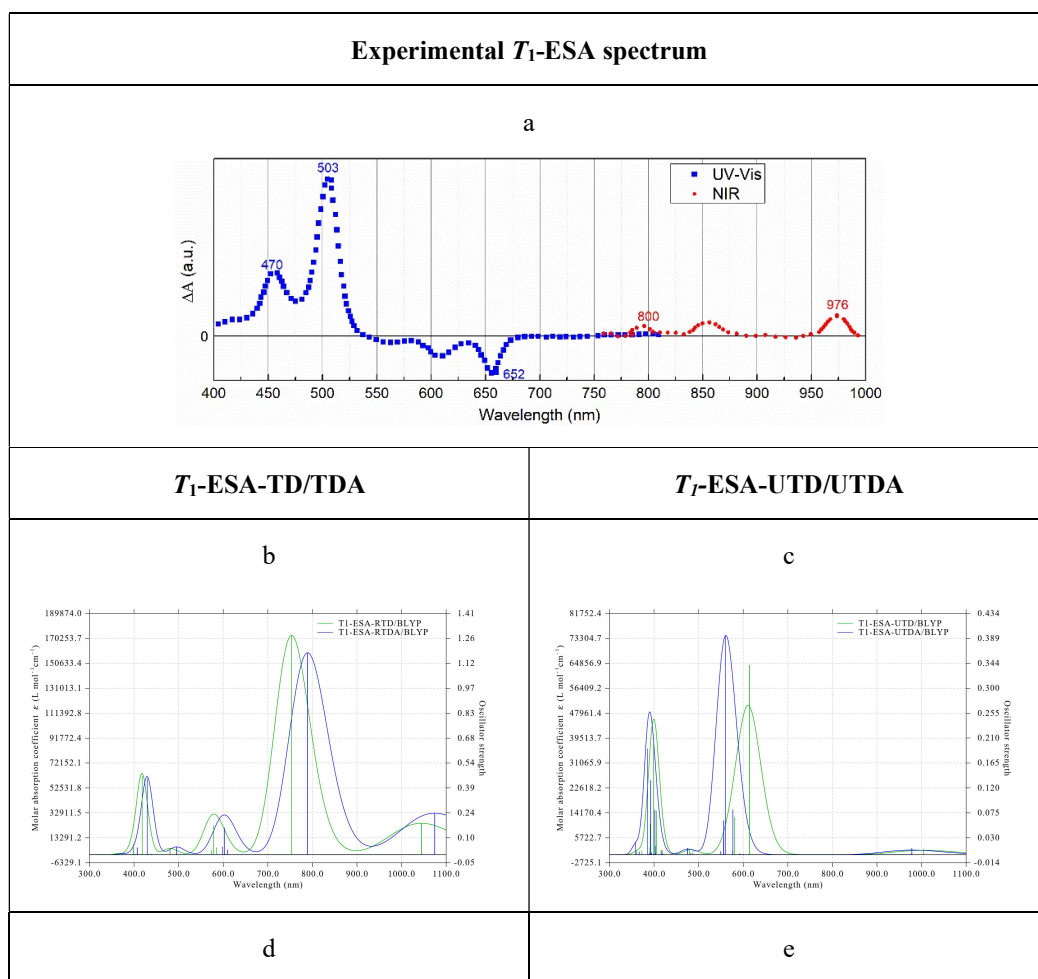
S0 → Sn							S1 → Sn			
State	eV	nm	f	MO Transition	Hole	Electron	Label	eV	nm	f
S1	2.04	607	0.28	H → L 100.3%						
S2	3.35	371	0.00	H-1 → L 94.0%			ESA1	1.30	952	0.45
S3	3.44	361	0.04	H-2 → L 60.0% H → L+2 34.7%				1.39	890	0.00
S4	3.87	321	0.00	H → L+1 91.7%			ESA2	1.82	680	1.10
S5	3.89	319	0.15	H-3 → L 93.3%				1.85	672	0.01
S9	4.47	278	0.01	H-4 → L 51.2% H-8 → L 12.8% H-2 → L+1 7.8% H-1 → L+2 6.2% H-6 → L 6.0%			ESA3	2.43	512	0.35
S10	4.53	274	2.60	H → L+2 61.2% H-2 → L 36.6%				2.49	498	0.00
S11	4.92	252	0.00	H → L+4 34.5% H-1 → L+2 20.1% H-4 → L 16.8% H-2 → L+1 9.2% H-13 → L 8.8%			ESA4	2.87	432	0.03

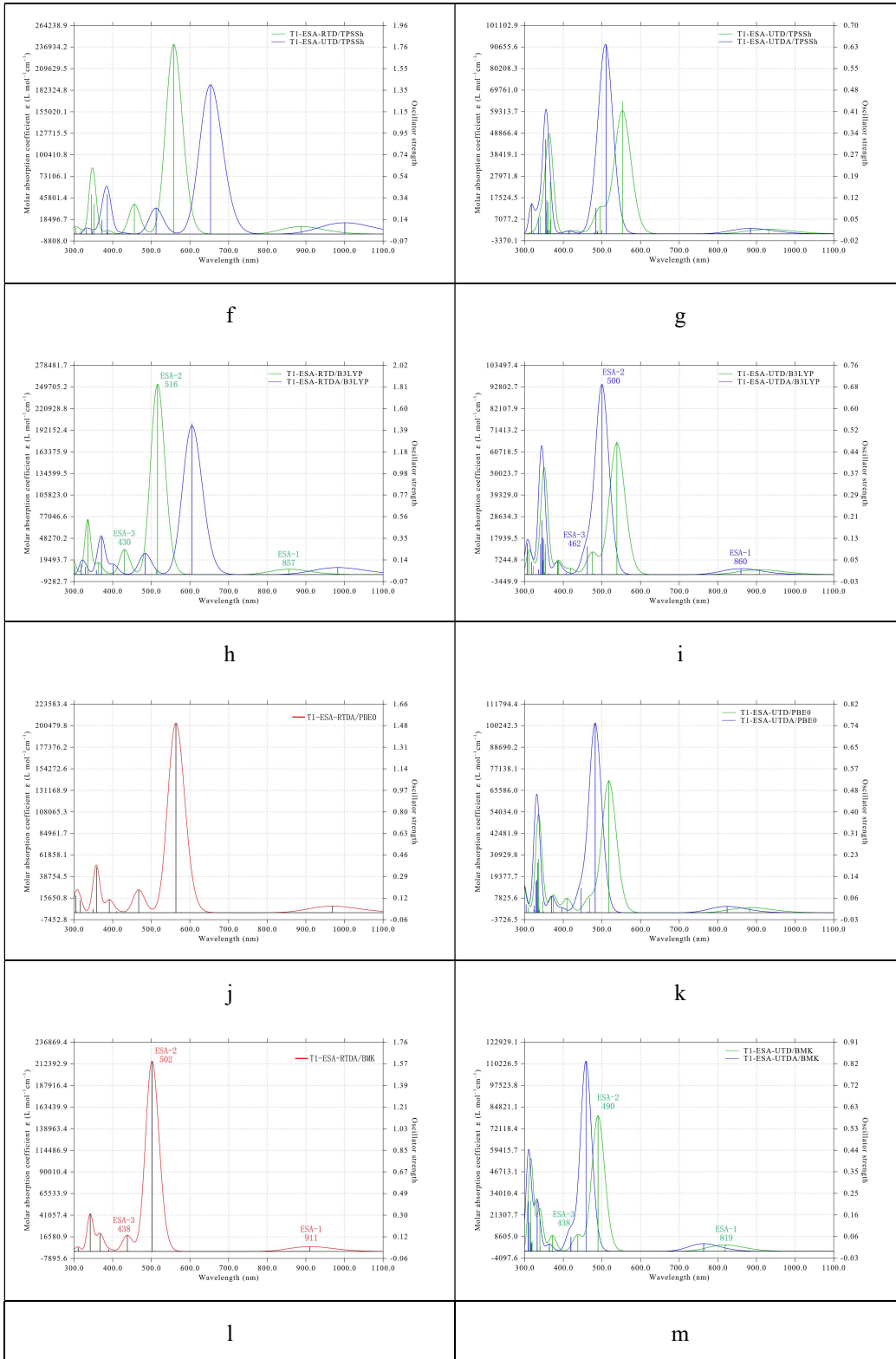
T₁ ESA spectra of TDDFT/TDA/UTDDFT/UTDA

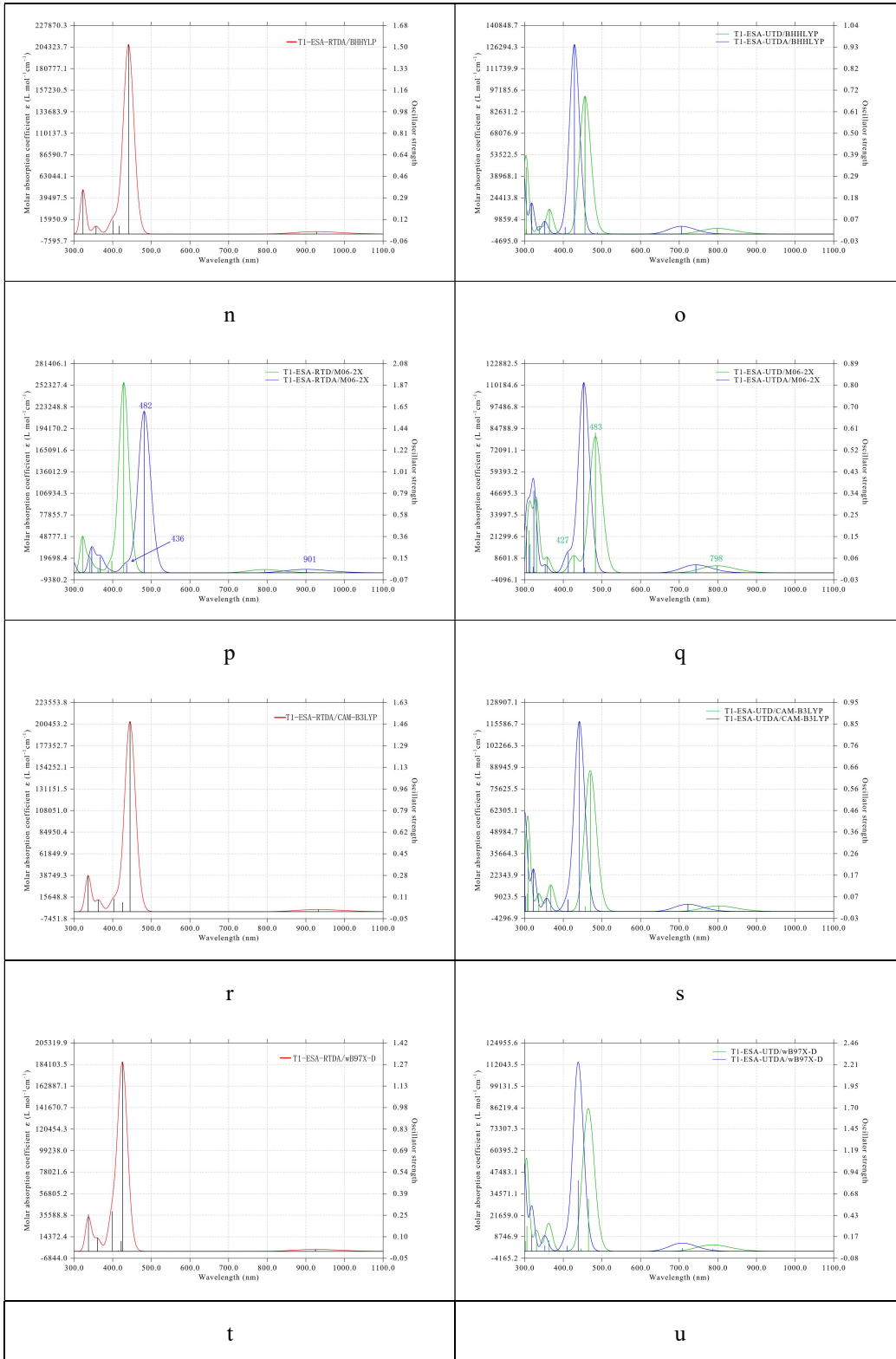
Turning to the results of triplet excited states, T_1 energies obtained from TDDFT exhibit considerable underestimation compared with the reference values. It is noted that the experimental T_1 energy (0.78 eV) was derived from the maxima of phosphorescence emission spectrum, which is more related to the adiabatic excitation energy. Dependence on the exact exchange admixture for triplet excitations is not as sensitive as singlet excitations. TDDFT with high exact exchange functionals is generally not capable of giving T_1 energy, although M06-2X is exceptional. This is due to the well-known triplet instabilities^[174, 175] of TDDFT calculations. The triplet instabilities can be overcome with using TDA, where the B matrix of the TDDFT Casida equations is neglected. Moreover, the usage of TDA also remarkably increases the energies and hence improves the accuracy. The calculated UDFT T_1 energies are not spin-contaminated with all $\langle S^2 \rangle$ values are around 2.0. The UDFT provides slightly lower energies than TDA but is still overall much better than TDDFT. Although BMK and M06-2X with TDA and UDFT predict much higher T_1 energies than the PPP-MRSDCI reference value (0.89 eV), it is essential to note that they performed very well for pentacene molecule, in comparison with the vertical T_1 energy of Multi-State-CASPT2/cc-pVTZ (1.25 eV).^[99] Therefore, we believe that the vertical T_1 energies of BMK and M06-2X with TDA and UDFT would be much closer to the real values.

With respect to the T_1 ESA spectra, TDA results in systematically redshift and blueshift for the spin-restricted and spin-unrestricted calculations, respectively. Although the trend of the T_1 excitation energies concerning the HF admixture is not straightforward, it is clearly seen that the T_1 ESA spectra are gradually blue-shifted with an increasing amount of the HF admixture. Within the spin-restricted formalism, RTD/B3LYP, RTDA/BMK, and RTDA/M06-2X perform adequately well. Similarly, in the spin-unrestricted formalism, UTDA/B3LYP, UTD/BMK, and UTD/M06-2X show good agreement with the experiment. The above-mentioned methods all reproduce transitions at around 470, 503 in the UV-Vis region, where the maxima of the experimental T_1 ESA spectra are observed. The experimental T_1 ESA spectra show three bands in the NIR region, whereas the calculated T_1 ESA spectra only have one band. However, it is not clear whether the experimental bands correspond to one electronic transition with vibronic broadening or not.

In order to characterize the calculated T_1 ESA spectra, we analyzed transition character for UTDA/B3LYP (Table 4.4) and UTD/BMK (Table 4.5). The spin contamination is negligible for all allowed transitions since the $\langle S^2 \rangle$ values are all around 2.0. Again, the electron-hole pairs for the final states of lower energy transitions (T_1 ESA-1,2 bands) are correspondingly identical between UTDA/B3LYP and UTD/BMK. The hole character for the final state of the T_1 ESA-3 band with UTDA/B3LYP is somewhat different from UTD/BMK, with more hole density accumulate at the TIPS- side groups.







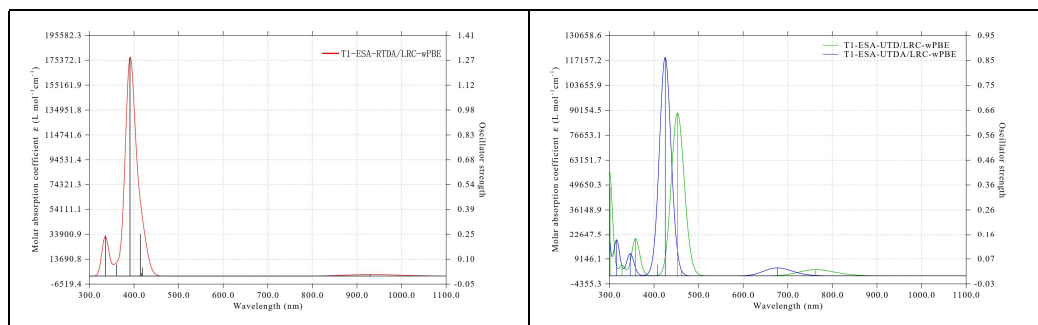
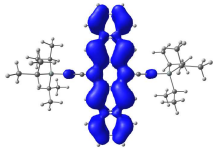
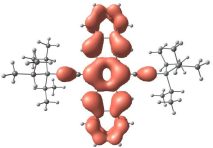
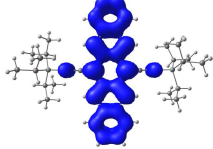
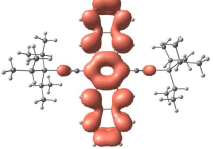
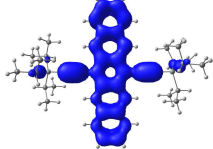
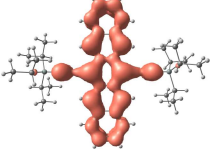


Figure 4.3. T_1 ESA spectra of TIPS-pentacene extracted from experiments (a) and calculated at TDDFT/TDA/UTDDFT/UTDA/6-31G* with 10 XC functionals (b-v). The experimental T_1 ESA spectrum was taken and combined from Ref. [56, 73].

Table 4.4. Transition analysis of T_1 ESA of TIPS-pentacene calculated at UTDA/B3LYP/6-31G* level. Isosurface values for electron and hole densities: 0.0005 a.u..

State	T1-ESA	$\langle S^2 \rangle$	eV	nm	f	MO Transition	Hole	Electron
T2	ESA1	2.04	1.44	859	0.02	Hb \rightarrow Lb 64.4% Ha \rightarrow La 33.9%		
T5	ESA2	2.06	2.48	500	0.69	Ha \rightarrow La 56.2% Hb \rightarrow Lb 27.5% Hb-2 \rightarrow Lb+1 9.2%		
T9	ESA3	2.09	2.68	462	0.10	Hb-3 \rightarrow Lb 76.1% Ha \rightarrow La+3 7.5% Hb-1 \rightarrow Lb+1 5.4%		

Table 4.5. Transition analysis of T_1 ESA of TIPS-pentacene calculated at UTD/BMK/6-31G* level. Isosurface values for electron and hole densities: 0.0005 a.u..

State	T1-ESA	<S2>	eV	nm	f	MO Transition	Hole	Electron
T2	ESA1	2.06	1.51	819	0.03	Hb -> Lb 70.6% Ha -> La 27.7%		
T5	ESA2	2.09	2.53	490	0.59	Ha -> La 68.1% Hb -> Lb 26.8%		
T8	ESA3	2.29	2.83	438	0.07	Hb-3 -> Lb 46.2% Hb-1 -> Lb+1 6.9% Ha -> La+3 7.7% Ha-1 -> La+1 7.1% Hb-7 -> Lb 5.8%		

4.4.2 TIPS-Pentacene Monomer Calculated with QR-TDDFT/SLR-TDDFT/SF-TDDFT

S_1 ESA spectra of QR-TDDFT and SLR-TDDFT

In order to evaluate the effect of orbital relaxation on the S_1 ESA spectra, we also performed QR-TDDFT and SLR-TDDFT calculations for TIPS-pentacene. Since GH meta-GGA functionals such as TPSSh are not available for QR-TDDFT and SLR-TDDFT methods, here we employed B3LYP and CAM-B3LYP. The corresponding spectra are shown in Figure 4.4, 5, and 6.

As can be seen from the figures, orbital relaxation has a negligible impact on the peak position, compared with the unrelaxed TDDFT results. However, orbital relaxation leads to considerable variations on the oscillator strength. The S_1 ESA spectra of QR-TDDFT show reduced absorptions in the NIR region for both B3LYP and CAM-B3LYP. On the other hand, the intensity of S_1 ESA band at 627 nm of QR-TDDFT/B3LYP are almost as twice as that of TDDFT/B3LYP. Whereas, the

absorptions of QR-TDDFT/CAM-B3LYP are dramatically enhanced in the range of 400-500 nm, especially for the band at around 510 nm.

The results of SLR-TDDFT depend on the choice of the parameters λ and C_{tol} . We progressively tuned λ from 0.01 to 0.2 and compared the resulting spectra with the experiment. Here we plot two sets of spectra with lower λ values and higher λ values for each functional. (Figure 4.5 and Figure 4.6). As found in the spectra of QR-TDDFT, the oscillator strengths of lower energy transitions are decreased to a great extent, in the case of SLR-TDDFT/CAM-B3LYP, the NIR absorptions are almost vanishing. Meanwhile, the relative intensities of ESAs in the UV-Vis region are increased. For SLR-TDDFT/B3LYP, the ESA-3 band at around 650 nm is decreased with a higher λ value. However, the band at 680 nm of SLR-TDDFT/B3LYP shows a much more prominent absorption with a higher λ value.

The relaxed S_1 ESA spectra calculated with QR-TDDFT and SLR-TDDFT indicate that the higher energy transition might be more intensive than the lower energy transition, which is in contrast to the experiment (Figure 4.2b). It also seems like either QR-TDDFT or SLR-TDDFT does not provide better results than the unrelaxed TDDFT.

However, it is noted that the experimental ESA spectra are usually plotted in a time-averaged way.^[114] Therefore, the unrelaxed TDDFT ESA spectra might be more closed to the time-averaged experimental ESA spectra, whereas the relaxed ESA spectra might be more related to experimental ESA spectra measured at an early time.

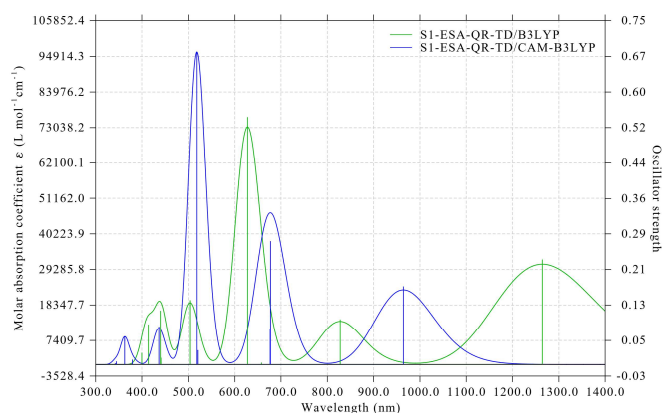


Figure 4.4. S_1 ESA spectra of TIPS-pentacene calculated at QR-TDDFT/6-31G* level with B3LYP and CAM-B3LYP.

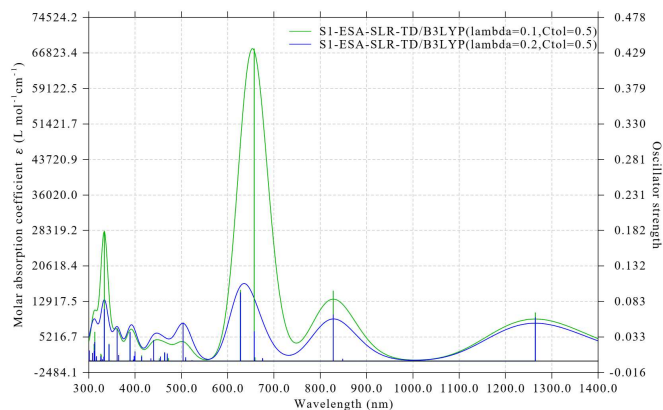


Figure 4.5. S_1 ESA spectra of TIPS-pentacene calculated at SLR-TDDFT/6-31G* level with B3LYP.

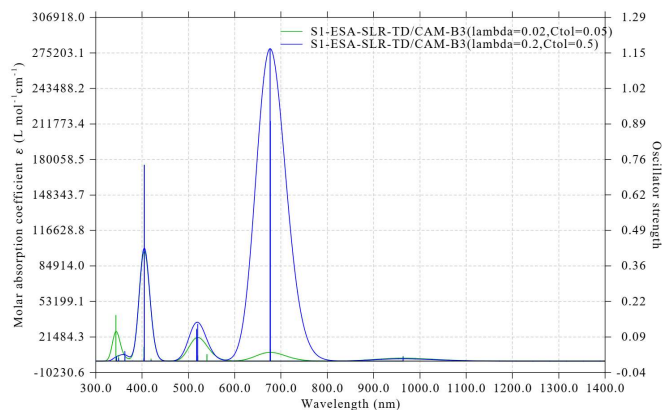


Figure 4.6. S_1 ESA spectra of TIPS-pentacene calculated at SLR-TDDFT/6-31G* level with CAM-B3LYP.

GSA and S_1 ESA spectra of SF-DFT

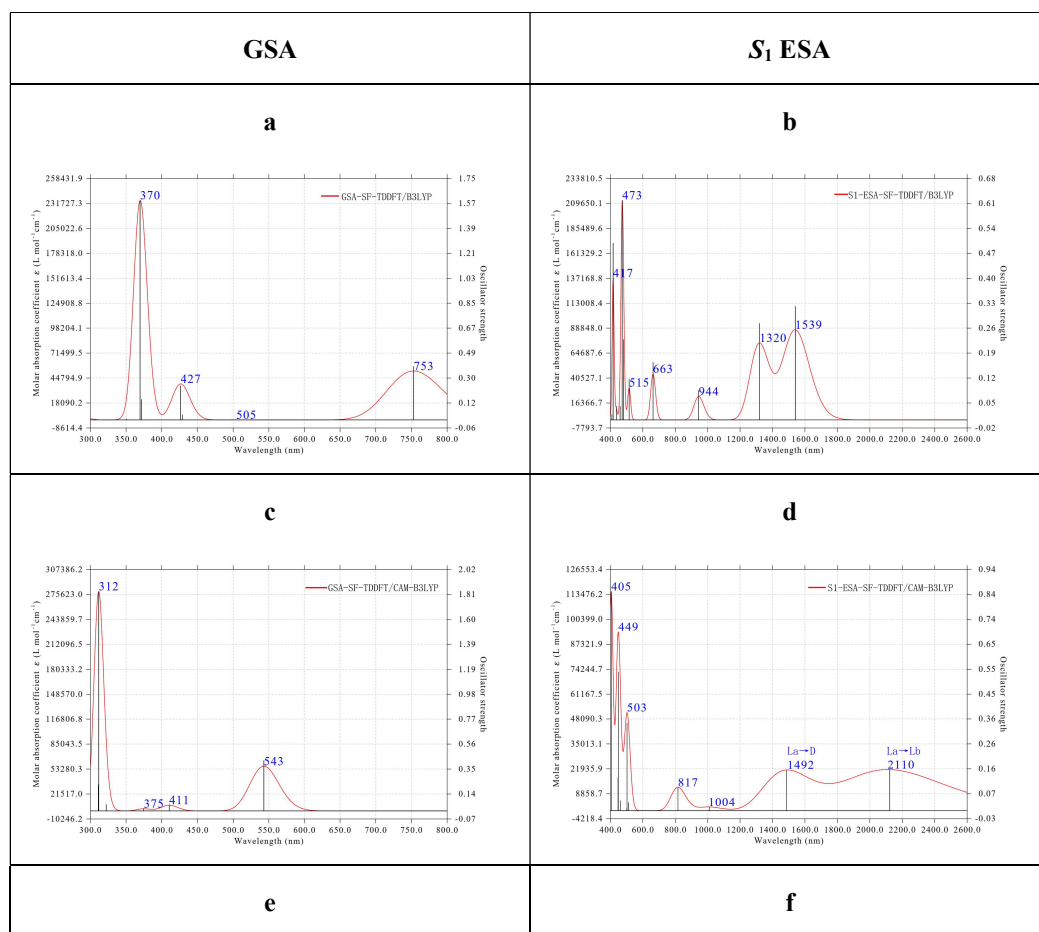
Although SF-TDDFT is a single-excitation method, it can recover double excitations (with respect to the singlet ground state configuration) by starting from the triplet reference configuration. In order to account for the double excitation in the singlet excited states, we computed GSA and S_1 ESA spectra of TIPS-pentacene with SF-TDDFT in combination with B3LYP, CAM-B3LYP, and BHHLYP. We have shown the resulting spectra and transition character in Figure 4.7 and Table 4.6, respectively. Since SF-TDDFT does not account for spin-adaptation, it usually leads to spin-incomplete singlet states. Here based on the assumption that any state with $\langle S^2 \rangle < 1.5$ is a singlet, we characterized the singlet excited states by the $\langle S^2 \rangle$ values and the MO transitions. We found that the L_a and low-lying doubly excited state (D) are nearly spin-pure with $\langle S^2 \rangle \approx 0$, the L_b and other singlet excited states are spin-impure with $\langle S^2 \rangle \approx 1$.

In general, the GSA spectra obtained by SF-TDDFT exhibit a significant improvement for the excited states in the high energy region but not for the low-lying excited states. For example, the strongest absorption of the GSA spectrum of TDA/CAM-B3LYP is located at 265 nm, and it is red-shifted to 314 nm by SF-TDDFT/CAM-B3LYP. The same redshift can also be seen for other high energy transitions and other functionals. In particular, the strongest ground state absorptions obtained by SF-TDDFT/CAM-B3LYP (312 nm) and SF-TDDFT/BHHLYP (312 nm) show excellent agreement with the experiment (310 nm). Transition analysis illustrates that the final state (S10 in CAM-B3LYP) is a BS singlet state with $\langle S^2 \rangle = 1.07$, and includes 66% contributions from double excitation. Therefore, energies of high-lying excited states can be considerably stabilized by mixing with double excitations in the framework of SF-TDDFT. Whereas, the first absorption bands of SF-TDDFT with CAM-B3LYP and BHHLYP are too much blue-shifted, compared to the experiment. This is due to the TDA formalism applied in SF-TDDFT. On the other hand, SF-TDDFT successfully predicts an additional absorption in the NIR+mid-NIR region of the S_1 ESA spectra, which is absent on the spectra of TDDFT but revealed by the experiment and CASSCF calculation^[115]. However, the order between these two absorptions is against previous studies. Transition analysis reveals that the S_1 -ESA and S_2 -ESA band are corresponding to $L_a \rightarrow L_b$ and $L_a \rightarrow D$ transitions, respectively. This means that the doubly excited state (D) is higher in energy than the L_b state. Although SF-TDDFT B3LYP provides a reasonable $L_a \rightarrow L_b$ transition at 1539 nm, the $L_a \rightarrow D$ transition is at 1320 nm, which is

much higher than CASSCF calculated (2175 nm) and experimentally measured values (5905 nm).

It is also noted that the S_1 -ESA spectra of SF-TDDFT also show enhanced features at 400-500 nm, as found in QR-TDDFT and SLR-TDDFT. The orbital relaxation is taken into account by mixed with double excitations within SF-TDDFT.

While SF-TDDFT shows good performance for the high-lying excited states, it does not provide a much superior GSA and S_1 ESA spectra than TDDFT due to the unbalanced description of the low-lying states. This might be improved by the spin-adapted version of SF-TDDFT (SA-SF-TDDFT)^[176] developed by Herbert and coworkers. However, we cannot converge the SA-SF-TDDFT calculations, which is usually the case for SA-SF-TDDFT, and as far as we know, the implementation of TDM for SA-SF-TDDFT is not available yet.



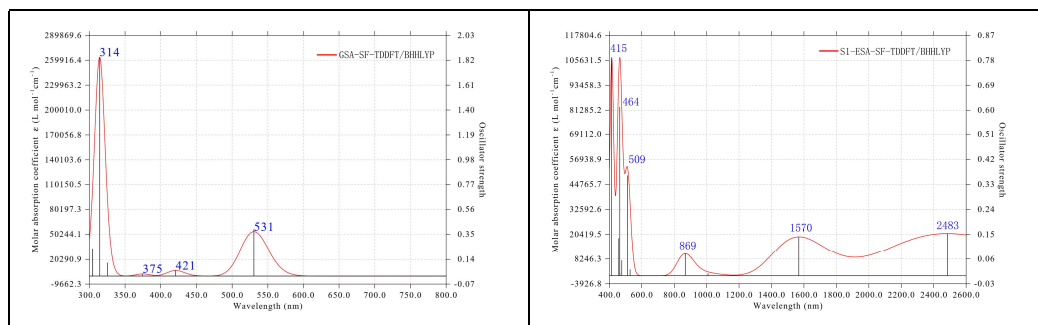


Figure 4.7. GSA and S_1 ESA of TIPS-pentacene calculated at SF-TDDFT/6-31G* with B3LYP, CAM-B3LYP, and BHLYP.

Table 4.6. Transition analysis of TIPS-pentacene for selected singlet-like excited states calculated at SF-TDDFT/6-31G* with B3LYP and CAM-B3LYP. In the column of MO transition, S refers to singly occupied molecular orbital (SOMO), HD is the highest doubly occupied molecular orbital (HDOMO), V represents virtual molecular orbital. Transitions with double excitation character are labeled as DE.

State	$\langle S^2 \rangle$	MO transition	$S_0 \rightarrow S_n$			$S_1 \rightarrow S_n$		
			eV	nm	f	eV	nm	f
SF-TDDFT/B3LYP/6-31G*								
S0	0.05	S(2) --> S(1) 0.9861	0.00					
S1, La	0.06	S(1) --> S(1) 0.7110 S(2) --> S(2) -0.7001	1.65	753	0.39	0.00		
S2, Lb	1.04	HD --> S(1) 0.9362 S(2) --> V(1) 0.3071(DE)	2.45	506	0.00	0.81	1540	0.32
S3, D	0.12	S(1) --> S(2) 0.9579(DE)	2.59	479	0.00	0.94	1318	0.27
S8	1.04	HD-1 --> S(1) -0.4014 S(2) --> V(3) 0.9025(DE)	3.36	369	1.60	1.71	726	0.00
SF-TDDFT/CAM-B3LYP/6-31G*								
S0	0.10	S(1) --> S(2) 0.1836 S(2) --> S(1) 0.9659	0.00					
S1, La	0.18	S(1) --> S(1) 0.7036 S(2) --> S(2) -0.6899	2.28	543	0.42	0.00		
S2, Lb	1.10	HD-7 --> S(1) 0.1880 HD --> S(1) 0.8549 S(1) --> V(2) -0.1816(DE) S(2) --> V(1) 0.3751(DE)	2.87	432	0.00	0.58	2122	0.16
S5, D	0.38	HD-3 --> S(1) -0.2926 HD --> V(1) 0.1823 (DE) S(1) --> S(2) 0.8493(DE) S(2) --> S(1) -0.2163 S(2) --> V(4) 0.1961(DE)	3.12	398	0.00	0.84	1484	0.16

S10	1.07	HD-1 --> S(1) 0.5241 HD --> S(2) 0.1560 (DE) S(2) --> V(2) 0.8141 (DE)	3.98	311	1.84	1.70	731	0.00
-----	------	--	------	-----	------	------	-----	------

4.4.3 BP0 Dimer Calculated with TDDFT/UTDDFT/BS-TDDFT

Vertical excitation energies

We have shown the feasibility of single-reference DFT-based methods for calculations of the electronic absorption spectra of the TIPS-pentacene monomer. In the following, we turn to the discussion for the BP0 dimer. Since the GSA spectra of SF-TDDFT and the S_1 ESA spectra of QR-TDDFT, SLR-TDDFT, and SF-TDDFT do not show significant improvement over the ones with TDDFT, we only computed the GSA and S_1 ESA spectra for the BP0 dimer within standard TDDFT formalism. For the sake of simplicity, we will restrict to functionals which show good agreement with the experiment for the investigation of BP0.

In Table 4.7, we list our calculated vertical excitation energies S_1 , S_0T_1 , and ${}^1(T_1T_1)$ states for the BP0 dimer, in comparison with experimental and PPP-MRSDCI values. Figure 4.8 and Figure 4.11 show the resulting GSA spectra and ESA spectra of S_1 , S_0T_1 , and ${}^1(T_1T_1)$ states.

Table 4.7. Vertical excitation energies of BP0 in eV of reference and calculated by TDDFT/UDFT/BS-DFT/6-31G* with various XC functionals for BP0 dimer. The excitation energies of S_1 , S_0T_1 , and ${}^1(T_1T_1)$ states are calculated with TDDFT, UDFT, and BS-DFT, respectively. The $\langle S^2 \rangle$ values for spin-unrestricted calculations are shown in parentheses.

	S_1	S_0T_1	${}^1(T_1T_1)$	$2 \times S_0T_1 - {}^1(T_1T_1)$
Experiment ^[119]	1.89	/	/	/
PPP-MRSDCI ^[118]	1.91	0.92	1.83	0.01
TPSSh	1.40	0.80 (2.03)	/	/
B3LYP	1.61	0.83 (2.04)	/	/
CAM-B3LYP	2.03	0.84 (2.06)	1.68 (2.09)	0.01
BMK	1.92	0.92 (2.05)	1.83 (1.94)	0.02
M06-2X	2.01	1.04 (2.03)	2.04 (2.01)	0.03

GSA and S_1 ESA of BP0

First of all, the S_1 excitation energies of BMK with TDDFT (1.92 eV) provide excellent agreement with reference values (around 1.90 eV),^[118, 119] CAM-B3LYP, M06-2X slightly overestimate the energies by around 0.12 eV. Whereas, as can be seen in Figure 4.8c, functionals with low HF exchange such as TPSSh predict much lower S_1 excitation energies (1.40 eV), and the improvement by TDA is negligible (1.44 eV). On the other hand, there is an additional absorption peak at around 500 nm on both the experimental and PPP-MRSDCI GSA spectra for BP0, which is absent on the GSA spectra for TIPS-Pn and assigned as a charge resonance state by exciton basis analysis with PPP-MRSDCI. This charge resonance excitation cannot be described appropriately by TPSSh (723 nm) but is adequately reproduced by functionals with a high amount of exact exchange such as CAM-B3LYP (415 nm), BMK (498 nm) and M06-2X (441 nm). Again, TDDFT/BMK performs the best in reproducing the GSA spectra of the BP0 dimer. Although TDA/TPSSh give the best agreement with experiment for the GSA spectrum of TIPS-pentacene (Figure 4.2e), it significantly underestimates the energies of low-lying excited states for BP0. This can be attributed to the poor description of low HF exchange functionals for the distance dependence of charge transfer or charge resonance excitations, especially for large molecules. It is also noted that the experimental GSA spectrum of BP0 is slightly red-shifted than that of TIPS-pentacene (Figure 4.2 and Figure 4.8). Whereas, as can be seen from the PPP-MRSDC, I calculated S_1 energies for BP0 (1.91 eV), and TIPS-pentacene (1.88 eV), the GSA spectrum of BP0 is slightly blue-shifted relative to TIPS-pentacene. This is owing to the consequence of incomplete active space, even a sizeable active space with 24 molecular orbitals was used in the PPP-MRSDCI calculations. Therefore, we conclude that TDDFT, in conjunction with a high amount of HF exchange or long-range-corrected functionals, can provide more consistent GSA spectra for simulating the experiment of large π conjugated systems.

The experimental S_1 ESA spectrum of BP0 reveals four maxima at 460, 544, 900, 1340 nm in the UV-Vis and NIR regions. PPP-MRSDCI calculations predicted additional absorptions at around 2000 nm (Figure 5 (a) of Ref. ^[119]), which were not reached by experiment. The final states of the transitions at around 2000 nm have considerable double excitation character, and hence cannot be captured by TDDFT. However,

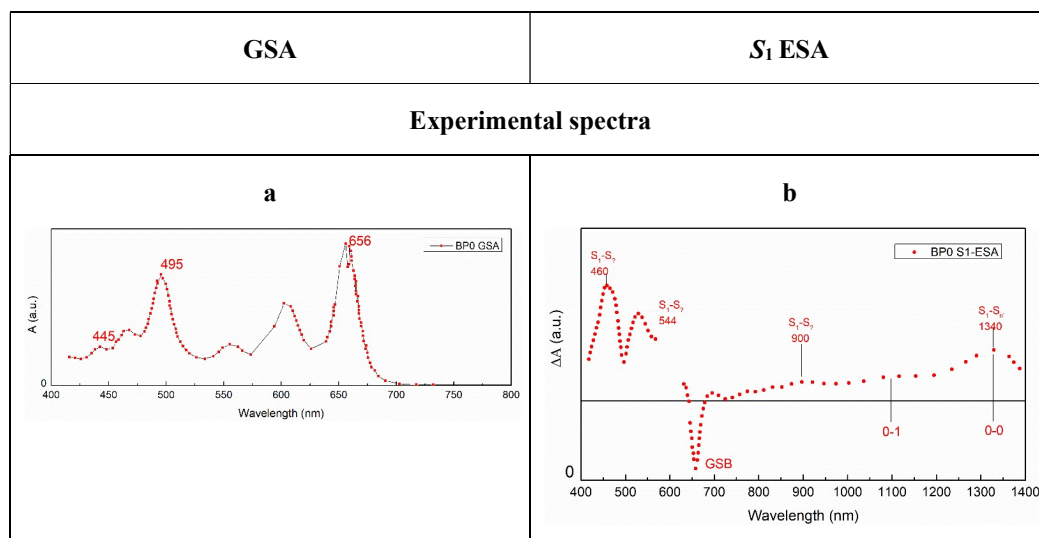
TDDFT has no problem in describing the transitions in the UV-Vis and NIR regions. For example, TDDFT/CAM-B3LYP (Figure 4.8j) produces five absorption bands located at 467, 546, 685, 936, 1386 nm. The band at 685 nm is likely to be overlapped by GSB at around 660 nm. This indicates an excellent agreement with the experiment. Moreover, due to the limitation of the active space, the high energy transitions are too expensive to compute with PPP-MRSDCI. Because of the inadequate description of excitations with charge-transfer character of low HF exchange functionals, TDDFT/TPSSh does not provide good performance for the S_1 ESA spectrum of BP0, as in the case of TIPS-pentacene. Although TDDFT/BMK and TDDFT/M06-2X show more consistent GSA spectra of BP0 than TDDFT/CAM-B3LYP, compared with the experiment, they exhibit inferior S_1 ESA spectra for BP0. In combination with the discussion of the spectra of TIPS-pentacene, it is suggested that functionals give good performance for the GSA (S_0 to S_n transitions), do not necessarily yield superior S_1 ESA spectra (S_1 to S_n transitions).

Comparison between BP0 and TIPS-pentacene monomer

Let us turn to the comparison between the S_1 ESA spectra of BP0 and TIPS-pentacene. Experimentally, the S_1 ESA spectrum of BP0 is slightly red-shifted relative to TIPS-pentacene, without introducing additional absorptions. If we compare the best fitting S_1 ESA spectra of BP0 (TDDFT/CAM-B3LYP) with TIPS-pentacene (TDDFT/TPSSh), the same conclusion can be made. This further confirms that the initial state of SF in BP0, is more a “monomeric” S_1 -like state rather than a coherent superposition state of both S_1 and $^1(T_1T_1)$ character. We have discussed that TDDFT/TPSSh cannot provide accurate S_1 ESA spectrum for BP0 due to the underestimation of excitations with charge-transfer character, a natural question is why TDDFT/CAM-B3LYP behaves much better in the BP0 dimer than the TIPS-pentacene monomer. First of all, it has already been found that a balanced description for the S_1 (L_a) and S_2 (L_b) is nearly impossible for oligoacenes.^[172, 173] The L_a state exhibits some “charge-transfer in disguise” character, which can be accurately described by LRC or high HF exchange functionals, but at the expense of overestimating the L_b energy. This explains that LRC and high HF exchange functionals with TDDFT can reproduce the GSA-1 band ($S_0 \rightarrow L_a$ transition) of TIPS-pentacene, whereas the S_1 ESA-1 band ($L_a \rightarrow L_b$ transition) is

considerably blue-shifted, compared to experiment. On the other hand, the L_b state has a significant double excitation contribution, which, in principle, cannot be accounted for by standard TDDFT. Although functionals with low HF exchange such as TPSSH significantly underestimate the L_a state, the $L_a \rightarrow L_b$ transition energy is in good agreement with the experiment. This is benefited from favorable error compensation.

Secondly, the final state of the S_1 ESA-1 band of BP0 at around 1350 nm was characterized by exciton basis analysis with PPP-MRSDCI, as a linear combination of single excitations on both TIPS-pentacene units, without any double excitation character. Therefore, the S_1 ESA-1 band of BP0 is free of double excitation and can be well described by functionals such as CAM-B3LYP. The electron-hole analysis of BP0 (Table 4.8) further shows that the final state of the S_1 ESA-1 band is a “monomeric” S_1 (L_a)-like state rather than an S_2 (L_b)-like state, and this transition is, of course, absent on the S_1 ESA-1 band of TIPS-pentacene calculated with TDDFT/CAM-B3LYP. Within TDDFT/CAM-B3LYP, the calculated S_1 ESA-2 band of BP0 at 936 nm corresponds to the S_1 ESA-1 band of TIPS-pentacene at 952 nm, which is of $L_a \rightarrow L_b$ transition character. It is unknown whether there is a substantial double excitation contribution to the final state of the S_1 ESA-2 band of BP0 or not. If it is not the case, then the S_1 ESA at around 900 nm in the experiment could also be well reproduced by TDDFT/CAM-B3LYP. The rest S_1 ESA-3,4,5 bands of BP0 possess similar transition character as S_1 ESA-2,3,4 bands of TIPS-pentacene.



Simulated spectra with TDDFT

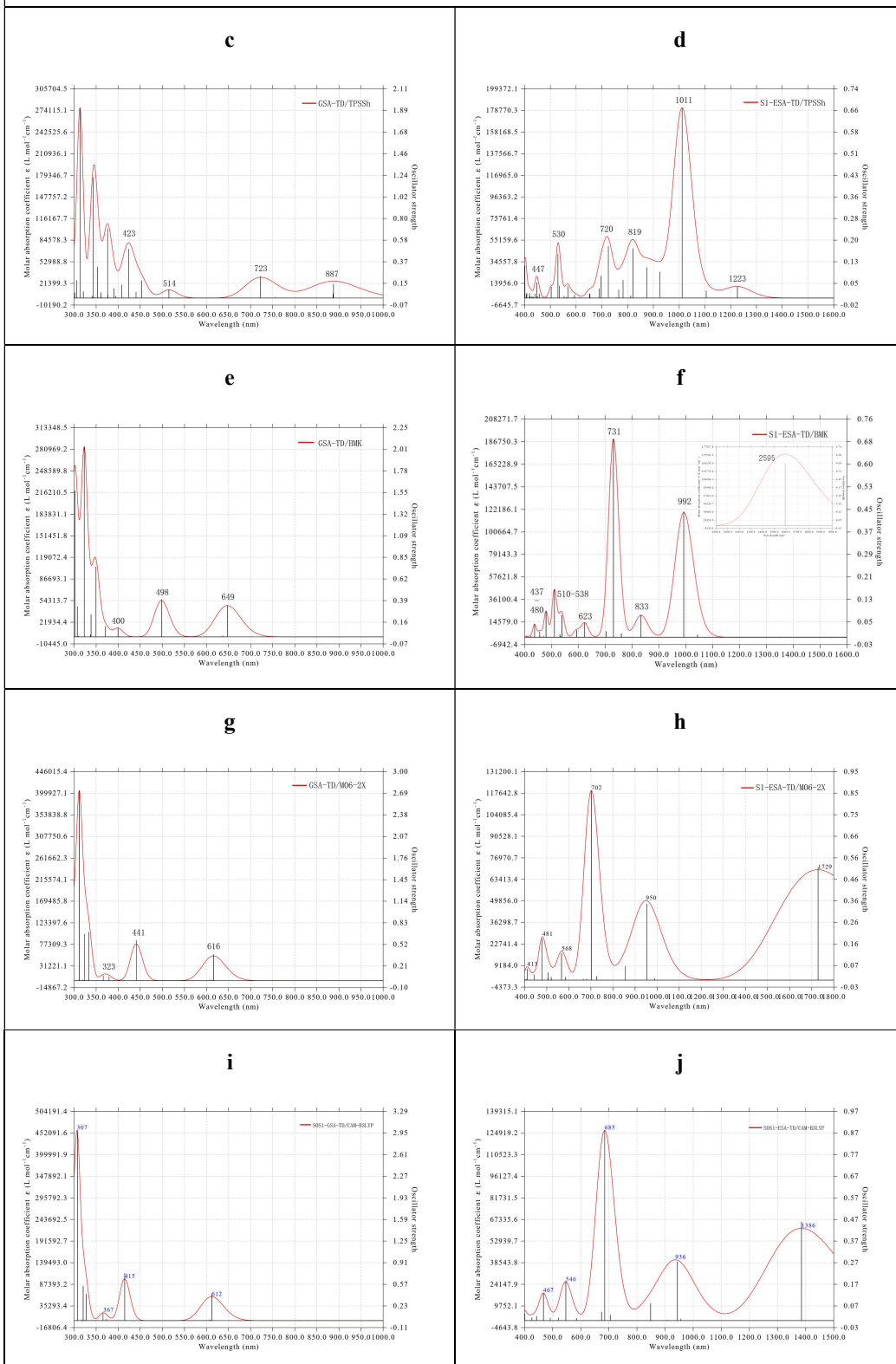
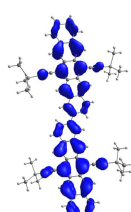
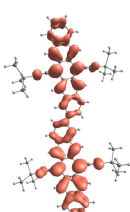
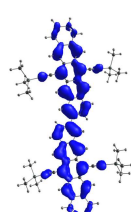
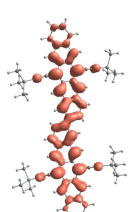
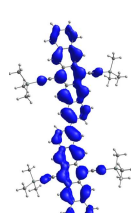
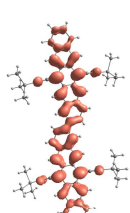
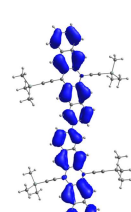
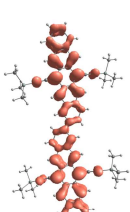
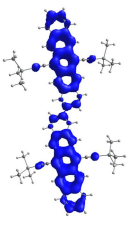
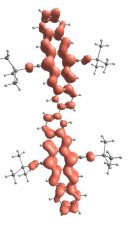
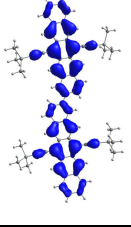
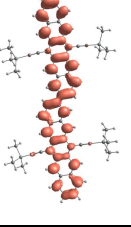
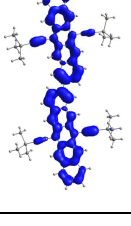
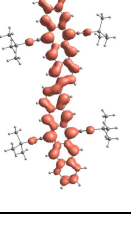
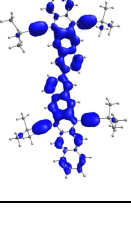
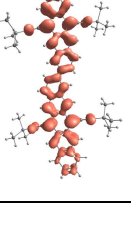


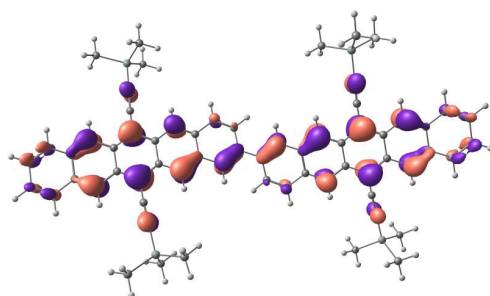
Figure 4.8. GSA and S_1 ESA of BP0 extracted from the experiment (a and b) and calculated at TDDFT/6-31G* with TPSSh, BMK, M06-2X, and CAM-B3LYP (c-j). The experimental spectra were taken from Ref. [118].

Table 4.8. Transition analysis of GSA and S_1 ESA of BP0 calculated at TDDFT/CAM-B3LYP/6-31G* level. Isosurface values for electron and hole densities: 0.0005 a.u..

S0→Sn						S1→Sn			
State	eV	nm	f	Hole	Electron	Label	eV	nm	f
S1	2.03	612	0.41						
S3	2.92	425	0.00			ESA1	0.90	1385	0.46
S4	2.99	415	0.75				0.97	1286	0.00
S6	3.34	371	0.00			ESA2	1.31	944	0.27
S7	3.39	366	0.12				1.37	908	0.00

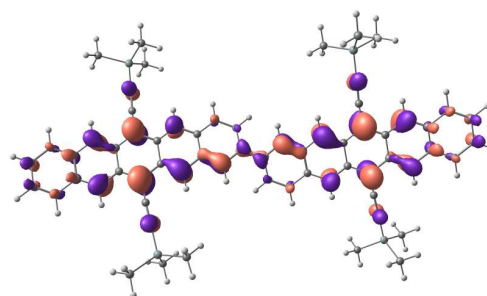
S8	3.49	356	0.00			ESA3	1.46	849	0.08
S10	3.84	323	0.01			ESA4	1.81	685	0.88
S16	4.30	289	0.00			ESA5	2.27	547	0.18
S24	4.68	265	0.00			ESA6	2.66	467	0.13

HOMO



HOMO-1

LUMO



LUMO+1

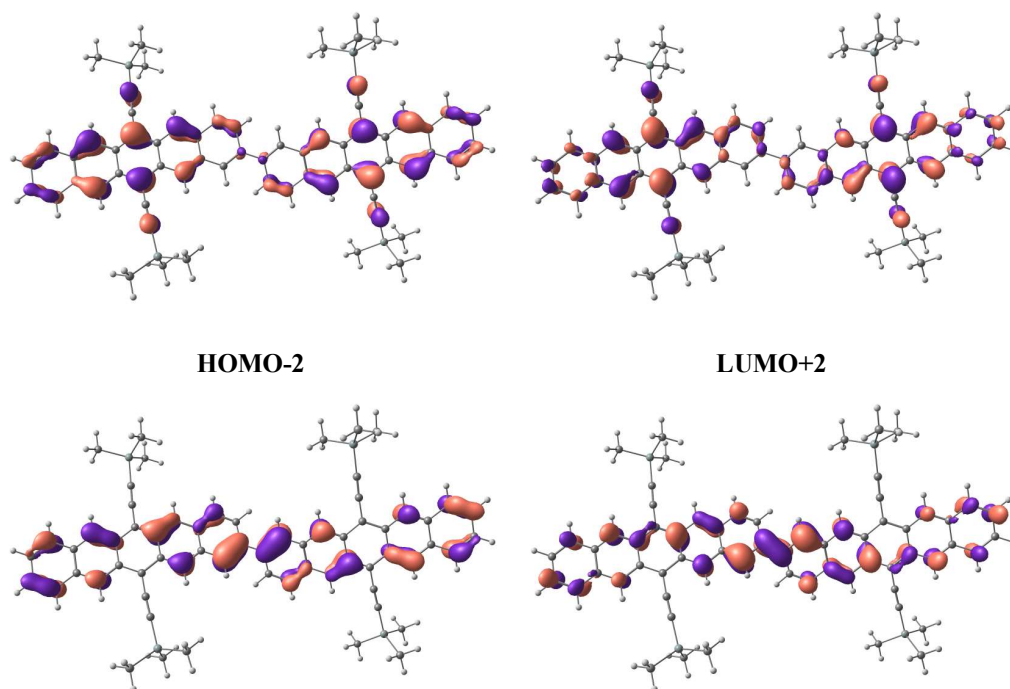
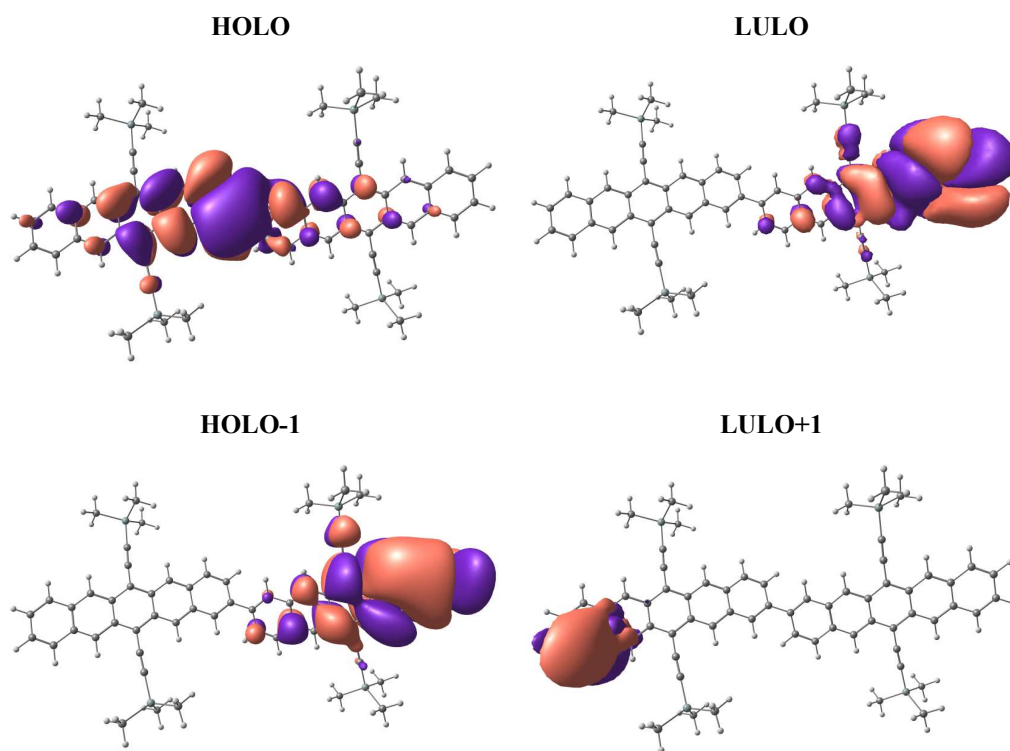


Figure 4.9. Frontier canonical molecular orbitals of BPO S_0 ground state calculated at TDDFT/BMK/6-31G* level. Isosurface values: 0.03 a.u..



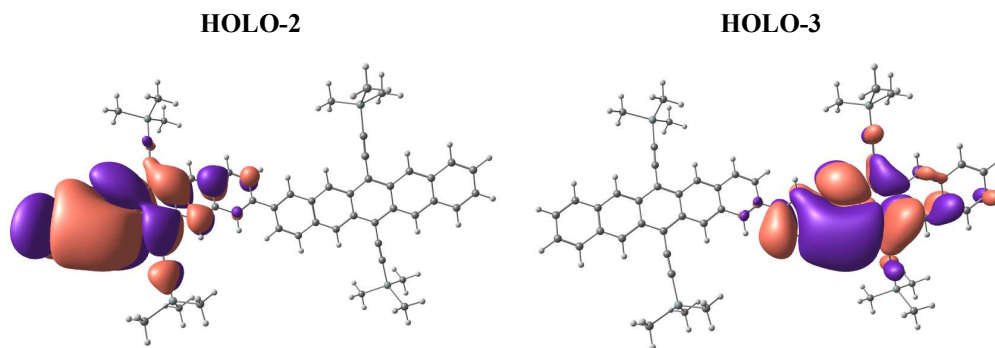


Figure 4.10. Frontier localized molecular orbitals of BP0 S_0 ground state calculated at TDDFT/BMK/6-31G* level. Isosurface values: 0.003 a.u..

S_0T_1 ESA of BP0

It has been confirmed that the interacting $^1(T_1T_1)$ state could be trapped in the BP0 dimer, and not separate into non-interacting $^1(T_1\dots T_1)$ or free triplets. However, S_0T_1 states in dimer systems would have a more closed relationship with $^1(T_1\dots T_1)$ states or free T_1 states in crystals or thin films, than T_1 states in monomer systems. Furthermore, it is of great importance to unambiguously identify the final state of SF, since harvesting electrons from the $^1(T_1T_1)$ state or the $^1(T_1\dots T_1)$ states requires different strategies.^[40, 123, 177] Therefore, although the S_0T_1 state in BP0 does not exist in the experiment, it is still included in our calculations and compared with PPP-MRSDCI. It is noted that the $^1(T_1T_1)$ state and its ESA were calculated with unrestricted BS-DFT and BS-TDDFT. We could not converge our calculations for the $^1(T_1T_1)$ state with low HF exchange functionals such as B3LYP, the SCF procedures were either hard to converge nor converged onto the S_0 ground state. This suggests that the stabilization of the $^1(T_1T_1)$ state requires favorable exchange energy interactions.

Nevertheless, since UTD/BMK and UTD/M06-2X have already been proven to give adequate results for the calculations of triplet excited states on TIPS-pentacene monomer, for the sake of consistency, our discussion and comparison between triplet and triplet pair states are within UTD/BMK and UTD/M06-2X calculations.

As can be seen from Table 4.9 and Table 4.5, the calculated vertical excitation energies of S_0T_1 states of BP0 are identical as T_1 states of TIPS-pentacene within UDFT. This

indicates that the triplet is localized on one fragment of BP0, which is further evidenced by the spin density (Figure 4.12) and frontier molecular orbitals (Figure 4.13) of the S_0T_1 state. Similar to the T_1 states of the monomer, all the S_0T_1 states obtained from UDFT exhibit negligible spin contamination, and BMK shows the best agreement with PPP-MRSDCI.

We have shown the S_0T_1 ESA spectra of BP0 in Figure 4.11 and given the detailed transition character analysis in Table 4.9. In contrast with three absorption maxima feature in the T_1 ESA spectra of TIPS-pentacene, S_0T_1 ESA spectra of BP0 calculated with UTD/BMK and UTD/M06-2X all show five maxima in the UV-Vis and NIR region, which are labeled as S_0T_1 ESA-1,2,3,4,5. The final state of the strongest S_0T_1 ESA-4 at around 500 nm is of the same local excitation character as that of T_1 ESA-2 (Table 4.5). This S_0T_1 ESA-4 peak is slightly red-shifted by around 100 meV, whereas the S_0T_1 ESA-1 in the NIR region is with more redshift by around 160 meV, which is owing to the mixed charge transfer character of the final state. The S_0T_1 ESA-2 and ESA-3 are unique for the BP0 dimer, which is in line with the PPP-MRSDCI calculations. The final state of the S_0T_1 ESA-2 is of charge resonance character, which, of course, does not exist in the monomer. The final state of S_0T_1 ESA-3 is a linear combination of local excitations on the S_0 fragment. Whereas, this state was characterized by the exciton basis analysis in the PPP-MRSDCI, as a double excitation on the S_0 fragment.

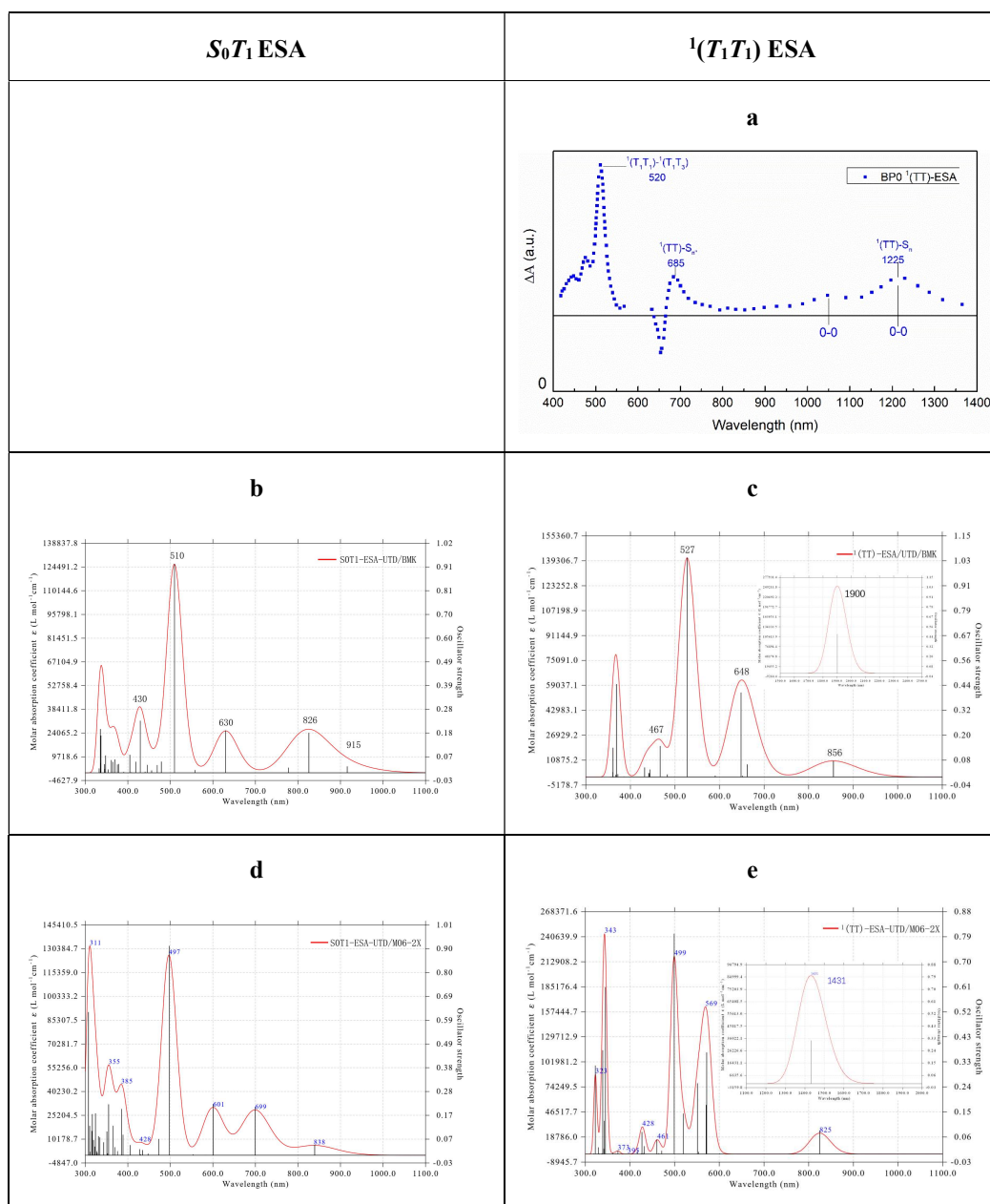
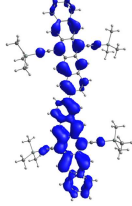
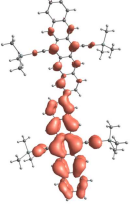
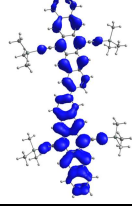
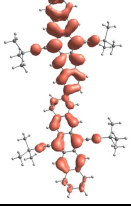
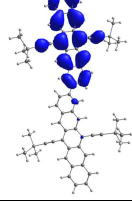
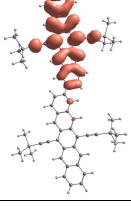
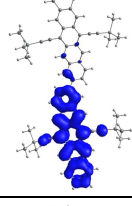
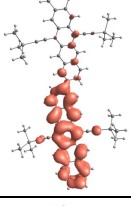
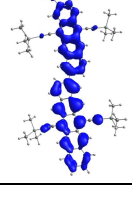
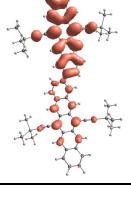


Figure 4.11. $^1(T_1T_1)$ ESA spectrum of BP0 extracted from experiment^[118] (a). S_0T_1 and $^1(T_1T_1)$ ESA spectra calculated at UTDDFT/BS-TDDFT/6-31G* with BMK, M06-2X (b-e).

Table 4.9. Transition analysis of S_0T_1 ESA of BP0 calculated at UTDDFT/BMK/6-31G* level. Isosurface values for electron and hole densities: 0.0005 a.u. Transition character is labeled with charge transfer (CT) or local excitation (LE).

State	S_0T_1 -ESA	$\langle S^2 \rangle$	eV	nm	f	MO Transition	Hole	Electron
2	ESA1	2.12	1.35	916	0.03	Hb -> Lb 39.9% (CT) Hb-1 -> Lb 26.5% (LE) Ha -> La 17.2% (CT) Ha -> La+1 10.9% (LE)		
3	ESA2	2.07	1.50	826	0.18	Ha -> La 64.8% (CT) Hb -> Lb 32.4% (CT)		
5	ESA3	2.04	1.97	630	0.19	Ha-1 -> La 49.8% (LE) Hb -> Lb+1 49.6% (LE)		
9	ESA4	2.12	2.43	510	0.93	Ha -> La+1 62.8% (LE) Hb-1 -> Lb 24.2% (LE)		
15	ESA5	2.52	2.89	430	0.23	Ha-2 -> La 53.6% (CT) Hb -> Lb+2 12.8% (CT) Ha-3 -> La 7.7%		

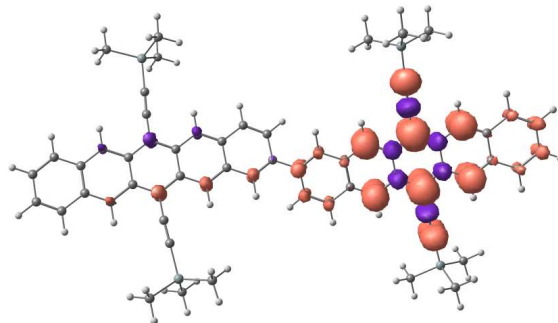


Figure 4.12. Spin density of BP0 S_0T_1 state calculated at UDFT/BMK/6-31G* level. Isosurface values: 0.003 a.u..

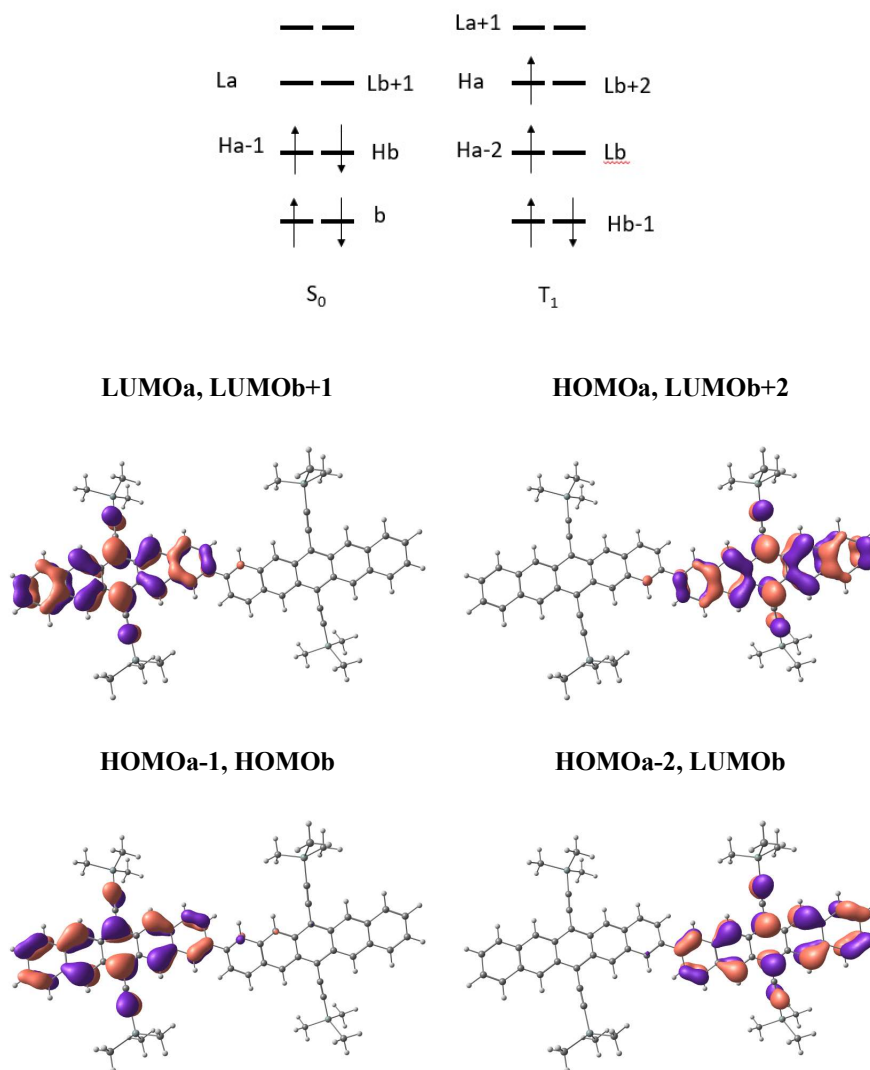


Figure 4.13. Frontier canonical molecular orbitals of BP0 S_0T_1 state calculated at UDFT/BMK/6-31G* level. Isosurface values: 0.03 a.u..

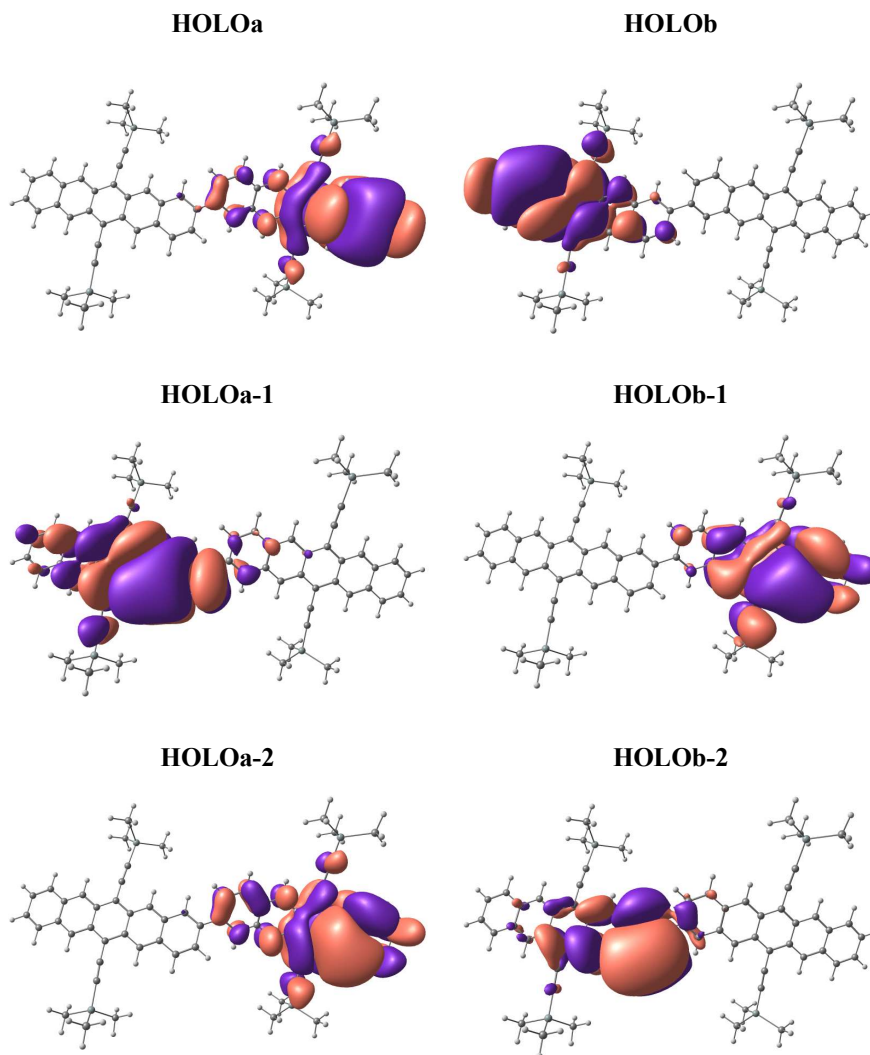


Figure 4.14. Frontier local molecular orbitals of BP0 S_0T_1 state calculated at UDFT/BMK/6-31G* level. Isosurface values: 0.003 a.u..

$^1(T_1T_1)$ ESA of BP0

As can be seen from Table 4.7, our calculated vertical energies of the spin-incomplete BS $^1(T_1T_1)$ state vary with the choice of functionals. BS-DFT/CAM-B3LYP predicts lower energy (1.68 eV) than the reference PPP-MRSDCI value (1.83 eV). BS-DFT/BMK shows a perfect agreement with the reference. Whereas, BS-DFT/M06-2X overestimates the excitation energies. On the other hand, the binding energy of the $^1(T_1T_1)$ state, defined as $E_b = 2 \times E(S_0T_1) - E(^1(T_1T_1))$, is expected to be much

higher than calculated values even with high-order CI methods.^[18, 122] Therefore, the relatively high bind energy predicted by M06-2X (0.03 eV) might be closer to the real value, and M06-2X could be a better choice over BMK.

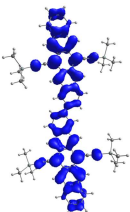
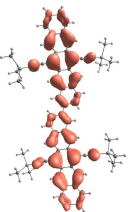
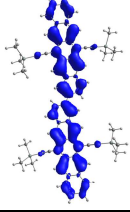
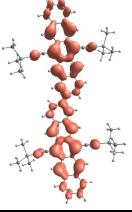
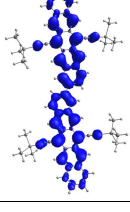
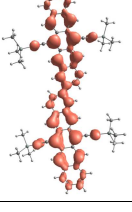
The BS-TDDFT calculated $^1(T_1T_1)$ ESA spectra of BP0 are plotted in Figure 4.11. The transition analysis within BS-TDDT/BMK is listed in Table 4.10. The experimental $^1(T_1T_1)$ ESA spectrum reveals three absorptions at 520, 685, and 1225 nm. In general, our calculated results are in good agreement with the experiment. The $^1(T_1T_1)$ ESA spectrum of BS-TDDFT/BMK shows four maxima at 527, 648, 856, and 1900 nm in the UV-Vis and NIR region. For BS-TDDFT/M06-2X, the spectrum is systematically blue-shifted with four maxima at 499, 569, 825, and 1431 nm. Consequently, BS-TDDFT/BMK provides a better description in the UV-Vis region; BS-TDDFT/M06-2X shows improvement in the NIR region. The calculated $^1(T_1T_1)$ ESA spectra are also slightly red-shifted to the S_0T_1 ESA and T_1 ESA spectra, which is also in line with the experiment. In addition, the ESA at in the longer wavelength (> 1000 nm) is missing in both T_1 ESA and S_0T_1 ESA spectra, and hence can be seen as a distinct spectroscopic signature for the $^1(T_1T_1)$ state. The $\langle S^2 \rangle$ value for the final state is 1.10, which indicates a BS singlet state. This is further evidenced by transition character analysis. The final state of the $^1(T_1T_1)$ ESA-1 is of both charge resonance and singlet character and can be approximately expressed as $\frac{1}{\sqrt{2}} \left(\left| \begin{array}{cc} \uparrow & \downarrow \\ \uparrow\downarrow & \uparrow\downarrow \end{array} \right\rangle + \left| \begin{array}{cc} \uparrow & \downarrow \\ \uparrow\downarrow & \downarrow \end{array} \right\rangle \right)$. PPP-MRSDCI calculations suggested that this state corresponded to the additional transition on the GSA spectra of BP0. The $^1(T_1T_1)$ ESA-2 bands at around 850 nm in our calculations are local excitations mixed with minor charge transfer character. This transition might be hard to observe in the experiment due to its low intensity. The $\langle S^2 \rangle$ value for the final state of $^1(T_1T_1)$ ESA-3 is 1.22, which is another singlet-like charge-resonance state. This state was characterized as a singlet 2e-2h charge transfer state by PPP-MRSDCI. Finally, the $^1(T_1T_1)$ ESA-4 is an analogy to the T_1 ESA-2, the transition of the final state is of local excitation character on one triplet unit, which is also in line with the assignment of the experiment and PPP-MRSDCI calculations.

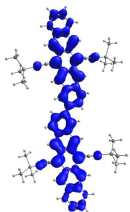
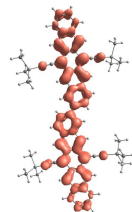
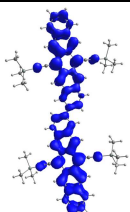
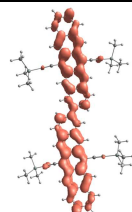
It is also important to note that the BS $^1(T_1T_1)$ in the present work shares a similar form with diabatic-like CDFT $^1(T_1T_1)$ state^[110, 127], especially when the promolecule density formalism is employed. The diabatic-like CDFT $^1(T_1T_1)$ state was considered to be the non-interacting $^1(T_1\dots T_1)$ state in a recent review paper.^[18] Here, we argue that the

diabatic-like $^1(T_1T_1)$ state does include the interaction between the two constituent triplets by orbital relaxation. The electronic interaction and orbital overlap in between the triplet pair are considered by finding the stationary point on the single-Slater-determinant energy surface of the BS $^1(T_1T_1)$ state. This can be evidenced by the considerable binding energy, and the distinct $^1(T_1T_1)$ to singlet absorptions, as well as the overlap of the frontier localized molecular orbitals. (Figure 4.17).

RAS-2SF calculations have already demonstrated that the adiabatic $^1(T_1T_1)$ wave function can involve contributions from S_1 and CT diabats [48, 135, 178, 179]. However, for most SF materials, the contribution of the $^1(T_1T_1)$ diabats is more than 80% and even 90%. In addition, we can expect that couplings between different spin-impure configurations of the spin complete $^1(T_1T_1)$ state are small and hence can be neglected. Therefore, we conclude that the energy and wave function of the adiabatic $^1(T_1T_1)$ can be approximated by the single determination BS

Table 4.10. Transition analysis of $^1(T_1T_1)$ ESA of BP0 calculated at BS-TDDFT/BMK/6-31G* level. Isosurface values for electron and hole densities: 0.0005 a.u.. Transition character is labeled with charge transfer (CT) or local excitation (LE).

State	ESA	$\langle S^2 \rangle$	eV	nm	f	MO transition	Hole	Electron
2	1	1.10	0.65	1902	0.47	Ha -> La 53.0% (CT) Hb -> Lb 52.6% (CT)		
3	2	1.92	1.45	856	0.08	Hb-2 -> Lb 29.7% (LE) Ha-2 -> La 27.1% (LE) Ha -> La+2 9.8% (LE) Hb -> Lb+2 9.1% (LE) Hb-1 -> Lb 8.0% (CT) Ha-1 -> La 7.1% (CT)		
8	3	1.22	1.91	648	0.40	Ha-1 -> La 30.2%(CT) Hb-1 -> Lb 22.9%(CT) Hb -> Lb+1 19.3% (CT) Ha -> La+1 14.5% (CT)		

13	4	2.03	2.35	527	1.05	Ha -> La+2 34.5% Hb -> Lb+2 32.3% Hb-2 -> Lb 10.3% Ha-2 -> La 10.0%		
16	5	2.06	2.66	467	0.15	Hb -> Lb+3 19.0% Ha -> La+3 15.4% Hb -> Lb+5 9.4% Ha -> La+5 8.6% Hb -> Lb+7 7.0% Ha -> La+7 6.3%		

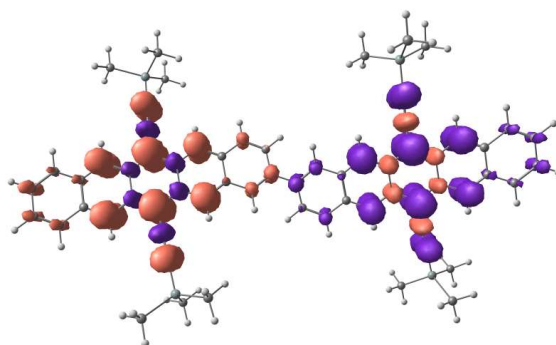
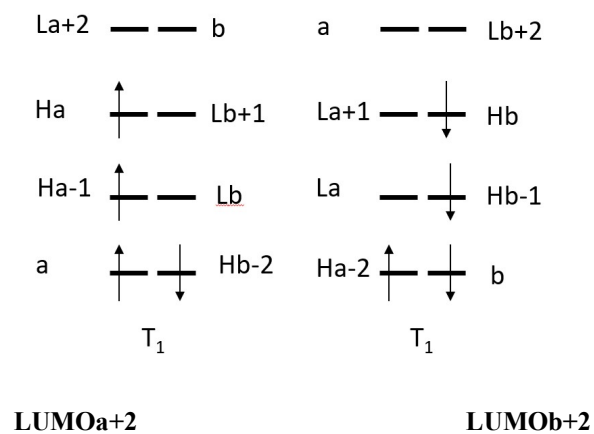


Figure 4.15. Spin density of BP0 $^1(T_1T_1)$ state calculated at BS-DFT/BMK/6-31G* level. Isosurface values: 0.0005 a.u..



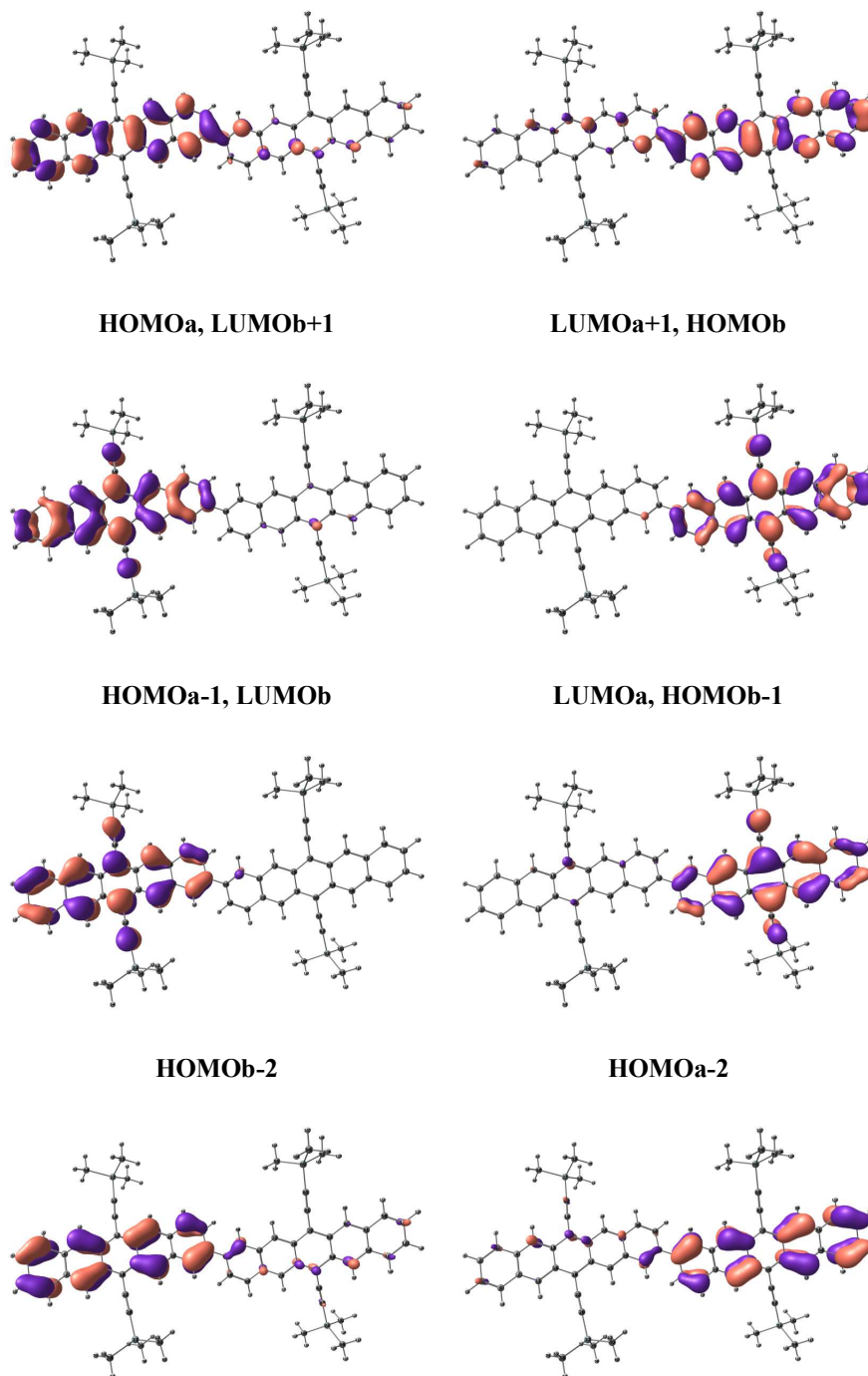


Figure 4.16. Frontier canonical molecular orbitals of BP0 $^1(T_1T_1)$ state calculated at BS-DFT/BMK/6-31G* level. Isosurface values: 0.03 a.u..

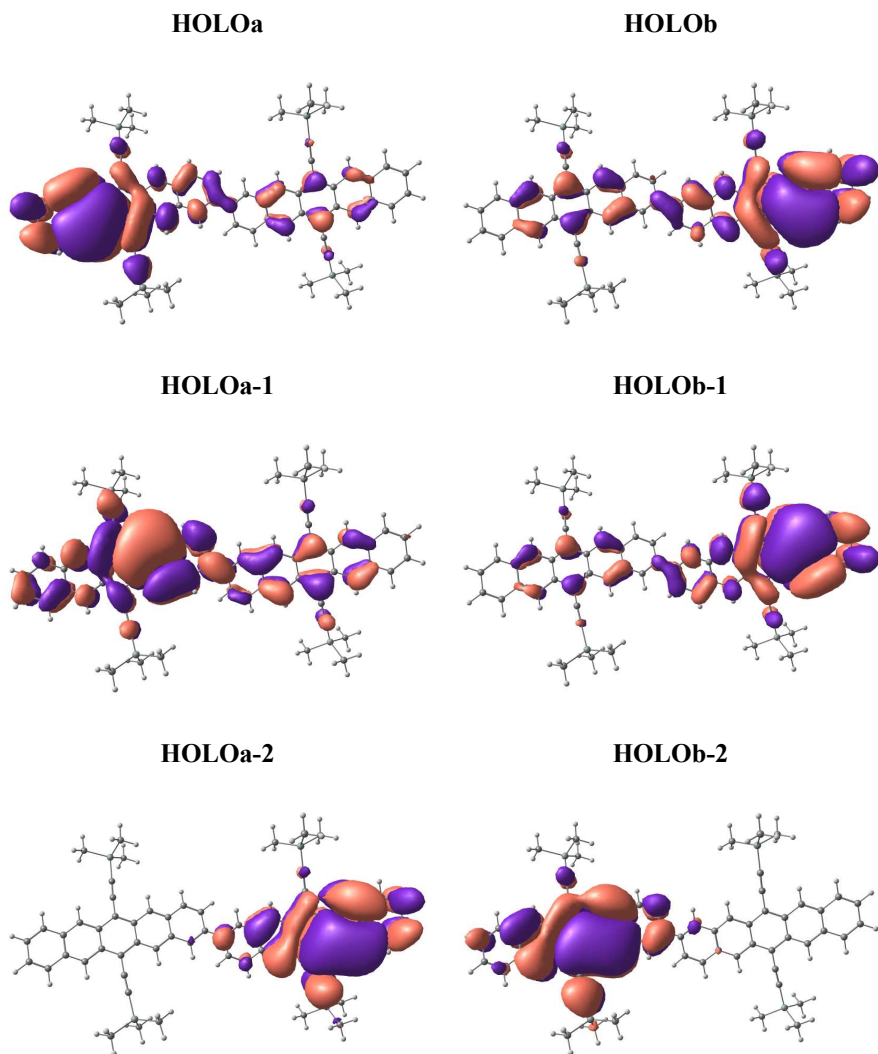


Figure 4.17. Frontier local molecular orbitals of BP0 $^1(T_1T_1)$ state calculated at BS-DFT/BMK/6-31G* level. Isosurface values: 0.003 a.u..

4.5 Conclusion

In the present work, we evaluated the performance of various single reference DFT based methods (TDDFT/TDA, SF-TDDFT, QR-TDDFT, SLR-TDDFT, BS-DFT/TDDFT) on the spectroscopic signatures of excited states involved in SF, i.e., GSA, S_1 , T_1 , S_0T_1 and $^1(T_1T_1)$ ESA spectra. Taking TIPS-pentacene monomer and BP0

dimer as examples and comparing the performance among 10 XC functionals, we found that triplet ESAs can be well reproduced by TDDFT and UTDDFT with functionals such as BMK and M06-2X. Although TDDFT is not capable of reproducing transitions with strong double excitation characters on the S_1 ESA spectra, such as the $L_a \rightarrow D$ transition in the mid-IR region, it has no problem to describe the transitions in the UV-vis and NIR region. This is already enough to assign the singlet species in SF. TDDFT with low HF exchange functionals such as TPSSh performs the best for TIPS-pentacene, while TDDFT with LRC or a large amount of exact exchange such as CAM-B3LYP is recommended for BP0.

SF-DFT can recover double excitations of singlet excited states and improve the description of the high-lying states for TIPS-pentacene. However, the GSA and S_1 ESA spectra are rather than satisfactory, due to the unbalanced description of the low-lying states. SA-SF-TDDFT might be a promising method, but we encountered severe convergence problems.

The orbital relaxation effect on the properties of excited states and their ESA spectra are also discussed and highlighted. The orbital relaxation tends to enhance the absorptions in the UV-Vis region while lower the intensities of the NIR absorptions for the S_1 ESA spectra, when using QR-TDDFT, SLR-TDDFT and SF-TDDFT. More importantly, it is always challenging to theoretically describe the $^1(T_1T_1)$ state due to its multiexciton and mixed-configuration character. We show that the BS-DFT formalism allows the orbitals to relax onto a BS $^1(T_1T_1)$ state, which is a good approximation of the real adiabatic $^1(T_1T_1)$ state and covers the essential character. The BS $^1(T_1T_1)$ state can, in turn, be taken as a reference state to perform UTDDFT calculations to obtain the $^1(T_1T_1)$ ESAs. The $^1(T_1T_1)$ ESAs of BS-TDDFT in conjunction with BMK and M06-2X show a good agreement with the experiment, and even more consistent than high-order CI methods.

In conclusion, single-reference DFT based approach in combination with a rational choice of the exchange-correlation functional, show good feasibility and applicability. This provides an alternative and computationally much less demanding way to predict and simulate the electronic spectra of various excited states involved in singlet fission.

5. Theoretical Description and Prediction of Molecular Properties of *N*- Heteropolycycles

This chapter is largely based on the results of theoretical calculations presented in following papers:

1. H. Reiss, L. Ji, **J. Han**, S. Koser, O. Tverskoy, J. Freudenberg, F. Hinkel, M. Moos, A. Friedrich, I. Krummenacher, C. Lambert, H. Braunschweig, **A. Dreuw**, T.B. Marder, and U.H.F. Bunz, Bromination Improves the Electron Mobility of Tetraazapentacene. *Angewandte Chemie International Edition*, 2018. 57(30): p. 9543.
2. S. Mueller, J. Lüttig, P. Malý, L. Ji, **J. Han**, M. Moos, T.B. Marder, U.H.F. Bunz, **A. Dreuw**, C. Lambert, and T. Brixner, Rapid multiple-quantum three-dimensional fluorescence spectroscopy disentangles quantum pathways. *Nature Communications*, 2019. 10(1): p. 4735.
3. L. Ji, A. Friedrich, I. Krummenacher, A. Eichhorn, H. Braunschweig, M. Moos, S. Hahn, F.L. Geyer, O. Tverskoy, **J. Han**, C. Lambert, **A. Dreuw**, T.B. Marder, and U.H.F. Bunz, Preparation, Properties, and Structures of the Radical Anions and Dianions of Azapentacenes. *Journal of the American Chemical Society*, 2017. 139(44): p. 15968.
4. L. Ji, M. Haehnel, I. Krummenacher, P. Biegger, F.L. Geyer, O. Tverskoy, M. Schaffroth, **J. Han**, **A. Dreuw**, T.B. Marder, and U.H.F. Bunz, The Radical Anion and Dianion of Tetraazapentacene. *Angewandte Chemie International Edition*, 2016. 55(35): p. 10498.
5. G. Xie, V. Brosius, **J. Han**, F. Rominger, **A. Dreuw**, J. Freudenberg, and U.H.F. Bunz, Stable Radical Cations of *N,N'*-Diarylated Dihydrodiazapentacenes. *Chemistry—A European Journal*, 2020. 26(1): p. 160.

6. L. Ji, S. Hahn, P. Biegger, H. Reiss, **J. Han**, A. Friedrich, I. Krummenacher, H. Braunschweig, M. Moos, J. Freudenberg, C. Lambert, **A. Dreuw**, T.B. Marder, and U.H.F. Bunz, Mono - and Dianion of a Bis(benzobuta)tetraazapentacene Derivative. *Chemistry—A European Journal*, 2019. 25(42): p. 9840.

Abstract

In this chapter, molecular properties for a series of N-heteropolycycles and their radical anions (cations) and dianions (dications) are investigated quantum chemically. This includes diazapentacenes, tetraazapentacenes (**TAP**), a brominated tetraazapentacene (**Br4-TAP**), a bis(benzobuta)tetraazapentacene derivative (**bis-TAP**) and a quinoidal *N,N'*-diaryldiaza-*N,N'*-dihydropentacene derivative (**Quino-CF₃**). DFT and TDDFT are employed to predict and describe structure, energetics, UV-vis-NIR, and EPR spectra, as well as charge population and aromaticity. In contrast to the acenes, the anions of the azapentacenes are persistent and are stable with respect to disproportionation into the dianion and the neutral compound. The radical anions show a strongly red-shifted absorption (into the NIR), while the dianions all have blue-shifted absorptions. Although there is no detectable charge pinning in the anionic azapentacenes, bromine substituents influence the distribution of the negative charge in the radical anion such that **Br4-TAP** has a higher probability of residing on the outer rings. This might lead to an increased transfer integral in the solid-state of the **Br4-TAP** in the presence of negative charges. In the case of **bis-TAP**, it shows different aromaticity and spectroscopic properties from the azaacenes. The lowest energy absorption in the UV-vis spectrum of the dianionic **bis-TAP** is redshifted in comparison to that of the neutral compound. Oxidation of **Quino-CF₃** furnishes stable radical cations, isoelectronic to the radical anions of the azaacenes, whereas the dicationic species are isoelectronic to neutral azapentacenes. The spectroscopic properties of the diaryldiazapentacenes and their oxidized mono- and dications are equivalent to that of the dianion of TAP, its radical anion, and the neutral species.

5.1 Introduction

Bis(triisopropylsilylethynyl)pentacene (TIPS-pen) and its heteroaromatic congeners,^[2, 4, 59, 180-184] particularly the N-Substituted pentacenes (azapentacenes),^[14, 185, 186] are essential semiconducting organic molecules.^[187-194]

TIPS-pen is a potent p-channel transporter, that is, the charge transport occurs via hopping of holes, produced by the oxidation of its electron-rich aromatic core.

Azapentacenes, on the other hand, are n-channel transport materials. The presence of nitrogen atoms in the π -system changes the electronic structure within the pentacene frame. In particular, the symmetrical tetraazapentacene (TAP, **4**) has been employed in thin-film transistors with mobilities of up to several $\text{cm}^2 \text{V}^{-1} \text{s}^{-1}$ ^[192]. At the electrode interface in a thin film transistor, TAP is reduced to its radical anion **4**⁻ and the injected electrons then “hop” through adjacent molecules; this process is responsible for charge transport in this material.

An important and not easily answered question is whether there is charge pinning in the the azaacene framework. If it is the case, the charge might be localized on a particular site in the molecule—most probably the nitrogen atoms. Such behavior could indicate that n-channel charge transport might be hindered, due to a trapping of the charge on the molecule.

In this context, charge pinning would entail that the electron density of the formed radical anions is localized on one or two of the nitrogen atoms—a reasonable assumption on first glance. Does the charge reside at a specific locus of **4**⁻ (the nitrogen atoms, form **L**) or is the charge delocalized over the whole π -system (form **D**)?^[186] This question is relatively difficult to answer when one looks at working devices, for example, transistors containing **4**, because, even if charge pinning would occur, the charge transfer between two adjacent TAP molecules could be degenerate or possibly without a significant activation barrier. Perhaps, more importantly, charge pinning could occur at the interface between the metal and **4** during injection of electrons. In the absence of charge pinning, one would assume the charge transfer to have a lower activation barrier. Besides the question of charge pinning, the molecular and electronic

structures of the radical anion and the dianion of compounds such as **4** are completely unknown. Thus, investigating their spectroscopic properties, stability, and structure would not only be of great fundamental interest but is also important due to the eminent role of **4** in charge transport in n-channel transistors.

In a more fundamental way, the anions and dianions of different azapentacenes are fascinating objects for study, as the azaacenes are relatively easily reduced by standard reducing agents such as potassium anthracenide or lithium naphthalenide; they give reasonably stable anionic species due to their low reduction potential. As the number and the position of the nitrogen atoms are easily permuted, a consequence of recent advances in synthetic methodology, one has an exquisitely tuned tool to examine the variation of structures, properties and spectra, depending upon position and number of nitrogen atoms. As a bonus, recent progress in azaacene chemistry allows the introduction of TIPS-acetylene groups as solubilizing and stabilizing substituents. These simplify the handling and crystallization of the radical anions and dianions. Interestingly enough, radical anions and dianions of larger aromatic hydrocarbons have been synthesized, but the number of crystal structures of such species is limited.

In addition, the peripheral substitution of the aromatic system can alter the electronic properties and the morphology further. Therefore, in order to discover the effect of the peripheral substitution with electronegative atoms, a brominated TAP (**Br4-TAP**) and its negatively charged species are also characterized and compared with TAP.

Furthermore, while the size of stable azaacenes is limited, interspersed cyclobutadiene units increase the number of Clar sextets and should allow the synthesis of larger targets.^[195, 196] Cyclobutadiene-fused acenes show high *p*-channel mobilities in organic thin-film transistors.^[197, 198] In this work, we also describe the properties of the radical anion and the dianion of a doubly benzobuta-annelated tetraazapentacene, **bis-TAP**, which also features TAP as a structural element (Figure 5.1, blue structure).

Moreover, larger *N*-heteroacenes are easily reduced into their *N,N'*-dihydro compounds, much longer known and more stable than the *N*-acenes themselves. There are only a few reports on the chemistry of the reduced compounds from Miao,^[199, 200] Beckert,^[201] and Koutentis,^[202] and surprisingly little is known for the redox chemistry of these materials.

Chi et al. spectacularly investigated sulfur- and oxygen-embedded quinodimethane acene analogs.^[203-205] They demonstrated that their dications display properties very similar to those of the acenes of similar length. However, for the larger representatives, these dications are—contrary to the isoelectronic acenes themselves—isolable, stable, and can be characterized. In this work, we extend this concept to *N*-heterocycles. A quinoidal *N,N'*-diaryldiaza-*N,N'*-dihydropentacene (**Quino-CF₃**), and its cation and dication are taken as examples.

In this chapter, employing DFT and TDDFT, we investigated the molecular properties of a series of *N*-heteropolycycles and their radical anions (cations) and dianions (dications). This includes diazapentacenes (5,14-diethynyldibenzo[*b,i*]phenazine (**1**), 6,13 diethynylnaphtho[2,3-*b*]phenazine (**2**)), and tetraazapentacenes (7,12-diethynylbenzo[*g*]quinoxalino[2,3-*b*]quinoxaline (**3**), 6,13-diethynylquinoxalino[2,3-*b*]phenazine (**4**, **TAP**)), as well as a brominated TAP (**Br4-TAP**), a bis(benzobuta)tetraazapentacene derivative (**bis-TAP**) and a quinoidal *N,N'*-diaryldiaza-*N,N'*-dihydropentacene derivative (**Quino-CF₃**). The structures of all the studied molecules are shown in Figure 5.1.

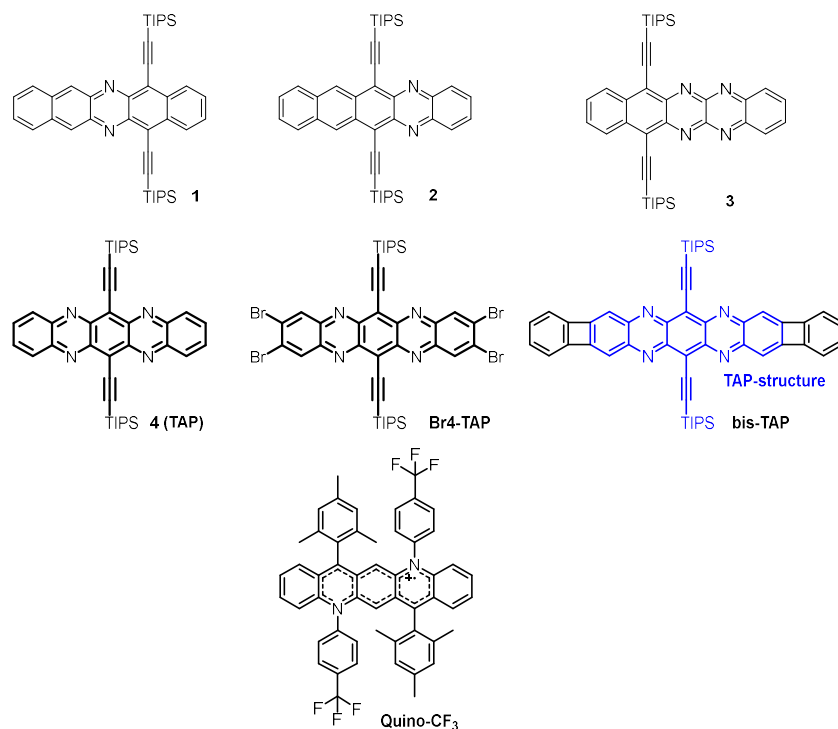


Figure 5.1. Molecular structures of **1**, **2**, **3**, **4 (TAP)**, **Br4-TAP**, **bis-TAP** and **Quino-CF₃**.

5.2 Computational Details

The geometries of the neutral, anionic, and dianionic species of **1**, **2**, **3**, **4**, **Br4-TAP**, and **bis-TAP** have been optimized using DFT^[206] in combination with the long-range corrected exchange-correlation functional CAM-B3LYP and the 6-311G** basis set, employing a polarizable continuum model using the integral equation formalism variant (IEFPCM)^[145, 146] for THF solvation. All the optimized geometries were confirmed to be local minima (all frequencies are real). Subsequent calculations for (nuclear-independent chemical shift) NICS values were performed at the same level of theory using gauge-independent atomic orbitals (GIAO)^[207, 208], whereas the energies of the optimized molecules were computed with 6-311++G**. The vertical excited states of the neutral, anionic, and dianionic molecules have been computed at the theoretical level of TDDFT/CAM-B3LYP/6-311++G**, again in combination with a PCM for THF solution. The hyperfine coupling constants of the radical anions were calculated by DFT using the UB3LYP/EPR-iii level of theory, based on the optimized geometry. The TIPS groups were replaced by protons because the basis set for EPR-iii does not include silicon.

The ground state geometries for the neutral, cationic, and dicationic of **Quino-CF₃** were optimized at the B3LYP/6-311G** level of theory, employing the PCM for DCM solvation. Upon these optimized geometries, additional calculations for NICS values as well as vertical excitations using TD-DFT^[23] were conducted at the same level of theory. All calculations have been performed using Gaussian 09 Rev. D.01.^[209]

5.3 Results and Discussion

5.3.1 Azapentacenes

The molecular structures of **4** in the neutral, monoanion, and dianion form are depicted in Figure 5.2. The changes of the bond lengths upon the reduction, are fairly small and

not easily interpreted. This follows the same trend as the experimentally determined X-ray structures.

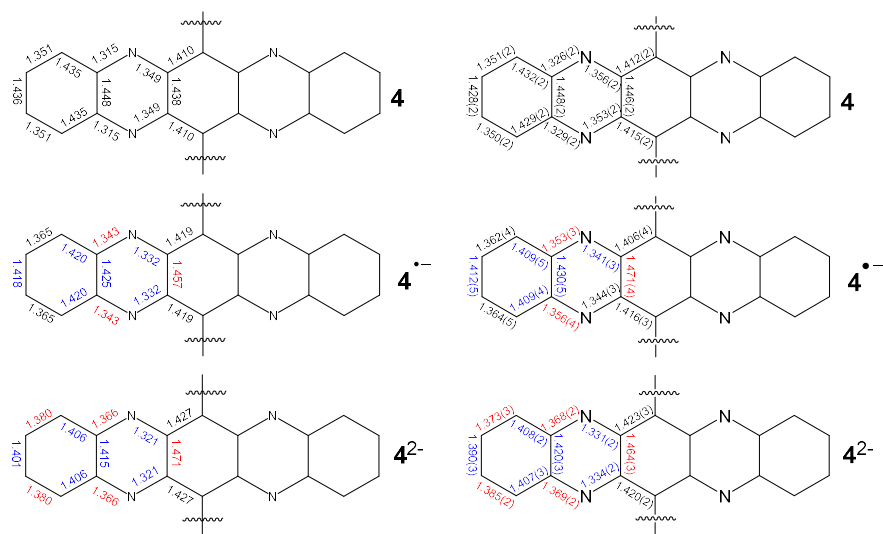


Figure 5.2. Main bond lengths of **4** in the neutral, monoanion, and dianion form. Left: bond lengths in DFT-optimized structure; right: bond length in X-ray determined structure. Blue color: shortening, red color: lengthening. The bond lengths change in neutral, monoanion, and dianion form of **4** in optimized structure agree with that in the X-ray determined structure.

As a first step, the relative stabilities of the anions and dianions of **1–4** in THF with respect to their neutral forms have been investigated. Therefore, based on the optimized geometries, the energy differences between the neutral species and the anion or dianion have been computed at DFT/CAM-B3LYP/6-311++G** level. In Table 5.1, it can be seen that the anions are strongly stabilized in THF by 300–400 kJ/mol. The same is true for all dianions, which are more stable than the neutral compounds by 600–700 kJ/mol and more stable than the anions. Hence, the dianions are also electronically stable entities in THF solution.

Table 5.1. Computed Energies of the Anions $E[M^{\cdot-}]$ and Dianions $E[M^{2-}]$ of **1–4** Relative to the Neutral Parent Molecule and Corresponding Disproportionation Reaction Energies ΔE_{dis} ^a

	$E[M^{\cdot-}]^b$ kJ/mol	$E[M^{2-}]^b$ kJ/mol	ΔE_{dis}^c kJ/mol
1	-361	-616	105
2	-357	-612	101
3	-404	-700	107
4	-391	-684	98

^aComputed using DFT/CAM-B3LYP/6-311++G** using a PCM model for THF solution. ^bA negative sign indicates the anion/dianion to be more stable than the neutral compound. ^cA positive energy means the disproportionation reaction is endothermic.

Bock et al. have prepared and structurally investigated tetracene and rubrene radical anions,^[210] which are structurally related to azaacenes. In the case of tetracene, it was not possible to obtain the radical anion, as it is thermodynamically unstable toward disproportionation, but the dianion of tetracene could be crystallized. Bock et al. also noted that, with the increasing size of the aromatic hydrocarbon frame, the disproportionation of the radical anion is thermodynamically advantageous. The bond lengths in the peripheral rings are equalized and, therefore, different from the bond lengths in tetracene itself, where the 1,2 bond is shorter than the 2,3 bond. This is entirely reasonable, as the dianion of tetracene is a $4n-\pi$ -system, in which the antiaromaticity has a strong delocalizing effect.^[211] Are the azapentacenes similar to tetracene and their relatives, or do they show differences with respect to reduction?

To investigate whether the anionic species disproportionate into neutral and dianionic species, the reaction energies of the disproportionation reactions were calculated for **1^{•-}–4^{•-}** (Table 5.1). This energy is given as $\Delta E_{\text{dis}} = E[M^{2-}] - 2E[M^{\cdot-}]$ and it can be seen that the disproportionation is endothermic by approximately 100 kJ/mol for all anions. Even though the dianion is strongly stabilized by THF solvation, it is not sufficient to provide a large enough driving force to make the disproportionation of the anions energetically feasible. For this to happen, an additional stabilization of the dianions (by the counterions, for instance) would be necessary. These results confirm the

experimental observation that **1–4** form stable isolated anions and dianions in THF solution.

With the help of density functional theory (DFT/UB3LYP/EPR-iii) calculations, the solution EPR spectra of the radical anions **1^{•-}**, **2^{•-}**, **3^{•-}** and **4^{•-}** could be satisfactorily simulated (Figure 5.3; best-fit parameters are given in the caption). The spectra show contributions from several partially resolved ¹H and ¹⁴N hyperfine couplings, which are smaller than those in azaacenes with fewer fused benzene rings, such as phenazine ($a(^{14}\text{N}) = 14.4$ MHz, $a(^1\text{H}) = 5.41$ and 4.51 MHz),^[212, 213] quinoxaline ($a(^{14}\text{N}) = 15.8$ MHz, $a(^1\text{H}) = 9.30, 6.50, 2.80$ MHz)^[212, 213] or 5,6,11,12-tetraazanaphthacene ($a(^{14}\text{N}) = 8.35$ MHz, $a(^1\text{H}) = 3.92$ and 2.35 MHz),^[212] consistent with an increased electron delocalization.

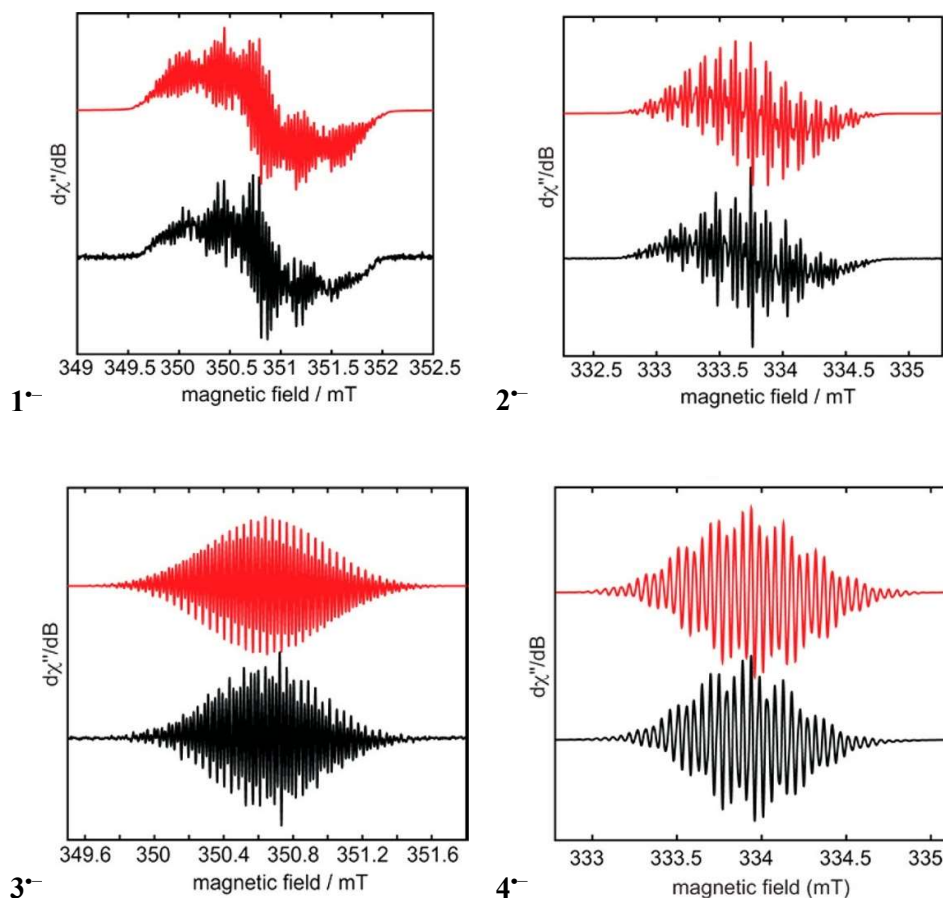


Figure 5.3. Experimental (black) and simulated (red) continuous-wave (CW) X-band EPR spectra of **1^{•-}**–**4^{•-}** in a toluene/THF mixture. Experimental parameters: temperature = 298 K; microwave frequency = 9.38 GHz (**1** and **3**), 9.85 GHz (**2** and **4**); modulation

amplitude = 0.1 G; conversion time = 60 ms; modulation frequency = 100 kHz. Simulation parameters: **1⁻**: $g = 2.004$, $a(^{14}\text{N}) = 9.67$ MHz, $a(^1\text{H}) = 5.52, 3.56, 2.72, 1.75, 1.05$ MHz; **2⁻**: $g = 2.004$, $a(^{14}\text{N}) = 6.80$ MHz, $a(^1\text{H}) = 5.28, 3.44, 3.42, 1.04, 0.97$ MHz; **3⁻**: $g = 2.004$, $a(^{14}\text{N}) = 5.79$ and 4.63 MHz, $a(^1\text{H}) = 2.38, 2.28, 1.66, 1.21$ MHz; **4⁻**: $g = 2.004$, $a(^{14}\text{N}) = 5.32$ MHz, $a(^1\text{H}) = 1.54, 1.40, \text{ and } 1.35$ (methine protons) MHz.

To further corroborate the existence of free anionic and dianionic species of **1–4** in THF, the vertical excited states of the parent neutral, anionic, and dianionic molecules have been computed at the theoretical level of TDDFT/CAM-B3LYP/6-311++G**, again in combination with a PCM for THF solution. The results for the first excited state of all molecules are in excellent agreement with the observed experimental absorption spectra (Table 5.2; the spectra of **TAP** is shown in Figure 5.4 as an example). While the neutral species exhibit a first excited S_1 state at excitation energies between 15 150 and 16 130 cm^{-1} , the corresponding open-shell anions have a strongly red-shifted first excited state between 7980 and 9030 cm^{-1} at the level of TDDFT/CAM-B3LYP. The first excited states of the dianions are then strongly blue-shifted, even with respect to the neutral compounds, and occur between 18 790 and 20 240 cm^{-1} .

Table 5.2. Computed Vertical Absorption Energies, Wavelengths and Oscillator Strengths of the Lowest Excited State of **1–4** and Their Anions and Dianions, as well as the Main Orbital Contributions^a

	$\nu_{\text{max}}^{\text{a}}/\text{cm}^{-1}$	$\lambda_{\text{abs}}/\text{nm}$	f_{osc}	excitation character ^b
1	16 050	623	0.26	H → L (98.9%)
2	15 320	653	0.27	H → L (99.4%)
3	15 160	660	0.21	H → L (98.4%)
4	16 130	620	0.32	H → L (99.2%)
1 ⁻	8950	1117	0.10	H _β → L _β (93.7%)
2 ⁻	7980	1253	0.11	H _β → L _β (95.2%)
3 ⁻	9030	1107	0.08	H _β → L _β (88.8%)
4 ⁻	8310	1203	0.12	H _β → L _β (96.6%)
1 ²⁻	18 790	532	1.00	H → L (95.8%)
2 ²⁻	20 160	496	0.98	H → L (93.9%)
3 ²⁻	19 360	517	1.06	H → L (97.2%)
4 ²⁻	20 240	494	1.11	H → L (96.7%)

^aComputed using TDDFT/CAM-B3LYP/6-311++G** using a PCM model for THF solution. ^bFor the shape of the orbitals see Figure 5.5-Figure 5.8.

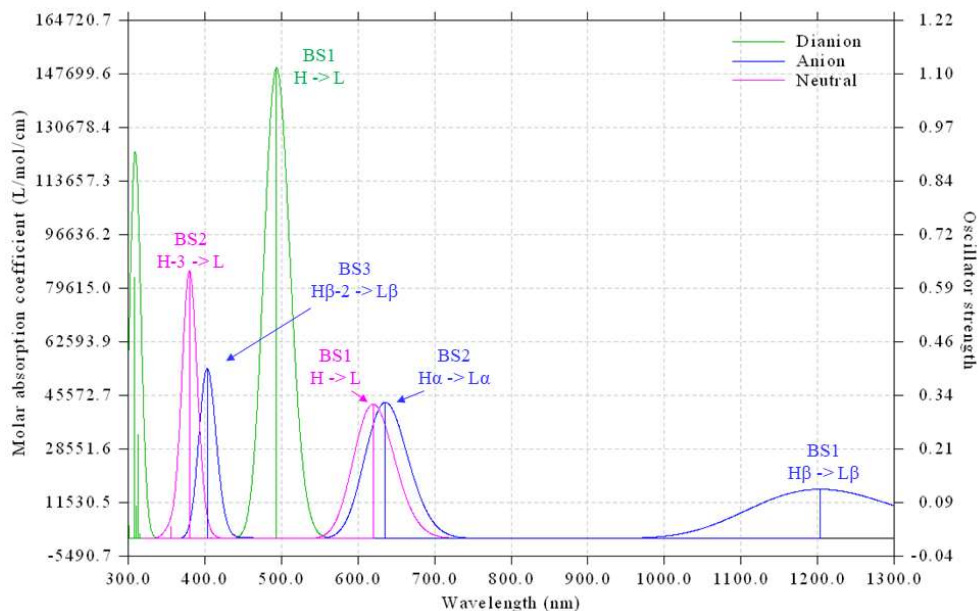


Figure 5.4 Simulated absorption spectra of neutral, anionic, and dianionic **TAP (1)** computed at TD-DFT/CAM-B3LYP/6-311++G** level. All spectra were broadened using Gaussian functions with a full-width at half maximum of 0.2 eV. BS refers to bright state.

All lowest excited states correspond to typical $\pi\pi^*$ excited states, as can be seen from the main orbital contributions to the electronic transitions. The $S_0 \rightarrow S_1$ transition of the closed-shell neutral and the dianions are typical HOMO \rightarrow LUMO transitions, but the latter has much larger oscillator strengths. This is in agreement with the larger molar extinction coefficients of the dianions, in comparison to those of the neutral compounds measured experimentally. The interpretation of the transitions in the open-shell anions is slightly more involved, as these anions possess two sets of orbitals, one for the alpha and one for the beta electrons. The molecular frontier orbitals and the energies are shown in Figure 5.5-Figure 5.8. In the azapentacenes **1⁻**-**4⁻**, however, the lowest excited state can be understood as an electronic transition from the HOMO of the neutral into the now half-filled LUMO of the anion. This is in accord with the fact that

the experimentally determined molar extinction coefficient of the $D_0 \rightarrow D_1$ transition of the monoanion is only half that of the corresponding neutral compound. The $D_0 \rightarrow D_2$ transition of the monoanion is from the half-filled LUMO to the LUMO+1 of the neutral compound, which is the same as the $S_0 \rightarrow S_1$ transition of the dianion. This again explains why the molar extinction coefficient of $D_0 \rightarrow D_2$ transition of the monoanion is smaller than that of the $S_0 \rightarrow S_1$ transition of the dianion.

Overall, our calculations fully support the interpretation of the measured absorption spectra as those of the free neutral, anionic and dianionic species of **1–4** and explain the observed trends nicely.

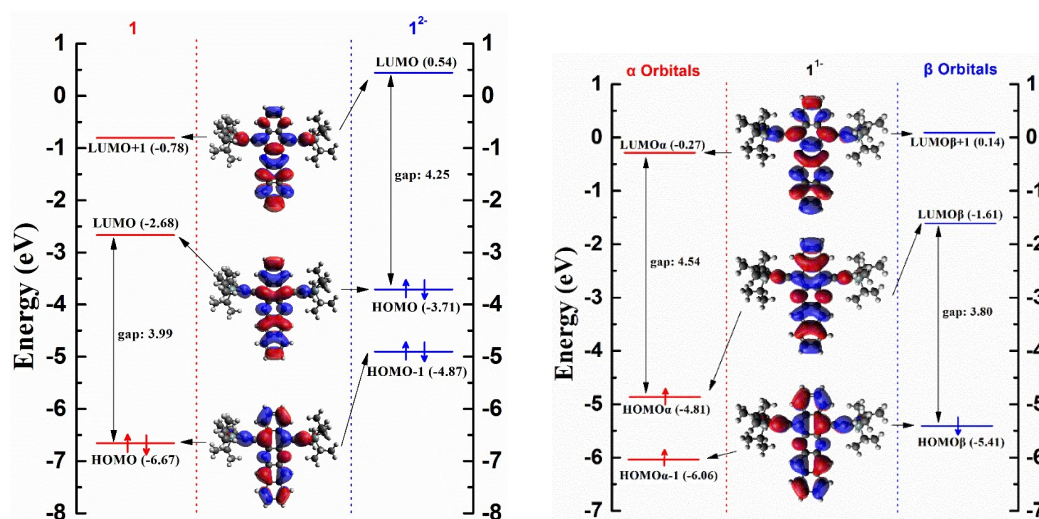


Figure 5.5. Kohn–Sham frontier molecular orbital diagrams and energies (in eV) for neutral, dianionic (left) and anionic **1** (right) in THF solution (isodensity value: ± 0.015).

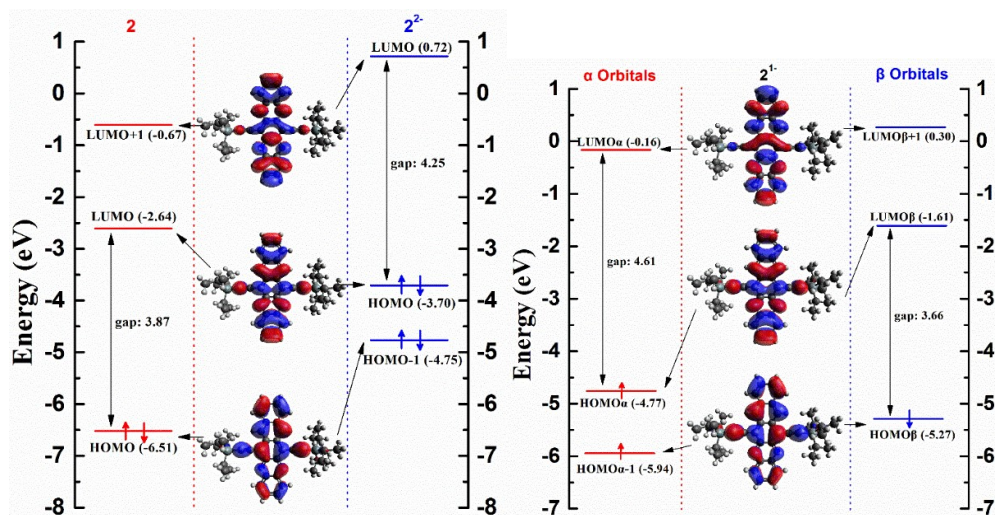


Figure 5.6. Kohn–Sham frontier molecular orbital diagrams and energies (in eV) for neutral, dianionic (left) and anionic **2** (right) in THF solution (isodensity value: ± 0.015).

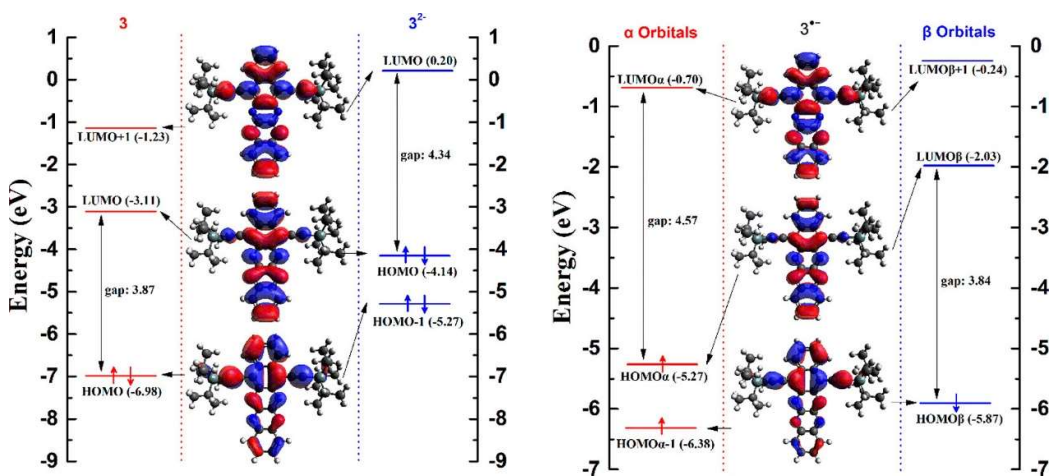


Figure 5.7. Kohn–Sham frontier molecular orbital diagrams and energies (in eV) for neutral, dianionic (left) and anionic **3** (right) in THF solution (isodensity value: ± 0.015).

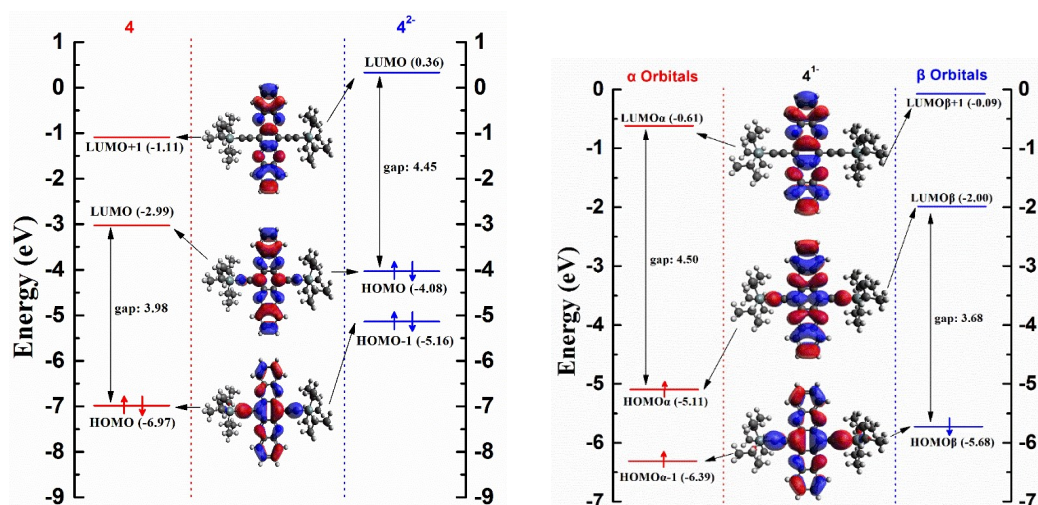


Figure 5.8. Kohn–Sham frontier molecular orbital diagrams and energies (in eV) for neutral, dianionic (left), and anionic **4** (right) in THF solution (isodensity value: ± 0.015).

In order to evaluate the origin of the two-quantum (2Q) resonance at 4.10 eV in the 2Q-associated 3D spectra^[214], we performed quantum chemical calculations by using DFT and TD-DFT. All calculations were carried out with the Gaussian program package^[209]. The ground state equilibrium structure of TIPS-TAP²⁻ was optimized with DFT/CAM-B3LYP/6-311G** and employing a polarizable continuum solvent model for tetrahydrofuran (THF) solvation. TD-DFT calculations were performed on the optimized structure with BLYP functional and 6-31+G* basis set for the first 100 vertical transitions ($S_0 \rightarrow S_n$). Subsequently, $S_1 \rightarrow S_n$ transitions were obtained by computing transition dipole moments between excited states. In the $S_0 \rightarrow S_n$ spectrum (Figure 5.9), the $S_0 \rightarrow S_1$ transition energy (590 nm, 2.10 eV) is in good agreement with the experimentally observed peak (602 nm, 2.06 eV). There are some higher excited states with nonzero oscillator strength. However, at nearly twice the energy of the $S_0 \rightarrow S_1$ transition (295 nm, 4.20 eV), there is no transition with significant oscillator strength present in the calculation, which is analogous to experimental observations. Thus, this reflects that the experimentally observed 2Q state at 4.10 eV is unlikely to be excited via a single one-photon transition due to the inversion symmetry of the molecule.

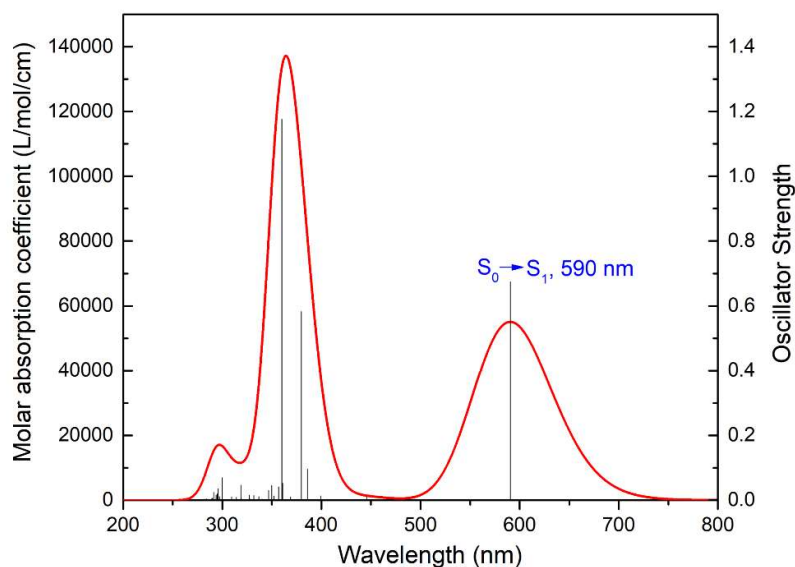


Figure 5.9. Calculated $S_0 \rightarrow S_n$ ($n = 1, \dots, 100$) absorption spectrum of TIPS-TAP²⁻, broadened using Gaussian functions with a full width at half maximum of 0.33 eV.

In contrast, the $S_1 \rightarrow S_n$ absorption spectrum (Figure 5.10) features a transition into S_{74} (579 nm, 2.14 eV) with relatively high oscillator strength at nearly the same energy as the $S_0 \rightarrow S_1$ transition. There is also a second optically bright transition at 1157 nm (1.07 eV), which is not of relevance within our experiments because it is not covered by the employed laser spectrum. Hence, we conclude that the 2Q resonance at 4.10 eV in the 3D spectra originates from S_{74} , which is only accessible via two consecutive one-photon transitions $S_0 \rightarrow S_1 \rightarrow S_{74}$. The calculated oscillator strength of the direct $S_0 \rightarrow S_{74}$ one-photon transition is zero, which further underlines that S_{74} is a two-photon allowed but a one-photon forbidden electronic state.

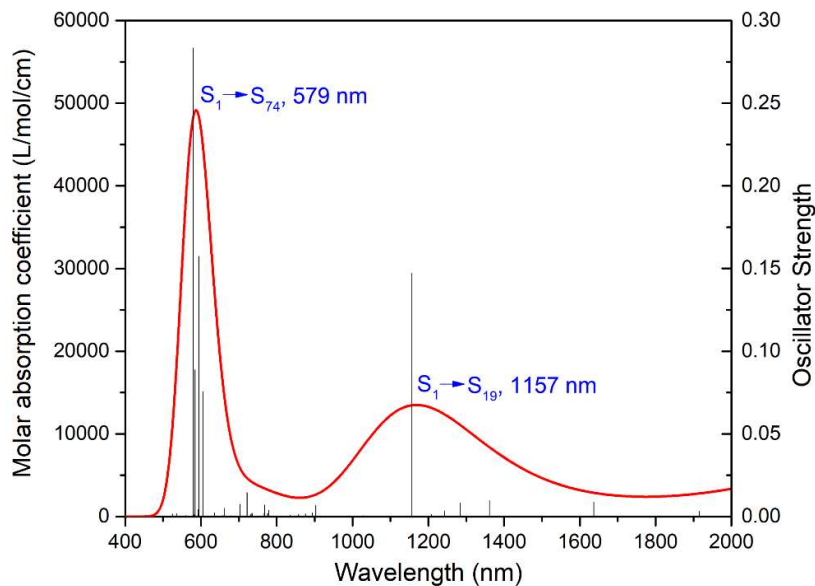


Figure 5.10. Calculated $S_1 \rightarrow S_n$ ($n = 2, \dots, 100$) absorption spectrum of TIPS-TAP²⁻, broadened using Gaussian functions with a full width at half maximum of 0.33 eV.

5.3.2 Br4-TAP

The electron affinities were calculated at the DFT/CAM-B3LYP level to be 4.03 eV for the parent **TAP** and 4.33 eV for **Br4-TAP**, thus making **Br4-TAP** attractive for n-channel semiconductors.

The lowest computed vertical electronic transitions of **Br4-TAP**, its monoanion, and dianion calculated at the TDDFT/CAM-B3LYP level follow the trend of the experimental data (Table 5.3 and Figure 5.11). As in the case of **TAP**, the spectrum of the radical anion is red-shifted the most, followed by that of neutral **Br4-TAP**. The dianion has the most blue-shifted absorption spectrum. The optical properties and excited electronic states of **Br4-TAP** are, in general, very similar to that of **TAP** and its reduced species.

Table 5.3. Computed relative energies (ΔE) and vertical excited states of **Br4-TAP**, its anion **Br4-TAP⁻**, and dianion **Br4-TAP²⁻** at the DFT(TDDFT)/CAM-B3LYP/6-311++G** level.

	Br4-TAP	Br4-TAP ⁻	Br4-TAP ²⁻
$\Delta E^{[a]}$	0	-4.33	-7.69
BS ₁ ^[b]	1.91 (0.27) [650 nm]	0.97 (0.10) [1280 nm]	2.39 (1.36) [519 nm]
BS ₂ ^[b]	3.09 (1.03) [401 nm]	1.87 (0.43) [662 nm]	

[a] Relative energies in eV. The energy of neutral **Br4-TAP** is set to zero. [b] Vertical excitation energies of bright states (BS) in eV, oscillator strengths in parentheses, absorption wavelengths in brackets.

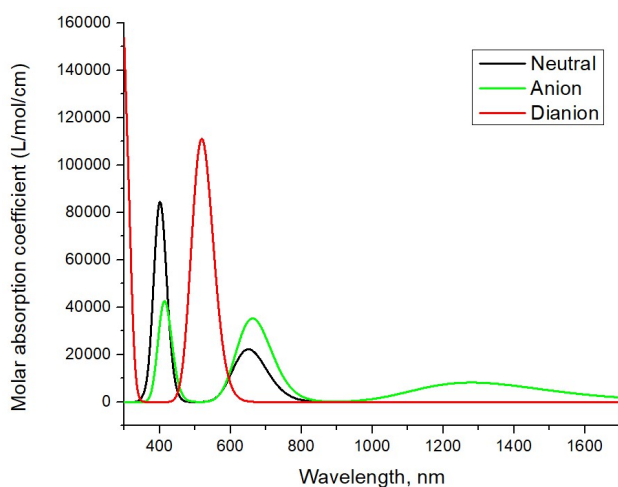


Figure 5.11. Simulated absorption spectra of neutral, anionic and dianionic **Br4-TAP** computed at TD-DFT/CAM-B3LYP/6-311++G** level. All spectra were broadened using Gaussian functions with a full-width at half maximum of 0.2 eV.

The EPR spectra of **Br4-TAP⁻** is shown in Figure 5.3. The simulated spectrum gives $g_{\text{iso}}=2.005$, $a(^{14}\text{N})=3.7$ MHz, $a(^1\text{H})=3.7$ MHz, and $a(^{79,81}\text{Br})=1.8$ MHz. The hyperfine coupling of nitrogen in **Br4-TAP⁻** is much smaller than that in the **TAP** radical anion ($a(^{14}\text{N})=5.32$ MHz), while the hyperfine coupling constants of the protons in **TAP⁻** are smaller than those in **Br4-TAP⁻**. This indicates that, in contrast to **TAP⁻**, the unpaired

electron in **Br4-TAP**⁻ resides more on the outer rings than on the inner rings. This is an indication of the inductive effect of the bromine substituents. The computed natural charges at the DFT/CAM-B3LYP level support this finding (see Table 5.4).

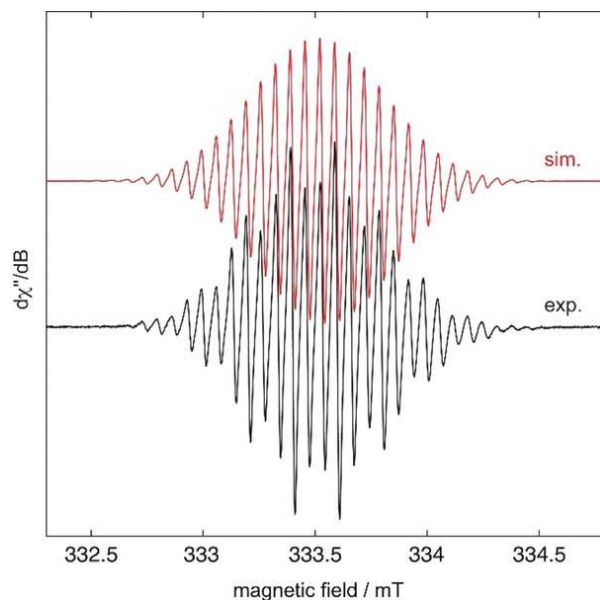
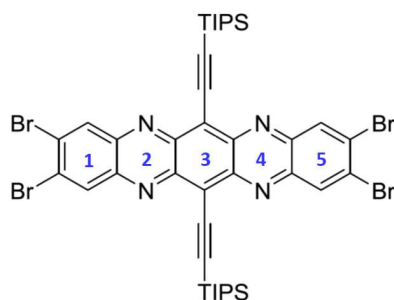


Figure 5.12. Simulated and experimental EPR spectra of **Br4-TAP**⁻.

The bromine atoms do indeed lead to a shift of the negative charge towards the outer rings. This effect is more pronounced for the anionic and dianionic species than for the neutral **Br4-TAP**. This observation will be important for the charge transport property. Quantum chemical calculations confirmed that **Br4-TAP**²⁻ is a singlet, as the triplet state lies 1.159 eV above that of the singlet.

Table 5.4. Difference of atomic natural charges between neutral, anionic and dianionic TAP and Br4-TAP. Δ corresponds to the charge shift induced by the bromine atoms. The charges of the rings are summed up according to the numbering scheme below, the TIPS groups are excluded. Charges of atoms belonging to two rings are split. The negative charge is shifted to the terminal ring in Br4-TAP compared to TAP.



	Br4-TAP	2	3	4	5
TAP(0)	0.307	-0.443	0.286	-0.442	0.307
Br4-TAP(0)	0.283	-0.396	0.317	-0.422	0.289
Δ	-0.024	+0.047	+0.031	+0.020	-0.018
TAP(-1)	0.116	-0.585	-0.037	-0.586	0.117
Br4-TAP(-1)	0.058	-0.569	0.025	-0.567	0.080
Δ	-0.058	+0.016	+0.062	+0.019	-0.037
TAP(-2)	-0.067	-0.698	-0.451	-0.698	-0.067
Br4-TAP(-2)	-0.148	-0.672	-0.346	-0.683	-0.143
Δ	-0.081	+0.026	+0.105	+0.015	-0.076

5.3.3 bis-TAP

The radical anion of **bis-TAP** is less stable than the **TAP** radical anion in air, as the electron affinity of **bis-TAP** is lower by about 0.6 eV. Calculations (Table 5.5) of the relative energies of the neutral, anion and dianion of **bis-TAP** reveal the anion to be more stable than the neutral form by 3.64 eV in THF, and the dianion to be more stable than the anion by another 2.8 eV at the DFT/CAM-B3LYP/6-311++G** level supporting the lack of disproportionation.

Table 5.5. Calculated relative energies and lowest vertical excited states of the neutral, anion, and dianion of **bis-TAP**. Relative energies in eV [kJ mol^{-1}]; vertical excitation energies in eV; oscillator strengths in parenthesis.

	bis-TAP	bis-TAP ⁻	bis-TAP ²⁻
Relative energies	0	-3.64 [-351]	-6.44 [-621]
Excited states			
1st	2.43 (0.34)	1.43 (0.12)	2.06 (1.89)
2nd	2.83 (1.81)	1.70 (0.57)	

The calculated vertical excitation energies follow exactly the trends observed in the experimental absorption spectra of **bis-TAP**, **bis-TAP⁻**, and **bis-TAP²⁻**, respectively (Table 5.5, Figure 5.13, and Figure 5.14). The lowest excited state of **bis-TAP** is a typical π - π^* HOMO-LUMO transition with excitation energy of 2.43 eV, which corresponds to an absorption wavelength of 511 nm. The lowest excited state of the anion exhibits excitation energy of 1.43 eV, and its absorption wavelength is redshifted to 866 nm. The lowest excited state of the dianion **bis-TAP²⁻** again occurs at a higher excitation energy of 2.06 eV, but still substantially lower than that for **bis-TAP**. Hence, the lowest computed absorption peak of **bis-TAP²⁻** is also redshifted, at 599 nm, compared to that of **bis-TAP**. This is different for the neutral and dianion of **TAP**, as the lowest absorption peak of **TAP²⁻** is blue-shifted compared to that of **TAP**.

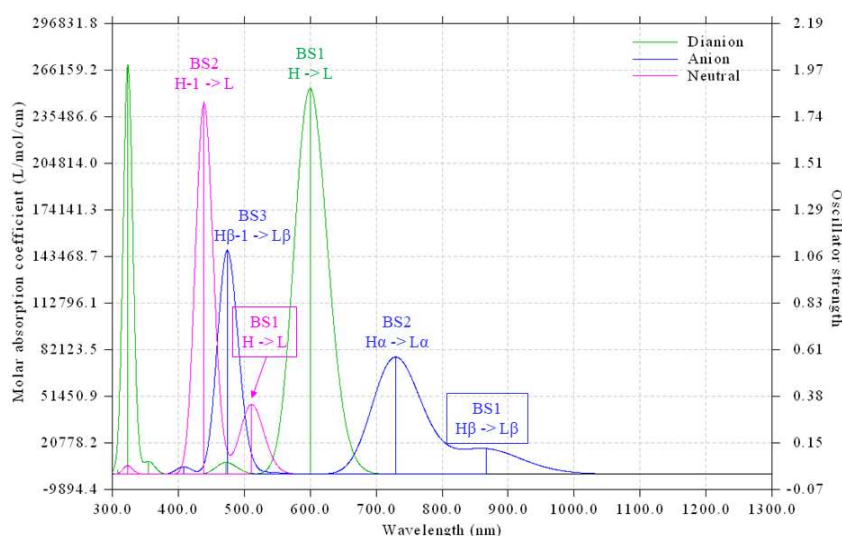


Figure 5.13. Simulated absorption spectra of neutral, anionic, and dianionic **bis-TAP** computed at TD-DFT/CAM-B3LYP/6-311++G** level. All spectra were broadened

using Gaussian functions with a full-width at half maximum of 0.2 eV. BS refers to bright state.

The trend observed for the lowest excited states of **bis-TAP** and **bis-TAP**²⁻ as well as **TAP** and **TAP**²⁻ is directly related to the computed HOMO–LUMO gap; in both systems these states correspond to one-electron transitions from the HOMO to the LUMO. In **bis-TAP** and **bis-TAP**²⁻, the gaps are 4.37 and 3.79 eV, respectively, whereas in **TAP** and **TAP**²⁻ they are 3.98 and 4.45 eV, respectively, at the DFT/CAM-B3LYP level.

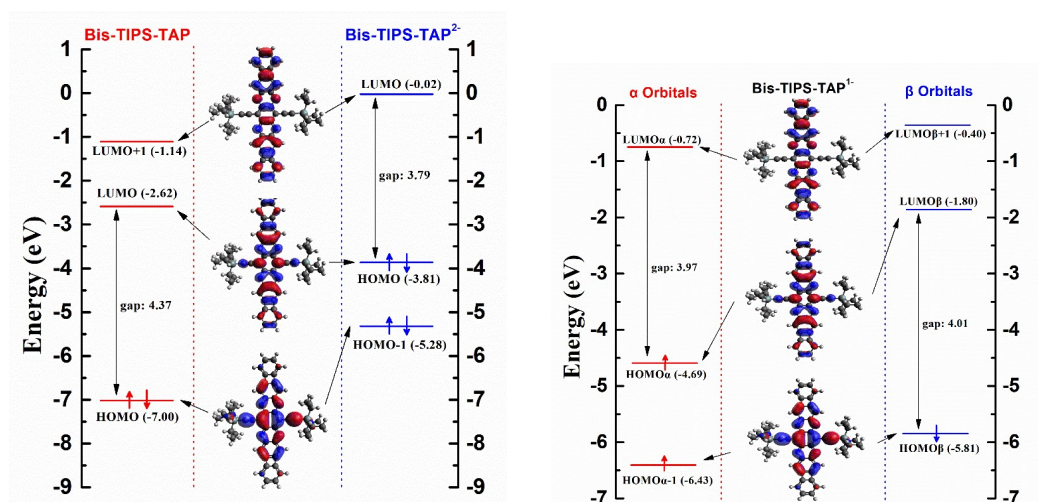


Figure 5.14. Kohn–Sham frontier molecular orbital diagrams and energies (in eV) for neutral, dianionic (left) and anionic **bis-TAP** (right) in THF solution (isodensity value: ± 0.015). The HOMO–LUMO gap decreases from the neutral to the dianion.

In the biphenylene radical anion, the spin distribution at the α -position ($a(\alpha\text{H})=0.53$ MHz) is much smaller than that at the β -position ($a(\beta\text{H})=7.8$ MHz), indicating an uneven distribution of the unpaired electron in the aromatic system.^[215] In the EPR spectrum of **bis-TAP**⁻ (Figure 5.15), the hyperfine coupling constant of ¹⁴N (**bis-TAP**⁻: $a(^{14}\text{N})=4.4$ MHz, **TAP**: $a(^{14}\text{N})=5.3$ MHz), and of the aryl protons (**bis-TAP**⁻: $a(^1\text{H})=1.0, 0.9, 1.1$ MHz, **TAP**: $a(^1\text{H})=1.5, 1.4$ MHz) are much smaller than those of

TAP; these numbers indicate the decrease of spin density on the azapentacene unit and confirm that the unpaired electron delocalizes on both the pentacene and the two phenylene units. In contrast to the biphenylene radical anion system, the hyperfine coupling constants of all aryl protons are similar to one another, indicating that the spin density is distributed much more evenly than in the biphenylene radical anion.

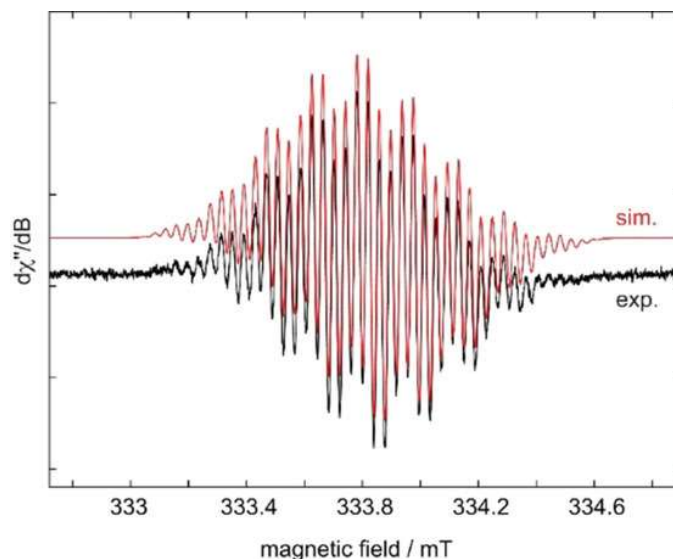
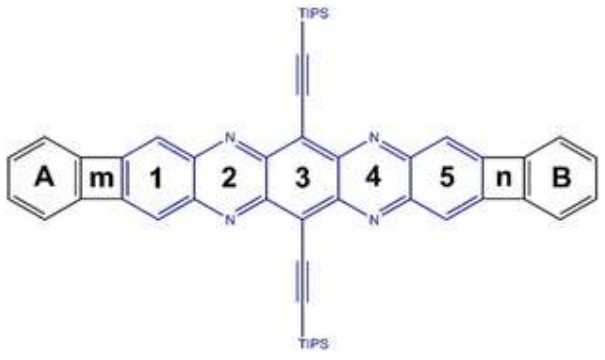


Figure 5.15. Experimental (black) and simulated (red) EPR spectra of **bis-TAP**^{•-}.

To investigate the aromaticity of the neutral and dianionic species we calculated the NICS(1)_{zz} values of **bis-TAP**, **bis-TAP**²⁻, **TAP**, and **TAP**²⁻ (Table 5.6). While negative NICS(1)_{zz} values indicate aromaticity, positive values refer to antiaromaticity. **TAP** is an aromatic system with five aromatic six-membered rings; its dianion has diminished aromaticity at the central ring and displays two antiaromatic pyrazine units. The terminal rings 1 and 5 remain aromatic. The situation is different for both **bis-TAP** and **bis-TAP**²⁻. While the terminal rings A and B are aromatic, the four-membered rings m and n are highly antiaromatic, with more antiaromaticity upon reduction. The incorporation of the four-membered rings reduces the aromaticity of rings 1 and 5 drastically. Also, in the dianion **bis-TAP**²⁻, the four-membered rings lead to an increased antiaromaticity of the core, compared to that of **TAP**²⁻.

Table 5.6. NICS(1)_{zz} values [ppm] of **bis-TAP** and **bis-TAP²⁻** compared to the NICS(1)_{zz} values of **TAP** and **TAP²⁻** computed at the DFT/CAM-B3LYP/6-311G** level.



The chemical structure shows a central benzene ring (labeled 3) substituted with two TIPS groups. This central ring is connected to two pyridine rings (labeled 2 and 4), which are further connected to two benzene rings (labeled 1 and 5). The outermost benzene rings are labeled A, m, n, and B. The NICS(1)_{zz} values are provided for each atom and species.

	TAP	bis-TAP	TAP ²⁻	bis-TAP ²⁻
A		-18.98		-12.73
m		23.37		33.54
bis-TAP	-18.78	-3.86	-19.79	-5.01
2	-29.47	-20.36	-1.12	0.73
3	-29.71	-25.04	8.35	9.97
4	-29.21	-19.97	-1.33	1.21
5	-18.38	-3.28	-19.72	-4.46
n		23.35		33.91
B		-18.50		-12.25

5.3.4 Quino-CF₃

Figure 5.16 displays the molecular structure and the bond distances of the neutral and the radical cation of Quino-CF₃. The neutral species displays a significant bond alternation, in accordance with the geometry derived from the single crystal structure, that strongly suggests a quinoidal structure, as expected from the simple resonance structures. The quinoidal character decreases when going from the neutral compound to the radical cation, as expected.

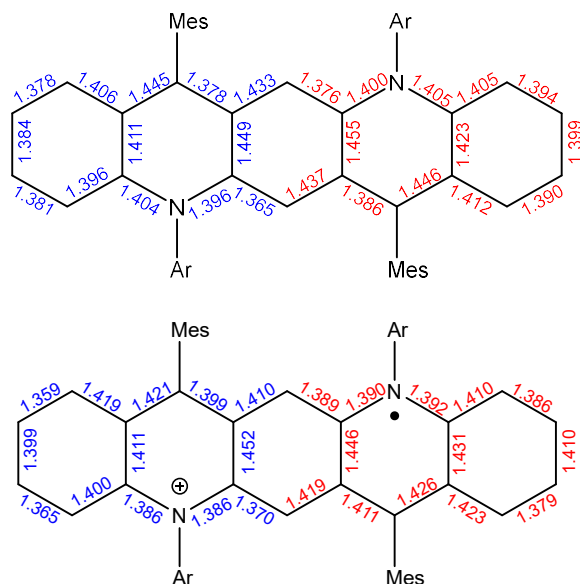


Figure 5.16. Molecular structures and bond lengths (blue: derived from the crystal structure; red: calculated at the DFT/B3LYP/6-311G** level) of neutral **Quino-CF₃** compound (top) and its radical cation (bottom).

As can be seen from Figure 5.17, the simulated absorption spectra of the Quino-CF₃ species are consistent with the experiment. The lowest electronic transition of Quino-CF₃ is a HOMO–LUMO transition with an excitation energy of 2.22 eV located at 559 nm in the simulated absorption spectrum. Due to neglect of vibrational effects, the broadening of the absorption bands is not reproduced. The lowest absorption band of Quino-CF₃⁺ is redshifted to the near-infrared region with contributions from two electronic transitions of HOMO α –LUMO α and HOMO β –LUMO β characters. Furthermore, the first bright state of Quino-CF₃²⁺ lies in between those of Quino-CF₃ and Quino-CF₃⁺ with a λ_{max} of 653 nm. Therefore, the first absorption band of Quino-CF₃ is blueshifted compared to its cationic and dicationic species. A similar blueshift feature also exhibits in dianionic TAPs²⁻, when compared with TAP and TAP⁻. Hence, the character of each vertical transition for Quino-CF₃ and TAP is compared and shown in Table 5.7. It can be easily found that Quino/TAP²⁻, Quino⁺/TAP⁻ and Quino²⁺/TAP share common transition characters. For example, the most important contribution to the first bright state (BS1) of Quino-CF₃ is a HOMO to LUMO transition, the BS1 of TAP²⁻ is analogously also mainly a HOMO–LUMO transition with similar molecular

orbital shapes. Thus, the resemblance of the peak position in the absorption spectra and the similar characteristics of the electronic transitions corroborate the isoelectronic properties of Quino/TAP²⁻, Quino⁺/TAP⁻ and Quino²⁺/TAP.

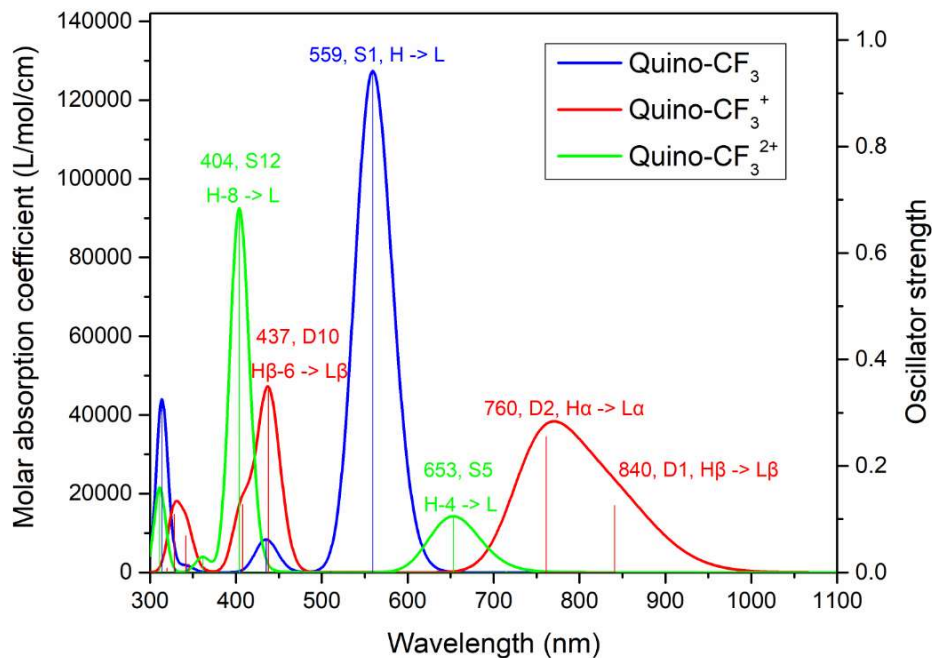
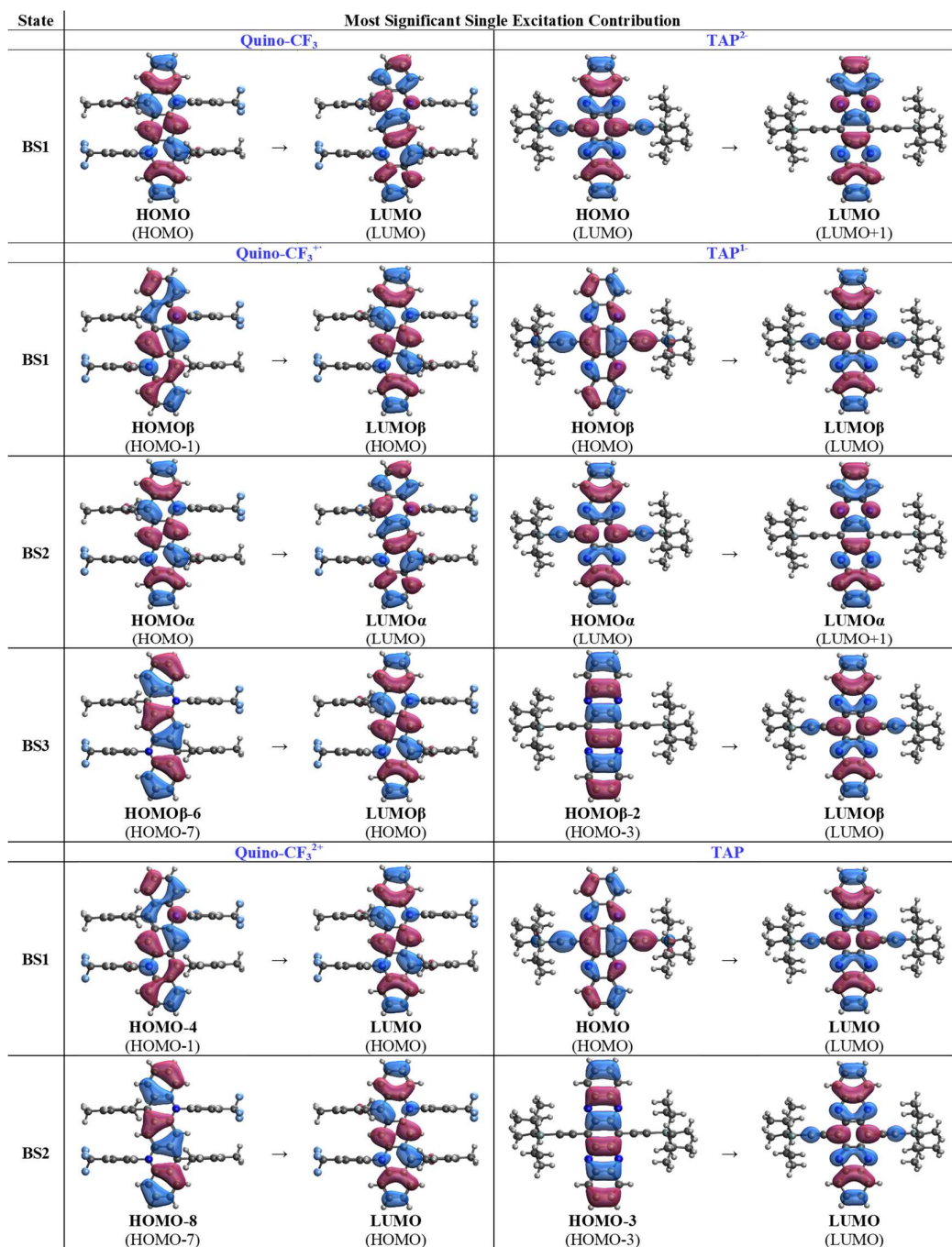


Figure 5.17. Simulated absorption spectra of neutral, cationic and dicationic **Quino-CF₃** computed at TD-DFT/B3LYP/6-311G** level. All spectra were broadened using Gaussian functions with a full-width at half maximum of 0.2 eV.

Table 5.7. Comparison of most significant single excitation contributions of the bright states (BS) for **Quino-CF₃** versus **TAP²⁻**, **Quino-CF₃¹⁺** versus **TAP¹⁻**, and **Quino-CF₃²⁺** versus **TAP**. The MO numbers are indicated below the MO pictures, where the MO numbers in respective neutral specie are written in parentheses. The **Quino-CF₃** and **TAP** species were computed at B3LYP/6-311G**/DCM and CAM-B3LYP/6-311++G**/THF level of theory, respectively.



To shed further light on this aromaticity, we performed quantum chemical NICS-calculations (Figure 5.18). In the neutral Quino-CF₃, NICS-values of the three interior rings are positive with the maximum value up to +9.5, yet smaller than those reported for the formally antiaromatic ring in *N,N'*-dihydroetraazapentacene (+23, NICS (0)_{zz}).^[211] Upon monooxidation, the overall aromaticity of the open-shell system, as

calculated by NICS, increases, and all of the rings now display negative NICS-values, with the outer ones and the middle one being more aromatic than the formal pyridine-like ones. Further oxidation to the closed-shell Quino-CF₃²⁺, necessitating a stronger oxidant preparatively, also results in a fully aromatic system with similarly negative NICS values.

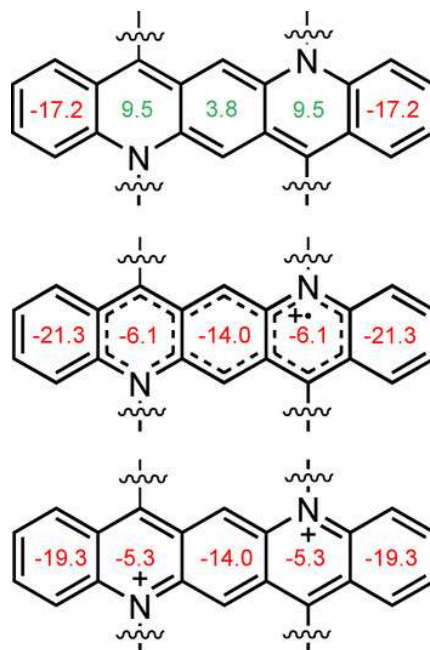


Figure 5.18. NICS(1)_{zz} values of Quino-CF₃ (top), Quino-CF₃⁺ (middle), and Quino-CF₃²⁺ (bottom) calculated at B3LYP/6-311G** level employing a PCM model for DCM solution.

5.4 Conclusions

In this work, we have investigated the molecular properties of a series of N-heteropolycycles and their charged species. The theoretical description and prediction were obtained by electronic structures, energetics, UV-vis-NIR spectra, NICS values, and EPR spectra (radical anions).

For the symmetrical tetraazapentacene (TAP, **4**), there is no detectable charge pinning in 4⁻. The reason for the lack of charge pinning is probably the size of TAP, which allows the negative charge to be easily distributed over the whole molecule. That is

perhaps not too surprising as, if one looks at the LUMO, its coefficients are equally distributed over the whole of the molecule. So, the larger the molecule, we posit, the less of an issue charge pinning is, even though electronegative atoms are present in the molecular framework as in **4**.

The reduction of four different azapentacenes containing two or four nitrogen atoms (**1-4**) in the ring systems results in radical anions that are stable with respect to disproportionation into the dianion and the neutral compound. The radical anions show a strongly red-shifted absorption (into the NIR), while the dianions all have blue-shifted absorptions. The one- and two-electron reductions do not lead to a dramatic change in the overall geometry of the investigated azapentacenes, even though for the dianions, the loss of bond length alternation is in line with the formation of an antiaromatic $4n$ π -system. Overall, our investigations have shed considerable light on the reduction of azapentacenes. We conclude that the presence of the electronegative nitrogen atoms in the rings is more important than their position to stabilize the radical anions, which do not disproportionate.

Br4-TAP shows similar properties as **TAP**. However, several important trends emerge. 1) The addition of four bromine substituents increases the electron affinity as it drastically stabilizes the anionic and dianionic species. 2) The bromine substituents influence the distribution of the negative charge in the radical anion such that it has a higher probability of residing on the outer rings. This might lead to an increased transfer integral in the solid state of **Br4-TAP** in the presence of negative charges, which is examined in **Chapter 5**.

The radical anion and the dianion of **bis-TAP** have been also studied. Both species differ—due to the presence of the two benzocyclobutadiene units—in their properties from those of the **TAP** radical anion and dianion. An important aspect is that upon reduction of **bis-TAP** into its dianion antiaromaticity significantly increases according to NICS-calculations, different from **TAP** (aromatic) and **TAP**-dianion (antiaromatic). The distinctly different aromatic character of **bis-TAP** also goes along with a change in spectroscopic properties, namely, that the dianion of **bis-TAP** displays a surprisingly redshifted absorption when compared to that of the neutral compound. For **TAP**, the opposite is true, that is, the dianion's longest wavelength absorption feature is

blueshifted compared to that of the neutral compound. The conceptual reason for this behavior is not easily understood and awaits further clarification.

The geometry, electronic structure, and spectroscopic data for the Quino-CF₃ and its radical cation and dication display a significant resemblance to the data collected for the series of TAP dianion, radical anion, and TAP as neutral compound. The resemblance is most striking if one looks at the spectroscopic data, and while the TAP dianion does not feature a distinct quinoidal structure, Quino-CF₃ does so. Yet the spectra are very similar. More remarkable is that the TAP radical anion and the Quino-CF₃ radical cations display red shifted spectra similar to each other suggesting an extensive isoelectronic relationship.

6. Theoretical Simulation of Electron Transport Process in Halogenated N-Heteroacenes

6.1 Abstract

Over the last decades, organic electronics has emerged as a vibrant, interdisciplinary field of research. New organic semiconductors with excellent semiconducting properties are considered as role models of their inorganic counterparts. In addition, organic materials are modifiable, which might be a key feature for new innovative technologies.

To specifically synthesize new organic semiconductors, a theoretical understanding of charge transfer is essential. The popular Marcus theory offers a good opportunity to calculate electron transfer rates of organic molecules due to its comparatively low computational effort. Despite being a semi-classical theory, it can correctly predict transfer rates on a qualitative level.

In this work, the Marcus theory is used to calculate the electron transfer properties of N-heteroacenes. These are a promising class of organic semiconductors and are the subject of this current research. The applicability of the approach is examined by comparing results to available theoretical and experimental data. In the end, novel derivatives are examined to reveal their potential as organic semiconductors.

6.2 Introduction

6.2.1 Acenes

Larger acenes and their derivatives are commonly known p-type semiconductors. A selection of them is shown in Figure 6.1.

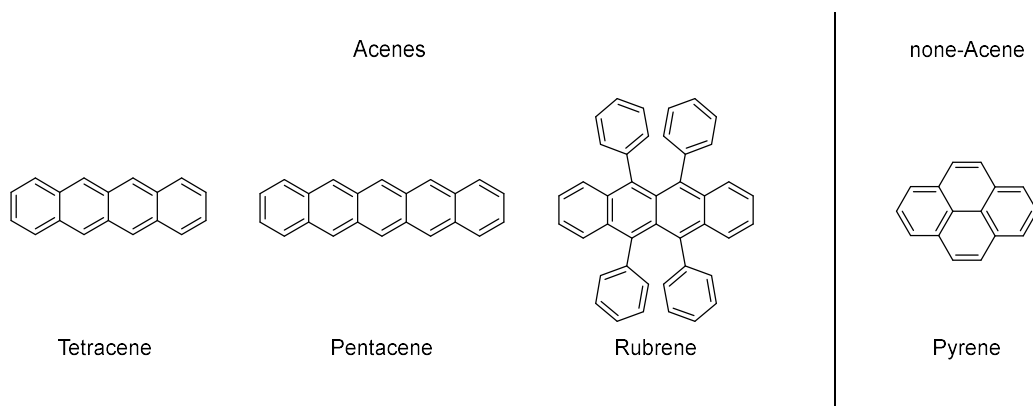


Figure 6.1. Two important acenes, a substituted acene derivative, and one polycyclic aromatic carbon not belonging to the class of acenes.

Acenes, typically described by the fewest localized Clar resonant sextets per number of aromatic rings, have been studied for over a century.^[4] They are made up of linearly fused benzene rings, thus contain only one single Clar resonant sextet. Therefore, pyrene, despite having the same number of aromatic rings as Tetracene, does not belong to the class of acenes because of a nonlinear structure. Due to this fact, it does not exhibit the same typical properties of an acene. Acenes always have smaller HOMO-LUMO gaps than any other hydrocarbon with an equal number of aromatic rings.^[216] Since a sizeable HOMO-LUMO gap typically implies high kinetic stability and low chemical reactivity,^[216] acenes are per definition the most unstable class of polycyclic aromatic hydrocarbons. The HOMO-LUMO gap is also closely related to the number of benzene rings. It decreases with increasing acene length, which is why pentacene is the largest well-characterized example.^[4] Larger acenes such as hexacene are extremely unstable, undergoing dimerization and oxidation.^[217]

On the other hand, the larger acenes turned out to have excellent semiconducting properties. Pentacene can show hole mobilities as high as $35 \text{ cm}^2/\text{Vs}$ at room temperature^[218] and is used as reference material for p-type semiconductors. However, the electron-rich middle ring tends to be oxidized by atmospheric oxygen in a Diels-Alder reaction at the 6,13-position leading to pentacenequinone. This is found to be one of the major impurities in pentacene crystals and acts as an energy trap, thus decreasing the charge mobility.^[218] Additionally, pentacene has very poor solubility in organic solvents^[4] and crystalizes in a herringbone packing motif with only minimal π -stacking leading to aromatic edge-to-face interactions. In Figure 6.2, this herringbone packing motif of unsubstituted pentacene is schematically depicted.^[183]

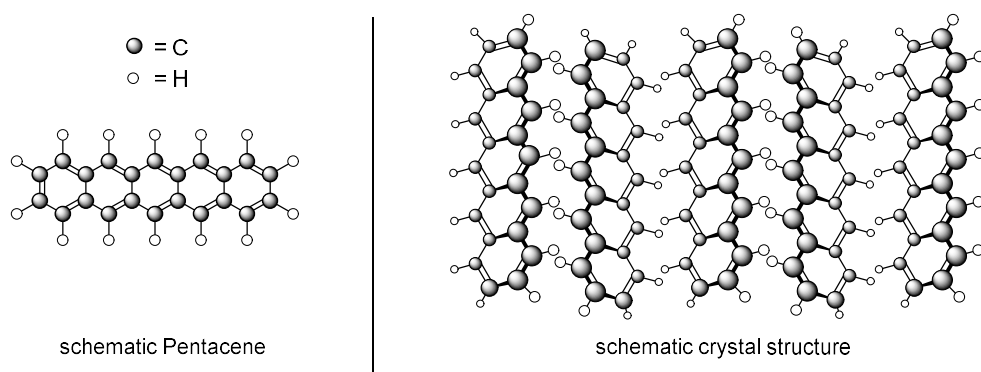


Figure 6.2. Crystal structure of pentacene (herringbone arrangement).^[4]

Fortunately, all problems mentioned above can be circumvented through functionalization with acetylene units, as shown by Anthony *et al.*^[183] Introducing bulky triisopropylsilyl (TIPS) substituents at the chemically active carbon positions 6 and 13, improves the stability, and pentacene becomes soluble in many organic solvents. Furthermore, this modification changes the crystallization motif. A brickwork arrangement is therefore favored leading to a robust face-to-face interaction, which in turn means strong intermolecular coupling essential for excellent electronic performance.^[2] The functionalized pentacene, as well as the brickwork arrangement, are shown in Figure 6.3.

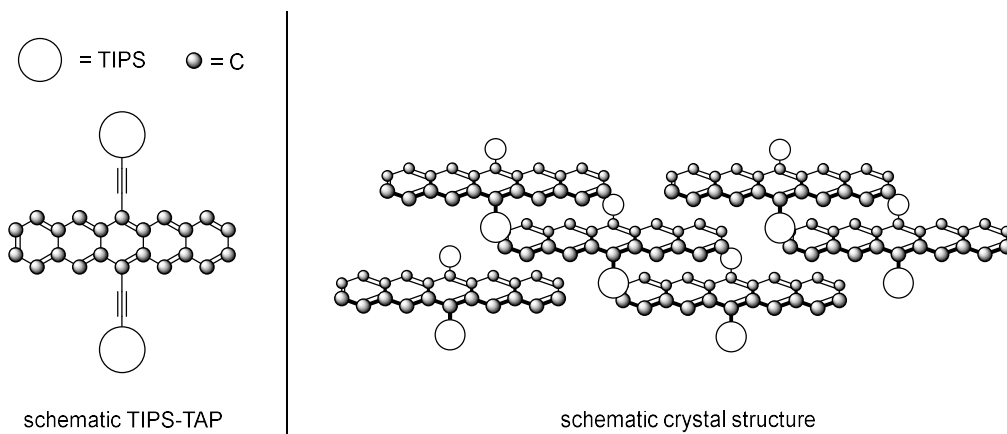


Figure 6.3. Crystal structure of TIPS-pentacene (brickwork arrangement).^[2] For better clarity, hydrogen atoms are not shown.

6.2.2 N-Heteroacenes

Acenes are unsuitable n-type semiconductors due to the formation of unstable radical anions, which lose their charge in trap states or in the presence of oxygen. This can be altered by the introduction of electronegative elements like nitrogen into the framework of the acenes. Therefore, so-called N-heteroacenes are obtained in which one or more rings have been substituted by pyridine or pyridazine rings. The overall structure remains the same as for the acenes described above. Some of the problems of acenes such as insolubility and lack of optimal packing are also directly translated to the N-heteroacenes. Fortunately, they can be solved using the same method. Functionalization with acetylene units leads to the substituted N-heteroacenes. What changes are their electronic properties. The electronegative nitrogen atoms lead to a stable anionic state giving them properties of an n-type semiconductor.^[189] A common example, TIPS-tetraazapentacene (TIPS-TAP) shown in Figure 6.4 exhibits excellent n-type semiconducting properties with electron mobilities up to $11.1 \frac{cm^2}{Vs}$.^[219]

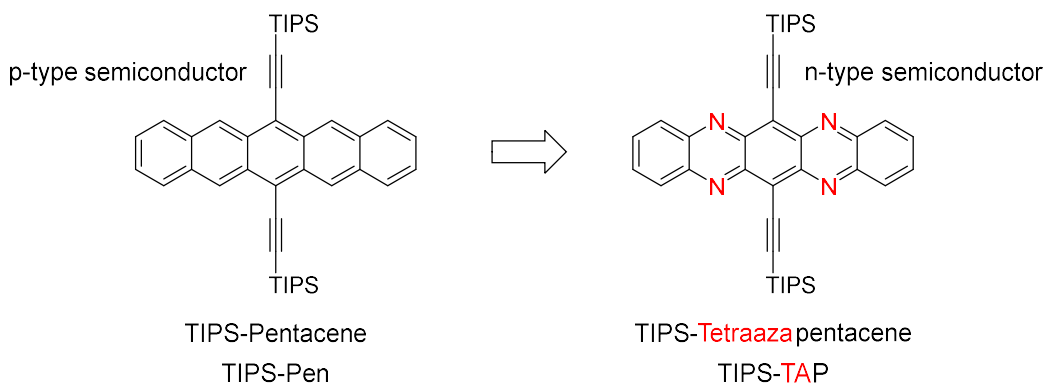


Figure 6.4. Two acene based organic semiconductors: TIPS-Pen (p-type), TIPS-TAP (n-type).

6.2.3 Halogenated TIPS-TAP-Derivatives

Hydrogen atoms of TIPS-TAP can be substituted by halogen atoms, as shown in Figure 6.5. The electronegative halogen atoms further change the electronic properties of N-heteroacenes and influence their semiconducting abilities.^[108, 109] In particular, the central symmetrical 4X-TAPs received significant attention due to excellent performance as n-type semiconductors. With 4Cl-TAP, Miao *et al.* even set a new record for the electron mobility of n-channel organic field-effect transistors, reaching electron mobilities as high as $27.8 \frac{cm^2}{Vs}$. However, the fluorination of TIPS-TAP drastically weakens their semiconducting properties, leading to rather poor electron mobilities.^[108] Bromination, on the other hand, also seems to improve the electron mobility of TIPS-TAP. On similar fabricated devices, it shows electron mobilities 43 times higher than TIPS-TAP. Although, the reported electron mobility of $0.56 \frac{cm^2}{Vs}$ is not nearly as good as the values measured from Miao *et al.*^[108] Nevertheless, it shows the potential of 4Br-TIPS-TAP and leaves the question of what electron mobilities might be achievable when fabricated similar to 4Cl-TIPS-TAP. 4I-TIPS-TAP, recently synthesized by Hilmar Reiss^[220], also lacks measured values for the electron mobility.

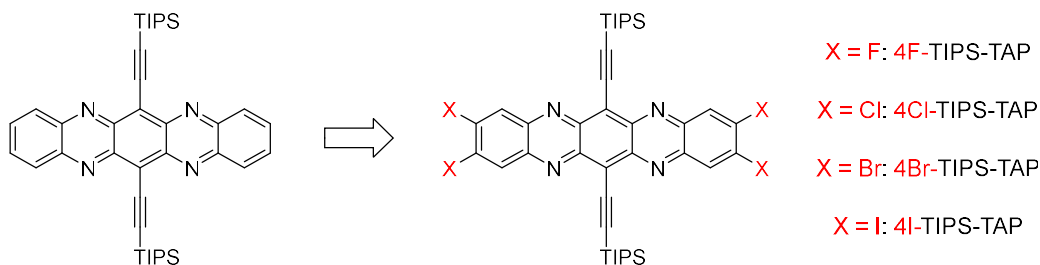


Figure 6.5. Symmetric halogen derivatives of TIPS-TAP.

6.2.4 Aim of this Work

The halogenation of TIPS-TAP significantly changes its properties as a semiconductor. Although Miao *et al.* compared the TIPS-TAP, 4F- and 4Cl-TIPS-TAP on a theoretical and experimental basis,^[108] a comparison to the heavier TIPS-TAP derivatives 4Br-TIPS-TAP and 4I-TIPS-TAP does not exist.

The subject of this work is the theoretical investigation of possible electron mobilities for the tetra halogenated TIPS-TAP molecules, including fluorine, chlorine, bromine, and iodine. Based on the crystal structure of these TIPS-TAP derivatives, electron transfer rates for different dimer structures are calculated using the Marcus theory. With the electron transfer rates and data of crystal structures, the electron mobilities are estimated. The transfer integrals and reorganization energies used within the Marcus theory framework, the Marcus electron transfer rates, and the approximated electron mobilities achieved for the halogenated TIPS-TAPs are compared. Based on the comparison, a statement about the potential of 4Br- and 4I-TIPS-TAP is given.

6.3 Theory

6.3.1 Organic Semiconductors

Organic semiconductors are organic materials that show semiconducting properties. The critical quantity that characterizes the charge transport in such semiconductors is the carrier mobility μ . Based on the ease of charge injection from electrodes, organic semiconductors can be separated into two classes. If the Fermi level of an electrode is close to the electron affinity of the material, injecting an electron into the material is favored. Such materials are called n-type semiconductors. On the other hand, if its ionization energy closely matches the Fermi level of an electrode, the material would be used as a hole transporter and called a p-type semiconductor. Independent of the carrier, in the absence of an external electric field the charge transfer is purely diffusive, and the charge mobility can be calculated by the Einstein-Smoluchowski equation:^[3]

$$\mu = \frac{eD}{k_B T}, \quad (6.3.1)$$

where e is the electron charge, k_B the Boltzmann constant, T the temperature, and D refers to the diffusion coefficient. Diffusion in the absence of an external field can generally be described by^[3]

$$D = \frac{1}{2n} \frac{\langle x^2 \rangle}{t}, \quad (6.3.2)$$

where n is the spatial dimensionality of the system, t is the time, and $\langle x^2 \rangle$ represents the mean-square displacement of the charges. It can be seen as a local displacement of the charge carriers around an average position. To change the average position, an external electric field needs to be applied. It induces a drift of the charge carriers across the organic semiconductor, which is the primary way of charge migration in fabricated devices. Here, the charge mobility can be alternatively defined as:

$$\mu = \frac{v}{F}, \quad (6.3.3)$$

where v is the velocity of the charges, and F is the amplitude of the external electric field. ^[3]

In this work, the charge mobility is calculated through the definition of a purely diffusive process. For evaluating the diffusion coefficient D , many different approaches are used in the literature.^[221-224] Assuming no correlation between hopping events and that the charge motion is a homogeneous random walk seems to provide^[222, 224]

$$D = \lim_{t \rightarrow \infty} \frac{1}{2n} \frac{\langle x(t)^2 \rangle}{t} \approx \frac{1}{2n} \sum_i r_i^2 W_i P_i, \quad (6.3.4)$$

where n is the spatial dimensionality of the system, t is the time, and $\langle x(t)^2 \rangle$ refers to the mean-square displacement of the charges; i represents a specific hopping pathway, r_i is the distance between the center of mass of two adjacent molecules along pathway i (hopping distance), and W_i is the hopping rate between neighbors along pathway i . P_i is the hopping probability and is calculated with

$$P_i = \frac{W_i}{\sum_i W_i}. \quad (6.3.5)$$

Miao *et al.* also used equations 6.3.4 and 6.3.5 to evaluate the charge mobility of TIPS-TAP, 4F-TIPS-TAP, and 4Cl-TIPS-TAP and correctly predicted the trend.^[10] Since we aim to reproduce their results and calculate the bromine and iodine derivatives for comparison, this approach seems reasonable. However, equation 6.3.4 predicts different diffusion coefficients for two seemingly similar systems shown in Figure 6.6.

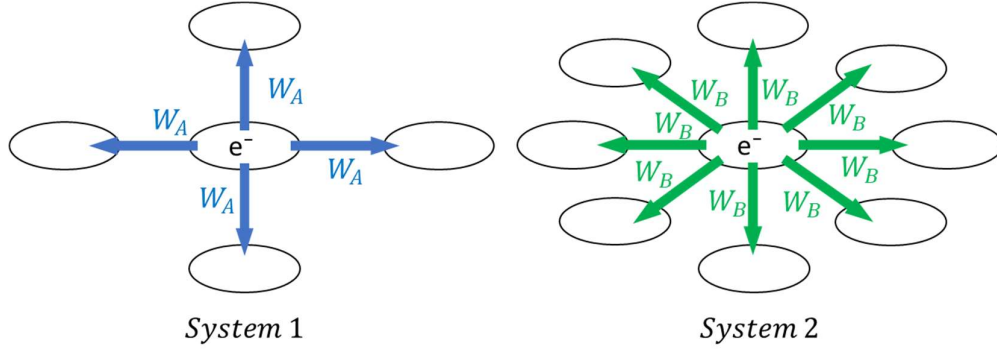


Figure 6.6: Two model systems to demonstrate the behavior of equation 6.3.4.

Here, the hopping rates are $W_A = 2W_B$, and the distances r are assumed to be equal in the two systems. The dwell time $\tau = (\sum_i W_i)^{-1}$ is also identical for both system, and the charge carrier jumps with distance r after time τ . However, evaluating the diffusion coefficient with equation 6.3.4 provides:

$$\begin{aligned}
 \text{System 1: } D &= \frac{1}{2n} \sum_i r_i^2 W_i P_i = \frac{1}{2 \cdot 2} 4 \cdot r^2 W_A \frac{W_A}{4W_A} \\
 &= \frac{1}{4} r^2 W_A,
 \end{aligned} \tag{6.3.6}$$

$$\begin{aligned}
 \text{System 2: } D &= \frac{1}{2n} \sum_i r_i^2 W_i P_i = \frac{1}{2 \cdot 2} 8 \cdot r^2 W_B \frac{W_B}{8W_B} \\
 &= \frac{1}{4} r^2 \frac{1}{2} W_A.
 \end{aligned} \tag{6.3.7}$$

System 2 only shows half of the diffusion coefficient of 1. Furthermore, when adding more pathways to system B with W_B and r , the resulting diffusion coefficient remains the same even though τ decreases. The actual number of paths with the same hopping rate and hopping distance in one system is meaningless after equation 6.3.4.

Stehr *et al.* made similar considerations for the charge mobility as mentioned above and gave^[223]

$$D = \frac{1}{2n} \frac{d}{dt} \langle r^2 \rangle = \frac{1}{2n} \sum_i \frac{p_i \langle r^2 \rangle_i}{\tau_i}, \tag{6.3.8}$$

where i represents the different lattice sites and p_i the probability that lattice site i is occupied. Other variables are the same as defined above. For the one dimensional ($n = 1$) case, the resulting diffusion coefficient is

$$D = \frac{1}{2} \sum_{ij} p_i W_{ji} (\vec{r}_{ji} \vec{e})^2, \quad (6.3.9)$$

where \vec{e} is the unit vector along the direction of the diffusion. In the absence of an external electrical field, all lattice sites are equally populated since all lattice sites can be taken as equal and the last equation simplifies to^[223]

$$D = \frac{1}{2} \sum_j W_j (\vec{r}_j \vec{e})^2. \quad (6.3.10)$$

Equation 6.3.10 and 6.3.4 are similar (also in the 1D case) with the exception of P_i . Assuming the 2D (3D) coefficient is just the mean of 2 (3) 1D coefficients, equation 6.3.10 could also be used to calculate the model system in Figure 6.6. Now the two systems indeed show the same diffusion coefficient. Also, adding more paths with the same hopping rate and hopping distance actually changes the diffusion coefficient, which is contrary to equation 6.3.4.

In this work, the equation 6.3.4 is used, since it is the equation used by Miao *et al.* to calculate the diffusion coefficient, and we intend to produce comparable results. Additionally, all of the investigated systems show the same number of paths, which is why the results can certainly be used to compare the substances. However, in future works D should be calculated with a Monte Carlo simulation since it is used as a reference method to simulate the random walk behavior of charge transport processes.^[223]

6.3.2 Charge-Transport Mechanism

Many models have been suggested for the charge transport in organic semiconductors. From one-dimensional band transport to a variety of polaron-band/hopping models with different kinds and degrees of electron-phonon coupling.^[225] Hopping models describe

the thermally activated hopping of a charge over a barrier, which results in the mobility increasing with higher temperatures. On the other hand, in a band-like regime, the charge is fully delocalized and undergoes coherent motion. Due to higher phonon scattering, mobility should decrease with higher temperatures.^[226] These are the two extreme models for describing the charge transport, and typically none of these two models can be applied exclusively in the case of organic semiconductors.

According to more general models the total mobility μ can be approximated as a sum of two contributions:^[3]

$$\mu = \mu_{tun} + \mu_{hop}, \quad (6.3.11)$$

where μ_{tun} is related to the tunneling of electrons, a coherent electron transfer decreasing with higher temperatures. The latter μ_{hop} is related to the hopping motion, an incoherent electron transfer increasing with higher temperatures. The relative contributions do not depend solely on the temperature but on actual microscopic parameters like electron-phonon coupling, electronic and phonon bandwidths, and phonon energy. In this work only the hopping contribution is examined but for a complete calculation of the mobility μ_{tun} needs to be considered too. It is important to note, however, that the trend of the mobilities is the same with and without considering the tunneling effect in the case of TIPS-TAP and 4F/4Cl-TIPS-TAP.^[108] Therefore although no quantitative mobilities are expected here, a qualitative comparison between the TIPS-TAP derivatives should be possible.

An equation for the hopping mobility μ_{hop} can be given in the framework of small polaron theory. In the classical limit, when the energy of an optical phonon $\hbar\omega_0$ is much smaller than $k_B T$ an Arrhenius-type law for the electron transfer rate W is obtained:^[3]

$$W = \frac{|V_{if}|^2}{\hbar} \left(\frac{\pi}{2E_{pol}k_B T} \right)^{0.5} e^{-\frac{E_{pol}}{2k_B T}}, \quad (6.3.12)$$

where V is the transfer integral of the molecules between which the electron is transferred. The polaron binding energy E_{pol} is obtained by dividing the reorganization energy λ by 2 as shown in equation 6.3.13

$$E_{pol} = \frac{\lambda}{2}. \quad (6.3.13)$$

Taking this into account equation 6.3.12 becomes

$$W = \frac{|V_{if}|^2}{\hbar} \left(\frac{\pi}{\lambda k_B T} \right)^{0.5} e^{-\frac{\lambda}{4k_B T}}, \quad (6.3.14)$$

which is the classical Marcus equation^[227] when the standard Gibbs free energy change ΔG^o is zero. Since the electron transfer in TIPS-TAP crystals is a self-exchange reaction, this holds true in our case. This is also the equation employed by Miao *et al.* to calculate the hopping mobility and is used here in a similar manner.^[108] The next two chapters are about the calculation of the transfer integrals V and reorganization energies λ .

6.3.3 Reorganization Energy

The reorganization energy is one of the key quantities that influence the electron transfer rate. In organic crystals, it can be usually expressed as the sum of inter- and intramolecular contributions due to the weakness of van der Waals interactions between organic molecules. The intermolecular reorganization energy is the result of the electronic and nuclear relaxation of the surrounding medium.^[228] It is typically much smaller than the intramolecular reorganization energies and can, therefore, be neglected.^[229, 230] The physical meaning of the intramolecular reorganization energy is illustrated in Figure 6.7.

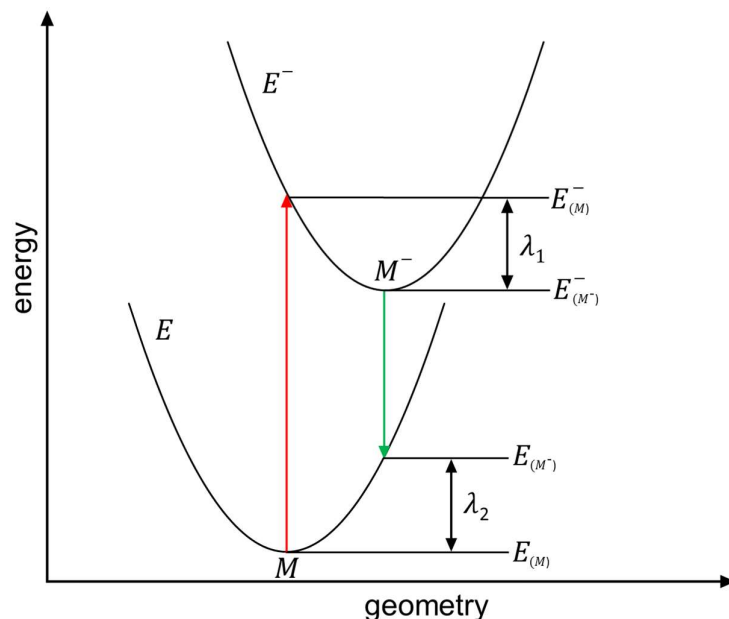


Figure 6.7. Sketch of the potential energy surfaces (PETs) for the neutral state **E** and the anionic state **E⁻**. The red (green) arrow indicates the vertical transition from the neutral (anionic) state to the anionic (neutral) state at the optimized neutral (anionic) state geometry **M** (**M⁻**). λ_1 and λ_2 represent the two terms of the intramolecular reorganization energy.^[223, 224]

For an intermolecular electron transfer between similar molecules, the reorganization energies can be obtained by calculating the energies $E_{(M)}$, $E_{(M^-)}$, $E_{(M^-)}$ and $E_{(M^-)}$. In the case of an electron transfer between two TIPS-TAP molecules **1** and **2**: The acceptor **1** is in the neutral state at the minimum of the PES $E_{(M)}$ while the donor is at the minimum of the anionic state PES $E_{(M^-)}$. If an electron is “hopping” from a neighbored, negatively charged TIPS-TAP **2** to **1**, two transitions will occur. **1** will be reduced (red arrow). At the same time, **2** will be oxidized (green arrow) at frozen reactant geometries as a consequence of the Franck-Condon principle, which requires the same nuclear configuration immediately before and after the electron transfer. **1** is now on the anionic state PES but has the optimal geometry for the neutral state $E_{(M^-)}$ which means it will relax to the minimum of this PES $E_{(M^-)}$. The same applies to **2**, and it will relax from $E_{(M^-)}$ to E_M and concludes the electron transfer. For an electron transfer to occur, the principle of energy conservation should also be satisfied. However, as shown in Figure 6.7, the electronic vertical transitions (red and

green arrows) do not match. It follows that thermal fluctuations from the equilibrium nuclear configurations of the reactants are needed prior to the electron transfer.^[228]

As shown in Figure 6.7, the reorganization energies can be calculated via:

$$\lambda = \lambda_1 + \lambda_2, \quad (6.3.15)$$

$$\lambda_1 = E_{(M^-)} - E_{(M)}, \quad (6.3.16)$$

$$\lambda_2 = E_{(M)}^- - E_{(M^-)}^-. \quad (6.3.17)$$

6.3.4 Electronic Coupling

The electronic coupling is of central importance for the charge transport in organic semiconductors. If an electron is transferred from a donor D^- to an acceptor A , the Hamiltonian matrix is

$$\mathbf{H} = \begin{pmatrix} E_i & H_{if} \\ H_{if} & E_f \end{pmatrix}, \quad (6.3.18)$$

where E_i is the energy of the initial state corresponding to the D^-A state and E_f is the energy of the final state corresponding to the DA^- state. The off-diagonal matrix elements are

$$H_{if} = \langle \Psi_i | H | \Psi_f \rangle, \quad (6.3.19)$$

where H is the electronic Hamiltonian of the system, and Ψ_i and Ψ_f are the wavefunctions of the two charge-localized (diabatic) states D^-A and AD^- respectively which are the states obtained in the hypothetical absence of any coupling between the donor and acceptor. H_{if} is the transfer integral (when Ψ_i and Ψ_f are orthogonal) and rigorously define the magnitude of the electronic coupling. In the basis of eigenstates, \mathbf{H} is

$$\mathbf{H} = \begin{pmatrix} E_1 & 0 \\ 0 & E_2 \end{pmatrix}, \quad (6.3.20)$$

with the eigenvalues

$$E_{1,2} = \frac{E_i + E_f}{2} \pm \sqrt{\left(\frac{E_i - E_f}{2}\right)^2 + H_{if}^2}. \quad (6.3.21)$$

In the more general case, where Ψ_i and Ψ_f are not orthogonal

$$S_{if} = \langle \Psi_i | \Psi_f \rangle \neq 0, \quad (6.3.22)$$

an effective Hamiltonian can be obtained by symmetric Löwdin orthogonalization with the off-diagonal elements (when Ψ_i and Ψ_f are normalized)

$$V_{if} = H_{if}^{eff} = \frac{H_{if} - (E_i + E_f)S_{if}/2}{1 - S_{if}^2}, \quad (6.3.23)$$

where V_{if} is the transfer integral and will be used in the Marcus equation 6.3.14. ^[3, 231]

V_{if} can be calculated based on the Hartree-Fock (HF) method or with correlated methods like Configuration Interaction (CI). Since correlated methods are costly, they impose computational challenges and are not practical to be used in large systems. On the other hand, Hartree-Fock is less accurate due to the lack of electron correlation. An alternative is the density functional theory (DFT), which can be very accurate while maintaining low computational costs. Based on DFT, a possibility to calculate V_{if} is by constraining charges to the individual fragments and thus constructing the charge-localized (diabatic) states (CDFT).^[232] One disadvantage of existing DFT functionals is that, while capturing a large part of dynamic correlation efficiently, they tend to behave erratically when it comes to static correlation. To include the static correlation, CI has been incorporated in the CDFT method while retaining the efficiency of DFT.^[30] Therefore, CDFT-CI approach is used to calculate V_{if} in this work.

6.4 Methods

6.4.1 Analysis of Crystal Structures

The crystal structures of TIPS-TAP^[185], 4F-TIPS-TAP^[108], and 4Cl-TIPS-TAP^[108] were obtained from the Cambridge Structural Database.^[233] 4Br-TIPS-TAP and 4I-TIPS-TAP structures were provided by Hilmar Reiss.^[220] In Mercury,^[234] the 22 atoms of the planar tetraazapentacene framework were taken to make planes, and the π - π distances were measured. Mass weighted centroids of the complete molecules were calculated and the distances were measured using Avogadro.^[235] Taking both distances into account, different dimer structures were identified and used for the calculation of transfer integrals. The displacement of the π stacking was measured in Avogadro using the align molecules feature. The procedure is illustrated in below.

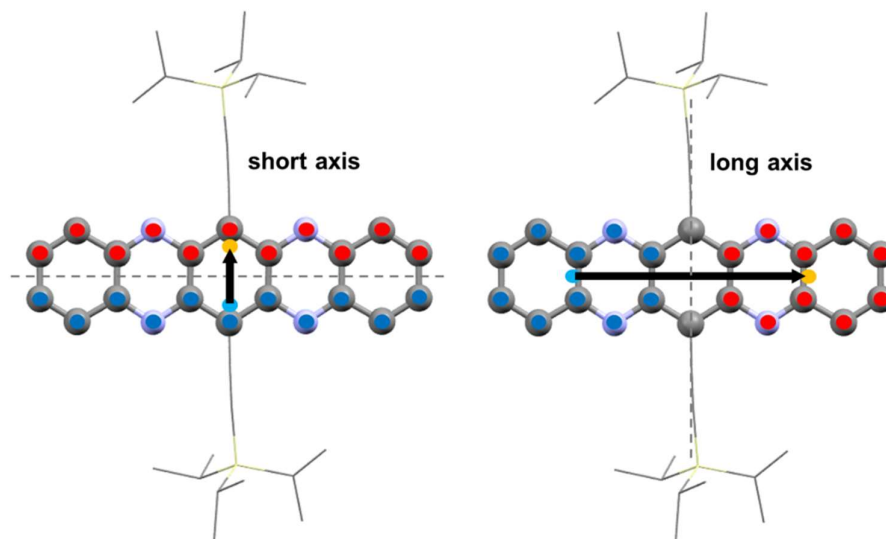


Figure 6.8. Defining the axis in the case of TIPS-TAP as an example. Hydrogen atoms are removed for clarity, and TIPS, along with the acetylene linker are shown as wires, which will be the case for all following pictures. Red marked atoms are taken to calculate the orange centroid, and blue marked atoms are taken to calculate the light blue centroid.

First, two centroids were calculated, including the corresponding 11 atoms of the tetraazapentacene framework when it is divided along its short axis. Second, two centroids were calculated, including the corresponding 10 atoms of the tetraazapentacene framework when it is divided along its long axis. By aligning the molecules along with those four centroids, the displacement between the centroids created from the total 22 atoms of the tetraazapentacene framework could be measured, giving the mean displacement of the π stacking along its short and long axis.

6.4.2 Computational Details

Transfer Integrals

Transfer integrals V were calculated using the Configuration Interaction with Constrained Density Functional Theory (CDFT-CI) method in Q-Chem 5.1^[168] along with the PBE50 functional^[236] and the 6-31G* basis set. The choice of the method, as well as the functional, was made taking a benchmark by Blumberger *et al.* into account. In their work, a comparison of High-level *ab initio* calculations to three DFT methods was carried out, and CDFT in combination with a modified PBE functional containing 50% Hartree-Fock exchange gave the best results.^[237] Calculations with basis sets containing diffuse functions as well as basis sets of triple zeta quality could not be converged. However, when constraining Becke weight population, the use of diffuse functions is not crucial since the obtained values with and without diffuse functions are comparable.^[232] For Iodine, the LANL2DZ ECP^[238] was used to take the relativistic effects of heavy elements into account. Because, in the case of 4Br-TIPS-TAP, the LANL2DZ ECP gave similar results to the 6-31G* basis set. However, there are no references further supporting this choice.

Reorganization Energies

The reorganization energies λ were calculated using the four-point method as described in the theoretical part. Geometry optimization, as well as the single point calculations, were done in Gaussian 09^[209] on the B3LYP^[156, 157]/6-31G** level of theory. It was shown that the B3LYP functional could adequately describe the

relaxation process in oligoacenes.^[239, 240] The 6-31G** basis set is mostly used alongside the B3LYP functional in the literature. Therefore, for the sake of consistency and comparison, B3LYP/6-31G** is employed here. In addition, the combination B3LYP/6-31G** has already shown to describe the reorganization energies of 4F-, 4Cl-TIPS-TAP, and TIPS-TAP correctly.^[108] For Iodine, the LANL2DZ ECP was used to model the relativistic effects of heavy elements, retrieved from the Basis Set Exchange.^[241]

6.5 Results and Discussion

6.5.1 Transfer Integrals

In Figure 6.9 to Figure 6.14, electron pathways of the crystal structures TIPS-TAP and 4F-, 4Cl-, 4Br-, 4I-TIPS-TAP are displayed with their transfer integrals V . These transfer integrals were calculated for each dimer and are labeled from A to C. Since in the context of Marcus theory, the sign of V is irrelevant, only the absolute values of V are given. In the case of TIPS-TAP two different crystal structures were investigated, one obtained from Bunz *et al.*^[185] and the other one obtained from Miao *et al.*^[108]

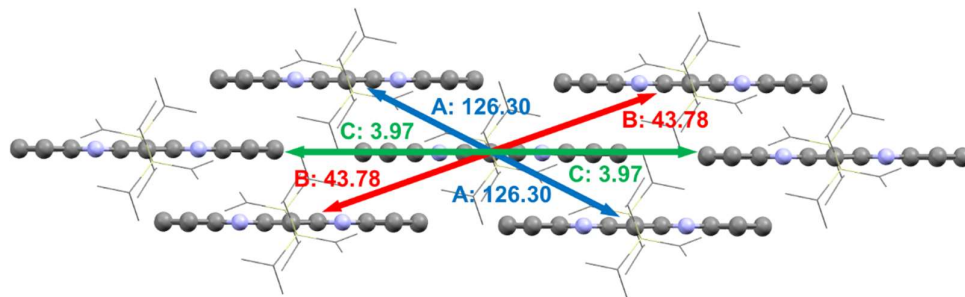


Figure 6.9. Electron transport pathways in the crystal structure of TIPS-TAP (Bunz) and their electron coupling in meV .

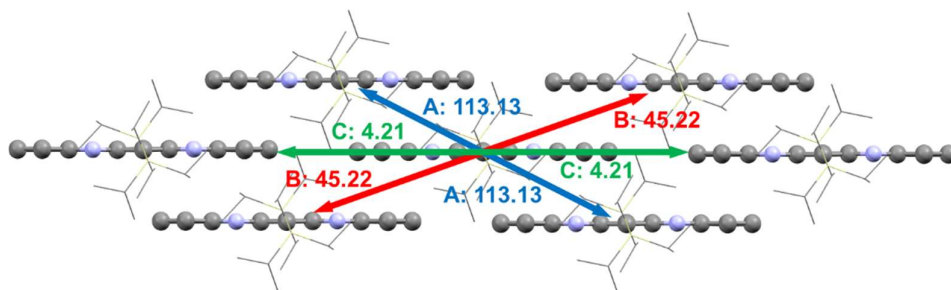


Figure 6.10. Electron transport pathways in the crystal structure of TIPS-TAP (Miao) and their electron coupling in *meV*.

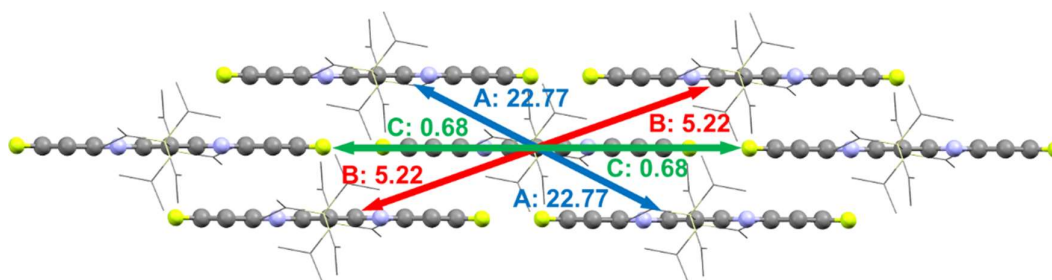


Figure 6.11. Electron transport pathways in the crystal structure of 4F-TIPS-TAP and their electron coupling in *meV*.

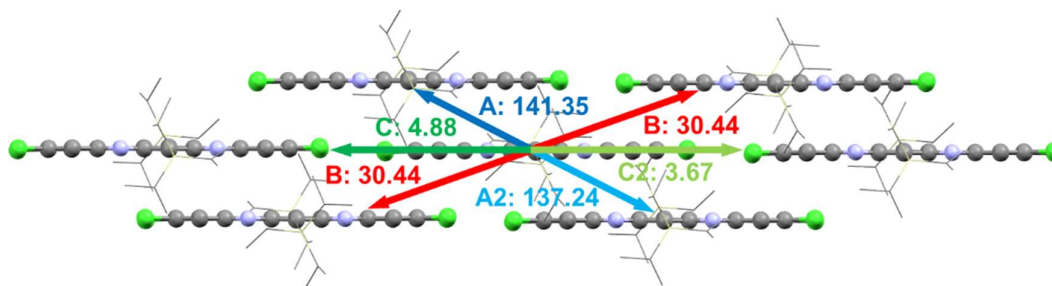


Figure 6.12. Electron transport pathways in the crystal structure of 4Cl-TIPS-TAP and their electron coupling in *meV*.

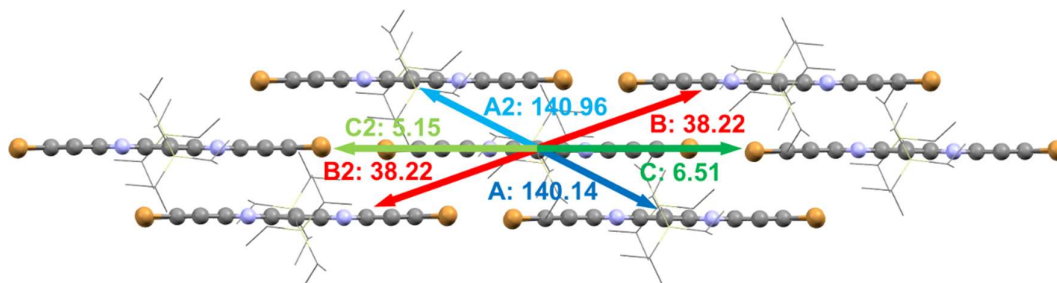


Figure 6.13. Electron transport pathways in the crystal structure of 4Br-TIPS-TAP and their electron coupling in *meV*.

The shown pathways of 4Cl-TIPSTAP and 4Br-TIPS-TAP are simplified to make this kind of graphic possible. In the crystal structure, the transfer integrals are alternating along their respective electron paths. Therefore, different parts of the crystal structure where A swapped places with A2, and C swapped places with C2 do exist. However, since these parts of the crystal structure are centrosymmetric to the parts displayed in Figure 6.12/Figure 6.13, the overall number of different dimers remains the same.

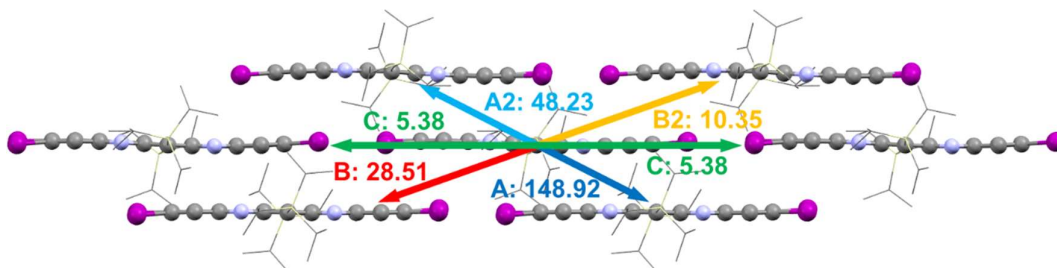


Figure 6.14. Electron transport pathways in the crystal structure of 4I-TIPS-TAP and their electron coupling in *meV*.

In the case of 4I-TIPS-TAP, it is more complicated. Along the electron pathway A/A2 and B/B2, the dimers and their transfer integrals are not alternating. Instead, an A-A-A2 pattern, as well as a B-B-B2 pattern along their respective electron transport paths, could be observed. Therefore, a part of the crystal structure exists where the dimer A2 is exchanged with a second dimer A, and dimer B2 is exchanged with a second dimer B. This part has two A dimers and two B dimers (and two C dimers), differently to the one in Figure 6.14. Other parts of the crystal structure are centrosymmetric to one of these two parts, thus showing the same number of different dimers.

In Figure 6.15, the transfer integrals are compared.

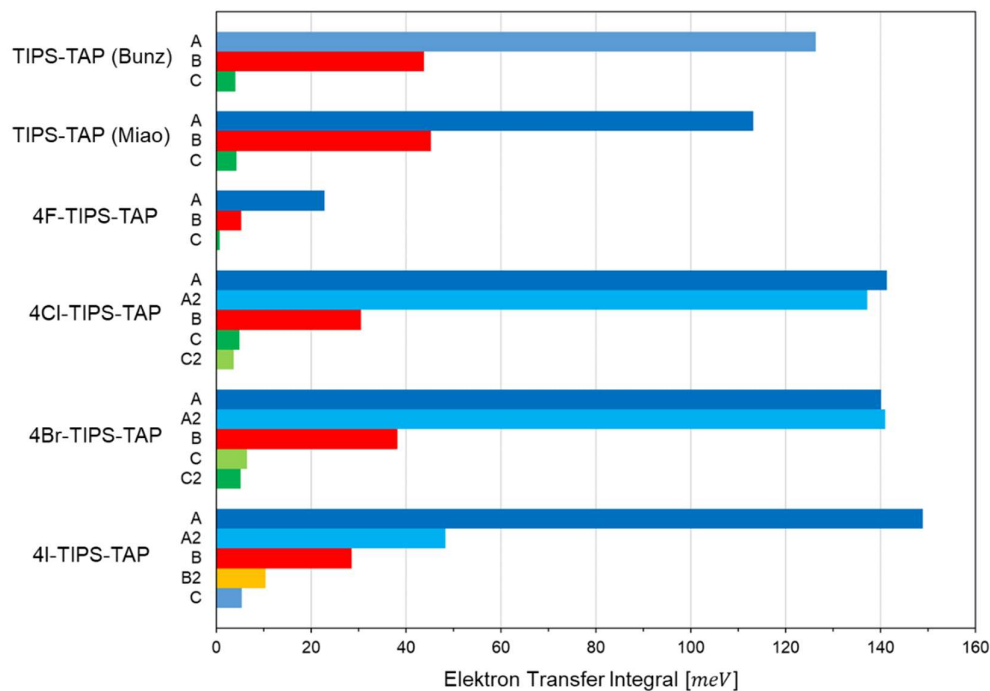


Figure 6.15. Electron transfer integrals of different dimers in the crystals of TIPS-TAP and 4F-, 4Cl-, 4Br-, 4I-TIPS-TAP.

In Table 6.1, results are summarized, and detailed information about the crystal structure is added. In Figure 6.16, the axes used are illustrated exemplarily for TIPS-TAP. The axes for other dimers were chosen similarly.

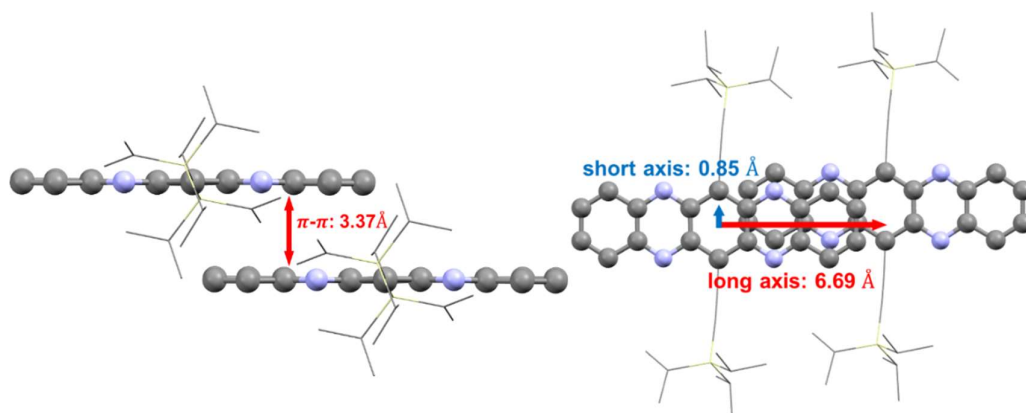


Figure 6.16. Illustration of the axis used for the measurement of the π - π distance and the displacement of the π -stacking.

Table 6.1. Displacement of the π -stacking, π - π distances, distances between the center of mass r and the transfer integrals V for different dimers in the crystal structure of TIPS-TAP and 4F-, 4Cl-, 4Br-, 4I-TIPS-TAP.

		Displacement of the π -stacking [\AA]		π - π distance [\AA]	r [\AA]	V [meV]
		along the short axis	along the long axis			
TIPS-TAP (Bunz)	A	6.69	0.85	3.37	7.53	126.30
	B	9.24	1.73	3.26	9.96	43.78
	C	15.93	0.89	0.12	15.95	3.97
TIPS-TAP (Miao)	A	6.75	0.94	3.38	7.61	113.13
	B	9.26	1.70	3.28	9.96	45.22
	C	16.01	0.75	0.10	16.02	4.21
4F-TIPS-TAP	A	7.35	1.10	3.33	8.13	22.77
	B	9.57	1.76	3.26	10.22	5.22
	C	16.92	0.67	0.07	16.93	0.68
4Cl-TIPS-TAP	A	6.25	0.27	3.42	7.19	141.35
	A2	6.30	0.70	3.40	7.13	137.24
	B	11.76	1.57	3.30	12.32	30.44
	C	18.02	1.30	0.12	18.04	4.88
	C2	18.06	2.27	0.09	18.23	3.67
4Br-TIPS-TAP	A	6.30	0.11	3.40	7.22	140.14
	A2	6.33	0.69	3.42	7.16	140.96
	B	12.02	1.53	3.40	12.58	38.22
	C	18.32	1.42	0.00	18.37	6.51
	C2	18.34	2.22	0.03	18.48	5.15
4I-TIPS-TAP	A	6.21	0.48	3.40	7.13	148.92
	A2	7.51	1.11	3.44	8.17	48.23
	B	12.61	1.43	3.66	13.16	28.51
	B2	11.31	0.80	3.87	12.18	10.35
	C	18.82	1.91	0.07	18.92	5.38

Transfer integrals along the same pathway share the same letter, as shown in Figure 6.9 to Figure 6.14. The two examined crystal structures of TIPS-TAP show different transfer integrals for pathway A. This should not be the case since they are the same molecules, but as shown in Table 6.1, the displacement π -stacking and the π - π distance in crystal measured by Bunz *et al.* are slightly different. As pointed out by Miao *et al.*, the transfer integral is very sensitive to subtle changes in the 2D π -stacking which is likely the reason for the difference. This sensitivity is likely due to the fact that the electronic coupling is not related to the spatial overlap between adjacent molecules but rather to the degree of wavefunction overlap.^[3] The electronic coupling can often be estimated by only taking the LUMO (or HOMO) of a dimer into account. In that scenario, the extreme dependence on the π -stacking can be rationalized by imagining the bonding-antibonding pattern.^[3, 242] For example, when displacing two dimers along the long axis, minima and maxima of the transfer integral could be reached, while the mean amplitude continuously decreases and reaches zero when there is no more spatial overlap. The difference in the measured crystal structure could be caused by the inaccuracy of x-ray crystallography, which is why only crystal structures with very high quality can be used to estimate transfer integrals.

4F-TIPS-TAP is another prime example of the sensitivity of the transfer integral. It has the smallest π - π distance while showing by far the smallest transfer integrals. Since smaller π - π distances should result in larger transfer integrals, the importance of the π -displacements is shown again. These are quite different from all other derivatives, and this kind of displacement is likely particularly unfavorable for wavefunction overlap.

4Cl-TIPS-TAP and 4Br-TIPS-TAP both exhibit a slightly larger π - π distances as TIPS-TAP; thus, smaller transfer integrals could be expected. However, the π -displacements are different and lead to a greater spatial overlap and, in this case, probably also to a better wavefunction overlap for A dimers since transfer integrals are larger. The B dimers have a larger π - π distance and less spatial overlap, which indeed leads to smaller transfer integrals compared to B dimers of TIPS-TAP.

The A dimer of 4I-TIPS-TAP has the most significant transfer integral, thus exhibiting the best wavefunction overlap out of all examined dimers. This might be partly due to the smallest π -displacement along the long axis. However, as mentioned above, while spatial overlap is necessary, it does not guarantee considerable wavefunction overlap.

The transfer integrals of TIPS-TAP and 4F-,4Cl-TIPS-TAP were calculated previously and are comparable to our values, though being smaller in general.^[10] However, the same trend could be observed; that is, 4F-TIPS-TAP shows very small transfer integrals, and 4Cl-TIPS-TAP exhibits the largest. Smaller transfer integrals are due to the different methods being used, but since both methods take significant approximations, the exact reason is not clear yet.

6.5.2 Reorganization Energies

The geometries of the neutral and anionic TIPS-TAP, 4F-, 4Cl-, 4Br-, 4I-TIPS-TAP were optimized, and the respective energies were obtained subsequently. Then the energies of the neutral states at the optimized anionic geometries as well as the anionic states at the optimized neutral geometries were calculated. The results are shown in Table 6.2.

Table 6.2. Energies of the optimized geometries for the neutral $E_{(M)}$ and anionic $E_{(M^-)}$ state, the energies of the neutral states at the optimized anionic geometries $E_{(M^-)}$ and the energies of the anionic states at the optimized neutral geometries $E_{(M)}$.

	$E_{(M)}$ [a. u.]	$E_{(M^-)}$ [a. u.]	$E_{(M^-)}$ [a. u.]	$E_{(M)}$ [a. u.]
TIPS-TAP	-2352.42641874	-2352.51252572	-2352.42273710	-2352.51630472
4F-TIPS-TAP	-2749.33912462	-2749.43324885	-2749.33479210	-2749.43769946
4Cl-TIPS-TAP	-4190.78791297	-4190.89217492	-4190.78428483	-4190.89596497
4Br-TIPS-TAP	-12636.8266817	-12636.9310069	-12636.8234171	-12636.9346194
4I-TIPS-TAP	-2395.470221	-2395.576076	-2395.466939	-2395.579387

The reorganization energies of TIPS-TAP and 4F-, 4Cl-, 4Br-, 4I-TIPS-TAP were calculated with

$$\lambda = \lambda_1 + \lambda_2, \quad (6.5.24)$$

$$\lambda_1 = E_{(M^-)} - E_{(M)}. \quad (6.5.25)$$

$$\lambda_2 = E_{(M)}^- - E_{(M^-)}^-. \quad (6.5.26)$$

The obtained reorganization energies are shown in Table 6.3.

Table 6.3. Reorganization energies of the neutral state λ_1 , the anionic state λ_2 and the total reorganization energies λ .

	λ_1 [meV]	λ_2 [meV]	λ [meV]
TIPS-TAP	100.18	102.83	203.01
4F-TIPS-TAP	117.89	121.11	239.00
4Cl-TIPS-TAP	98.73	103.13	201.86
4Br-TIPS-TAP	88.83	98.30	187.14
4I-TIPS-TAP	89.31	90.10	179.41

The reorganization energies for TIPS-TAP and 4F-/4Cl-TIPS-TAP match the previously reported results.^[108] The increased reorganization energy of 4F-TIPS-TAP was attributed to the enhancement of breathing, stretching vibrations of its pentacene framework, and the additional stretching of C-F bonds.^[108] On the contrary, four Cl substituents seem to suppress the breathing and stretching vibration of the pentacene framework. The weaker C-Cl bond further attenuates the additional contribution to the reorganization energy from the halogen-C bond, which leads to a rather similar reorganization energy as TIPS-TAP.^[108]

4Br-TIPS-TAP is the first halogenated TIPS-TAP, which has reorganization energy considerably lower than TIPS-TAP itself. This may be due to the weaker C-Br bonds

and further suppression of other vibrations. 4I-TIPS-Tap has the lowest reorganization energy from all of the symmetric tetra halogenated TIPS-TAPs, which could be attributed to further weaker C-halogen bond. Weaker C-halogen bonds lead in the case of 4X-TIPS-TAP to smaller reorganization energies, which supports earlier findings^[10,44], but further contributions cannot be excluded.

6.5.3 Marcus Electron Transfer Rates

With the obtained reorganization energies and transfer integrals, the Marcus rate equation^[228]

$$W = \frac{V^2}{\hbar} \left(\frac{\pi}{\lambda k_B T} \right)^{0.5} e^{-\frac{\lambda}{4k_B T}}, \quad (6.5.27)$$

was used to calculate electron transfer rates displayed in Table 6.4. As indicated by the formula, large transfer integrals and small reorganization energies will result in a large electron transfer rate. Therefore, dimer A in 4I-TIPS-TAP has the largest electron transfer rate since it has the largest transfer integral, and 4I-TIPS-TAP has the lowest reorganization energy. 4F-TIPS-TAP has especially low electron transfer rates due to the high reorganization energy and small transfer integrals.

Table 6.4. Resulting electron transfer rates for different electron pathways in the crystal structures of TIPS-TAP and 4F-, 4Cl-, 4Br-, 4I-TIPS-TAP.

		V [meV]	λ [meV]	W [s^{-1}]
TIPS-TAP (Bunz)	A	-126.30	203.01	8.24×10^{13}
	B	-43.78		9.91×10^{12}
	C	-3.97		8.15×10^{10}
TIPS-TAP (Miao)	A	113.13	203.01	6.61×10^{13}
	B	-45.22		1.06×10^{13}
	C	4.21		9.15×10^{10}
4F-TIPS-TAP	A	-22.77	239.00	1.74×10^{12}
	B	5.22		9.14×10^{10}
	C	0.68		1.55×10^9
4Cl-TIPS-TAP	A	-141.35	201.86	1.05×10^{14}
	A2	137.24		9.87×10^{13}
	B	30.44		4.86×10^{12}
	C	4.88		1.25×10^{11}
	C2	3.67		7.04×10^{10}
4Br-TIPS-TAP	A	-140.14	187.14	1.23×10^{14}
	A2	-140.96		1.25×10^{14}
	B	38.22		9.18×10^{12}
	C	6.51		2.66×10^{11}
	C2	5.15		1.67×10^{11}
4I-TIPS-TAP	A	148.92	179.41	1.53×10^{14}
	A2	-48.23		1.61×10^{13}
	B	-28.51		5.62×10^{12}
	B2	10.35		7.41×10^{11}
	C	-5.38		2.00×10^{11}

6.5.4 Electron Mobilities

The diffusion coefficient D could be estimated with^[108, 222]

$$D \approx \frac{1}{2n} \sum_i r_i^2 W_i P_i, \quad (6.5.28)$$

$$P_i = \frac{W_i}{\sum_i W_i}. \quad (6.5.29)$$

Table 6.5 shows the calculated diffusion coefficients for the diffusion in all directions (3D) and the diffusion in the plane of the brickwork stacked molecules (2D). This plane is close to the plane formed by the long and the π - π axis defined in Figure 6.16. However, the plane is slightly sloped because of the π -displacement along the short axis. Since there is no notable electron transport perpendicular to this plane, the 3D diffusion coefficient is exactly 2/3 of the 2D diffusion coefficient. The electron transfer rates were taken from Table 6.4, and the differences between the center of masses were taken from Table 6.1. Since electron transfer rates are calculated with transfer integrals, they change for every dimer. As explained in section 6.5.1, the electron transfer rates along one pathway can be different. This is the case for 4Cl-, 4Br- and 4I-TIPS-TAP. Here, the transfer rates and the center of mass distances along one pathway were averaged.

Table 6.5. Diffusion coefficients for the diffusion in the plane of the stacked molecules $D(2D)$ and for the diffusion in all directions $D(3D)$.

	$D(2D)$ [$10^1 \text{ cm}^2 \text{ s}^{-1}$]	$D(3D)$ [$10^1 \text{ cm}^2 \text{ s}^{-1}$]
TIPS-TAP (Bunz)	1.07	0.71
TIPS-TAP (Miao)	0.86	0.57
4F-TIPS-TAP	0.03	0.02
4Cl-TIPS-TAP	1.25	0.84
4Br-TIPS-TAP	1.52	1.01
4I-TIPS-TAP	1.80	1.20

The drift mobility of charge hopping μ was evaluated with the Einstein-Smoluchowski equation below^[3], which also gives the bulk mobility of the crystals. The results are summarized in

Table 6.6.

$$\mu = \frac{e}{k_B T} D. \quad (6.5.30)$$

Table 6.6. Electron mobilities in the plane of the brick wall stacked molecules μ (**2D**) and the general electron mobility of the entire crystal μ (**3D**).

	μ (2D) [$cm^2 V^{-1} s^{-1}$]	μ (3D) [$cm^2 V^{-1} s^{-1}$]
TIPS-TAP (Bunz)	4.16	2.78
TIPS-TAP (Miao)	3.35	2.24
4F-TIPS-TAP	0.11	0.07
4Cl-TIPS-TAP	4.89	3.26
4Br-TIPS-TAP	5.91	3.94
4I-TIPS-TAP	7.03	4.69

6.6 Conclusion and Outlook

The aim of this work is to examine important electron transfer properties of TIPS-TAP and 4F-, 4Cl-, 4Br-, 4I-TIPS-TAP on a theoretical basis. Particular attention was paid to the bromine and iodine derivatives since no experimental data is available yet. First of all, transfer integrals and reorganization energies of TIPS-TAP and 4F-, 4Cl-, 4Br-, 4I-TIPS-TAP were calculated. The substitution with bromine seems to fine-tune the crystal structure in a similar way as chlorine, since they are, as well as the transfer integrals, very similar. 4I-TIPS-TAP has a more complex crystal structure but also shows the largest transfer integral. Reorganization energies follow the trend: 4F-TIPS-TAP > TIPS-TAP \approx 4Cl-TIPS-TAP > 4Br-TIPS-TAP > 4I-TIPS-TAP, which further indicates that lowering the carbon-halogen bond strength can be used to reduce the reorganization energy. The fact that halogen atoms can fine-tune the crystal structure to increase the electronic coupling and that lowering the C-halogen bond strength

decreases the reorganization energy should be considered when designing new semiconductors.

The estimated electron mobility of 4Br- and 4I-TIPS-TAP surpasses 4Cl-TIPS-TAP, which shows their potential as semiconductors. However, many approximations were used to calculate the electron mobility. For a better estimation of the electron mobility, the diffusion coefficient should be calculated through a Monte Carlo simulation, the tunneling effect should also be taken into account by estimating vibronic coupling, and dynamic disorder effect should be included by molecular dynamics. By incorporating those effects, the prediction of electron mobility should be much more accurate. Nevertheless, since not all effects can be considered in theoretical simulations, the experimental data is also very important. There might be new effects that need to be considered when estimating the electron mobility of 4Br- and 4I-TIPS-TAP.

Although not all the effects were considered in this work, the trend of the electron mobility, as demonstrated above, matches existing experimental values. Therefore, 4Br- and 4I-TIPS-TAP should definitely be tested since they might show even larger electron mobilities than 4Cl-TIPS-TAP, which sets the current record for charge mobility in n-type semiconductors.

7. Global Summary and Outlook

In the present thesis, a series of novel N-heteropolycycles has been studied using various quantum chemical methods. Particular interest lies in their molecular properties, electron transport, and SF performance. In **chapter 3**, I have demonstrated that PTDs are promising SF materials by calculating the energies of low-lying excited states and electronic couplings in the diabatic representation. This approach would be extended to other materials such as perfluorobutyldicyanoperylene carboxydiimide and derivatives of tetraazaperopyrene, which have been recently synthesized. On the other hand, vibronic coupling plays an essential role in SF, and this would be taken into account in future work. After all, SF is a dynamics process, a quantum dynamics simulation with the multi-configuration time-dependent Hartree (MCTDH) algorithm is also in progress. In **chapter 4**, I have simulated ESAs of various excited states (S_1 , T_1 , S_0T_1 , and $^1(T_1T_1)$) involved in SF, based on single-reference DFT based approach. The results showed good agreement with the experiment. Future work will include vibrational effects in the simulation of absorption spectra, other excited states such as CT and quintet states will also be considered. In **chapter 5**, I have shown that the negative charges of N-heteroacenes are stable with respect to electron loss. A natural question is whether their excited states are still stable against electron emission? If they are not stable, what are their lifetimes? These are the future plan for studying the radicals of N-heteropolycycles. In **chapter 6**, the excellent performance of electron transport has been proved on halogenated TAP, especially for 4Br-TIPS-TAP and 4I-TIPS-TAP. However, the calculated charge mobilities can not be directly compared with the experimental values yet, since effects such as nuclear tunneling and dynamic disorder are ignored in the calculations. Molecular dynamics and kinetic Monte Carlo simulations are also required in future work.

Acknowledgments

First of all, I would like to express my sincere gratitude to Prof. Andreas Dreuw, who is not only my supervisor but also my doctoral father. Thank you for all of your support, patience, concern, and encouragement during my Ph.D. study. Your guidance and immense knowledge helped me in all the time of research and writing of this thesis. More importantly, your sense of humor and your jokes always made my day. I could not have imagined having a better advisor and mentor for my Ph.D. study.

My sincere thanks also go to Ellen Vogel, for taking care of my life, contract and paperwork in Germany. Thank you for everything!

I am also pleased to say thank you to my senior colleagues, Dr. Dirk Rehn, Dr. Tim Stauch, Dr. Jan Wenzel, Dr. Matthias Schneider, Dr. Maximilian Krämer, Dr. Michael Herbst, Dr. Jan Mewes, Dr. Stefanie Mewes, Dr. Stefan Prager, Dr. Tobias Setzer, Dr. Daniel Lefrancois, Dr. Felix Plasser, Dr. Chong Yang and Dr. Thomas Fransson. Thank you all for always taking care of me like big brothers and sisters.

I would always remember my fellow officemates, Dr. Mercedes Bohnwagner, Reena Sen and Maximilien Ambroise, for the fun-time we spent together and continuous moral support for me. It was really lovely to share the same office with you!

For the rest members of the group of Dreuw (Michael Rogo Opata, Marvin Hoffmann, Manuel Hodecker, Adrian Dempwolff, Benjamin Thomitzni, Sebastian Thielen and Maximilian Scheurer), I wish to thank you all for the great working atmosphere and useful discussions. It was much fun to work with you guys!

I express my thanks to Prof. Marcus Motzkus, Prof. Uwe H. F. Bunz, Dr. Tiago Buckup, Dr. Lie Ji, Dr. J. Luis Perez Lustres, Nicolás Alagna, and Nikolaus Wollscheid, for the excellent experimental work and collaboration.

I would like to acknowledge the Chinese Scholarship Council (CSC), Deutsche Forschungsgemeinschaft (DFG), and the University of Heidelberg for financial support of my Ph.D. study.

Last but not least, I am very grateful to my parents, grandparents, family, and friends in my hometown, who always care for me and give me enough support. I consider myself nothing without you.

References

- [1]. Hsu, C., The electronic couplings in electron transfer and excitation energy transfer. *Accounts of chemical research*, 2009. 42(4): p. 509-518.
- [2]. Anthony, J.E., Functionalized Acenes and Heteroacenes for Organic Electronics. *Chemical Reviews*, 2006. 106(12): p. 5028-5048.
- [3]. Coropceanu, V., J. Cornil, D.A. Da Silva Filho, Y. Olivier, R. Silbey, and J. Brédas, Charge Transport in Organic Semiconductors. *Chemical Reviews*, 2007. 107(4): p. 926-952.
- [4]. Anthony, J.E., The Larger Acenes: Versatile Organic Semiconductors. *Angewandte Chemie International Edition*, 2008. 47(3): p. 452-483.
- [5]. Chen, S., L. Deng, J. Xie, L. Peng, L. Xie, Q. Fan, and W. Huang, Recent Developments in Top-Emitting Organic Light-Emitting Diodes. *Advanced Materials*, 2010. 22(46): p. 5227-5239.
- [6]. Sasabe, H. and J. Kido, Development of high performance OLEDs for general lighting. *Journal of Materials Chemistry C*, 2013. 1(9): p. 1699-1707.
- [7]. Clarke, T.M. and J.R. Durrant, Charge Photogeneration in Organic Solar Cells. *Chemical Reviews*, 2010. 110(11): p. 6736-6767.
- [8]. Ameri, T., N. Li and C.J. Brabec, Highly efficient organic tandem solar cells: a follow up review. *Energy & Environmental Science*, 2013. 6(8): p. 2390-2413.
- [9]. Smith, M.B. and J. Michl, Singlet Fission. *Chemical Reviews*, 2010. 110(11): p. 6891-6936.
- [10]. Smith, M.B. and J. Michl, Recent Advances in Singlet Fission. *Annual Review of Physical Chemistry*, 2013. 64(1): p. 361-386.
- [11]. Shirakawa, H., E.J. Louis, A.G. MacDiarmid, C.K. Chiang, and A.J. Heeger, Synthesis of electrically conducting organic polymers: halogen derivatives of polyacetylene, (CH). *Journal of the Chemical Society, Chemical Communications*, 1977(16): p. 578-580.
- [12]. Shuai, Z., L. Wang and C. Song, Theory of charge transport in carbon electronic materials. 2012: Springer Science & Business Media.
- [13]. Winkler, M. and K.N. Houk, Nitrogen-Rich Oligoacenes: Candidates for n-Channel Organic Semiconductors. *Journal of the American Chemical Society*, 2007. 129(6): p. 1805-1815.
- [14]. Miao, S., A.L. Appleton, N. Berger, S. Barlow, S.R. Marder, K.I. Hardcastle, and U.H.F. Bunz, 6,13-Diethynyl-5,7,12,14-tetraazapentacene. *Chemistry - A European Journal*, 2009. 15(20): p. 4990-4993.

- [15]. Shockley, W. and H.J. Queisser, Detailed Balance Limit of Efficiency of p-n Junction Solar Cells. *Journal of Applied Physics*, 1961. 32(3): p. 510-519.
- [16]. Hanna, M.C. and A.J. Nozik, Solar conversion efficiency of photovoltaic and photoelectrolysis cells with carrier multiplication absorbers. *Journal of Applied Physics*, 2006. 100(7): p. 074510.
- [17]. Krishnapriya, K.C., A.J. Musser and S. Patil, Molecular Design Strategies for Efficient Intramolecular Singlet Exciton Fission. *ACS Energy Letters*, 2019. 4(1): p. 192-202.
- [18]. Miyata, K., F.S. Conrad-Burton, F.L. Geyer, and X.Y. Zhu, Triplet Pair States in Singlet Fission. *Chemical Reviews*, 2019. 119(6): p. 4261-4292.
- [19]. Japahuge, A. and T. Zeng, Theoretical Studies of Singlet Fission: Searching for Materials and Exploring Mechanisms. *ChemPlusChem*, 2018: p. n/a-n/a.
- [20]. Szabo, A. and N.S. Ostlund, *Modern quantum chemistry: introduction to advanced electronic structure theory*. 2012: Courier Corporation.
- [21]. Piela, L., *Ideas of quantum chemistry*. 2006: Elsevier.
- [22]. Foresman, J.B., M. Head-Gordon, J.A. Pople, and M.J. Frisch, Toward a systematic molecular orbital theory for excited states. *The Journal of Physical Chemistry*, 1992. 96(1): p. 135-149.
- [23]. Dreuw, A. and M. Head-Gordon, Single-Reference ab Initio Methods for the Calculation of Excited States of Large Molecules. *Chemical Reviews*, 2005. 105(11): p. 4009-4037.
- [24]. Dreuw, A., J.L. Weisman and M. Head-Gordon, Long-range charge-transfer excited states in time-dependent density functional theory require non-local exchange. *The Journal of Chemical Physics*, 2003. 119(6): p. 2943-2946.
- [25]. Marques, M.A., N.T. Maitra, F.M. Nogueira, E.K. Gross, and A. Rubio, *Fundamentals of time-dependent density functional theory*. Vol. 837. 2012: Springer Science & Business Media.
- [26]. May, V. and K. Oliver, *Charge and energy transfer dynamics in molecular systems*. 2008: John Wiley & Sons.
- [27]. Köppel, H., W. Domcke and L.S. Cederbaum, Multimode Molecular Dynamics Beyond the Born-Oppenheimer Approximation. *Advances in Chemical Physics*, Volume 57, 1984: p. 59-246.
- [28]. You, Z. and C. Hsu, Theory and calculation for the electronic coupling in excitation energy transfer. *International Journal of Quantum Chemistry*, 2014. 114(2): p. 102-115.
- [29]. Van Voorhis, T., T. Kowalczyk, B. Kaduk, L. Wang, C. Cheng, and Q. Wu, The Diabatic Picture of Electron Transfer, Reaction Barriers, and Molecular Dynamics. *Annual Review of Physical Chemistry*, 2010. 61(1): p. 149-170.

- [30]. Wu, Q., C. Cheng and T. Van Voorhis, Configuration interaction based on constrained density functional theory: A multireference method. *The Journal of Chemical Physics*, 2007. 127(16): p. 1641-19.
- [31]. Lewis, N.S. and D.G. Nocera, Powering the planet: Chemical challenges in solar energy utilization. *Proceedings of the National Academy of Sciences*, 2006. 103(43): p. 15729.
- [32]. Grätzel, M., Photoelectrochemical cells. *Nature*, 2001. 414(6861): p. 338-344.
- [33]. Paulus, F., J.U. Engelhart, P.E. Hopkinson, C. Schimpf, A. Leineweber, H. Sirringhaus, Y. Vaynzof, and U.H.F. Bunz, The effect of tuning the microstructure of TIPS-tetraazapentacene on the performance of solution processed thin film transistors. *Journal of Materials Chemistry C*, 2016. 4(6): p. 1194-1200.
- [34]. Hahn, L., A. Hermannsdorfer, B. Günther, T. Wesp, B. Bühler, U. Zschieschang, H. Wadepohl, H. Klauk, and L.H. Gade, (Oligo-)Thiophene Functionalized Tetraazaperopyrenes: Donor-Acceptor Dyes and Ambipolar Organic Semiconductors. *The Journal of Organic Chemistry*, 2017. 82(23): p. 12492-12502.
- [35]. Leibold, D., V. Lami, Y.J. Hofstetter, D. Becker Koch, A. Weu, P. Biegger, F. Paulus, U.H.F. Bunz, P.E. Hopkinson, A.A. Bakulin, and Y. Vaynzof, Triptycenyphenazino-thiadiazole as acceptor in organic bulk-heterojunction solar cells. *Organic Electronics*, 2018. 57: p. 285-291.
- [36]. Singh, S., W.J. Jones, W. Siebrand, B.P. Stoicheff, and W.G. Schneider, Laser Generation of Excitons and Fluorescence in Anthracene Crystals. *The Journal of Chemical Physics*, 1965. 42(1): p. 330-342.
- [37]. Swenberg, C.E. and W.T. Stacy, Bimolecular radiationless transitions in crystalline tetracene. *Chemical Physics Letters*, 1968. 2(5): p. 327-328.
- [38]. Yarnus, L., J. Rosenthal and M. Chopp, EPR of triplet excitons in tetracene crystals: spin polarization and the role of singlet exciton fission. *Chemical Physics Letters*, 1972. 16(3): p. 477-481.
- [39]. Chan, W., M. Ligges and X. Zhu, The energy barrier in singlet fission can be overcome through coherent coupling and entropic gain. *Nature chemistry*, 2012. 4(10): p. 840-845.
- [40]. Chan, W., M. Ligges, A. Jailaubekov, L. Kaake, L. Miaja-Avila, and X.Y. Zhu, Observing the Multiexciton State in Singlet Fission and Ensuing Ultrafast Multielectron Transfer. *Science*, 2011. 334(6062): p. 1541.
- [41]. Tomkiewicz, Y., R.P. Groff and P. Avakian, Spectroscopic Approach to Energetics of Exciton Fission and Fusion in Tetracene Crystals. *The Journal of Chemical Physics*, 1971. 54(10): p. 4504-4507.
- [42]. Stern, H.L., A. Cheminal, S.R. Yost, K. Broch, S.L. Bayliss, K. Chen, M. Tabachnyk, K. Thorley, N. Greenham, J.M. Hodgkiss, J. Anthony, M. Head-Gordon, A.J. Musser, A. Rao, and R.H. Friend, Vibronically coherent ultrafast triplet-pair formation and subsequent thermally activated dissociation control efficient endothermic singlet fission. *Nature Chemistry*, 2017. 9: p. 1205.

- [43]. Burdett, J.J. and C.J. Bardeen, Quantum Beats in Crystalline Tetracene Delayed Fluorescence Due to Triplet Pair Coherences Produced by Direct Singlet Fission. *Journal of the American Chemical Society*, 2012. 134(20): p. 8597-8607.
- [44]. Wilson, M.W.B., A. Rao, K. Johnson, S. Gélinas, R. di Pietro, J. Clark, and R.H. Friend, Temperature-Independent Singlet Exciton Fission in Tetracene. *Journal of the American Chemical Society*, 2013. 135(44): p. 16680-16688.
- [45]. Kolomeisky, A.B., X. Feng and A.I. Krylov, A Simple Kinetic Model for Singlet Fission: A Role of Electronic and Entropic Contributions to Macroscopic Rates. *The Journal of Physical Chemistry C*, 2014. 118(10): p. 5188-5195.
- [46]. Müller, A.M., Y.S. Avlasevich, W.W. Schoeller, K. Müllen, and C.J. Bardeen, Exciton Fission and Fusion in Bis(tetracene) Molecules with Different Covalent Linker Structures. *Journal of the American Chemical Society*, 2007. 129(46): p. 14240-14250.
- [47]. Ito, S., T. Nagami and M. Nakano, Design Principles of Electronic Couplings for Intramolecular Singlet Fission in Covalently-Linked Systems. *The Journal of Physical Chemistry A*, 2016. 120(31): p. 6236-6241.
- [48]. Korovina, N.V., S. Das, Z. Nett, X. Feng, J. Joy, R. Haiges, A.I. Krylov, S.E. Bradforth, and M.E. Thompson, Singlet Fission in a Covalently Linked Cofacial Alkynyltetracene Dimer. *Journal of the American Chemical Society*, 2016. 138(2): p. 617-627.
- [49]. Korovina, N.V., J. Joy, X. Feng, C. Feltenberger, A.I. Krylov, S.E. Bradforth, and M.E. Thompson, Linker-Dependent Singlet Fission in Tetracene Dimers. *Journal of the American Chemical Society*, 2018. 140(32): p. 10179-10190.
- [50]. Rao, A., M.W.B. Wilson, J.M. Hodgkiss, S. Albert-Seifried, H. Bäessler, and R.H. Friend, Exciton Fission and Charge Generation via Triplet Excitons in Pentacene/C60 Bilayers. *Journal of the American Chemical Society*, 2010. 132(36): p. 12698-12703.
- [51]. Jundt, C., G. Klein, B. Sipp, J. Le Moigne, M. Joucla, and A.A. Villaeys, Exciton dynamics in pentacene thin films studied by pump-probe spectroscopy. *Chemical Physics Letters*, 1995. 241(1): p. 84-88.
- [52]. Pugliesi, I., B. Nickel, S. Lochbrunner, and H. Marciniak, Ultrafast singlet and triplet dynamics in microcrystalline pentacene films. *Physical Review B*, 2009. 79(23): p. 235318.
- [53]. Thorsmølle, V.K., R.D. Averitt, J. Demsar, D.L. Smith, S. Tretiak, R.L. Martin, X. Chi, B.K. Crone, A.P. Ramirez, and A.J. Taylor, Morphology Effectively Controls Singlet-Triplet Exciton Relaxation and Charge Transport in Organic Semiconductors. *Physical Review Letters*, 2009. 102(1): p. 017401.

- [54]. Wilson, M.W.B., A. Rao, J. Clark, R.S.S. Kumar, D. Brida, G. Cerullo, and R.H. Friend, Ultrafast Dynamics of Exciton Fission in Polycrystalline Pentacene. *Journal of the American Chemical Society*, 2011. 133(31): p. 11830-11833.
- [55]. Sanders, S.N., E. Kumarasamy, A.B. Pun, M.T. Trinh, B. Choi, J. Xia, E.J. Taffet, J.Z. Low, J.R. Miller, X. Roy, X.Y. Zhu, M.L. Steigerwald, M.Y. Sfeir, and L.M. Campos, Quantitative Intramolecular Singlet Fission in Bipentacenes. *Journal of the American Chemical Society*, 2015. 137(28): p. 8965-8972.
- [56]. Zirzmeier, J., D. Lehnerr, P.B. Coto, E.T. Chernick, R. Casillas, B.S. Basel, M. Thoss, R.R. Tykwinski, and D.M. Guldi, Singlet fission in pentacene dimers. *Proceedings of the National Academy of Sciences*, 2015. 112(17): p. 5325 -5330.
- [57]. Lee, J., P. Jadhav and M.A. Baldo, High efficiency organic multilayer photodetectors based on singlet exciton fission. *Applied Physics Letters*, 2009. 95(3): p. 33301.
- [58]. Congreve, D.N., J. Lee, N.J. Thompson, E. Hontz, S.R. Yost, P.D. Reusswig, M.E. Bahlke, S. Reineke, T.V. Voorhis, and M.A. Baldo, External Quantum Efficiency Above 100% in a Singlet-Exciton-Fission-Based Organic Photovoltaic Cell. *Science*, 2013. 340(6130): p. 334-337.
- [59]. Anthony, J.E., J.S. Brooks, D.L. Eaton, and S.R. Parkin, Functionalized Pentacene: Improved Electronic Properties from Control of Solid-State Order. *Journal of the American Chemical Society*, 2001. 123(38): p. 9482-9483.
- [60]. Herz, J., T. Buckup, F. Paulus, J. Engelhart, U.H.F. Bunz, and M. Motzkus, Acceleration of Singlet Fission in an Aza-Derivative of TIPS-Pentacene. *The Journal of Physical Chemistry Letters*, 2014. 5(14): p. 2425-2430.
- [61]. Herz, J., T. Buckup, F. Paulus, J.U. Engelhart, U.H.F. Bunz, and M. Motzkus, Unveiling Singlet Fission Mediating States in TIPS-pentacene and its Aza Derivatives. *The Journal of Physical Chemistry A*, 2015. 119(25): p. 6602-6610.
- [62]. Pensack, R.D., A.J. Tilley, S.R. Parkin, T.S. Lee, M.M. Payne, D. Gao, A.A. Jahnke, D.G. Oblinsky, P. Li, J.E. Anthony, D.S. Seferos, and G.D. Scholes, Exciton Delocalization Drives Rapid Singlet Fission in Nanoparticles of Acene Derivatives. *Journal of the American Chemical Society*, 2015. 137(21): p. 6790-6803.
- [63]. Casanova, D., Theoretical Modeling of Singlet Fission. *Chemical Reviews*, 2018. 118(15): p. 7164-7207.
- [64]. Minami, T., S. Ito and M. Nakano, Fundamental of Diradical-Character-Based Molecular Design for Singlet Fission. *The Journal of Physical Chemistry Letters*, 2013. 4(13): p. 2133-2137.
- [65]. Minami, T. and M. Nakano, Diradical Character View of Singlet Fission. *The Journal of Physical Chemistry Letters*, 2012. 3(2): p. 145-150.

- [66]. Nakano, M., N. Nakagawa, S. Ohta, R. Kishi, T. Kubo, K. Kamada, K. Ohta, B. Champagne, E. Botek, H. Takahashi, S. Furukawa, Y. Morita, K. Nakasuji, and K. Yamaguchi, Second hyperpolarizabilities of polycyclic diphenalenyl radicals: Effects of para/ortho-quinoid structures and central ring modification. *Chemical Physics Letters*, 2006. 429(1): p. 174-179.
- [67]. Chen, Y., L. Shen and X. Li, Effects of Heteroatoms of Tetracene and Pentacene Derivatives on Their Stability and Singlet Fission. *The Journal of Physical Chemistry A*, 2014. 118(30): p. 5700-5708.
- [68]. Fiebig, M., M. Huth, S. Schiefer, B. Nickel, F. Selmaier, S. Lochbrunner, and H. Marciniak, Ultrafast Exciton Relaxation in Microcrystalline Pentacene Films. *Physical Review Letters*, 2007. 99(17): p. 176402.
- [69]. Sakuma, T., H. Sakai, Y. Araki, T. Mori, T. Wada, N.V. Tkachenko, and T. Hasobe, Long-Lived Triplet Excited States of Bent-Shaped Pentacene Dimers by Intramolecular Singlet Fission. *The Journal of Physical Chemistry A*, 2016. 120(11): p. 1867-1875.
- [70]. Sanders, S.N., E. Kumarasamy, A.B. Pun, K. Appavoo, M.L. Steigerwald, L.M. Campos, and M.Y. Sfeir, Exciton Correlations in Intramolecular Singlet Fission. *Journal of the American Chemical Society*, 2016. 138(23): p. 7289-7297.
- [71]. Sanders, S.N., E. Kumarasamy, A.B. Pun, M.L. Steigerwald, M.Y. Sfeir, and L.M. Campos, Intramolecular Singlet Fission in Oligoacene Heterodimers. *Angewandte Chemie International Edition*, 2016. 55(10): p. 3373-3377.
- [72]. Stern, H.L., A.J. Musser, S. Gelinias, P. Parkinson, L.M. Herz, M.J. Bruzek, J. Anthony, R.H. Friend, and B.J. Walker, Identification of a triplet pair intermediate in singlet exciton fission in solution. *Proceedings of the National Academy of Sciences*, 2015. 112(25): p. 7656 -7661.
- [73]. Walker, B.J., A.J. Musser, D. Beljonne, and R.H. Friend, Singlet exciton fission in solution. *Nature Chemistry*, 2013. 5(12): p. 1019-1024.
- [74]. Zirzmeier, J., R. Casillas, S.R. Reddy, P.B. Coto, D. Lehnerr, E.T. Chernick, I. Papadopoulos, M. Thoss, R.R. Tykwinski, and D.M. Guldi, Solution-based intramolecular singlet fission in cross-conjugated pentacene dimers. *Nanoscale*, 2016. 8(19): p. 10113-10123.
- [75]. Wu, Y., Y. Wang, J. Chen, G. Zhang, J. Yao, D. Zhang, and H. Fu, Intramolecular Singlet Fission in an Antiaromatic Polycyclic Hydrocarbon. *Angewandte Chemie International Edition*, 2017. 56(32): p. 9400-9404.
- [76]. Fuemmeler, E.G., S.N. Sanders, A.B. Pun, E. Kumarasamy, T. Zeng, K. Miyata, M.L. Steigerwald, X.Y. Zhu, M.Y. Sfeir, L.M. Campos, and N. Ananth, A Direct Mechanism of Ultrafast Intramolecular Singlet Fission in Pentacene Dimers. *ACS Central Science*, 2016. 2(5): p. 316-324.

- [77]. Kuhlman, T.S., J. Kongsted, K.V. Mikkelsen, K.B. Møller, and T.I. Sølling, Interpretation of the Ultrafast Photoinduced Processes in Pentacene Thin Films. *Journal of the American Chemical Society*, 2010. 132(10): p. 3431-3439.
- [78]. Zimmerman, P.M., F. Bell, D. Casanova, and M. Head-Gordon, Mechanism for Singlet Fission in Pentacene and Tetracene: From Single Exciton to Two Triplets. *Journal of the American Chemical Society*, 2011. 133(49): p. 19944-19952.
- [79]. Zimmerman, P.M., C.B. Musgrave and M. Head-Gordon, A Correlated Electron View of Singlet Fission. *Accounts of Chemical Research*, 2013. 46(6): p. 1339-1347.
- [80]. Zimmerman, P.M., Z. Zhang and C.B. Musgrave, Singlet fission in pentacene through multi-exciton quantum states. *Nature Chemistry*, 2010. 2(8): p. 648-652.
- [81]. Greyson, E.C., J. Vura-Weis, J. Michl, and M.A. Ratner, Maximizing Singlet Fission in Organic Dimers: Theoretical Investigation of Triplet Yield in the Regime of Localized Excitation and Fast Coherent Electron Transfer. *The Journal of Physical Chemistry B*, 2010. 114(45): p. 14168-14177.
- [82]. Wang, L., Y. Olivier, O.V. Prezhdo, and D. Beljonne, Maximizing Singlet Fission by Intermolecular Packing. *The Journal of Physical Chemistry Letters*, 2014. 5(19): p. 3345-3353.
- [83]. Parker, S.M., T. Seideman, M.A. Ratner, and T. Shiozaki, Model Hamiltonian Analysis of Singlet Fission from First Principles. *The Journal of Physical Chemistry C*, 2014. 118(24): p. 12700-12705.
- [84]. Ito, S., T. Nagami and M. Nakano, Molecular design for efficient singlet fission. *Journal of Photochemistry and Photobiology C: Photochemistry Reviews*, 2018. 34: p. 85-120.
- [85]. Chan, W., T.C. Berkelbach, M.R. Provorse, N.R. Monahan, J.R. Tritsch, M.S. Hybertsen, D.R. Reichman, J. Gao, and X.Y. Zhu, The Quantum Coherent Mechanism for Singlet Fission: Experiment and Theory. *Accounts of Chemical Research*, 2013. 46(6): p. 1321-1329.
- [86]. Berkelbach, T.C., M.S. Hybertsen and D.R. Reichman, Microscopic theory of singlet exciton fission. I. General formulation. *The Journal of Chemical Physics*, 2013. 138(11): p. 114102.
- [87]. Zeng, T., R. Hoffmann and N. Ananth, The Low-Lying Electronic States of Pentacene and Their Roles in Singlet Fission. *Journal of the American Chemical Society*, 2014. 136(15): p. 5755-5764.
- [88]. Lindner, B.D., F. Paulus, A.L. Appleton, M. Schaffroth, J.U. Engelhart, K.M. Schelkle, O. Tverskoy, F. Rominger, M. Hamburger, and U.H.F. Bunz, Electron-transporting phenazinothiadiazoles with engineered microstructure. *Journal of Materials Chemistry C*, 2014. 2(45): p. 9609-9612.
- [89]. Lukman, S., K. Chen, J.M. Hodgkiss, D.H.P. Turban, N.D.M. Hine, S. Dong, J. Wu, N.C. Greenham, and A.J. Musser, Tuning the role of charge-transfer states in intramolecular singlet exciton fission through side-group engineering. *Nature Communications*, 2016. 7: p. 13622.

[90]. Berkelbach, T.C., M.S. Hybertsen and D.R. Reichman, Microscopic theory of singlet exciton fission. II. Application to pentacene dimers and the role of superexchange. *The Journal of Chemical Physics*, 2013. 138(11): p. 114103.

[91]. Berkelbach, T.C., M.S. Hybertsen and D.R. Reichman, Microscopic theory of singlet exciton fission. III. Crystalline pentacene. *The Journal of Chemical Physics*, 2014. 141(7): p. 074705.

[92]. Xu, X., B. Shan, S. Kalytchuk, M. Xie, S. Yang, D. Liu, S.V. Kershaw, and Q. Miao, Synthesis, solution-processed thin film transistors and solid solutions of silylethynylated diazatetracenes. *Chemical Communications*, 2014. 50(85): p. 12828-12831.

[93]. Lindner, B.D., B.A. Coombs, M. Schaffroth, J.U. Engelhart, O. Tverskoy, F. Rominger, M. Hamburger, and U.H.F. Bunz, From Thia- to Selenadiazoles: Changing Interaction Priority. *Organic Letters*, 2013. 15(3): p. 666-669.

[94]. Campbell, R.B., J.M. Robertson and J. Trotter, The crystal structure of hexacene, and a revision of the crystallographic data for tetracene. *Acta Crystallographica*, 1962. 15(3): p. 289-290.

[95]. Shao, Y., Z. Gan, E. Epifanovsky, A.T.B. Gilbert, M. Wormit, J. Kussmann, A.W. Lange, A. Behn, J. Deng, X. Feng, D. Ghosh, M. Goldey, P.R. Horn, L.D. Jacobson, I. Kaliman, R.Z. Khaliullin, T. Kuś, A. Landau, J. Liu, E.I. Proynov, Y.M. Rhee, R.M. Richard, M.A. Rohrdanz, R.P. Steele, E.J. Sundstrom, H.L. Woodcock, P.M. Zimmerman, D. Zuev, B. Albrecht, E. Alguire, B. Austin, G.J.O. Beran, Y.A. Bernard, E. Berquist, K. Brandhorst, K.B. Bravaya, S.T. Brown, D. Casanova, C. Chang, Y. Chen, S.H. Chien, K.D. Closser, D.L. Crittenden, M. Diedenhofen, R.A. DiStasio, H. Do, A.D. Dutoi, R.G. Edgar, S. Fatehi, L. Fusti-Molnar, A. Ghysels, A. Golubeva-Zadorozhnaya, J. Gomes, M.W.D. Hanson-Heine, P.H.P. Harbach, A.W. Hauser, E.G. Hohenstein, Z.C. Holden, T. Jagau, H. Ji, B. Kaduk, K. Khistyayev, J. Kim, J. Kim, R.A. King, P. Klunzinger, D. Kosenkov, T. Kowalczyk, C.M. Krauter, K.U. Lao, A.D. Laurent, K.V. Lawler, S.V. Levchenko, C.Y. Lin, F. Liu, E. Livshits, R.C. Lochan, A. Luenser, P. Manohar, S.F. Manzer, S. Mao, N. Mardirossian, A.V. Marenich, S.A. Maurer, N.J. Mayhall, E. Neuscammann, C.M. Oana, R. Olivares-Amaya, D.P. O'Neill, J.A. Parkhill, T.M. Perrine, R. Peverati, A. Prociuk, D.R. Rehn, E. Rosta, N.J. Russ, S.M. Sharada, S. Sharma, D.W. Small, A. Sodt, T. Stein, D. Stück, Y. Su, A.J.W. Thom, T. Tsuchimochi, V. Vanovschi, L. Vogt, O. Vydrov, T. Wang, M.A. Watson, J. Wenzel, A. White, C.F. Williams, J. Yang, S. Yeganeh, S.R. Yost, Z. You, I.Y. Zhang, X. Zhang, Y. Zhao, B.R. Brooks, G.K.L. Chan, D.M. Chipman, C.J. Cramer, W.A. Goddard, M.S. Gordon, W.J. Hehre, A. Klamt, H.F. Schaefer, M.W. Schmidt, C.D. Sherrill, D.G. Truhlar, A. Warshel, X. Xu, A. Aspuru-Guzik, R. Baer, A.T. Bell, N.A. Besley, J. Chai, A. Dreuw, B.D. Dunietz, T.R. Furlani, S.R. Gwaltney, C. Hsu, Y. Jung, J. Kong, D.S. Lambrecht, W. Liang, C. Ochsenfeld, V.A. Rassolov, L.V. Slipchenko, J.E. Subotnik, T. Van Voorhis, J.M. Herbert, A.I. Krylov, P.M.W. Gill, and M. Head-Gordon, *Advances in molecular quantum chemistry contained in the Q-Chem 4 program package. Molecular Physics*, 2014. 113(2): p. 184-215.

[96]. Fiolhais, C., F. Nogueira and M.A. Marques, *A primer in density functional theory. Vol. 620. 2003: Springer Science & Business Media.*

- [97]. Hirata, S. and M. Head-Gordon, Time-dependent density functional theory within the Tamm–Dancoff approximation. *Chemical Physics Letters*, 1999. 314(3): p. 291-299.
- [98]. Grotjahn, R., T.M. Maier, J. Michl, and M. Kaupp, Development of a TDDFT-Based Protocol with Local Hybrid Functionals for the Screening of Potential Singlet Fission Chromophores. *Journal of Chemical Theory and Computation*, 2017. 13(10): p. 4984-4996.
- [99]. Brückner, C. and B. Engels, Benchmarking singlet and triplet excitation energies of molecular semiconductors for singlet fission: Tuning the amount of HF exchange and adjusting local correlation to obtain accurate functionals for singlet–triplet gaps. *Chemical Physics*, 2017. 482: p. 319-338.
- [100]. Yamaguchi, K., The electronic structures of biradicals in the unrestricted Hartree-Fock approximation. *Chemical Physics Letters*, 1975. 33(2): p. 330-335.
- [101]. Ito, S., T. Minami and M. Nakano, Diradical Character Based Design for Singlet Fission of Condensed-Ring Systems with $4n\pi$ Electrons. *The Journal of Physical Chemistry C*, 2012. 116(37): p. 19729-19736.
- [102]. Kaduk, B., T. Kowalczyk and T. Van Voorhis, Constrained Density Functional Theory. *Chemical Reviews*, 2012. 112(1): p. 321-370.
- [103]. Kowalczyk, T., S.R. Yost and T.V. Voorhis, Assessment of the Δ SCF density functional theory approach for electronic excitations in organic dyes. *The Journal of Chemical Physics*, 2011. 134(5): p. 054128.
- [104]. Figari, G. and V. Magnasco, On the evaluation of the cofactors occurring in the matrix elements between multiply-excited determinantal wavefunctions of non-orthogonal orbitals. *Molecular Physics*, 1985. 55(2): p. 319-330.
- [105]. Elenewski, J.E., U.S. Cubeta, E. Ko, and H. Chen, Functional Mode Singlet Fission Theory. *The Journal of Physical Chemistry C*, 2017. 121(8): p. 4130-4138.
- [106]. Farazdel, A., M. Dupuis, E. Clementi, and A. Aviram, Electric-field induced intramolecular electron transfer in spiro .pi.-electron systems and their suitability as molecular electronic devices. A theoretical study. *Journal of the American Chemical Society*, 1990. 112(11): p. 4206-4214.
- [107]. Shen, L., Y. Chen, X. Li, and J. Gao, Effects of substituents on tetracene derivatives on their stabilities and singlet fission. *Journal of Molecular Graphics and Modelling*, 2014. 51: p. 86-96.
- [108]. Chu, M., J. Fan, S. Yang, D. Liu, C.F. Ng, H. Dong, A. Ren, and Q. Miao, Halogenated Tetraazapentacenes with Electron Mobility as High as $27.8 \text{ cm}^2 \text{ V}^{-1} \text{ s}^{-1}$ in Solution-Processed n-Channel Organic Thin-Film Transistors. *Advanced Materials*, 2018. 30(38): p. 1803467.
- [109]. Reiss, H., L. Ji, J. Han, S. Koser, O. Tverskoy, J. Freudenberg, F. Hinkel, M. Moos, A. Friedrich, I. Krummenacher, C. Lambert, H. Braunschweig, A. Dreuw, T.B. Marder, and U.H.F. Bunz,

Bromination Improves the Electron Mobility of Tetraazapentacene. *Angewandte Chemie International Edition*, 2018. 57(30): p. 9543-9547.

[110]. Yost, S.R., J. Lee, M.W.B. Wilson, T. Wu, D.P. McMahon, R.R. Parkhurst, N.J. Thompson, D.N. Congreve, A. Rao, K. Johnson, M.Y. Sfeir, M.G. Bawendi, T.M. Swager, R.H. Friend, M.A. Baldo, and T. Van Voorhis, A transferable model for singlet-fission kinetics. *Nature Chemistry*, 2014. 6(6): p. 492-497.

[111]. Havlas, Z. and J. Michl, Guidance for Mutual Disposition of Chromophores for Singlet Fission. *Israel Journal of Chemistry*, 2015. 56(1): p. 96-106.

[112]. Nagami, T., S. Ito, T. Kubo, and M. Nakano, Intermolecular Packing Effects on Singlet Fission in Oligorylene Dimers. *ACS Omega*, 2017. 2(8): p. 5095-5103.

[113]. Singh, J., The theory of fission of a singlet frenkel exciton into two localised triplet excitations. *Journal of Physics and Chemistry of Solids*, 1978. 39(11): p. 1207-1209.

[114]. Pensack, R.D., E.E. Ostroumov, A.J. Tilley, S. Mazza, C. Grieco, K.J. Thorley, J.B. Asbury, D.S. Seferos, J.E. Anthony, and G.D. Scholes, Observation of Two Triplet-Pair Intermediates in Singlet Exciton Fission. *The Journal of Physical Chemistry Letters*, 2016. 7(13): p. 2370-2375.

[115]. Grieco, C., E.R. Kennehan, H. Kim, R.D. Pensack, A.N. Brigeman, A. Rimshaw, M.M. Payne, J.E. Anthony, N.C. Giebink, G.D. Scholes, and J.B. Asbury, Direct Observation of Correlated Triplet Pair Dynamics during Singlet Fission Using Ultrafast Mid-IR Spectroscopy. *The Journal of Physical Chemistry C*, 2018. 122(4): p. 2012-2022.

[116]. Pensack, R.D., A.J. Tilley, C. Grieco, G.E. Purdum, E.E. Ostroumov, D.B. Granger, D.G. Oblinsky, J.C. Dean, G.S. Doucette, J.B. Asbury, Y. Loo, D.S. Seferos, J.E. Anthony, and G.D. Scholes, Striking the right balance of intermolecular coupling for high-efficiency singlet fission. *Chemical Science*, 2018. 9(29): p. 6240-6259.

[117]. Chien, A.D., A.R. Molina, N. Abeyasinghe, O.P. Varnavski, T. Goodson, and P.M. Zimmerman, Structure and Dynamics of the I(TT) State in a Quinoidal Bithiophene: Characterizing a Promising Intramolecular Singlet Fission Candidate. *The Journal of Physical Chemistry C*, 2015. 119(51): p. 28258-28268.

[118]. Trinh, M.T., A. Pinkard, A.B. Pun, S.N. Sanders, E. Kumarasamy, M.Y. Sfeir, L.M. Campos, X. Roy, and X.Y. Zhu, Distinct properties of the triplet pair state from singlet fission. *Science Advances*, 2017. 3(7).

[119]. Khan, S. and S. Mazumdar, Diagrammatic Exciton Basis Theory of the Photophysics of Pentacene Dimers. *The Journal of Physical Chemistry Letters*, 2017. 8(18): p. 4468-4478.

[120]. Khan, S. and S. Mazumdar, Optical probes of the quantum-entangled triplet-triplet state in a heteroacene dimer. *Physical Review B*, 2018. 98(16): p. 165202.

- [121]. Tayebjee, M.J.Y., S.N. Sanders, E. Kumarasamy, L.M. Campos, M.Y. Sfeir, and D.R. McCamey, Quintet multiexciton dynamics in singlet fission. *Nature Physics*, 2017. 13(2): p. 182-188.
- [122]. Kim, H. and P.M. Zimmerman, Coupled double triplet state in singlet fission. *Physical Chemistry Chemical Physics*, 2018. 20(48): p. 30083-30094.
- [123]. Kim, H., B. Keller, R. Ho-Wu, N. Abeyasinghe, R.J. Vázquez, T. Goodson, and P.M. Zimmerman, Enacting Two-Electron Transfer from a Double-Triplet State of Intramolecular Singlet Fission. *Journal of the American Chemical Society*, 2018. 140(25): p. 7760-7763.
- [124]. Ruckebusch, C., M. Sliwa, P. Pernot, A. de Juan, and R. Tauler, Comprehensive data analysis of femtosecond transient absorption spectra: A review. *Journal of Photochemistry and Photobiology C: Photochemistry Reviews*, 2012. 13(1): p. 1-27.
- [125]. Musser, A.J. and J. Clark, Triplet-Pair States in Organic Semiconductors. *Annual Review of Physical Chemistry*, 2019. 70(1): p. 323-351.
- [126]. Sanders, S.N., A.B. Pun, K.R. Parenti, E. Kumarasamy, L.M. Yablon, M.Y. Sfeir, and L.M. Campos, Understanding the Bound Triplet-Pair State in Singlet Fission. *Chem*, 2019. 5(8): p. 1988-2005.
- [127]. Alagna, N., J. Han, N. Wollscheid, J.L. Perez Lustres, J. Herz, S. Hahn, S. Koser, F. Paulus, U.H.F. Bunz, A. Dreuw, T. Buckup, and M. Motzkus, Tailoring Ultrafast Singlet Fission by the Chemical Modification of Phenazinothiadiazoles. *Journal of the American Chemical Society*, 2019. 141(22): p. 8834-8845.
- [128]. Alagna, N., J.L. Pérez Lustres, N. Wollscheid, Q. Luo, J. Han, A. Dreuw, F.L. Geyer, V. Brosius, U.H.F. Bunz, T. Buckup, and M. Motzkus, Singlet Fission in Tetraaza-TIPS-Pentacene Oligomers: From fs Excitation to μ s Triplet Decay via the Biexcitonic State. *The Journal of Physical Chemistry B*, 2019. 123(50): p. 10780-10793.
- [129]. Chien, A.D. and P.M. Zimmerman, Recovering dynamic correlation in spin flip configuration interaction through a difference dedicated approach. *The Journal of Chemical Physics*, 2017. 146(1): p. 014103.
- [130]. Khan, S. and S. Mazumdar, Theory of Transient Excited State Absorptions in Pentacene and Derivatives: Triplet-Triplet Biexciton versus Free Triplets. *The Journal of Physical Chemistry Letters*, 2017. 8(23): p. 5943-5948.
- [131]. Hashimoto, T., H. Nakano and K. Hirao, Theoretical study of the valence $\pi \rightarrow \pi^*$ excited states of polyacenes: Benzene and naphthalene. *The Journal of Chemical Physics*, 1996. 104(16): p. 6244-6258.
- [132]. Casanova, D. and A.I. Krylov, Quantifying local exciton, charge resonance, and multiexciton character in correlated wave functions of multichromophoric systems. *The Journal of Chemical Physics*, 2016. 144(1): p. 014102.

- [133]. Casanova, D., Electronic Structure Study of Singlet Fission in Tetracene Derivatives. *Journal of Chemical Theory and Computation*, 2014. 10(1): p. 324-334.
- [134]. Lin, H., K.Y. Kue, G.C. Claudio, and C. Hsu, First Principle Prediction of Intramolecular Singlet Fission and Triplet Triplet Annihilation Rates. *Journal of Chemical Theory and Computation*, 2019. 15(4): p. 2246-2253.
- [135]. Feng, X., A.V. Luzanov and A.I. Krylov, Fission of Entangled Spins: An Electronic Structure Perspective. *The Journal of Physical Chemistry Letters*, 2013. 4(22): p. 3845-3852.
- [136]. Hättig, C., A. Köhn and K. Hald, First-order properties for triplet excited states in the approximated coupled cluster model CC2 using an explicitly spin coupled basis. *The Journal of Chemical Physics*, 2002. 116(13): p. 5401-5410.
- [137]. Salek, P., O. Vahtras, T. Helgaker, and H. Ågren, Density-functional theory of linear and nonlinear time-dependent molecular properties. *The Journal of Chemical Physics*, 2002. 117(21): p. 9630-9645.
- [138]. Mosquera, M.A., L.X. Chen, M.A. Ratner, and G.C. Schatz, Sequential double excitations from linear-response time-dependent density functional theory. *The Journal of Chemical Physics*, 2016. 144(20): p. 204105.
- [139]. Ling, S., S. Schumacher, I. Galbraith, and M.J. Paterson, Excited-State Absorption of Conjugated Polymers in the Near-Infrared and Visible: A Computational Study of Oligofluorenes. *The Journal of Physical Chemistry C*, 2013. 117(13): p. 6889-6895.
- [140]. Mosquera, M.A., N.E. Jackson, T.J. Fauvell, M.S. Kelley, L.X. Chen, G.C. Schatz, and M.A. Ratner, Exciton Absorption Spectra by Linear Response Methods: Application to Conjugated Polymers. *Journal of the American Chemical Society*, 2017. 139(10): p. 3728-3735.
- [141]. Nakano, M., Open-Shell-Character-Based Molecular Design Principles: Applications to Nonlinear Optics and Singlet Fission. *The Chemical Record*, 2017. 17(1): p. 27-62.
- [142]. Rinkevicius, Z., O. Vahtras and H. Ågren, Spin-flip time dependent density functional theory applied to excited states with single, double, or mixed electron excitation character. *The Journal of Chemical Physics*, 2010. 133(11): p. 114104.
- [143]. Barca, G.M.J., A.T.B. Gilbert and P.M.W. Gill, Simple Models for Difficult Electronic Excitations. *Journal of Chemical Theory and Computation*, 2018. 14(3): p. 1501-1509.
- [144]. Grimme, S., J.G. Brandenburg, C. Bannwarth, and A. Hansen, Consistent structures and interactions by density functional theory with small atomic orbital basis sets. *The Journal of Chemical Physics*, 2015. 143(5): p. 054107.
- [145]. Tomasi, J., Selected features of the polarizable continuum model for the representation of solvation. *Wiley Interdisciplinary Reviews: Computational Molecular Science*, 2011. 1(5): p. 855-867.

- [146]. Tomasi, J., B. Mennucci and E. Cancès, The IEF version of the PCM solvation method: an overview of a new method addressed to study molecular solutes at the QM ab initio level. *Journal of Molecular Structure: THEOCHEM*, 1999. 464(1): p. 211-226.
- [147]. Hodecker, M., D.R. Rehn, A. Dreuw, and S. Höfener, Similarities and differences of the Lagrange formalism and the intermediate state representation in the treatment of molecular properties. *The Journal of Chemical Physics*, 2019. 150(16): p. 164125.
- [148]. Norman, P., D.M. Bishop, H.J.A. Jensen, and J. Oddershede, Nonlinear response theory with relaxation: The first-order hyperpolarizability. *The Journal of Chemical Physics*, 2005. 123(19): p. 194103.
- [149]. Olsen, J. and P. Jørgensen, Linear and nonlinear response functions for an exact state and for an MCSCF state. *The Journal of Chemical Physics*, 1985. 82(7): p. 3235-3264.
- [150]. Parker, S.M., D. Rappoport and F. Furche, Quadratic Response Properties from TDDFT: Trials and Tribulations. *Journal of Chemical Theory and Computation*, 2018. 14(2): p. 807-819.
- [151]. Shao, Y., M. Head-Gordon and A.I. Krylov, The spin-flip approach within time-dependent density functional theory: Theory and applications to diradicals. *The Journal of Chemical Physics*, 2003. 118(11): p. 4807-4818.
- [152]. Wang, F. and T. Ziegler, The performance of time-dependent density functional theory based on a noncollinear exchange-correlation potential in the calculations of excitation energies. *The Journal of Chemical Physics*, 2005. 122(7): p. 074109.
- [153]. Khaliullin, R.Z., M. Head-Gordon and A.T. Bell, An efficient self-consistent field method for large systems of weakly interacting components. *The Journal of Chemical Physics*, 2006. 124(20): p. 204105.
- [154]. Becke, A.D., Density-functional exchange-energy approximation with correct asymptotic behavior. *Physical Review A*, 1988. 38(6): p. 3098-3100.
- [155]. Yang, W., R.G. Parr and C. Lee, Development of the Colle-Salvetti correlation-energy formula into a functional of the electron density. *Physical Review B*, 1988. 37(2): p. 785-789.
- [156]. Stephens, P.J., F.J. Devlin, C.F. Chabalowski, and M.J. Frisch, Ab Initio Calculation of Vibrational Absorption and Circular Dichroism Spectra Using Density Functional Force Fields. *The Journal of Physical Chemistry*, 1994. 98(45): p. 11623-11627.
- [157]. Becke, A.D., Density-functional thermochemistry. III. The role of exact exchange. *The Journal of Chemical Physics*, 1993. 98(7): p. 5648-5652.
- [158]. Ernzerhof, M. and G.E. Scuseria, Assessment of the Perdew-Burke-Ernzerhof exchange-correlation functional. *The Journal of Chemical Physics*, 1999. 110(11): p. 5029-5036.

- [159]. Adamo, C. and V. Barone, Toward reliable density functional methods without adjustable parameters: The PBE0 model. *The Journal of Chemical Physics*, 1999. 110(13): p. 6158-6170.
- [160]. Becke, A.D., A new mixing of Hartree–Fock and local density-functional theories. *The Journal of Chemical Physics*, 1993. 98(2): p. 1372-1377.
- [161]. Staroverov, V.N., G.E. Scuseria, J. Tao, and J.P. Perdew, Comparative assessment of a new nonempirical density functional: Molecules and hydrogen-bonded complexes. *The Journal of Chemical Physics*, 2003. 119(23): p. 12129-12137.
- [162]. Boese, A.D. and J.M.L. Martin, Development of density functionals for thermochemical kinetics. *The Journal of Chemical Physics*, 2004. 121(8): p. 3405-3416.
- [163]. Zhao, Y. and D.G. Truhlar, The M06 suite of density functionals for main group thermochemistry, thermochemical kinetics, noncovalent interactions, excited states, and transition elements: two new functionals and systematic testing of four M06-class functionals and 12 other functionals. *Theoretical Chemistry Accounts*, 2008. 120(1): p. 215-241.
- [164]. Yanai, T., D.P. Tew and N.C. Handy, A new hybrid exchange–correlation functional using the Coulomb-attenuating method (CAM-B3LYP). *Chemical Physics Letters*, 2004. 393(1): p. 51-57.
- [165]. Chai, J. and M. Head-Gordon, Long-range corrected hybrid density functionals with damped atom–atom dispersion corrections. *Physical Chemistry Chemical Physics*, 2008. 10(44): p. 6615-6620.
- [166]. Vydrov, O.A. and G.E. Scuseria, Assessment of a long-range corrected hybrid functional. *The Journal of Chemical Physics*, 2006. 125(23): p. 234109.
- [167]. Ditchfield, R., W.J. Hehre and J.A. Pople, Self-Consistent Molecular-Orbital Methods. IX. An Extended Gaussian-Type Basis for Molecular-Orbital Studies of Organic Molecules. *The Journal of Chemical Physics*, 1971. 54(2): p. 724-728.
- [168]. Shao, Y., Z. Gan, E. Epifanovsky, A.T.B. Gilbert, M. Wormit, J. Kussmann, A.W. Lange, A. Behn, J. Deng, X. Feng, D. Ghosh, M. Goldey, P.R. Horn, L.D. Jacobson, I. Kaliman, R.Z. Khaliullin, T. Kuś, A. Landau, J. Liu, E.I. Proynov, Y.M. Rhee, R.M. Richard, M.A. Rohrdanz, R.P. Steele, E.J. Sundstrom, H.L. Woodcock, P.M. Zimmerman, D. Zuev, B. Albrecht, E. Alguire, B. Austin, G.J.O. Beran, Y.A. Bernard, E. Berquist, K. Brandhorst, K.B. Bravaya, S.T. Brown, D. Casanova, C. Chang, Y. Chen, S.H. Chien, K.D. Closser, D.L. Crittenden, M. Diedenhofen, R.A. DiStasio, H. Do, A.D. Dutoi, R.G. Edgar, S. Fatehi, L. Fusti-Molnar, A. Ghysels, A. Golubeva-Zadorozhnaya, J. Gomes, M.W.D. Hanson-Heine, P.H.P. Harbach, A.W. Hauser, E.G. Hohenstein, Z.C. Holden, T. Jagau, H. Ji, B. Kaduk, K. Khistyayev, J. Kim, J. Kim, R.A. King, P. Klunzinger, D. Kosenkov, T. Kowalczyk, C.M. Krauter, K.U. Lao, A.D. Laurent, K.V. Lawler, S.V. Levchenko, C.Y. Lin, F. Liu, E. Livshits, R.C. Lochan, A. Luenser, P. Manohar, S.F. Manzer, S. Mao, N. Mardirossian, A.V. Marenich, S.A. Maurer, N.J. Mayhall, E. Neuscamman, C.M. Oana, R. Olivares-Amaya, D.P. O'Neill, J.A. Parkhill, T.M. Perrine, R. Peverati, A. Prociuk, D.R. Rehn, E. Rosta, N.J. Russ, S.M. Sharada, S. Sharma, D.W. Small, A. Sodt, T. Stein, D. Stück, Y. Su, A.J.W. Thom, T. Tsuchimochi, V. Vanovschi, L. Vogt, O. Vydrov, T. Wang, M.A. Watson,

J. Wenzel, A. White, C.F. Williams, J. Yang, S. Yeganeh, S.R. Yost, Z. You, I.Y. Zhang, X. Zhang, Y. Zhao, B.R. Brooks, G.K.L. Chan, D.M. Chipman, C.J. Cramer, W.A. Goddard, M.S. Gordon, W.J. Hehre, A. Klamt, H.F. Schaefer, M.W. Schmidt, C.D. Sherrill, D.G. Truhlar, A. Warshel, X. Xu, A. Aspuru-Guzik, R. Baer, A.T. Bell, N.A. Besley, J. Chai, A. Dreuw, B.D. Dunietz, T.R. Furlani, S.R. Gwaltney, C. Hsu, Y. Jung, J. Kong, D.S. Lambrecht, W. Liang, C. Ochsenfeld, V.A. Rassolov, L.V. Slipchenko, J.E. Subotnik, T. Van Voorhis, J.M. Herbert, A.I. Krylov, P.M.W. Gill, and M. Head-Gordon, *Advances in molecular quantum chemistry contained in the Q-Chem 4 program package. Molecular Physics*, 2015. 113(2): p. 184-215.

[169]. Aidas, K., C. Angeli, K.L. Bak, V. Bakken, R. Bast, L. Boman, O. Christiansen, R. Cimiraglia, S. Coriani, P. Dahle, E.K. Dalskov, U. Ekström, T. Enevoldsen, J.J. Eriksen, P. Ettenhuber, B. Fernández, L. Ferrighi, H. Fliegl, L. Frediani, K. Hald, A. Halkier, C. Hättig, H. Heiberg, T. Helgaker, A.C. Hennum, H. Hettema, E. Hjertenæs, S. Høst, I. Høyvik, M.F. Iozzi, B. Jansík, H.J.A. Jensen, D. Jonsson, P. Jørgensen, J. Kauczor, S. Kirpekar, T. Kjærgaard, W. Klopper, S. Knecht, R. Kobayashi, H. Koch, J. Kongsted, A. Krapp, K. Kristensen, A. Ligabue, O.B. Lutnæs, J.I. Melo, K.V. Mikkelsen, R.H. Myhre, C. Neiss, C.B. Nielsen, P. Norman, J. Olsen, J.M.H. Olsen, A. Osted, M.J. Packer, F. Pawłowski, T.B. Pedersen, P.F. Provasi, S. Reine, Z. Rinkevicius, T.A. Ruden, K. Ruud, V.V. Rybkin, P. Sałek, C.C.M. Samson, A.S. de Merás, T. Saue, S.P.A. Sauer, B. Schimmelpfennig, K. Sneskov, A.H. Steindal, K.O. Sylvester-Hvid, P.R. Taylor, A.M. Teale, E.I. Tellgren, D.P. Tew, A.J. Thorvaldsen, L. Thøgersen, O. Vahtras, M.A. Watson, D.J.D. Wilson, M. Ziolkowski, and H. Ågren, *The Dalton quantum chemistry program system. WIREs Computational Molecular Science*, 2014. 4(3): p. 269-284.

[170]. Valiev, M., E.J. Bylaska, N. Govind, K. Kowalski, T.P. Straatsma, H.J.J. Van Dam, D. Wang, J. Nieplocha, E. Apra, T.L. Windus, and W.A. de Jong, *NWChem: A comprehensive and scalable open-source solution for large scale molecular simulations. Computer Physics Communications*, 2010. 181(9): p. 1477-1489.

[171]. Lu, T. and F. Chen, *Multiwfn: A multifunctional wavefunction analyzer. Journal of Computational Chemistry*, 2012. 33(5): p. 580-592.

[172]. Prlj, A., M.E. Sandoval-Salinas, D. Casanova, D. Jacquemin, and C. Corminboeuf, *Low-Lying $\pi\pi^*$ States of Heteroaromatic Molecules: A Challenge for Excited State Methods. Journal of Chemical Theory and Computation*, 2016. 12(6): p. 2652-2660.

[173]. Richard, R.M. and J.M. Herbert, *Time-Dependent Density-Functional Description of the 1La State in Polycyclic Aromatic Hydrocarbons: Charge-Transfer Character in Disguise? Journal of Chemical Theory and Computation*, 2011. 7(5): p. 1296-1306.

[174]. Seeger, R. and J.A. Pople, *Self-consistent molecular orbital methods. XVIII. Constraints and stability in Hartree-Fock theory. The Journal of Chemical Physics*, 1977. 66(7): p. 3045-3050.

[175]. Bauernschmitt, R. and R. Ahlrichs, *Stability analysis for solutions of the closed shell Kohn-Sham equation. The Journal of Chemical Physics*, 1996. 104(22): p. 9047-9052.

- [176]. Zhang, X. and J.M. Herbert, Spin-flip, tensor equation-of-motion configuration interaction with a density-functional correction: A spin-complete method for exploring excited-state potential energy surfaces. *The Journal of Chemical Physics*, 2015. 143(23): p. 234107.
- [177]. Xia, J., S.N. Sanders, W. Cheng, J.Z. Low, J. Liu, L.M. Campos, and T. Sun, Singlet Fission: Progress and Prospects in Solar Cells. *Advanced Materials*, 2017. 29(20): p. 1601652-n/a.
- [178]. Feng, X., D. Casanova and A.I. Krylov, Intra- and Intermolecular Singlet Fission in Covalently Linked Dimers. *The Journal of Physical Chemistry C*, 2016. 120(34): p. 19070-19077.
- [179]. Matsika, S., X. Feng, A.V. Luzanov, and A.I. Krylov, What We Can Learn from the Norms of One-Particle Density Matrices, and What We Can't: Some Results for Interstate Properties in Model Singlet Fission Systems. *The Journal of Physical Chemistry A*, 2014. 118(51): p. 11943-11955.
- [180]. Payne, M.M., S.R. Parkin, J.E. Anthony, C. Kuo, and T.N. Jackson, Organic Field-Effect Transistors from Solution-Deposited Functionalized Acenes with Mobilities as High as $1 \text{ cm}^2/\text{V}\cdot\text{s}$. *Journal of the American Chemical Society*, 2005. 127(14): p. 4986-4987.
- [181]. Xia, D., X. Guo, L. Chen, M. Baumgarten, A. Keerthi, and K. Müllen, Layered Electron Acceptors by Dimerization of Acenes End-Capped with 1,2,5-Thiadiazoles. *Angewandte Chemie International Edition*, 2016. 55(3): p. 941-944.
- [182]. Guo, S., S.K. Mohapatra, A. Romanov, T.V. Timofeeva, K.I. Hardcastle, K. Yesudas, C. Risko, J. Brédas, S.R. Marder, and S. Barlow, n-Doping of Organic Electronic Materials Using Air-Stable Organometallics: A Mechanistic Study of Reduction by Dimeric Sandwich Compounds. *Chemistry - A European Journal*, 2012. 18(46): p. 14760-14772.
- [183]. Anthony, J.E., D.L. Eaton and S.R. Parkin, A Road Map to Stable, Soluble, Easily Crystallized Pentacene Derivatives. *Organic Letters*, 2002. 4(1): p. 15-18.
- [184]. Holy, N.L., Reactions of the radical anions and dianions of aromatic hydrocarbons. *Chemical Reviews*, 1974. 74(2): p. 243-277.
- [185]. Liang, Z., Q. Tang, J. Xu, and Q. Miao, Soluble and Stable N-Heteropentacenes with High Field-Effect Mobility. *Advanced Materials*, 2011. 23(13): p. 1535-1539.
- [186]. Liang, Z., Q. Tang, R. Mao, D. Liu, J. Xu, and Q. Miao, The Position of Nitrogen in N-Heteropentacenes Matters. *Advanced Materials*, 2011. 23(46): p. 5514-5518.
- [187]. Bunz, U.H.F. and J.U. Engelhart, The Palladium Way to N-Heteroacenes. *Chemistry - A European Journal*, 2016. 22(14): p. 4680-4689.
- [188]. Bunz, U.H.F., The Larger Linear N-Heteroacenes. *Accounts of Chemical Research*, 2015. 48(6): p. 1676-1686.
- [189]. Bunz, U.H.F., J.U. Engelhart, B.D. Lindner, and M. Schaffroth, Large N-Heteroacenes: New Tricks for Very Old Dogs? *Angewandte Chemie International Edition*, 2013. 52(14): p. 3810-3821.

- [190]. Bunz, U.H.F., The larger N-heteroacenes. *Pure and Applied Chemistry*, 2010. 82(4): p. 953-968.
- [191]. Bunz, U.H.F., N-Heteroacenes. *Chemistry - A European Journal*, 2009. 15(28): p. 6780-6789.
- [192]. Miao, Q., N-Heteropentacenes and N-Heteropentacenequinones: From Molecules to Semiconductors. *Synlett*, 2012. 23(03): p. 326-336.
- [193]. Li, J. and Q. Zhang, Linearly Fused Azaacenes: Novel Approaches and New Applications Beyond Field-Effect Transistors (FETs). *ACS Applied Materials & Interfaces*, 2015. 7(51): p. 28049-28062.
- [194]. Richards, G.J., J.P. Hill, T. Mori, and K. Ariga, Putting the 'N' in ACENE: Pyrazinacenes and their structural relatives. *Organic & Biomolecular Chemistry*, 2011. 9(14): p. 5005.
- [195]. Parkhurst, R.R. and T.M. Swager, Synthesis and Optical Properties of Phenylene-Containing Oligoacenes. *Journal of the American Chemical Society*, 2012. 134(37): p. 15351-15356.
- [196]. Vollhardt, K.P.C., The phenylenes. *Pure and Applied Chemistry*, 1993. 65(1): p. 153-156.
- [197]. Wang, J., M. Chu, J. Fan, T. Lau, A. Ren, X. Lu, and Q. Miao, Crystal Engineering of Biphenylene-Containing Acenes for High-Mobility Organic Semiconductors. *Journal of the American Chemical Society*, 2019. 141(8): p. 3589-3596.
- [198]. Yang, S., D. Liu, X. Xu, and Q. Miao, Molecular packing and n-channel thin film transistors of chlorinated cyclobuta[1,2-b:3,4-b']diquinoxalines. *Chemical Communications*, 2015. 51(20): p. 4275-4278.
- [199]. Gu, X., B. Shan, Z. He, and Q. Miao, N-Phenylated N-Heteroacenes: Synthesis, Structures, and Properties. *ChemPlusChem*, 2017. 82(7): p. 1034-1038.
- [200]. Tang, Q., J. Liu, H.S. Chan, and Q. Miao, Benzenoid and Quinonoid Nitrogen-Containing Heteropentacenes. *Chemistry - A European Journal*, 2009. 15(16): p. 3965-3969.
- [201]. Fleischhauer, J., S. Zahn, R. Beckert, U. Grummt, E. Birckner, and H. Görls, A Way to Stable, Highly Emissive Fluorubine Dyes: Tuning the Electronic Properties of Azaderivatives of Pentacene by Introducing Substituted Pyrazines. *Chemistry - A European Journal*, 2012. 18(15): p. 4549-4557.
- [202]. Zissimou, G.A., A. Kourtellaris and P.A. Koutentis, Synthesis and Characterization of Isodiphenylfluorindone and Isodiphenylfluorindinone. *The Journal of Organic Chemistry*, 2018. 83(8): p. 4754-4761.
- [203]. Chen, Y., H. Kueh, T.Y. Gopalakrishna, S. Dong, Y. Han, and C. Chi, Sulfur-Containing, Quinodimethane-Embedded Acene Analogue with Nine Consecutively Fused Six-Membered Rings. *Organic Letters*, 2019. 21(9): p. 3127-3130.

- [204]. Dong, S., T.Y. Gopalakrishna, Y. Han, H. Phan, T. Tao, Y. Ni, G. Liu, and C. Chi, Extended Bis(anthraoxa)quinodimethanes with Nine and Ten Consecutively Fused Six-Membered Rings: Neutral Diradicaloids and Charged Diradical Dianions/Dications. *Journal of the American Chemical Society*, 2019. 141(1): p. 62-66.
- [205]. Shi, X. and C. Chi, Heterocyclic Quinodimethanes. *Topics in Current Chemistry*, 2017. 375(4).
- [206]. Hohenberg, P. and W. Kohn, Inhomogeneous Electron Gas. *Physical Review*, 1964. 136(3B): p. B864-B871.
- [207]. Cheeseman, J.R., G.W. Trucks, T.A. Keith, and M.J. Frisch, A comparison of models for calculating nuclear magnetic resonance shielding tensors. *The Journal of Chemical Physics*, 1996. 104(14): p. 5497-5509.
- [208]. London, F., Théorie quantique des courants interatomiques dans les combinaisons aromatiques. *Journal de Physique et le Radium*, 1937. 8(10): p. 397-409.
- [209]. Frisch, M.J., G.W. Trucks, H.B. Schlegel, G.E. Scuseria, M.A. Robb, J.R. Cheeseman, G. Scalmani, V. Barone, B. Mennucci, G.A. Petersson, H. Nakatsuji, M. Caricato, X. Li, H.P. Hratchian, A.F. Izmaylov, J. Bloino, G. Zheng, J.L. Sonnenberg, M. Hada, M. Ehara, K. Toyota, R. Fukuda, J. Hasegawa, M. Ishida, T. Nakajima, Y. Honda, O. Kitao, H. Nakai, T. Vreven, J.A. Montgomery, J.E. Peralta, F. Ogliaro, M. Bearpark, J.J. Heyd, E. Brothers, K.N. Kudin, V.N. Staroverov, T. Keith, R. Kobayashi, J. Normand, K. Raghavachari, A. Rendell, J.C. Burant, S.S. Iyengar, J. Tomasi, M. Cossi, N. Rega, J.M. Millam, M. Klene, J.E. Knox, J.B. Cross, V. Bakken, C. Adamo, J. Jaramillo, R. Gomperts, R.E. Stratmann, O. Yazyev, A.J. Austin, R. Cammi, C. Pomelli, J.W. Ochterski, R.L. Martin, K. Morokuma, V.G. Zakrzewski, G.A. Voth, P. Salvador, J.J. Dannenberg, S. Dapprich, A.D. Daniels, O. Farkas, J.B. Foresman, J.V. Ortiz, J. Cioslowski, and D.J. Fox, *Gaussian 09*, rev. D.01; Gaussian, Inc., Wallingford, CT., 2013.
- [210]. Bock, H., K. Gharagozloo-Hubmann, C. Näther, N. Nagel, and Z. Havlas, [$\text{Na}^+(\text{thf})_2$] $_4$ (rubrene $^{4-}$): Crystallization and Structure Determination of a Contact-Ion Quintuple for the First π -Hydrocarbon Tetraanion. *Angewandte Chemie International Edition in English*, 1996. 35(6): p. 631-632.
- [211]. Wu, J.I., C.S. Wannere, Y. Mo, P.V.R. Schleyer, and U.H.F. Bunz, $4n \pi$ Electrons but Stable: N,N-Dihydrodiazapentacenes. *The Journal of Organic Chemistry*, 2009. 74(11): p. 4343-4349.
- [212]. Gerson, F. and W. Huber, *Electron spin resonance spectroscopy of organic radicals*. 2003: John Wiley & Sons.
- [213]. Carrington, A. and J. Dos Santos-Veiga, Electron spin resonance spectra of nitrogen heterocyclic radical ions. *Molecular Physics*, 1962. 5(1): p. 21-29.

- [214]. Mueller, S., J. Lüttig, P. Malý, L. Ji, J. Han, M. Moos, T.B. Marder, U.H.F. Bunz, A. Dreuw, C. Lambert, and T. Brixner, Rapid multiple-quantum three-dimensional fluorescence spectroscopy disentangles quantum pathways. *Nature Communications*, 2019. 10(1): p. 4735.
- [215]. Davies, A.G., G. Gescheidt, K.M. Ng, and M.K. Shepherd, The EPR spectrum of the dibenzo[b,h]biphenylene radical anion and cation: the pairing principle and the Mills–Nixon effect. *Journal of the Chemical Society, Perkin Transactions 2*, 1994(12): p. 2423-2426.
- [216]. Ruiz-Morales, Y., HOMO–LUMO Gap as an Index of Molecular Size and Structure for Polycyclic Aromatic Hydrocarbons (PAHs) and Asphaltenes: A Theoretical Study. I. *The Journal of Physical Chemistry A*, 2002. 106(46): p. 11283-11308.
- [217]. Mondal, R., R.M. Adhikari, B.K. Shah, and D.C. Neckers, Revisiting the Stability of Hexacenes. *Organic Letters*, 2007. 9(13): p. 2505-2508.
- [218]. Jurchescu, O.D., J. Baas and T.T.M. Palstra, Effect of impurities on the mobility of single crystal pentacene. *Applied Physics Letters*, 2004. 84(16): p. 3061-3063.
- [219]. Xu, X., Y. Yao, B. Shan, X. Gu, D. Liu, J. Liu, J. Xu, N. Zhao, W. Hu, and Q. Miao, Electron Mobility Exceeding $10 \text{ cm}^2 \text{ V}^{-1} \text{ s}^{-1}$ and Band-Like Charge Transport in Solution-Processed n-Channel Organic Thin-Film Transistors. *Advanced Materials*, 2016. 28(26): p. 5276-5283.
- [220]. Reiss, H., Laufende Dissertation im Arbeitskreis Bunz. 2019.
- [221]. Bisquert, J., Interpretation of electron diffusion coefficient in organic and inorganic semiconductors with broad distributions of states. *Physical Chemistry Chemical Physics*, 2008. 10(22): p. 3175-3194.
- [222]. Wen, S., A. Li, J. Song, W. Deng, K. Han, and W.A. Goddard, First-Principles Investigation of Anisotropic Hole Mobilities in Organic Semiconductors. *The Journal of Physical Chemistry B*, 2009. 113(26): p. 8813-8819.
- [223]. Pfister, J., R.F. Fink, B. Engels, C. Deibel, and V. Stehr, First-principles calculations of anisotropic charge-carrier mobilities in organic semiconductor crystals. *Physical Review B*, 2011. 83(15): p. 155208.
- [224]. Deng, W. and W.A. Goddard, Predictions of Hole Mobilities in Oligoacene Organic Semiconductors from Quantum Mechanical Calculations. *The Journal of Physical Chemistry B*, 2004. 108(25): p. 8614-8621.
- [225]. Karl, N., Charge carrier transport in organic semiconductors. *Synthetic Metals*, 2003. 133-134: p. 649-657.
- [226]. Yang, X., L. Wang, Z. Shuai, Y. Zhao, and G. Nan, Nuclear tunneling effects of charge transport in rubrene, tetracene, and pentacene. *Physical Review B*, 2009. 79(11): p. 115203.

- [227]. Marcus, R.A., Electron transfer reactions in chemistry. Theory and experiment. *Reviews of Modern Physics*, 1993. 65(3): p. 599-610.
- [228]. Brédas, J., D. Beljonne, V. Coropceanu, and J. Cornil, Charge-Transfer and Energy-Transfer Processes in π -Conjugated Oligomers and Polymers: A Molecular Picture. *Chemical Reviews*, 2004. 104(11): p. 4971-5004.
- [229]. Norton, J.E. and J. Brédas, Polarization Energies in Oligoacene Semiconductor Crystals. *Journal of the American Chemical Society*, 2008. 130(37): p. 12377-12384.
- [230]. McMahon, D.P. and A. Troisi, Evaluation of the External Reorganization Energy of Polyacenes. *The Journal of Physical Chemistry Letters*, 2010. 1(6): p. 941-946.
- [231]. Newton, M.D., Quantum chemical probes of electron-transfer kinetics: the nature of donor-acceptor interactions. *Chemical Reviews*, 1991. 91(5): p. 767-792.
- [232]. Wu, Q. and T. Van Voorhis, Extracting electron transfer coupling elements from constrained density functional theory. *The Journal of Chemical Physics*, 2006. 125(16): p. 164105.
- [233]. Groom, C.R., I.J. Bruno, M.P. Lightfoot, and S.C. Ward, The Cambridge Structural Database. *Acta Crystallographica Section B*, 2016. 72(2): p. 171-179.
- [234]. Macrae, C.F., P.R. Edgington, P. McCabe, E. Pidcock, G.P. Shields, R. Taylor, M. Towler, and J. van de Streek, Mercury: visualization and analysis of crystal structures. *Journal of Applied Crystallography*, 2006. 39(3): p. 453-457.
- [235]. Avogadro: an open-source molecular builder and visualization tool. Version 1.2.0. <http://avogadro.cc/>.
- [236]. Bernard, Y.A., Y. Shao and A.I. Krylov, General formulation of spin-flip time-dependent density functional theory using non-collinear kernels: Theory, implementation, and benchmarks. *The Journal of Chemical Physics*, 2012. 136(20): p. 204103.
- [237]. Kubas, A., F. Gajdos, A. Heck, H. Oberhofer, M. Elstner, and J. Blumberger, Electronic couplings for molecular charge transfer: benchmarking CDFT, FODFT and FODFTB against high-level ab initio calculations. II. *Physical Chemistry Chemical Physics*, 2015. 17(22): p. 14342-14354.
- [238]. Hay, P.J. and W.R. Wadt, Ab initio effective core potentials for molecular calculations. Potentials for the transition metal atoms Sc to Hg. *The Journal of Chemical Physics*, 1985. 82(1): p. 270-283.
- [239]. Sánchez-Carrera, R.S., V. Coropceanu, D.A. Da Silva Filho, R. Friedlein, W. Osikowicz, R. Murdey, C. Suess, W.R. Salaneck, and J. Brédas, Vibronic Coupling in the Ground and Excited States of Oligoacene Cations. *The Journal of Physical Chemistry B*, 2006. 110(38): p. 18904-18911.
- [240]. Delgado, M.C.R., E. Kim, D.A.D.S. Filho, and J. Bredas, Tuning the Charge-Transport Parameters of Perylene Diimide Single Crystals via End and/or Core Functionalization: A Density

Functional Theory Investigation. *Journal of the American Chemical Society*, 2010. 132(10): p. 3375-3387.

[241]. Feller, D., The role of databases in support of computational chemistry calculations. *Journal of Computational Chemistry*, 1996. 17(13): p. 1571-1586.

[242]. Brédas, J.L., J.P. Calbert, D.A. Da Silva Filho, and J. Cornil, Organic semiconductors: A theoretical characterization of the basic parameters governing charge transport. *Proceedings of the National Academy of Sciences*, 2002. 99(9): p. 5804.

Publications During Ph.D. Study

1. **J. Han**, D. Rehn, and **A. Dreuw**, Theoretical Simulation of Electron Transport Process in Halogenated N-Heteroacenes. Prepared for submission (Chapter 6 of my Ph.D. thesis), 2020.
2. **J. Han**, P. Ludwig, and **A. Dreuw**, Evaluation of Single-reference DFT-based Approaches on Spectroscopic Signatures of Excited States Involved in Singlet Fission. Prepared for submission (Chapter 4 of my Ph.D. thesis), 2020.
3. N. Alagna, **J. Han (co-first author)**, N. Wollscheid, J.L. Perez Lustres, J. Herz, S. Hahn, S. Koser, F. Paulus, U.H.F. Bunz, **A. Dreuw**, T. Buckup, and M. Motzkus, Tailoring Ultrafast Singlet Fission by the Chemical Modification of Phenazinothiadiazoles. *Journal of the American Chemical Society*, 2019. 141(22): p. 8834. **IF**=14.695
4. H. Reiss, L. Ji, **J. Han**, S. Koser, O. Tverskoy, J. Freudenberg, F. Hinkel, M. Moos, A. Friedrich, I. Krummenacher, C. Lambert, H. Braunschweig, **A. Dreuw**, T.B. Marder, and U.H.F. Bunz, Bromination Improves the Electron Mobility of Tetraazapentacene. *Angewandte Chemie International Edition*, 2018. 57(30): p. 9543. **IF**=12.257
5. S. Mueller, J. Lüttig, P. Malý, L. Ji, **J. Han**, M. Moos, T.B. Marder, U.H.F. Bunz, **A. Dreuw**, C. Lambert, and T. Brixner, Rapid multiple-quantum three-dimensional fluorescence spectroscopy disentangles quantum pathways. *Nature Communications*, 2019. 10(1): p. 4735. **IF**=11.878
6. L. Ji, A. Friedrich, I. Krummenacher, A. Eichhorn, H. Braunschweig, M. Moos, S. Hahn, F.L. Geyer, O. Tverskoy, **J. Han**, C. Lambert, **A. Dreuw**, T.B. Marder, and U.H.F. Bunz, Preparation, Properties, and Structures of the Radical Anions and Dianions of Azapentacenes. *Journal of the American Chemical Society*, 2017. 139(44): p. 15968. **IF**=14.695
7. L. Ji, M. Haehnel, I. Krummenacher, P. Biegger, F.L. Geyer, O. Tverskoy, M. Schaffroth, **J. Han**, **A. Dreuw**, T.B. Marder, and U.H.F. Bunz, The Radical Anion

- and Dianion of Tetraazapentacene. *Angewandte Chemie International Edition*, 2016. 55(35): p. 10498. **IF**=12.257
8. G. Xie, V. Brosius, **J. Han**, F. Rominger, **A. Dreuw**, J. Freudenberg, and U.H.F. Bunz, Stable Radical Cations of N,N'—Diarylated Dihydrodiazapentacenes. *Chemistry—A European Journal*, 2020. 26(1): p. 160. **IF**=5.160
 9. L. Ji, S. Hahn, P. Biegger, H. Reiss, **J. Han**, A. Friedrich, I. Krummenacher, H. Braunschweig, M. Moos, J. Freudenberg, C. Lambert, **A. Dreuw**, T.B. Marder, and U.H.F. Bunz, Mono - and Dianion of a Bis(benzobuta)tetraazapentacene Derivative. *Chemistry—A European Journal*, 2019. 25(42): p. 9840. **IF**=5.160
 10. V.J. Rao, M. Matthiesen, K.P. Goetz, C. Huck, C. Yim, R. Siris, **J. Han**, S. Hahn, U.H.F. Bunz, **A. Dreuw**, G.S. Duesberg, A. Pucci, and J. Zaumseil, AFM-IR and IR-SNOM for the Characterization of Small Molecule Organic Semiconductors. *The Journal of Physical Chemistry C*, 2020. 124(9): p. 5331. **IF**=4.309
 11. N. Alagna, J.L. Pérez Lustres, N. Wollscheid, Q. Luo, **J. Han**, **A. Dreuw**, F.L. Geyer, V. Brosius, U.H.F. Bunz, T. Buckup, and M. Motzkus, Singlet Fission in Tetraaza-TIPS-Pentacene Oligomers: From fs Excitation to μ s Triplet Decay via the Biexcitonic State. *The Journal of Physical Chemistry B*, 2019. 123(50): p. 10780. **IF**=2.923